An Investigation of the Composite Polymer Electrolytes and Electrocatalysts for the Proton Exchange Membrane Fuel cell

A Thesis Submitted By

Ravi Kumar. M.Sc.

For the Degree of Doctor of Philosophy

School of Chemical Engineering and Advanced Materials
Newcastle University

February 2014

Abstract

Durability is one of the major issues for the successful commercialisation of polymer electrolyte membrane fuel cells (PEMFCs) and it mainly depends on the stability of the individual cell components. In order to minimise the durability issues, the development of new materials or modification to replace the existing fuel cell components is required. The typically used proton exchange membrane (PEM) is the perfluorosulfonated polymer such as Nafion® and electrocatalysts for PEMFC is high surface area carbon supported platinum electrocatalyst (Pt/C). A higher temperature of operation (>80 ^{o}C) of PEMFC would boost their performance by enhancing the electrochemical kinetics and also improve the carbon monoxide tolerance of platinum catalysts. A Nafion® type membrane is not suitable for higher temperature operation as its proton conductivity mainly depends on the hydration level.

An approach to improve the proton conductivity of Nafion® based membranes is the incorporation of hydrophilic inorganic oxide materials into the Nafion® polymer matrix. A composite membrane based on graphite oxide (GO) has been developed and demonstrated as an alternative PEM for high temperature operation up to 120 ^{o}C. GO is an insulator and hydrophilic in nature. GO exhibits proton conductivity due to the presence of acidic functional groups like, carboxylic acid, hydroxyl groups and epoxy groups. Further functionalisation of GO with sulfonic acid (called SGO) improves the proton transport properties of GO which in turn improves the composite membrane proton conductivity. Free standing GO and SGO papers were fabricated and evaluated to understand their proton transport mechanism. The in-plane and through-plane proton conductivities of GO paper were 0.008 and 0.004 S.cm^{-1} at 30 ^{o}C and 25% RH respectively. The in-plane and through-plane proton conductivities of SGO paper were 0.04 and 0.012 S.cm^{-1} at 30 ^{o}C and 25% RH respectively. The fuel cell performance of a membrane electrode assembly made with SGO paper gave a maximum power density of 113 mW cm^{-2}.

GO/Nafion composite membranes were fabricated with different GO content. The composite membranes with an optimum of 4 wt% GO showed better mechanical strength (tensile strength of 8.17 MPa) and water uptake (37.2%) compared to recast Nafion. A GO (4 wt%) /Nafion composite membrane gave a high ion exchange capacity (IEC) value of 1.38 meq g^{-1}. The proton conductivity of GO (4 wt%) /Nafion was 0.026 S.cm^{-1} at 120 ^{o}C. SGO/Nafion composite membrane showed improved proton

conductivity (0.029 $S.cm^{-1}$). The SGO/Nafion composite membrane gave peak power density of 240 mW cm^{-2}, whereas GO/Nafion composite membrane gave a power density of 200 mW cm^{-2} at 120 ^{o}C and 25% RH. The stability and durability of GO and SGO/Nafion composite membranes was investigated under fuel cell operating conditions and compared with recast Nafion.

A non fluorinated proton exchange membrane based sulfonated poly ether-ether ketone (SPEEK) was used to develop a composite membrane with SGO. SGO (4 wt%) /SPEEK composite membrane showed high IEC of 2.3 meq g^{-1} and proton conductivity of 0.055 $S.cm^{-1}$ at 80 ^{o}C and 30% RH. SGO (4 wt%) /SPEEK composite membrane gave a power density of 378 mW cm^{-2} at 80 ^{o}C and 30% RH, which was higher than that of recast SPEEK (254 mW cm^{-2}).

Transition metal nitride based electrocatalyst support such as titanium nitride (TiN), has been used to replace carbon to support Pt and Pt-Co alloy for PEMFC cathode. Nafion® stabilised Pt nanoparticles supported on TiN (Pt/TiN) were prepared and evaluated as cathode electrocatalyst for PEMFC. Pt/TiN showed better electrocatalytic activity, stability and durability under fuel cell operating conditions compared to commercial Pt/C. Pt/TiN retained 66% of electrochemical active surface area (ECSA) after 1000 potential cycles (cycled between the potential range of +0.6 to +1.20 V vs. RHE) under fuel cell operating conditions. The ECSA of the Pt/C catalyst fell by 75%.

Pt/TiN was also evaluated for its suitability in phosphoric acid based PEMFCs. Pt/TiN showed better durability than Pt/C under fuel cell operating conditions. Pt/TiN showed a two-fold increase in mass and specific activities than Pt/C as calculated from oxygen reduction reaction data at 0.9 V. An improved durability of Pt/TiN resulted from a Nafion® layer surrounding the Pt protecting from phosphate ion adsorption.

Alloying of Pt with 3d transition metals changes the electronic structure of Pt (Pt becomes e^{-} deficient) and enhances the electrocatalytic activity of PtM alloy compared to Pt. 3d transition metals such as Fe, Co and Ni are reported to be more active than other metals. Pt-Co alloy supported on TiN was prepared and evaluated. Pt-Co/TiN showed about +21 and +32 mV positive shifts in half-wave potential compare to Pt/TiN and conventional Pt/C respectively. After 5000 potential cycles, the ECSA of Pt-Co/TiN had decayed by about 55%, whereas Pt/TiN and Pt/C showed a greater loss in ECSA of 70%.

Acknowledgements

I believe very honestly that my thesis would be incomplete without thanking the people who really helped me during my various stages of research activities at the School of Chemical Engineering and Advanced Materials (SCEAM) of the Newcastle University. Let me share some of my personal anecdotes which I have had during my years of stay in this beautiful campus.

I thank from the bottom of my heart, Prof. Keith Scott for giving me an opportunity to work in his fuel cell research group. His constant vigil and encouraging guidance has finally shaped up this work to an awesome conclusion. I am always grateful to him for introducing me to the field of electrochemical energy conversion system.

I take this opportunity to express my gratitude to Dr. Mohamed Mamlouk (Moody) for his enormous help throughout the study.

I thank my seniors, Dr. SMS Kumar (CECRI, India), Dr. Anca, Dr. Cao, Dr. Wu Xu, Dr. Xu Wang, Dr. Chenxi Xu, Dr. Xioteng Liu (Terry) and Mr. Aris. I thank you all of my friends and colleagues in the lab for their wonderful time Asier, Vinod, Ukrit, Lei, Taiwo, Kemi, Luke and Richard.

I thank Dr. Mohammed Mustafa (University of St. Andrews) for his wonderful time and fruitful discussion.

I am extremely grateful to Professor P.V. Kamath for his inspiring lectures and encouragement to do research during my M.Sc days.

I acknowledge Ms. Pauline Clark, Dr. Maggie white (Chemical and Material Analysis) for helping me with morphological and structural characterisation. I also acknowledge Mr. Richard Baron (School of Chemistry) for FT-IR analysis of the membrane samples and Mr. Malcolm Black (School of Mechanical and Systems Engineering) who helped me to do mechanical testing of the membranes. I am very much great full to NEXUS (School of Mechanical and Systems Engineering) for XPS facility. I also acknowledge LENNF User's facility at Leeds University, an EPSRC facility for HRTEM analysis. I honestly accept that without their help, this work would not have materialized.

I would like to thank all our SCEAM technical support team and office staff for their valuable suggestions and advice.

I thank all my family members for being with me and understanding me in this endeavour.

Finally, I thank Engineering and Physical Sciences Research Council (EPSRC) through supergen fuel cell consortium for financial support.

Table of contents

List of Figures

Chapter 2

Chapter 3

Chapter 4

Chapter 5

List of Schemes

Chapter 4

List of Tables

Chapter 2

Chapter 4

Chapter 5

Chapter 7

List of Symbols and Abbreviations

α	Charge Transfer Coefficient
η	Overpotential
ω	Rotation Rate
υ	Kinematic Viscosity of the Electrolyte
θ	Angle of Incidence/Coverage
λ	Wavelength of X-ray beam
μm	Micrometer (10^{-6} meters)
σ	Ionic Conductivity
Ω	Ohms
$\Delta H°$	Standard Enthalpy Change
$\Delta G°$	Standard Gibbs Free Energy
ΔG	Gibbs Free Energy
$\Delta S°$	Standard Entropy Change
Å	Angstroms (10^{-10} meters)
atm	Atmospheric Pressure
A	Ampere
B	Levich Constant
C	Coulombs
^{o}C	Degree Celsius
C_{O2}	Concentration of Molecular Oxygen
D_o	Diffusion Coefficient
e^-	Electron
eV	Electron Volts
Eo	Binding Energy
E°	Standard Reduction Potential
E	Formal Potential
E_P	Peak Potential
Epa	Anodic Peak Potential
Epc	Cathodic Peak Potential
F	Faraday's Constant
h	Hour
ħ	Planck's Constant
i	Current Density

i_k	Kinetic Current Density
i_{lim}	Limiting Current Density
i_o	Exchange Current Density
i_m	Mass activity
i_s	Specific activity
I	Current
I_o	Intensity of Incident X-ray Beam
L	Membrane Thickness
n	Number of Electrons Transferred
nm	Nanometre (10^{-9} meters)
R	Gas Constant
T	Temperature
Tg	Glass Transition Temperature
V	Volts
Ve	Equilibrium Voltage
W	Watt
Z	Atomic Number
Z’	Real impedance
Z’’	Imaginary impedance
AAEM	Alkaline Anion Exchange Membrane
ADT	Accelerated Degradation Test
AFC	Alkaline Fuel Cell
AMFC	Alkaline Membrane Fuel Cell
BCC	Body Centered Cubic
CE	Counter Electrode
CV	Cyclic Voltammetry
DFT	Density Functional Theory
ECSA	Electrochemical Active Surface Area
EDAX/EDS	Energy Dispersive Analysis of X-rays
FCC	Face Centered Cubic
FTIR	Fourier-Transform Infrared Spectroscopy
FRA	Frequency Response Analyzer
GC	Glassy Carbon
GDE	Gas Diffusion Electrode
GDL	Gas Diffusion Layer

HRTEM	High Resolution Transmission Electron Microscopy
IEC	Ion Exchange Capacity
MEA	Membrane Electrode Assembly
OCP	Open Circuit Potential
ORR	Oxygen Reduction Reaction
PAFC	Phosphoric Acid Fuel Cells
PEM	Proton Exchange Membrane
PEMFC	Proton Exchange Membrane Fuel Cell
RH	Relative Humidity
RHE	Reversible Hydrogen Electrode
RPM	Revolutions Per Minute
RDE	Rotating Disk Electrode
RE	Reference Electrode
SLPM	Standard Litres Per Minute
SEM	Scanning Electron Microscope
SHE	Standard Hydrogen Electrode
TEM	Transmission Electron Microscopy
WE	Working Electrode
XRD	X-ray Diffraction
XPS	X-ray photo electron spectroscopy

Chapter 1. Introduction and Overview

1.1 Overview

Polymer electrolyte membrane fuel cells (PEMFCs) are promising candidates for portable power source, electric vehicles and transport applications [1, 2]. The large scale commercialisation of PEMFC is hindered by durability, stability and degradation of its components [3, 4]. The performance of a PEM fuel cell or stack is affected by many internal and external factors, such as fuel cell design and assembly, degradation of materials, operational conditions, and impurities or contaminants present in the fuel [5, 6]. The development of suitable materials for the PEMFC technology is more challenging. The typical polymer electrolyte membrane (PEM) used currently for fuel cells are perfluorosulfonicacid (PFSA) based polymer electrolyte membranes such as Nafion® and are limited to an operating temperature of 60 to 80 ^{o}C [7]. In order to enhance the electrochemical kinetics, and improve the CO tolerance of Pt (to reduce the poisoning of Pt with CO) operation of fuel cell at above 100 ^{o}C is required [8, 9, 10]. The proton transport of PFSA based membranes mainly depends on the hydration level and fuel cells operating above 80 ^{o}C with this membrane is not practical [11]. To improve the performance of polymer electrolyte membranes, different approaches have been employed. Synthesis of high temperature polymer electrolytes such as the phosphoric acid doped polybenzimidazole (PBI) membrane that could operate without humidification is widely employed [12, 13]. Another approach is to use inorganic-organic composite materials to fabricate Nafion® based composite membranes to increase the proton conductivity, mechanical strength, chemical stability and durability for high temperature operation [14, 15].

The widely used electrocatalyst for fuel cells is Pt and Pt alloy nanoparticles supported on high surface area carbon (Pt/C). The degradation of Pt or Pt alloy based catalysts, caused mainly by support oxidation, and is recognized as one of the most important reasons for the loss of fuel cell performance [16]. The Pt nanoparticles detach from conventional carbon supports because of the corrosion they suffered under extremely harsh working environments, part of them dissolving with cationic Pt (Pt^{2+}, Pt^{4+}) and some others agglomerating into larger particles [17]. Moreover, a portion of the Pt particles is trapped in the microspores of porous carbon support surfaces and are isolated from the ionomer phase which is essential for PEMFCs. Thus, considerable efforts have been devoted to the development of new alternative support materials to improve the stability of catalysts.

1.2 Objectives

The aim of the research was the fabrication, characterisation and electrochemical evaluation of components like composite polymer electrolyte membrane, electrocatalyst and catalyst support under fuel cell operating conditions.

The research was comprised of the following aims.

1. Preparation and characterisation of graphite oxide (GO) and sulfonated graphite oxide (SGO).
2. Preparation, characterisation and evaluation of GO/Nafion and SGO/Nafion composite membranes for PEMFCs.
3. Preparation, characterisation and evaluation of SGO/SPEEK composite membrane for PEMFCs.
4. Durability and degradation studies of GO/Nafion, SGO/Nafion composite membranes under PEMFC operating conditions.
5. Synthesis, characterisation and evaluation of Pt and Pt-Co nanoparticles supported on titanium nitride (TiN) as cathode electrocatalysts for PEMFCs.

The work is presented in the following sections as detailed below

Chapter 1 gives introduction and the aim of the present investigation.
Chapter 2 provides the literature survey related to the present study.
Chapter 3 comprises experimental and theoretical methods adopted in the present work.

Chapter 4 furnishes detailed characterisation of GO and SGO using various physicochemical and electrochemical techniques. Evaluation of SGO paper as a polymer electrolyte for PEMFCs.

Chapter 5 details the studies on GO and SGO/Nafion composite membrane physicochemical characterisation, proton conductivity test, fuel cell analysis and degradation studies.

Chapter 6 describes the SGO/SPEEK composite membrane physicochemical characterisation, proton conductivity test and fuel cell analysis.

Chapter 7 explains the physicochemical and electrochemical evaluation of Nafion® stabilised Pt and Pt-Co alloy nanoparticles supported on TiN in sulfuric acid and phosphoric acid medium.

Chapter 8 gives the conclusions and future work of the study.

References

[1] J. Wu, X. Z. Yuan, J. J. Martin, H. Wang, J. Zhang, J. Shen, S. Wu, W. Merida, *A review of PEM fuel cell durability: Degradation mechanisms and mitigation strategies*, Journal of Power Sources, **2008**, 184, 104-119.

[2] R. Kannan, M. Parthasarathy, S. U. Maraveedu, S. Kurungot, V. K. Pillai. *Domain Size Manipulation of Perflouorinated Polymer Electrolytes by Sulfonic Acid-Functionalized MWCNTs To Enhance Fuel Cell Performance*, Langmuir, **2009**, 25 (14), 8299–8305.

[3] S.P. Tung, B.J. Hwang, *Special Issue Lucerne FUEL CELL FORUM (2005) I*, Fuel Cells, **2007**, ***7***, 32.

[4] V. Baglio, A. Stassi, F.V. Matera, A. Di Blasi, V. Antonucci, A.S. Arico, *Optimization of properties and operating parameters of a passive DMFC mini-stack at ambient temperature*, Journal of Power Sources, **2008**, 180, 797–802.

[5] P. L. Antonucci, A. S. Arico, P. Creti, et al. *Investigation of a direct methanol fuel cell based on a composite Nafion®-silica electrolyte for high temperature operation*, Solid State Ionics, **1999**, 125, 431-437.

[6] N. Miyake, J. S. Wainright, R. F. Savinell, *Water and Methanol Uptakes in Nafion Membranes and Membrane Effects on Direct Methanol Cell Performance*, J. Electrochem.Soc, **2001**, 184, A898.

[7] R.Kannan, Bhalchandr A. Kakade, V. K. Pillai. *Polymer Electrolyte Fuel Cells Using Nafion-Based Composite Membranes with Functionalized Carbon Nanotube*, Angew.Chem. Int. Ed, **2008,** 47, 2653.

[8] Wainright, J.S., et al. *Acid doped polybenzimidazole, a new polymer electrolyte*. In Proc.Electrochem. Soc. **1994**.

[9] Chenxi Xu, Yuancheng Cao, Ravi Kumar, Xu Wu, Xu Wang and Keith Scott, *A polybenzimidazole/sulfonated graphite oxide composite membrane for high temperature polymer electrolyte membrane fuel cells*, J. Mater. Chem, **2011**, 21, 11359-11364.

[10] Hadis Zarrin, Drew Higgins, Yu Jun, Zhongwei Chen, and Michael Fowler, *Functionalized Graphene Oxide Nanocomposite Membrane for Low Humidity and High Temperature Proton Exchange Membrane Fuel Cells*, J. Phys. Chem. C, **2011**, 115, 20774–20781.

[11] Mamlouk M, Scott K, *Phosphoric acid-doped electrodes for a PBI polymer membrane fuel cell*, International Journal of Energy Research, **2011**, 35(6), 507-519.

[12] K.D. Kreur, *Proton Conductivity: Materials and Applications*, Chem. Mater. **1996**, 8, 610.

[13] Ravikumar, Scott K, *Freestanding sulfonated graphene oxide paper: a new polymer electrolyte for polymer electrolyte fuel cells*, Chemical communications, **2012,** 48(45), 5584-5586.

[14] G. Alberti, M. Casciola, *composite membranes FOR medium-temperature PEM fuel cells*, Ann. Rev. Mater. Res, **2003**, 33, 129.

[15] Mamlouk M, Jang JH, Scott K. *Intermediate Temperature Fuel Cell and Oxygen Reduction Studies with Carbon-Supported Platinum Alloy Catalysts in Phosphoric Acid Based Systems.* Journal of Fuel Cell Science and Technology, **2012**, 9(1), 011002**.**

[16] Ruben Ornelas, Alessandro Stassi, Ester Modica, Antonino S. Arico and Vincenzo Antonucci, *Proton Exchange Membrane Fuel Cells*, ECS Transactions, **2006**, 3 (1) 633-641.

[17] Kumar SMS, Hidyatai N, Herrero JS, Irusta S, Scott K, *Efficient tuning of the Pt nano-particle mono-dispersion on Vulcan XC-72R by selective pre-treatment and electrochemical evaluation of hydrogen oxidation and oxygen reduction reactions*, International Journal of Hydrogen energy International Journal of Hydrogen Energy**,** **2011**,36(9),5453-5465.

Chapter 2. Literature review

2.1 History of fuel cells

Fuel cells are electrochemical devices that convert the chemical energy of a fuel into electrical energy. Electrochemical redox reactions on respective electrodes of fuel cells can provide electricity continuously, as long as the fuel is supplied. Among the three types of electrochemical energy systems namely, fuel cells, batteries and capacitors, the fuel cell occupies a special position because of the high specific energy associated with the device [1]. Moreover, specific energy of a fuel cell is far superior to a battery and a capacitor. This is further augmented from the plot of specific power (the rate at which energy can be released) vs. specific energy which is known as Ragone plot shown in figure 2.1. However, fuel cells do not possess high power density. Hence, fuel cell should be coupled with a capacitor when both energy density and power density requirements are high.

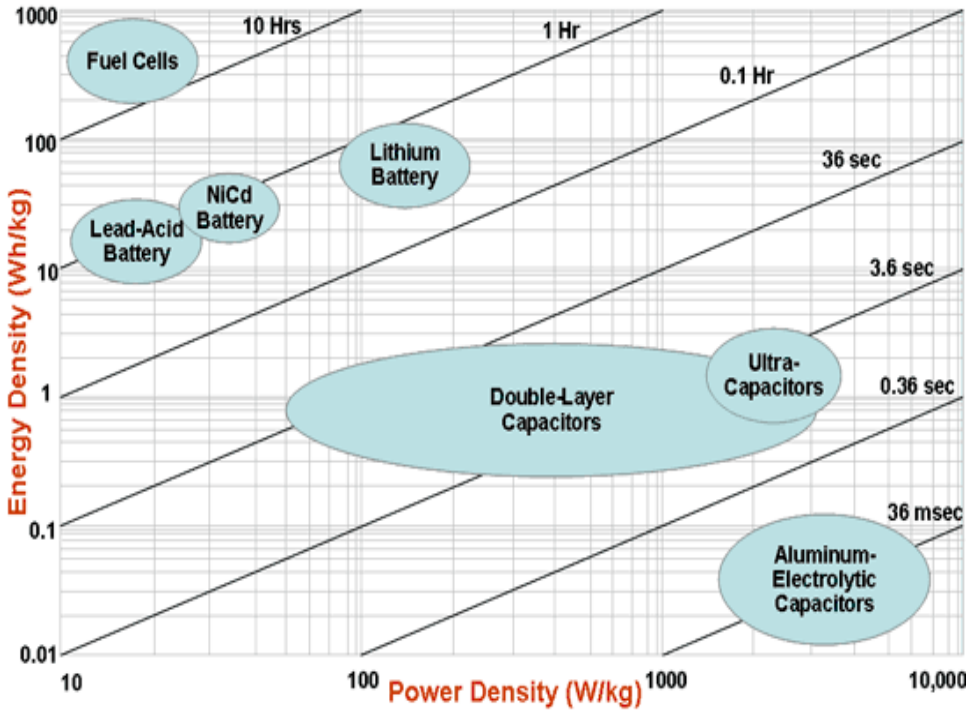

Figure 2.1, Ragone plot for electrochemical energy systems [2]

The history of fuel cell (FC) begins with Sir William Grove who started experiments on the hydrogen/oxygen fuel cell consisting of platinised electrodes immersed in sulphuric acid as shown in figure 2.2 in 1839 [3]. The basic electrochemical reactions occur in the fuel cells are as follows.

$$H_2 \rightarrow 2H^+ + 2e^- \qquad (E^0 = 0\ V) \qquad (2.1)$$

$$1/2\ O_2 + 2H^+ + 2e^- \rightarrow H_2O \qquad (E^0 = 1.23\ V) \qquad (2.2)$$

Francis Bacon developed his first successful fuel cell using hydrogen and oxygen, with an alkaline electrolyte and nickel electrodes in 1932, finally Bacon and co-worker developed 5 kW fuel cell. In 1960s, NASA demonstrated alkaline polymer electrolyte fuel cells in their space shuttle vehicles [4].

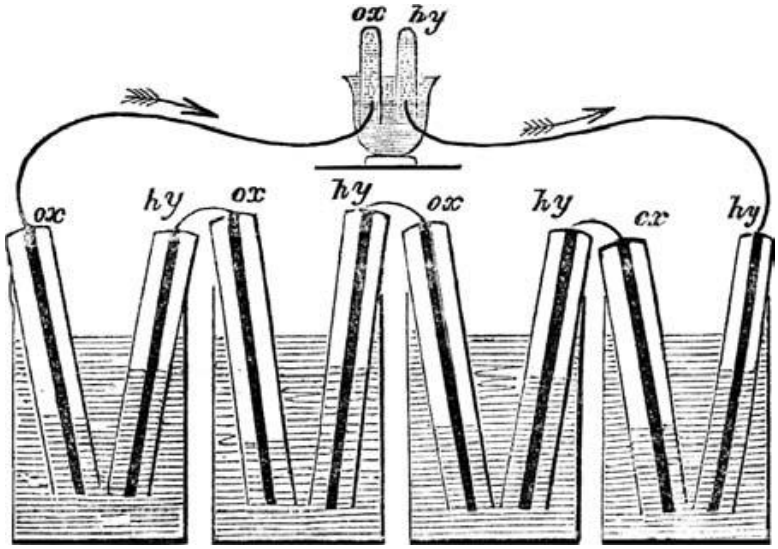

Figure 2.2, Schematic presentation of Grove gas batteries with four cells in series [3]

Hydrogen is an ideal fuel for all types of fuel cells however; there are different types of fuel cells based on electrolyte used and temperature of operation [5]. Oxygen or air is the oxidant used in all types of fuel cells. The major types of fuel cells are alkaline fuel cells (AFC), molten carbonate fuel cells (MCFC), phosphoric acid fuel cells (PAFC), polymer electrolyte membrane fuel cells (PEMFC), and solid oxide fuel cells (SOFC) [6, 7,]. The Table 2.1 provides the power levels and applications of different fuel cells [8]. Based on this information fuel cells can be fabricated for various applications. The overall cell reactions can be divided in to two half cell reactions and are shown in Table 2.2 [9].

Table 2.1, The characteristics and power levels of different fuel cells [8]

Typical applications	Portable electronic equipments	Automobiles	Distributed power generation
Power (W)	1 10 100	1K 10K 100K	1M 10M
Main advantageous	High energy density; Fast recharge	Potential for zero emission; High efficiency	High efficiency; Pollution levels low; Quiet

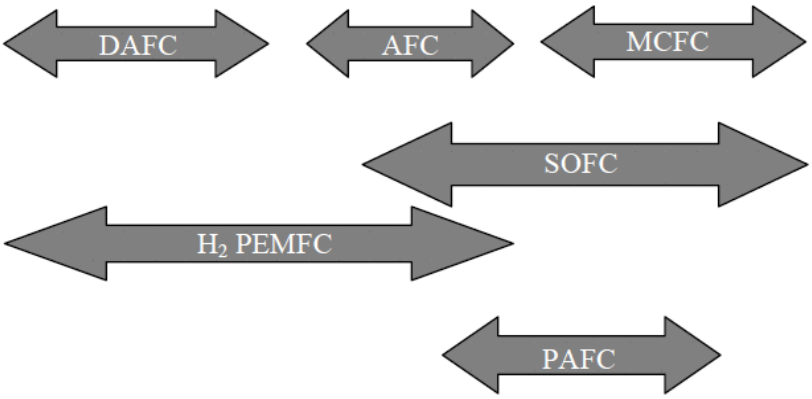

Table 2.2, Half cell reactions of various types of fuel cells [9]

Fuel cell	Anode reaction	Cathode reaction	Mobile Ion
PEMFC	$H_2 \rightarrow 2H^+ + 2e^-$	$^1/_2\,O_2 + 2H^+ + 2e^- \rightarrow H_2O$	H^+
DMFC	$CH_3OH + H_2 \rightarrow CO_2 + 6H^+ + 6e^-$	$^1/_2\,O_2 + 2H^+ + 2e^- \rightarrow H_2O$	H^+
AFC	$H_2 + 2OH^- \rightarrow 2H_2O + 2e^-$	$^1/_2\,O_2 + H_2O + 2e^- \rightarrow 2OH^-$	OH^-
PAFC	$H_2 \rightarrow 2H^+ + 2e^-$	$^1/_2\,O_2 + 2H^+ + 2e^- \rightarrow H_2O$	H^+
MCFC	$H_2 + CO_3^{2-} \rightarrow H_2O + CO_2 + 2e^-$	$^1/_2\,O_2 + CO_2 + 2e^- \rightarrow CO_3^{2-}$	CO_3^{2-}
SOFC	$H_2 + O_2^- \rightarrow H_2O + 2e^-$	$^1/_2\,O_2 + 2e^- \rightarrow O^{2-}$	O^{2-}

The direct conversion of chemical energy into electrical energy avoids the thermodynamic limitation such as Carnot efficiency in fuel cells [10]. What makes fuel cells most attractive for transport applications is the fact that they emit zero or ultralow emissions [11], and is what mainly inspired automotive companies and other fuel cell developers in the 1980s and 1990s to start developing fuel cell powered automotives [12].

Polymer electrolyte membrane fuel cells (figure 2.3) have been proposed as one of the most promising power sources for portable and automotive applications [13], Direct alcohol fuel cells (DAFCs) such as direct methanol fuel cells (DMFCs) and direct ethanol fuel cells (DEFCs) are attracted for very small and portable appliances such as mobile phones and laptops and they can replace batteries. Solid oxide fuel cells (SOFCs) operate at higher temperature and remove the use of noble metal catalyst and poisoning of catalyst, thus reducing the costs of the system [14]. However, these types of fuel cells need longer start up times and hydrocarbon reforming is necessary through a separate reformer or even within the stack module [15]. Proton exchange membrane fuel cells (PEMFCs) have captured the most attention and provided the strongest impetus for technological expansion due to their low temperature operation, fast start-up, and high specific power density. They are highly suitable for portable and vehicular applications [16].

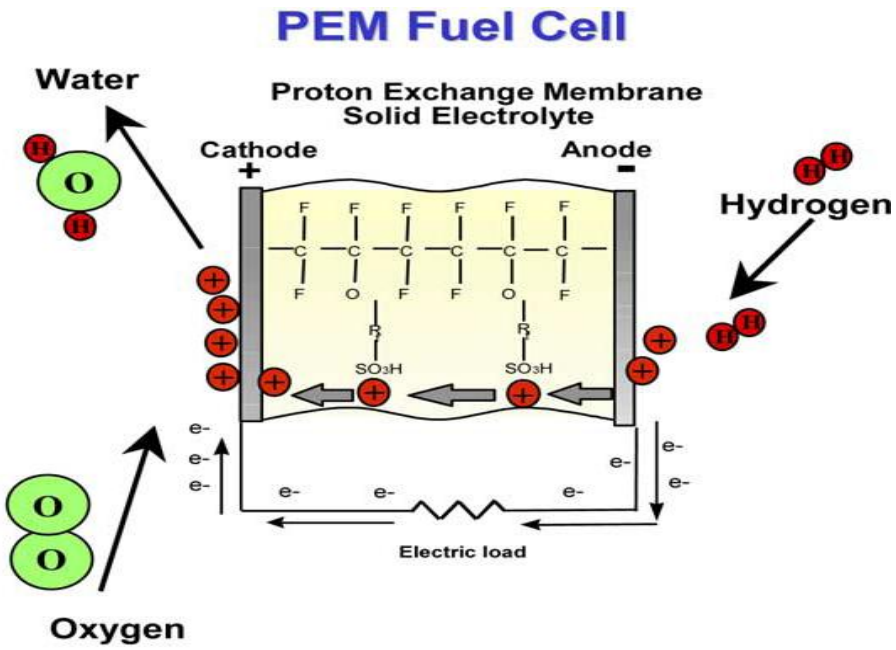

Figure 2.3, Schematic representation of polymer electrolyte fuel cells [14]

2.2 Thermodynamics of fuel cells

The operation and performance of the fuel cell can be explained based on the principles of thermodynamics and electrochemistry. The influence of thermodynamic variables like pressure, temperature, and gas concentration, etc., on the fuel cell performance has to be analysed and understood.

The most common reaction encountered in fuel cell is

$$H_2 + ½\ O_2 \longrightarrow H_2O \qquad (2.3)$$

From a thermodynamic point of view, the maximum work output obtained from the above reaction is related to the free energy change of the reaction [17]. The above reaction is spontaneous and thermodynamically favoured because the free energy of product is less than that of the reactants. The free energy change of the fuel cell reaction is given by the equation

$$\Delta G = -nFE \qquad (2.4)$$

Where ΔG is the free energy change, n is the number of moles of electrons involved, E is the reversible potential, and F is Faraday's constant (96500 C). If the reactants and the products are in their standard states, the equation can be represented as

$$\Delta G^0 = -nFE^0 \qquad (2.5)$$

The standard free energy change for the reaction (2.3) is -237 kJ mol^{-1}, n=2, F=96500 C/g. mole electron, using the equation (2.4) and hence the calculated value of E is 1.23 V [18, 19].

The Nernst equation is a representation of the relationship between the ideal standard potential E^0 for the fuel cell reaction and the ideal equilibrium potential E at other temperatures and pressures of reactants and products. Once the ideal potential at standard conditions is known, the ideal voltage can be determined at other temperatures and pressures through the use of equation (2.6) [20].

$$E = E^0 + (RT/2F) \ln [P_{H2}/P_{H2}O] + (RT/2F) \ln [P_{O2}]^{1/2} \qquad (2.6)$$

In the ideal case of an electrochemical energy conversion reaction such as a fuel cell the change in Gibbs free energy (ΔG) of the reaction is available as useful electric energy. The maximum efficiency of the electrochemical converter working under ideal condition is 100% of the ΔG, which is the intrinsically available work of chemical

reaction [21]. Therefore, fuel cells are not limited by the Carnot efficiency limit whereas other classical thermal energy converters are limited by the Carnot efficiency. A comparison has been made with the available energy in a reaction, ΔG, and it has been shown that the electrochemical method of energy conversion could convert to electricity all the energy intrinsically available as the result of a chemical reaction (independently of the method of conversion). However, even by the electrochemical method, because some of it is wasted in very fundamental processes connected with the ordering and disordering (i.e., the entropy losses and gains) that also occur in chemical reactions [22, 23].

At standard conditions of reaction the chemical energy in the hydrogen/oxygen reaction is 286 kJ mol^{-1} and the free energy available for useful work is 237 kJ mol^{-1}. Thus, efficiency of an ideal fuel cell operating reversibly on pure hydrogen and oxygen at standard conditions according to the equation (2.7) would be 83% [24].

$$\eta_e = \Delta G/\Delta H \qquad (2.7)$$

The maximum intrinsic efficiency of fuel cells based on a comparison of heat content is in the region of 90% compared with heat engines which have a maximum intrinsic efficiency of 20 to 40% [25]. In terms of Carnot expression, higher the T_H better the efficiency of heat engines. A Carnot engine would have to have a high temperature of 1753 K, with a corresponding low temperature of 298 K, to achieve an efficiency of 83% [26].

The fuel cell performance can be measured by the potential-current response of fuel cells (i-v curves) as shown in figure 2.4.

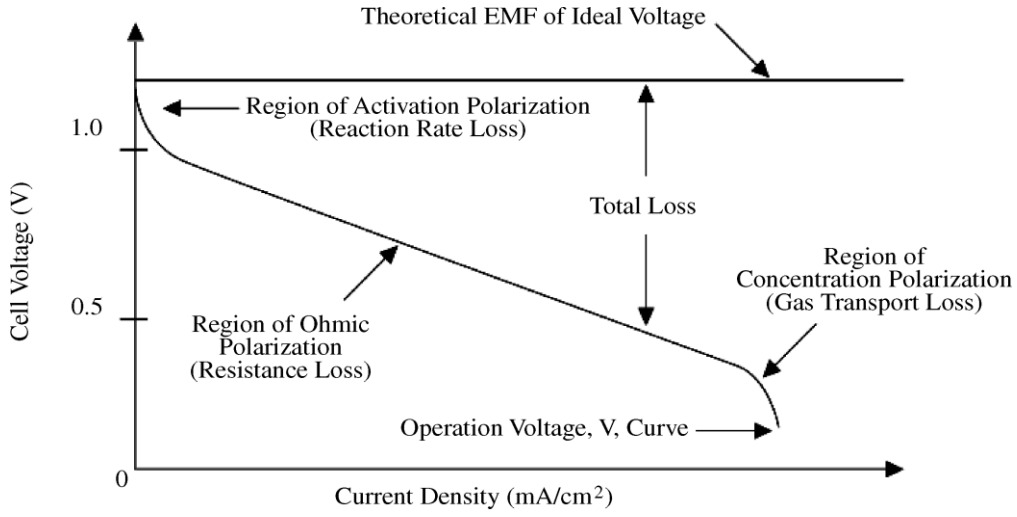

Figure 2.4, Typical i-v curve of fuel cell with various losses [27]

Electrical energy is obtained from a fuel cell when a current is drawn, but the actual cell potential is lowered from its equilibrium potential because of irreversible losses. Several factors contribute to the irreversible losses in a practical fuel cell. The losses, which are generally called polarisation or over potential, originate primarily from activation polarisation, ohmic polarisation, and gas concentration polarisation. These losses result in a cell potential for a fuel cell that is less than its ideal potential is given in the equation 2.8 [28, 29].

$$V_{cell} = V_{ocv} - \Delta V_{act} - \Delta V_{ohmic} - \Delta V_{con} \qquad (2.8)$$

Where V_{cell} is the cell voltage at a specific operating condition, V_{OCV} is the open circuit voltage, ΔV_{act} is the voltage loss caused by the activation of both anode and cathode, ΔV_{ohmic} is the ohmic voltage drop caused by resistance to electron and proton conduction and ΔV_{con} is the voltage loss caused by mass transport limitation.

Activation losses are caused by the slowness of the reaction taking place on the surface of the electrodes. A proportion of the voltage generated is lost in driving the chemical reaction that transfers the electrons. The ohmic losses cause the voltage drop due to the resistance to the flow of electrons through the material of the electrodes. This loss varies linearly with current density. Concentration polarisation, result from the change in concentration of the reactants at the surface of the electrodes. As the current density increases the fuel gradient increases [30].

The overall performance of the fuel cell is the maximum power density (W cm^{-2}) at the peak current density (A cm^{-2}) (figure 2.5). However, operation at the higher power densities will mean operation at lower cell voltages or lower cell efficiency. The voltage efficiency ($E_{p)}$ can be calculated using the equation (2.8a) [31].

$$E_p = V/Ve \qquad (2.8a)$$

Where E_p is voltage efficiency, Ve is equilibrium cell potential and V is the actual cell potential.

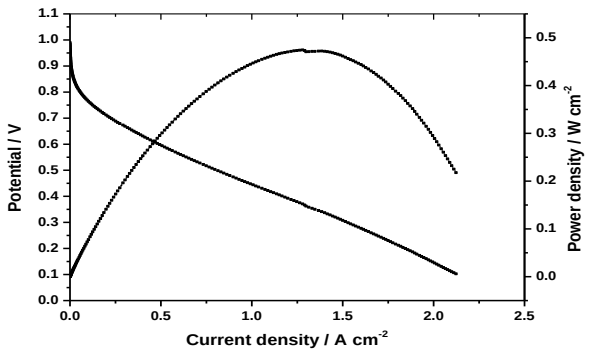

Figure 2.5, Polarisation (i-v curve) and power density curve

2.3 Kinetics of fuel cells

The kinetics of an electrochemical reaction can be described using the Butler-Volmer equation.

$$i = i_o\{\exp[\alpha nF\eta/RT] - \exp[-\beta nF\eta/RT]\} \quad (2.9)$$

Where i_o is the exchange current density of an electrochemical reaction at its reversible potential; α and β are the charge transfer coefficient; n is the number of electrons involved in the electrode reaction; and η *is* the overpotential (ε-ε^o) [20]. The equation (2.9) can be simplified to the following

$$i = i_o\,[10^{\eta/a} - 10^{\eta/a'}] \quad (2.10)$$

Where a and a' are so-called Tafel slopes and equal to 2.303 RT/αnF *and* 2.303 RT/βnF, respectively. The first term in the equation (2.10) represents the kinetics of the forward reaction (oxidation reaction) while the second term represents backward reaction (reduction reaction). Depending on the magnitude and sign of the applied overpotential, one of the reaction directions can be favoured.

In case of the fuel cell, hydrogen oxidation reaction (HOR) and oxygen reduction reaction (ORR) exhibit different exchange current densities. Because of the very fast kinetics of HOR, with negligible overpotential (< 20 mV) where the exchange current density is on the order of ~10^{-3} A cm^{-2}_{Pt}. In contrast, the ORR is very sluggish, where the exchange current density is extremely small on the order of 10^{-8} A cm^{-2}_{Pt}, and therefore large overpotential (~300 mV) is needed to drive the reaction even on the most active Pt based catalysts [20].

2.4 Polymer electrolyte membrane (PEM)

Polymer electrolyte membrane is an electrolyte made from ionic sites and designed to conduct cations or anions. In the fuel cells the PEM is sandwiched between an anode and cathode to form a so called membrane electrode assembly (MEA). The PEM plays a vital role in fuel cell by supporting the catalyst layer and transports the proton from anode to cathode and more importantly separates the oxidising and reducing environment of a fuel cell [32]. An excellent PEM should possess high proton conductivity (0.01 to 0.1 $S.cm^{-1}$), high ion exchange capacity (0.9 to 2 meq g^{-1}) and low gas permeability. Furthermore, it should possess good thermal, chemical and mechanical properties [33].

A most commonly used typical polymer electrolyte membrane for fuel cells are perfluorosulfonic acid (PFSA) based polymers such as Nafion®, developed in late 1960s by Walther Grot from DuPont [34]. Similar PFSA membranes have been developed by Dow Chemical, Asahi Glass, and Solvay Solexis. Nafion® is a first class of synthetic polymer with unique ionic properties and is result of incorporating perfluorovinyl ether groups terminated with sulfonate groups onto a PTFE back bone [35]. Superior proton conductivity of Nafion® remains major interest of research and proton transport is through hopping on sulfonic acid groups. Therefore Nafion® membrane is widely used as proton exchange membrane for fuel cells. Nafion® can be manufactured with various cationic conductivities (e.g. Na^+, K^+ etc) for chloro-alkali industry [36].

The general structure of Nafion® is shown in figure 2.6 and proton conductivity mainly depends on the hydration level and operating temperature [37]. The structure of Nafion® membrane has been explained by several models and while each model has its own limitations and it is generally accepted that there are distinct regions with in the membrane [38]. The PTFE backbone represents a hydrophobic region, whereas the sulfonic ester group is a hydrophilic region which is ionic in nature. There exists an intermediate region with some of both the phases [38]. This is called as an inverted micelle or ionic cluster containing hydrated ionic phase (figure 2.7), whereas increase in hydration level enlarges the cluster size and enhances the rate of proton transport [39].

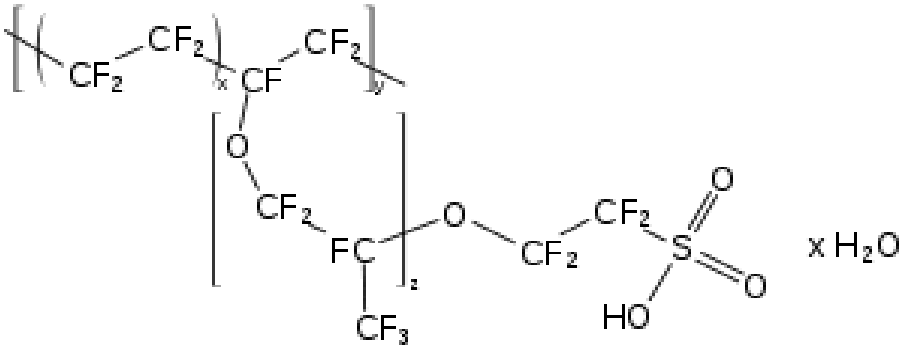

Figure 2.6, General structure Nafion® membrane [38]

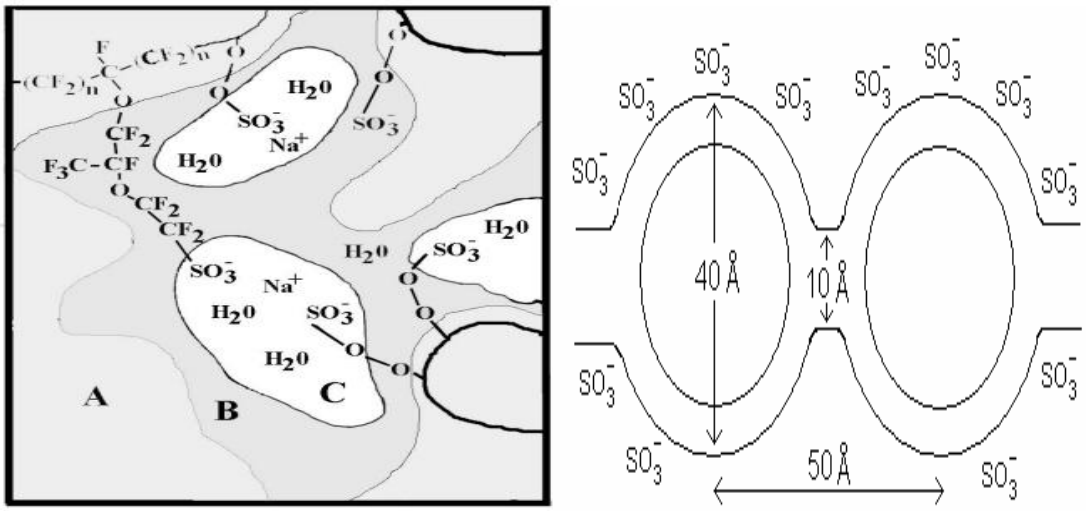

Figure 2.7, Hydrated region of Nafion® [40]

Proton conductivity measurement of Nafion® membrane has been reported under various experimental conditions and the data is shown Table 2.3. The effect of operating conditions such as water content, operating temperature, and relative humidity on conductivity of the Nafion® membrane has been widely exploited [41]. The effect of thickness has been reported by Kolde et al. for Nafion® 117 (210 µm) and Nafion® 112 (52µm) conductivities of 0.140 and 0.144 $S.cm^{-1}$ respectively [42].

Table 2.3, Proton conductivity of Nafion® membrane [41]

Nafion® membrane	Electrolyte	Technique	Membrane Thickness (µm)	Conductivity (S. cm^{-1})	Resistivity (Ω cm)
117	Water vapor RH 100% (25 ^{o}C)	AC impedance	175	0.070	14.3
117	1 M H2SO4 (20 and 80 ^{o}C)	DC current Pulse	231	0.088 and 0.231	11.4 and 4.33
117	Immersed in water (30 and 90 ^{o}C)	AC impedance	175	0.100 and 0.19	10.0 and 5.3
112	Water vapor 100% RH (65 ^{o}C)	AC impedance	60	0.100	10.0
112	Water vapor 100% RH (65 ^{o}C)	AC impedance	52	0.140	6.9
115	*In situ*, humidified gases (95 ^{o}C)	Ac impedance	125	0.074	14.1

There are different types of PEM other than Nafion® membranes used in fuel cells. These include fluoropolymers, partially fluorinated and aromatic polymers with phenylene backbone [43]. Fluorinated polymer such as sulfonated polystyrene has been evaluated as a polymer electrolyte for fuel cells; however this type of membrane suffers from a short life time because the tertiary C-H bonds in the styrene chains are sensitive to oxidation by oxygen and hydrogen peroxide [44, 45]. Partially fluorinated polymers such as sulfonated poly (tetrafluoroethylene-hexafluoropropylene) films have been tested in fuel cells with a life time over 5000 h at 85 ^{o}C [46, 47].

Aromatic hydrocarbons are a large group of polymers available commercially and are inexpensive. They possess good chemical stability due to the higher C-H bond strength

than aliphatic C-H bond strength. Sulfonation of these aromatic hydrocarbon based polymer provides proton transport. The Most widely used aromatic polymers are polysulfone (PSF), polyetheretherketone (PEEK) and polyetheretherketone ketone (PEEKK) [48, 49]. Another aromatic high performance polymer is polybenzimidazole (PBI) introduced by Aharoni and Litt [50] for the first time and later developed by Savinell, Wainright et al. as a Polymer electrolyte in its acid doped form [51]. PBI has good chemical, mechanical and thermal stability and can operate without humidification hence suitable for high temperature fuel cells (120-175 ^{o}C) [52, 53]. But the limitations of PBI membrane such as acid leaching and lower activity of catalyst [54]. The limited oxygen permeability and slow kinetics of oxygen reduction in phosphoric acid affects the overall cell performance [55].

PFSA based membranes are still the benchmark PEM for fuel cells, although despite their good proton conductivity, several limitations such as low operating temperature, durability; etc has lead to fabrication of composite membranes [56, 57].

2.5 High temperature fuel cells

The operation of fuel cells at high temperature (>80 to 250 ^{o}C) has several advantages over low temperature fuel cells. The high temperature operation of fuel cells would enhance the performance by increasing the electrode kinetics, reducing the loading of noble metal catalyst (Pt) used in the fuel cell electrodes. Furthermore, it improves the CO tolerance of Pt catalyst. A non-fluorinated polymer membranes (cost effective), introduces the simplified water management which in turn, alleviates the cathode flooding. However, selection of a suitable PEM for intermediate temperature fuel cell is challenging. Figure 2.8 shows the temperature dependant proton conductivity of the existing PEM.

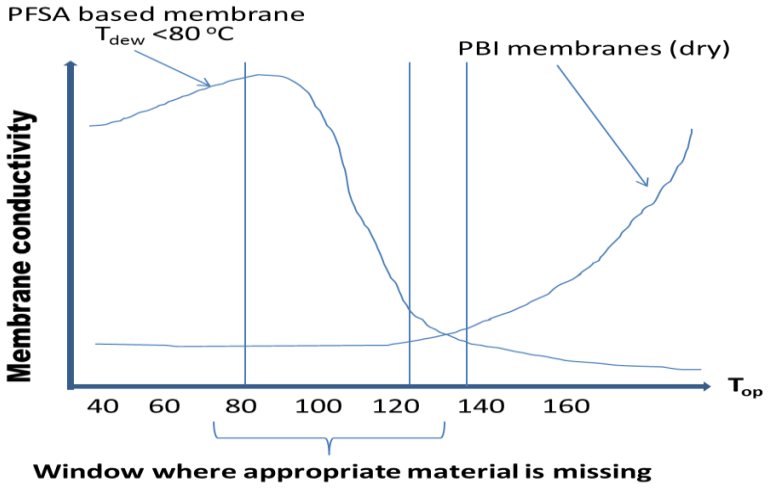

Figure 2.8, Temperature dependant proton conductivity of existing PEM [58].

It is very clear from figure 2.8 the PFSA based membranes can operate up to a maximum temperature of 80 ^{o}C. On the other hand, PBI (non-fluorinated) membrane can operate above 160 ^{o}C. A suitable PEM is missing to operate the fuel cell between 80 to 120 ^{o}C. The PBI membrane (acid doped) exhibited best performance at 180 ^{o}C with promising proton conductivity of 0.16 S.cm^{-1}(poor conductivity at low temperature). The PFSA composite membrane could fill the gap, where the appropriate material is missing (figure 2.8).

2.6 Composite polymer electrolyte membranes

The proton conductivity of PFSA based membrane depends on the hydration level and it is not practical to use this membrane above 80 ^{o}C [59]. In order to enhance the water retention capacity and proton conductivity of PFSA based membranes, considerable research efforts have been made to modify the PFSA membranes to enhance the proton conductivity under low humidification and at higher temperatures (> 80 ^{o}C) [60, 61].

The incorporation of inorganic hygroscopic oxide materials into the PFSA polymer matrix would enhance the water retention property and corresponding proton conductivity at higher temperature. The hygroscopic oxide materials such as ZrO_2, SiO_2, TiO_2 and SnO_2 have been incorporated into PFSA structure to make composite membranes for high temperature operation with low relative humidity [62-64]. It has been shown that the water uptake of oxide containing composite membrane is higher than that of pristine Nafion [65, 66]. These hygroscopic oxide materials are primarily single functional, they can enhance the water retention, but the proton conductivities of these composite membranes are less than pristine Nafion [67].

Several other solid inorganic materials (solid inorganic proton conductors), being both hydrophilic and proton conducting have also been incorporated with PFSA membranes [68, 69]. Among the solid inorganic proton conductors, phosphates of Zr, Ti, Ce, heteropolyacids and metal hydrogen sulphates have been used for the development of composite PFSA membranes [70, 71]. The organic derivatives of α and γ- Zirconium phosphates exhibit proton conductivity as high as 0.05 S.cm^{-1} at about 100 ^{o}C with good thermal stability at temperature up to 200 ^{o}C [72, 73]. Table 2.4, provides the list of proton conductivity of Zirconium phosphates and phosphonates at and above 100 ^{o}C. Some of the mixed zirconium alkyl-sulphophenyl phosphates exhibit proton conductivity as high as 0.02 S.cm^{-1} at about 100 °C [73].

Table 2.4, Proton conductivity of Zirconium phosphates and phosphonates

Compounds	Proton conductivity ($S.cm^{-1}$)
α-$Zr(O_3POH)_{2}.H_2O$	$5x10^{-6}$, 100 °C, 60% RH
α-$Zr(O_3PC_2H_5)_{1.15}(O_3PC_6H_4SO_3H)_{0.85}$	5-12 $x10^{-6}$, 180 °C, dry N_2
α-$Zr(O_3PCH_2OH)_{1.27}(O_3PC_6H_4SO_3H)_{0.73}$ .nH_2O	$8x10^{-3}$, 100 °C, 60% RH
α-$Zr(O_3PC_6H_4SO_3H)_2.3.6H_2O$	$2.1x10^{-2}$, 105 °C, 85% RH

Another class of solid inorganic proton conductors with high proton conductivity are heteropolyacids. The typical compounds of heteropolyacids (HPAs) include $H_3PW_{12}O_{40}.nH_2O$ (PWA), $H_3PMo_{12}O_{40}.nH_2O$ (PMA) and $H_4PSiW_{12}O_{40}.nH_2O$ (SiWA) has been widely studied [74]. The origin of proton conductivity of HPAs could be explained based on their structural properties. HPA possess several levels of structure called primary, secondary and tertiary. The primary structure is the building block of the HPA. The most common and thermally stable structure is the Keggin structure (figure 2.9a) [75]. The Keggin unit consists of a central atom (usually P, Si or Ge) in a tetrahedral arrangement of oxygen atoms, surrounded by 12 oxygen octahedral containing addenda atoms (W or Mo) [76]. There are four types of oxygen atoms found in the Keggin unit, the central oxygen atoms, two types of bridging oxygen atoms and terminal oxygen atoms. In phosphotungstic acid ($H_3PW_{12}O_{40}$), each Keggin unit has a (-3) charge and thus has 3 protons to balance this charge [77]. Heteropolyacids possess waters of crystallization that bind the Keggin units together in the secondary structure by forming water bridges as shown in figure 2.9b. The water combines with the protons in the HPA to form $H_5O_2^+$ acidic water clusters. These water molecules are hydrogen bonded to the terminal oxygen atoms of the Keggin unit [78]. The amount of hydration in the solid is critical in determining the crystal structure. The most common form of the Keggin-type HPAs at ambient conditions is the hexahydrate, which has a BCC crystal structure. The tertiary structure of the heteropolyacids can be found in partially neutralized materials containing heavy metal cations [79, 80].

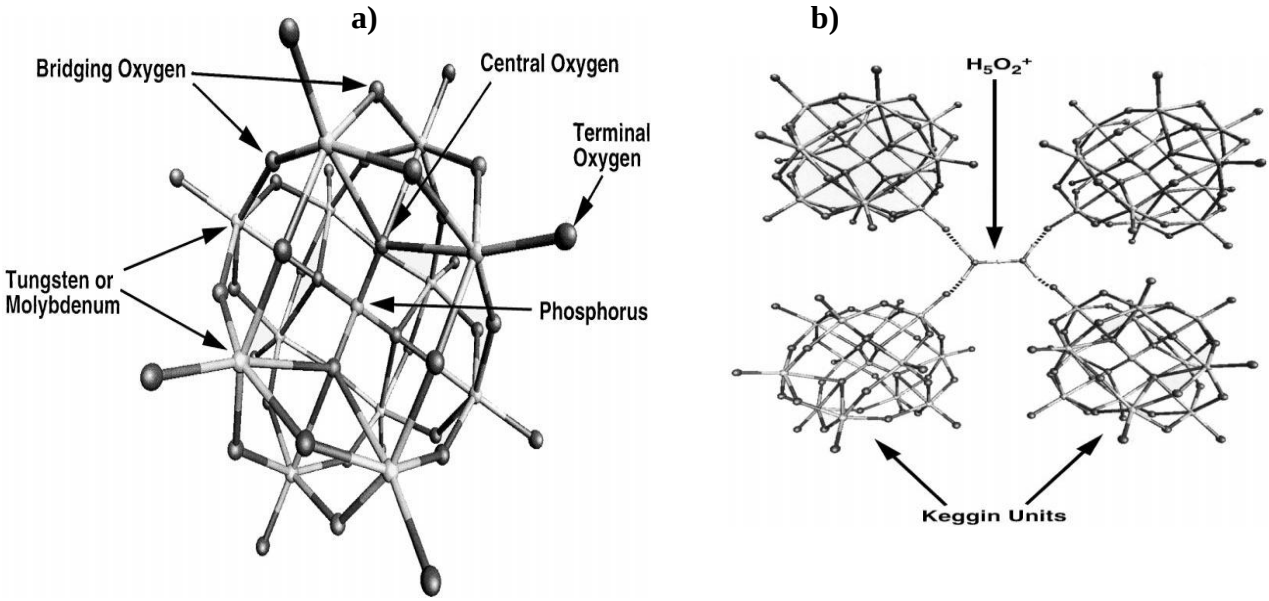

Figure 2.9, a) primary structure (Keggin unit) of HPA and b) secondary structure (hydrated) of HPA [80].

Among the HPAs, PWA exhibits high proton conductivity of 0.18 $S.cm^{-1}$[81]. As these HPAs have low surface area (less number of acid sites) and highly soluble in water [82]. Several research attempts have been made to modify HPAs by incorporating large monovalent ions, such as Cs^+, results in unique changes in the surface acidity and solubility. Ramani et al [83] reported the effect of size of these HPAs in the composite membranes. Among CsPWA and CsPMA, CsPMA/Nafion® composite membranes exhibit higher proton conductivity and stability [84]. The comparison of proton conductivities at various temperatures is shown in figure 2.10.

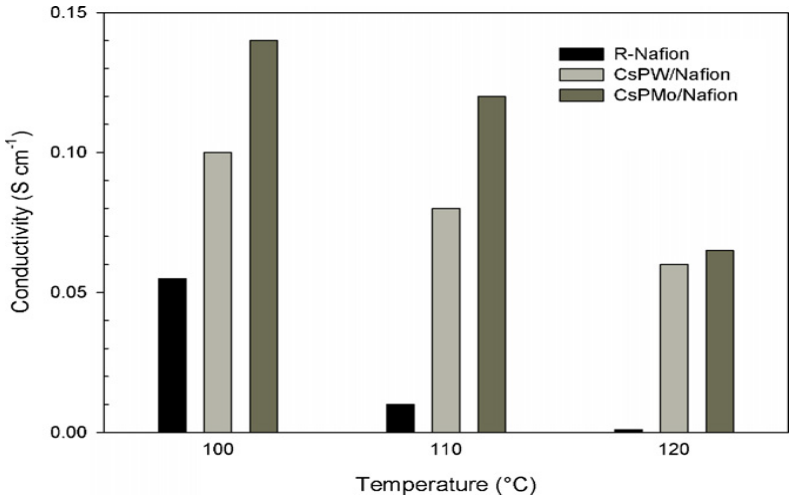

Figure 2.10, Proton conductivity values of HPA/Nafion composite membranes [84]

Although, CsPMA exhibited higher proton conductivity value compared to CsPWA, the fuel cell performance of CsPMA is lower than that of CsPWA [85]. Additives containing molybdenum were less stable in the membrane environment than those containing tungsten. Molybdates migrated into the catalyst layers, where they had a detrimental effect on performance by undergoing parasitic redox reactions on the surfaces of carbon and platinum, resulting in increased activation overpotential [86].

Also hydrogen sulphates such as $CsHSO_4.CsH_2PO_4$ and $2CsHSO_4.CsH_2PO_4$ have been reported with high proton conductivity [87, 88]. But they possess poor mechanical stability and water solubility, as well as volume expansion at elevated temperatures [89].

Anhydrous inorganic proton conductors such as metal diphosphates (MP_2O_7, where M= Sn, Ti, Ce and Zr) exhibit a monotonic decrease in proton conductivity with decreasing temperature from 250 °C to room temperature [90]. These proton conductors have also been explored as electrolytes for intermediate-temperature PEMFCs. For example, a PEMFC with a $Sn_{0.9}In_{0.1}P_2O_7$ electrolyte exhibited stable performance with non-humidified hydrogen and air [91]. However, the proton conductivities reported were in the range of 0.001-0.1 $S.cm^{-1}$, which is not sufficiently high to provide good PEMFC performance [92]. Y. Shen et al recently reported that $Fe_{0.4}Ta_{0.5}P_2O_7$ exhibits higher proton conductivities at 100–250 °C than those for $Sn_{0.9}In_{0.1}P_2O_7$. The proton conductivities of $Fe_{0.4}Ta_{0.5}P_2O_7$ are the highest among all other proton conductors reported to date in the same temperature range as shown in figure 2.11 [93].

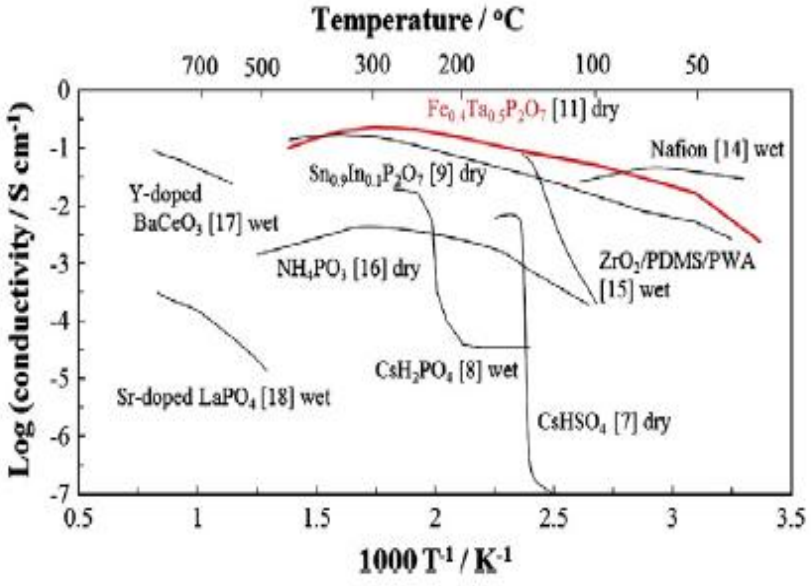

Figure 2.11, Temperature dependant proton conductivity of different proton conductors [93]

The highest proton conductivity of $Fe_{0.4}Ta_{0.5}P_2O_7$ is explained based on their crystalline structure and characterised by the presence of intersecting zigzag tunnels delimited by pentagonal windows [94]. The unique crystalline structure of $Fe_{0.4}Ta_{0.5}P_2O_7$ provides many proton exchange sites and transport pathways.

In the composite membrane, the presence of hydrophilic inorganic compounds reduces the chemical potential of water and therefore creates an alternative means for proton transport. At the same time, they facilitate hydrogen–bonding sites for water in the membrane; so that the hydration level of the membrane will be enhanced and eventually transport and evaporation of water will be lower [95]. The enhanced water retention enables low humidification and high temperature operation of fuel cells.

The inorganic additive materials are of two kinds one is single functional, as a means for water retention and the second is bifunctional, being both proton conducting and hydrophilic. The composite membrane fabricated with these inorganic additives shows significant improvement over PFSA membrane for high temperature operation of fuel cells. However, the proton conductivity of these composite membranes is still lower compare to Nafion® membrane because the incorporation of inorganic additives (an increase in inorganic particle agglomeration at higher concentrations of inorganic additives) [96]. The effects of additive particle size on the morphology of parent polymer govern the properties of resulting composite polymer [97].

Graphite oxide (GO) has been considered attractive for many applications due to its unique structural properties [98]. Graphite is a 2-D material upon chemical oxidation, and introduction of acidic functional groups (COOH, COC, OH) results in an insulating graphite oxide [99]. GO has high surface area (acidic sites) and exfoliate (Graphene oxide) in water as well as some organic solvents [100]. GO is hydrophilic in nature and it holds more water even at lower humidification, and the presence water between the GO nanosheets, presumably hydrogen bonded, provides the proton conducting channels [101]. The acidic functional groups (figure 2.12a) on edges and basal plane are a means of additional proton transport channels [102]. Sulfonic acid (SO_3H) is a key functional group of many polymers to transport the protons [103]. GO was further functionalised with sulfonic acid to make sulfonated graphite oxide (figure 2.12b) and this is more proton conducting than GO [104]. GO and SGO PFSA composite membranes have been reported for DMFCs with improved performance (reduced methanol crossover) [105]. These composite membranes have been reported for other applications such as sensors, actuators etc [106].

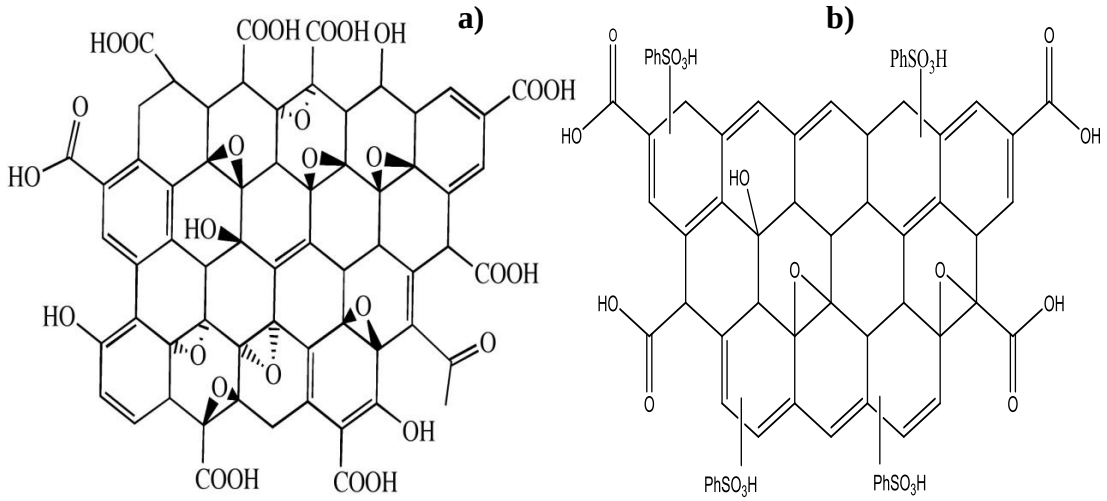

Figure 2.12, Structure of a) graphene oxide and b) sulfonated graphene oxide [103]

2.7 Polymer electrolyte membrane degradation

Polymer electrolyte membrane degradation significantly affects the life time of fuel cells. During the fuel cell operation several parameters such as temperature, pressure, humidity, and reducing and oxidising environments causes the membrane degradation. The membrane degradation is classified into three categories such as mechanical, thermal and chemical degradation. Among all degradation categories of membrane, mechanical degradation causes an early life failure due to perforations, pinholes, and tears which may results in improper membrane electrode assembly fabrication process [107]. Interface between channels of flow fields or sealing edges in a PEM fuel cell which are subjected to excessive or non-uniform mechanical stresses, are also vulnerable to small perforations or tears. The effect of relative humidity cycling (RH), low humidification, and non-humidification which are detrimental to mechanical stability have been reported by X. Huang et al. and they performed 1000 cycles from 0 to 100% RH at 80 ^{o}C. The test results showed that RH cycling creates number of discrete and localized defects, these defects results in reactive gas cross over into respective reverse electrodes consequently exothermic combustion of reactants on electrode surface creates local hotspots and accelerates the membrane degradation. The constrained membrane in an assembled fuel cell experiences in-plane tension resulting from shrinkage under low RH and in-plane compression during swelling under wet conditions. Mechanical failure of the membrane caused by local imperfections, leads to catastrophic failure of system [108, 109]. In order to enhance the electrochemical kinetics and reduce the CO poisoning, fuel cells need to be operating above 100 ^{o}C and also it is necessary to operate at subfreezing temperature for different types of

applications [110]. The proton conductivity of PFSA membrane depends on water content and usual operating temperature is limited to 60 to 80 ^{o}C, above this temperature the critical break down of PFSA membrane [111]. Several studies show that these membranes exhibit a fall in proton conductivity with decrease in water content when the cell is operated at higher temperature and under low humidity. Wilkie et al. reported that the stability of PTFE backbone until beyond 150 ^{o}C due to strong interaction of C-F bond and at higher temperature membrane starts decompose via its side sulfonate groups [112]. Kim et al. reported the freezing effect, and they suggested that there are three different states of water and only the "free water" would freeze below 0 ^{o}C and increase the contact resistance of the membrane and affects the proton conductivity [113]. The thermal cycling between +80 to -40 ^{o}C significantly affects the membrane property but no catastrophic failures were detected.

Chemical stability of polymer membrane in a strong reducing and oxidising environment is a very important factor to have good durability. The major factor for the chemical degradation is the effect of free radicals, generated on the electrode surface by reactant gas crossover [114].

$$H_2 + O_2 \rightarrow X \qquad (X = HO\bullet, HOO\bullet) \qquad (2.11)$$

The free radicals such as peroxy ($^{\cdot}$OH) and hydro peroxy ($^{\cdot}$OOH) are active oxygenated species that attack the polymer and chemically degrade the membrane [115]. Sulfonic acid and carboxylic end groups in the side chain are key to mechanism by which radical species can attack the polymer (SO_3H dominate the COOH). Depending on the types of membrane radicals can attack α-carbon atom of an aromatic group or the branching point of polymer. An example of radical attack on the polymer is shown below [103].

$$R_f\text{–}CF_2COOH + \bullet OH \rightarrow Rf\text{–}CF_2\bullet + CO_2 + H_2O \qquad (2.12)$$

$$R_f\text{–}CF_2\bullet + \bullet OH \rightarrow Rf\text{–}CF_2OH \rightarrow Rf\text{–}COF + HF \qquad (2.13)$$

$$R_f\text{–}COF + H_2O \rightarrow Rf\text{–}COOH + HF \qquad (2.14)$$

This mechanism shows the polymer decomposes into low molecular weight compounds, and eventually accelerates the membrane degradation. The effect of metal ion impurities (Fe^{2+}, Cu^{2+}) from corrosion of bipolar plates, end plates and also from water generates the free radicals by decomposing H_2O_2 which is formed at cathode [116].

M. Inaba et al. proposed a mechanism of H_2O_2 decomposition in the presence of Fe_2^+ in PEM fuel cell is shown below.

$$H_2O_2 + Fe^{2+} \rightarrow HO\bullet + OH^- + Fe^{3+} \quad (2.15)$$

$$Fe_2+ + HO\bullet \rightarrow Fe^{3+} + OH^- \quad (2.16)$$

$$H_2O_2 + HO\bullet \rightarrow HO_2\bullet + H_2O \quad (2.17)$$

$$Fe^{2+} + HO_2\bullet \rightarrow Fe^{3+} + HO_2^- \quad (2.18)$$

$$Fe^{3+} + HO_2\bullet \rightarrow Fe^{2+} + H^+ + O_2 \quad (2.19)$$

This mechanism leads to membrane thinning or formation of pinholes and eventually to the catastrophic failure of the system. On the basis of above mechanism, the formation of free radicals from H_2O_2 decomposition is assumed to be the principal degradation mechanism of PEMFC membranes. The Fenton test was widely used for testing the polymer electrolyte membrane degradation by oxidative radicals, a Fenton solution of 3% H_2O_2 containing 4 ppm Fe_2^+ was added as $(NH_4)Fe(SO_4)_2.6H_2O$ for accelerating the effect to produce hydroxide radicals [117].

2.8 Mitigation strategies for membrane degradation

Based on the degradation studies of polymer electrolyte membranes, it is important to prevent the mechanical failure of the membrane in order to avoid the catastrophic failure of the fuel cell. Careful designing of MEA and flow field structure can avoid the local drying of the membrane. To enhance the mechanical stability of the Nafion® membrane, Gore fuel cell technologies developed expanded PTFE reinforced membrane (incorporation of ePTFE into the Nafion® membrane called reinforcement to enhance the mechanical stability) and the results showed that reinforced membranes have longer relative life time than non-reinforced membrane (figure 2.13) [118].

Modified PFSA membranes are developed to enhance the operating temperature and durability by incorporating the hydrophilic oxides and inorganic proton conductors. Alternative to fluorinated polymers, several other membranes are developed such as SPEEK, PVDF and PBI based membranes. Recently, functionalised carbon nanotube (CNTs), Fullerene and graphene based PFSA composite membranes are developed to enhance the mechanical, thermal and ionic conductivities for hydrogen oxygen fuel cells [119].

Chemical stability of PEM is another important factor to withstand a strong oxidising and reducing environment. Radiation grafted FEP-g-polystyrene membranes are developed to improve chemical stability against free radical affect, in addition to this introduction of radical stabilizers and inhibiters such as amines or antioxidants reported by Curtin et al [120].

Hydrogen peroxide produced at cathode by 2 electron reduction of oxygen and decomposed by the presence of metal ion impurities generates the free radicals eventually to membrane degradation. It was reported that the Nafion® polystyrene sulfonic acid (PSSA) composite membrane, when positioned at cathode of the fuel cell could successfully prevent the oxidative degradation of the PSSA membrane. V. Ramani and Haugen et al. proved the introduction of peroxide-decomposing (decomposing H_2O_2 into H_2 and O_2) catalyst like heteropoly acids within the membrane eliminate the membrane deterioration [121].

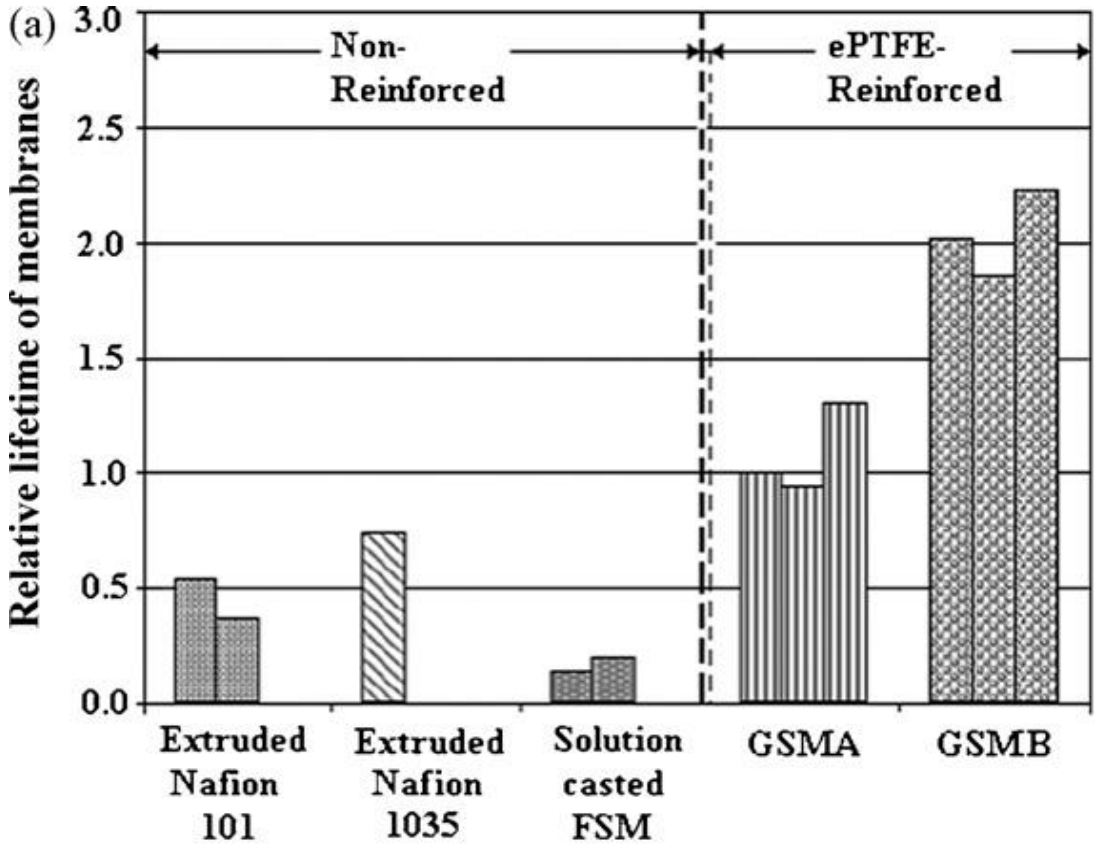

Figure 2.13, Comparison of Gore reinforced membranes and non-reinforced membranes [118]

2.9 Electrocatalyst

Electrodes are the main pillars of electrochemical devices, where electrochemical reactions occur. Electrochemical reactions are driven by electrocatalysts in order to speed up the kinetics of reaction [122]. In the case of fuel cells the anode is where hydrogen oxidation and the cathode oxygen reduction reaction (ORR) occur. The most commonly used electrocatalysts for fuel cells are platinum (Pt) and platinum based transition metal alloys [123]. Pt is the most active electrocatalyst for ORR compared to other metals [124]. The activity (exchange current density) is based on the electronic structure of metal and surface energy of metal towards adsorption and dissociation of O_2 [125]. The electronic structure of Pt (Pt d-band vacancy) and Pt-Pt interatomic distance can strongly affect the O_2 adsorption, dissociation and binding energies [126]. The theoretical calculations of O_2 binding energies on different metals have predicted that Pt has the highest ORR activity compared to Pd, Ir and Rh. The ORR catalytic activity of Pt and other metals are shown in the figure 2.14. The ORR on other metals such as Ir, Rh, Au, Cu, Ni, Co etc has been studied [127]. However, these metals show lower activity and electrochemical stability towards ORR compared to Pt [128].

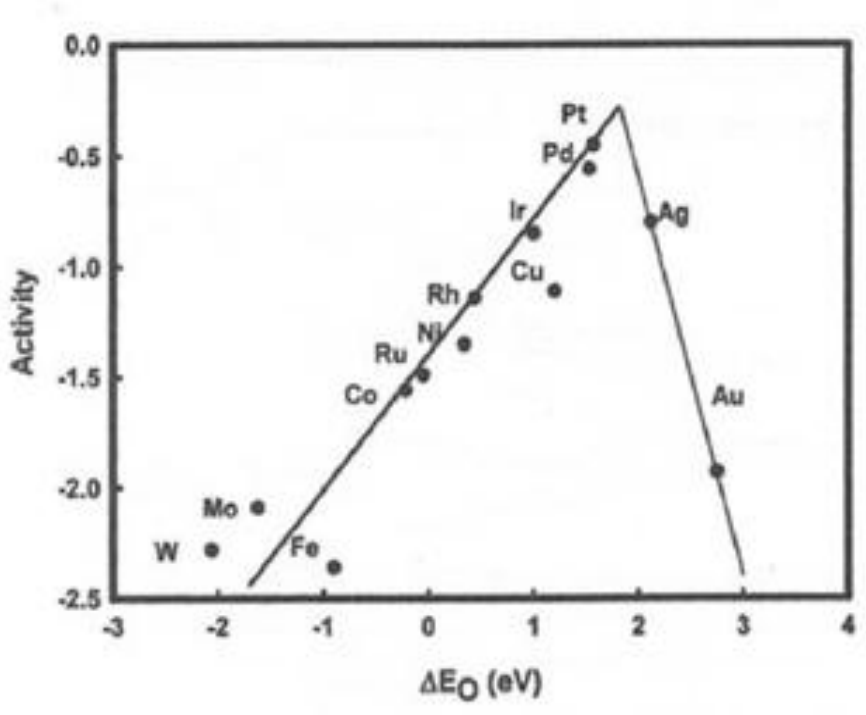

Figure 2.14, Oxygen reduction activity (Activity on the Y-axis represents exchange current density and ΔE_O (eV) on the X-axis represents oxygen binding energy) plotted as a function of the oxygen binding energy [127]

2.10 Development of fuel cell catalyst

Platinum black was the first catalyst used in PEMFCs as the anode and cathode electrocatalyst. The typical particle size of 50-100 nm and the physical surface area of Pt black is about10 $m^2\ g^{-1}_{pt}$. Due to the lower physical surface area, higher Pt loadings (> 4 $mg_{pt.}\ cm^{-2}$) were required to achieve useful power densities [129].

In the 1970s, most important development in the area of electrocatalyst was the advent of carbon supported electrocatalyst [130]. The support plays a major role in the electrocatalyst. The high surface area of carbon black is (300-1500 $m^2\ g^{-1}$), allowing excellent dispersion of Pt nanoparticles up to metal loadings of 60 wt%. The Pt nanoparticles supported homogeneously on the carbon support, avoiding agglomeration of Pt results and an increased physical surface of Pt (up to 120 $m^2\ g^{-1}_{pt}$). Although, the Pt is supported on the high surface area carbon the electrocatalytic activity remained relatively low. This is because reactions only occur at the reactant gas-catalytic surface-electrolyte interface. Such regions are called as triple-phase boundary [131]. Even though, reactions occur at the bulk of the electrocatalyst layer, due to the absence of an ionomer in the catalyst layer, proton transfer to the PEM relies on water alone through the catalyst layer.

A major breakthrough in the development of PEMFC electrocatalysts was achieved with the incorporation of proton-conducting ionomer within the pore structure of the catalyst layer in late 1980s [132]. By forming catalyst layers from inks containing dispersions of Pt/C catalyst along with Nafion® ionomer, the triple-phase boundary (figure 2.15) could be extended throughout the thickness of the catalyst layer, resulting in far more of the physical Pt surface area becoming electrochemically active.

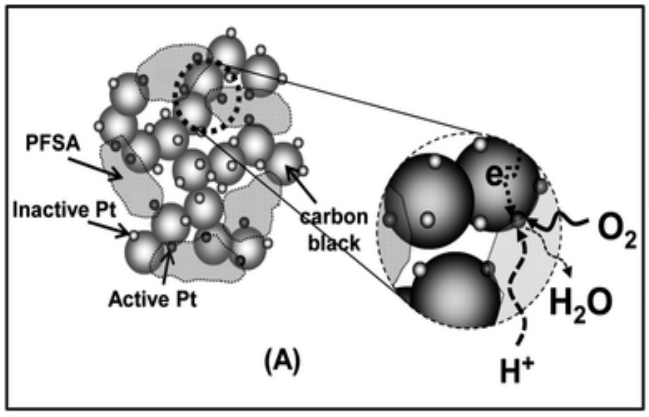

Figure 2.15, Schematic representation of three-phase boundary of Pt supported on carbon [132]

2.11 The mechanism of oxygen reduction reaction on Pt

The Pt shows better ORR activity and stability in relation to all other metals [133]. Figure 2.16 shows the free-energy diagram for ORR at the equilibrium potential (E=1.23 V) over Pt and other metals. It is seen from the figure, why metals that have either stronger or weaker bonding of oxygen than Pt are poorer oxygen-reduction catalysts. Pt balances O_2 adsorption strength to allow e^- transfer, and intermediates are sufficiently unstable for the reaction to complete. At the equilibrium cell potential, Ni binds O and OH so strongly on the surface such that an irreversible surface oxide is formed. Therefore, the proton-transfer steps become strongly activated, and thus e^- transfer is very slow. For Au, however, the proton transfer is exothermic and should be fast, but oxygen on the surface is considerably less stable than it is in the gas phase; therefore, no transfer of protons and electrons to oxygen can occur. The weak bonding of atomic oxygen is an indication that the barrier for oxygen dissociation is large [134].

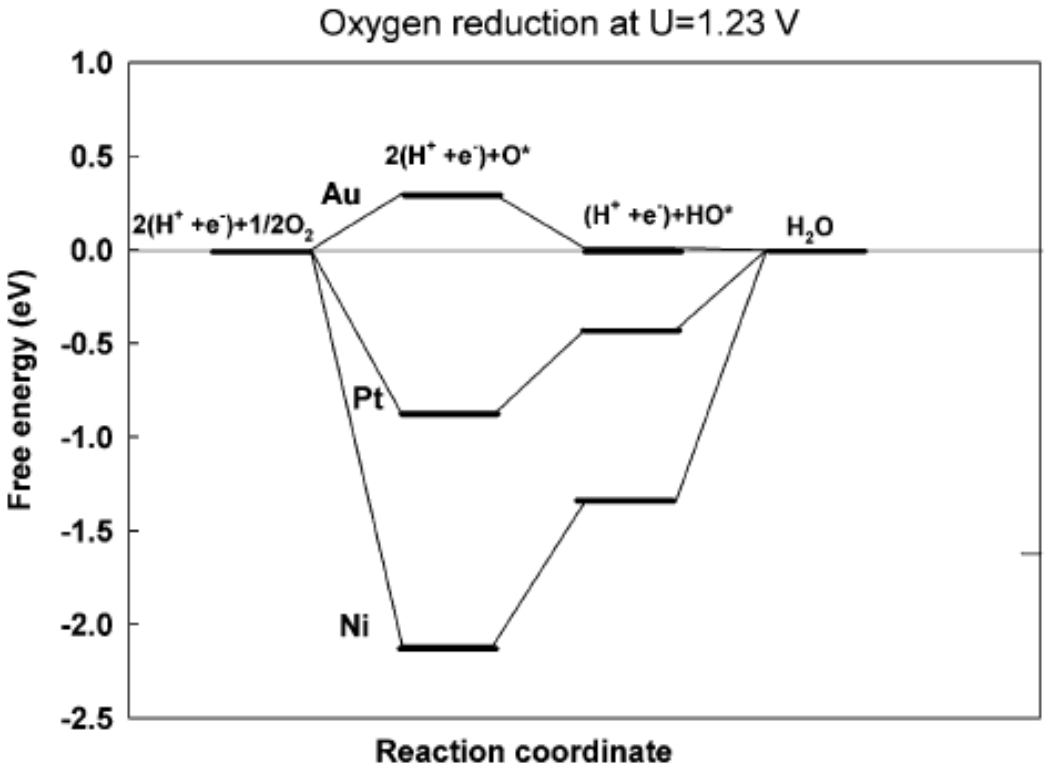

Figure 2.16, Free-energy diagram for oxygen reduction at the equilibrium potential *E*=1.23 V over Pt, Au, and Ni [133]

The mechanism of ORR on Pt surface has been widely studied. The ORR involves a multi-electron process in which O_2 is converted into H_2O or OH^-.

$$O_2 + 4H^+ + 4e^- \rightarrow 2H_2O \longrightarrow \quad (2.20)$$

$$O_2 + 2H^+ + 2e^- \rightarrow H_2O_2 \longrightarrow \quad (2.21a)$$

$$H_2O_2 + 2H^+ + 2e^- \rightarrow H_2O \longrightarrow \quad (2.21b)$$

Reactions 2.20, 2.21a and 2.21b show ORR in an acidic electrolyte. O_2 can be converted directly into H_2O by $4e^-$ process or O_2 may also undergo a partial $2e^-$ reduction to form hydrogen peroxide (H_2O_2), followed by another $2e^-$ reduction to convert H_2O_2 into H_2O. Reactions 2.22, 2.23a and 2.23b show ORR in an alkaline electrolyte.

$$O_2 + 2H_2O + 4e^- \rightarrow 4OH^- \longrightarrow \quad (2.22)$$

$$O_2 + H_2O + 2e^- \rightarrow HO_2^- + OH^- \longrightarrow \quad (2.23a)$$

$$HO_2^- + H_2O + 2e^- \rightarrow 3OH^- \longrightarrow \quad (2.23b)$$

O_2 can be reduced by $4e^-$ process to form OH^- or by $2e^-$ reduction to form HO_2^-, followed by another $2e^-$ reduction to convert OH^-.

O_2 may be converted into different intermediates, such as oxygenated (O*), hydroxyl (OH*) and superhydroxyl (OOH*) species, which are very difficult to analyse experimentally [135, 136]. Based on the density functional theory (DFT) calculations, two mechanisms have been proposed for ORR on Pt surface (figure 2.17a and 2.17b). The first one is, at high oxygen coverage that the ORR tends to follow an associative mechanism, in which OOH* is first formed and then the O-O bond is cleaved. The second is at lower oxygen coverage, ORR follows a dissociative mechanism in which the O-O bond is cleaved before OH* is produced [137]. In general ORR on a Pt catalyst surface usually follows a $4e^-$ pathway, the mechanism is complicated and not well understood [138].

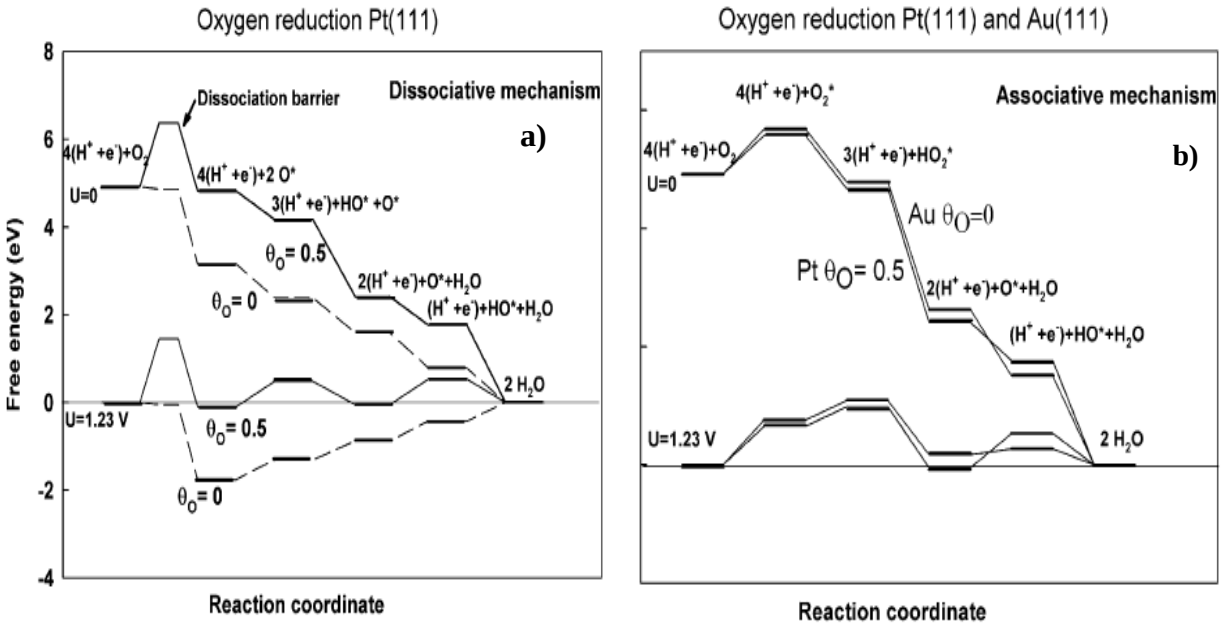

Figure 2.17, Free-energy diagram for oxygen reduction at two different potentials and at two different oxygen coverages, a) dissociative mechanism and b) associative mechanism [135]

2.12 The Oxygen reduction reaction on MPt alloys

Owing to its electronic structure, Pt electrocatalyst exhibited highest ORR activity compared to other metals [139]. However, studies reveal that the addition of transition metals to Pt can change the electronic structure of Pt and enhance the ORR catalytic performance [140, 141]. The improvement in catalytic activity when Pt is alloyed with transition metals is attributed to the increased Pt d-band vacancy and Pt-Pt interatomic distance [142]. The DFT calculations further indicate that the alloying of Pt with transition metals downshift the d-band centre of the Pt, leading to a lower degree of adsorption of oxygenated species and increases the number of active sites accessible to O_2 [143]. Transition metals such as Fe, Co and Ni show a volcano-type relation with alloy d-band centre position (Figure 2.18). The PtM alloys, with M=Fe, Co and Ni exhibited better ORR activities than any other PtM or pure Pt [144].

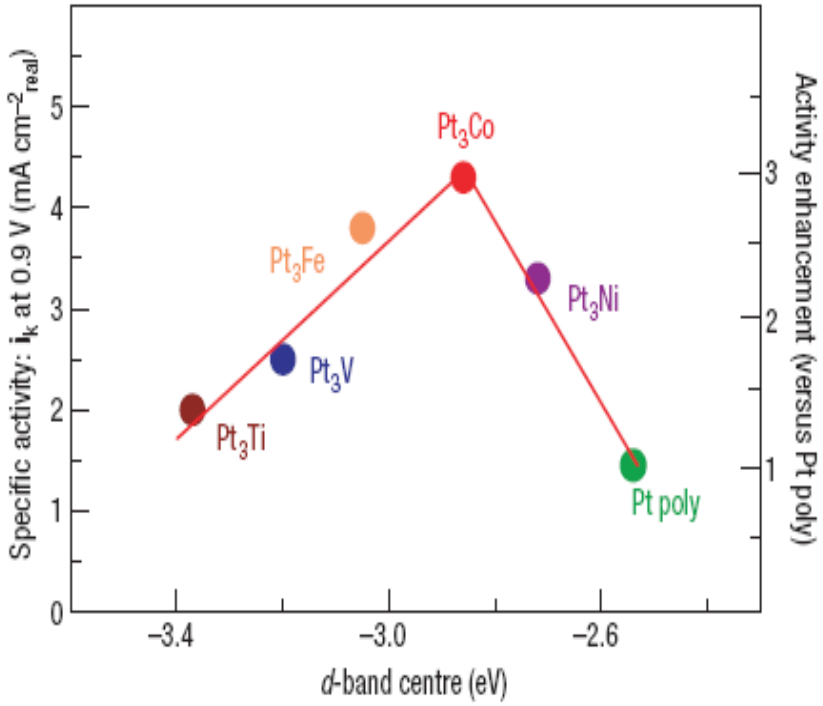

Figure 2.18, Volcano plots of PtM alloys [144]

2.13 Electrocatalyst layer degradation

The detailed examination of platinum catalyst degradation under long term operating condition has been reported. The contamination of pure catalyst by impurities present in the reactants or the fuel cell system [145]. Another important issue pertaining to the catalyst degradation is corrosion of the carbon support, due to the migration of Pt catalyst particles detached from the carbon support lose the catalyst activity [146, 147]. Several mechanisms have been proposed to explain coarsening of the catalyst particle during the fuel cell operation. (1) Small Pt particles may dissolve in the ionomer phase and redeposit on the larger particle leading to particle growth, called Ostwald ripening. Also the dissolved Pt particles may diffuse into the ionomer phase and subsequently precipitate in the membrane, via reduction by the crossover hydrogen, which affects the membrane stability and conductivity [148, 149]. (2) Agglomeration of the Pt particle on the carbon support leading to the higher particle size eventually decreases the surface area and activity of catalyst [150].

2.14 Carbon support and its corrosion

The electrocatalyst are supported on electronically conducting high surface area support to provide high electrochemical active area. The most commonly used catalyst support is carbon. The oxidation of carbon to carbon dioxide in the presence of water at 0.207 V vs. RHE shown in equation 2.24 and 2.25 called carbon corrosion [151].

$$2H_2O \leftrightarrow O_2 + 4H^+ + 4e^- \qquad E^\circ = 1.229 \text{ vs. RHE} \qquad (2.24)$$

$$C + 2H_2O \rightarrow CO_2 + 4H^+ + 4e^- \qquad E^\circ = 0.207 \text{ vs. RHE} \qquad (2.25)$$

Carbon support corrosion is one of the major issues for catalyst degradation [152]. In PEM fuel cells carbon corrosion is induced by two reasons: 1) during transition between start up and shutdown, carbon is exposed to electrochemical potential more than 1.4 V which accelerates the carbon corrosion. 2) Fuel starvation, caused by the non-uniform distribution of fuel on the anode, in an overall stack induces the water and carbon oxidation according to the above equations [153, 154].

Carbon corrosion in a normal PEM fuel cell is negligible at potentials lower than 1.1 V vs. RHE due to its slow kinetics, however recent experiments have proved that the presence of the electrocatalysts like Pt/C or Pt-Ru/C can enhance the carbon corrosion by reducing oxidation potential of carbon to 0.55 V vs. RHE [155, 156]. Carbon can protected from corrosion by virtue of water oxidation providing sufficient supply of water to the fuel cell, is maintained. Depletion of water or if the cell is subjected to high current density can mean that water oxidation alone cannot sustain the high current density and eventually carbon corrosion occur. Figure 2.19 depicts carbon corrosion and loss of active catalyst material during electrochemical reactions in fuel cells [157].

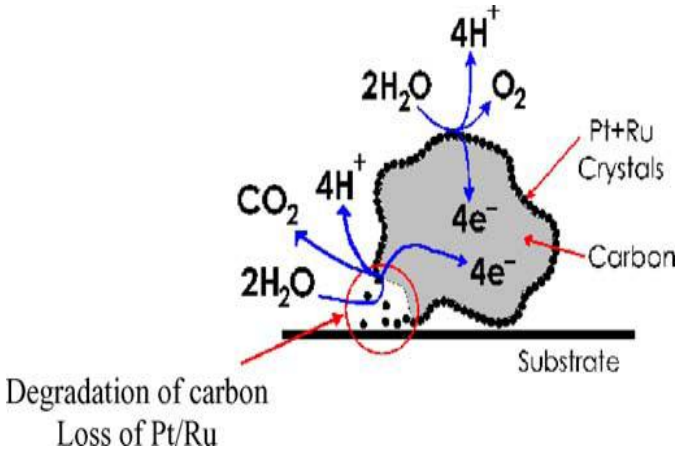

Figure 2.19, Schematic representation of carbon corrosion [157]

Carbon oxidation was investigated using highly oriented Pyrolytic graphite as carbonaceous material by Ogumi et al [158]. The Carbon surface is oxidised to different oxygen functionalities in sulphuric acid solution at potential lower than 1.0 V. Figure 2.20 shows the mechanism of oxidation of highly oriented pyrolytic graphite (HOPG) to carbon dioxide at potential > 0.75 V which is the accessible potential for cathode of PEMFC. Due to the presence of oxygen functionalities hydrophilicity of HOPG was increased and results in flooding of the cathode layer which affects the fuel cell performance [159, 160].

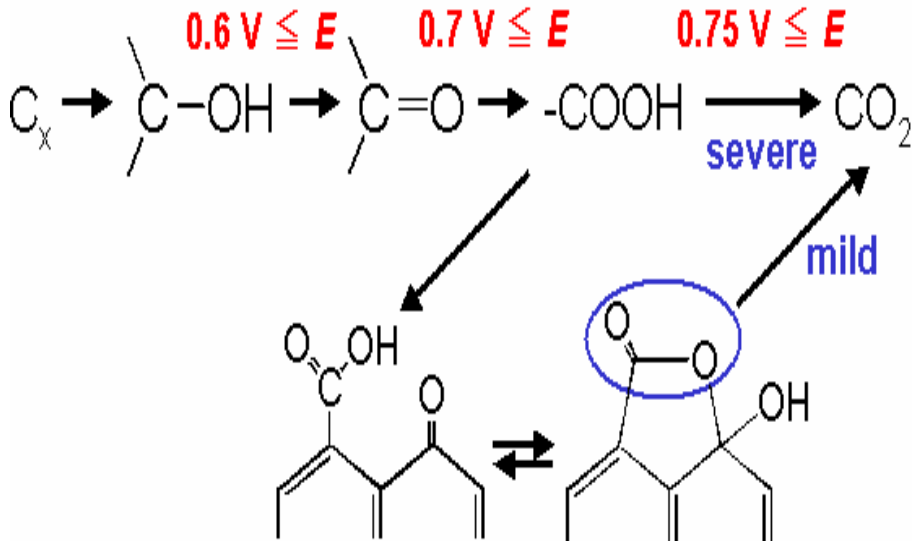

Figure 2.20, Mechanism of HOPG oxidation [158]

2.15 Mitigation strategies for electrocatalyst degradation

Several strategies have been employed to enhance catalyst durability. The dissolution and sintering of Pt can be controlled by employing capping surfactants, as is common in the synthesis of colloidal nanoparticles to control growth and prevent agglomeration via a steric and electrostatic stabilisation mechanism [161]. Surfactant based nanoparticles stabilisers are usually inert and must be removed to obtain good performance. Nafion® is used to stabilise the Pt nanoparticles, as Nafion® is an active component in the catalyst layer and thus it is not necessary to remove it from Pt [162].

2.16 Transition metal nitrides in electrochemistry

Transition metal compounds of the type MX, where M denotes a transition metal element and X denotes the non-metallic elements such as N are known to be very hard materials crystallizing in rock salt structure [163]. Transition metal nitrides (TMNs) are produced by incorporating nitrogen atoms into the interstitial sites of the parent metals,

which typically include all 3d elements and 4d/5d elements of group 3 to 6 early transition metals [164]. Table 2.5 shows the list of transition metal nitrides.

Table 2.5, Transition metal nitrides [163]

Group 4	Group 5	Group 6	Group 7	Group 8	Group 9	Group 10
Ti_2N $TiN_{0.9}$ TiN	V_2N VN	Cr_2N CrN	Mn_4N Mn_2N Mn_3N_2	Fe_4N Fe_2N	Co_3N Co_2N	Ni_3N
ZrN	Nb_4N_3 Nb_2N NbN $NbN_{0.95}$	Mo_2N MoN	$TcN_{0.75}$			
Hf_3N_2 HfN	Ta_3N_5 Ta_2N TaN $TaN_{0.8}$ $TaN_{0.1}$	W_2N WN	Re_2N			

These compounds have great scientific and technological interest. The type of bonding found in the MX systems is not typically ionic but more covalent and the occurrence of an ionic-like structure in combination with covalent like hardness is very interesting [165]. In addition, they show metallic conductivities comparable with those of pure transition metals. TMNs of group 4 to 6 are thermodynamically more stable and catalytically more active. Thermodynamic stability decreases with increasing group due to decrease in size, as they cannot accommodate interstitial nitrogen atom [166]. TMNs behave like noble metals for electrochemical reaction [167-170]. The formation of nitrides increases the metal-metal distance, and causes contraction of d-band. Contraction would give greater density of states near the Fermi level which resembles the electronic structure of noble metals [171, 172]. Therefore TMNs exhibit similar catalytic properties to that of noble metals.

Among TMNs, TiN has attracted attention as a promising material and it has been mainly devoted to establish corrosion and oxidation resistance under various conditions [173, 174]. The TiN coating on glass substrates shows the onset for corrosion at +0.6 V (vs. SSE) in 0.5 M H_2SO_4 electrolyte. This indicates that TiN is stable up to +0.6 V (vs. SSE) without electrochemical redox reaction. The corrosion resistance in neutral ~3 M $NaNO_3$ solutions is extended up to +3.0 V for TiN [175]. TiN has a significantly lower

rate of electrochemical oxidation than carbon due to its inert nature and presence of native oxide or oxynitride layer on its surface [176-178].

Considerable research efforts have been devoted to design corrosion resistant electrocatalyst support based on transition metal nitrides and carbides. In general, transition metal nitrides exhibit more activity than transition metal carbides for oxygen reduction reaction (ORR) [179-183]. Of special interest, TiN shows more activity for ORR than titanium carbide. TiN is considered as a promising catalyst support for noble metal catalyst like platinum [173]. Owing to its unique properties like good electrical conductivity, outstanding corrosion resistance TiN can outperform the carbon support in stability and activity under fuel cell operating conditions. TiN has the potential to act as durable electrocatalyst materials [184].

2.3 Conclusions

Proton exchange membrane fuel cells are attracting attention in realising the hydrogen economy as an alternative power sources for automotive applications. Several issues such as, stability, durability, and high cost of fuel cell components hinders the widespread commercialisation of PEMFC technology. A most important issues pertaining to the fuel cell performance degradation are both electrocatalyst and membrane degradation. The development of cost effective, sustainable materials is attracting much attention. The development of proton exchange membranes for high temperature (>100 ^{o}C) operation is an advantage, so this will enhance the performance and reduce the cost. There are several approaches to develop proton exchange membranes for high temperature operation. One of the approaches is the incorporation of bi-functional inorganic filler materials into the Nafion or SPEEK polymer matrix to make composite membranes. The electrocatalyst degradation can be alleviated by replacing carbon support with corrosion resistant titanium nitride support.

References

[1] Winter, M, Brodd, R. J, *What Are Batteries, Fuel Cells, and Supercapacitors?* Chem. Rev. **2004**, 104, 4245.

[2] http://www.mpoweruk.com/performance.htm. Accessed on August 13th **2013**.

[3] Grove, William Robert, *On Voltaic Series and the Combination of Gases by Platinum,*
Philosophical Magazine and Journal of Science vol. XIV, **1839**, 127-130

[4] Bacon, Francis T. and T. M. Fry, *Proceedings of the Royal Society of London*, Series A, Mathematical and Physical Sciences, 25 September **1973,** V.334, #1599, 431.

[5] Appleby, A. John, *Fuel Cell Handbook*, New York: Van Reinhold Co., **1989**.

[6] Blomen, Leo, and Michael Mugerwa, *Fuel Cell Systems*, New York: Plenum Press, **1993**.

[7] Kordesch, Karl, and Günter Simader, *Fuel Cells and Their Applications,* New York: VCH, **1996**.

[8] Srinivasan, S., Mosdale, R., Stevens, P., Yang, C., *Fuel cells: reaching the era of clean and efficient power generation in the twenty-first century*, Annu. Rev. Energy Environ. **1999**. 24, 281.

[9] Wand, G. *Fuel Cell Today, fuel cell history,* Part 2, 19th Jan **2007**.

[10] Bompard, E. and Napoli, R., *Economics evaluation of a 5 kW SOFC power system for residential use,* International Journal of Hydrogen Energy, **2008**, 33, 12, 3243-3247.

[11] De Geeter, E. and Mangan, M., *Alkaline fuel cells for road traction*, Journal of Power Sources, **1999**, 80, 207–212.

[12] Appleby, A. John, *Scientific American*, July, **1999**, 74.

[13] T. D. Gierke and W. S. Hsu, A. Eisenberg and H. L. Yeager, Editors, p. 283, *ACS Symposium Series 180,* American Chemical Society, Washington, DC (**1982**).

[14] M. Eikerling, A. A. Kornyshev, and U. Stimming, *Electrophysical Properties of Polymer Electrolyte Membranes: A Random Network Model,* J. Phys. Chem. B, **1997**, 101, 10807.

[15] D.E. Curtin, R.D. Lousenberg, T.J. Henry, P.C. Tangeman, M.E. Tisack, *Advanced materials for improved PEMFC performance and life,* J. Power Sources, **2004**, 131, 41–48.

[16] http://www.greencarcongress.com/2005/03/hsub2sub_genera.html, accessed on 13th August **2013**.

[17] I. Pilatowsky, R. J. Romero, *Thermodynamics of fuel cells*, Springer, **2011**.

[18] Cairns E. J, Liebhafsky H. A, *Irreversibility caused by composition changes in fuel cells*, Energy Conversion, 9:63, **1969.**

[19] Srinivasan S, *Fuel cells: from fundamentals to applications*, Springer, New York, **2006**.

[20] Angrist S.W, *Direct energy conversion*, 3rd edn. Allyn and Bacon, Boston, **2000**.

[21] Atkins P.W, *Physical chemistry*, 3rd edn. W.H. Freeman and Company, New York, **1986**.

[22] EG&G Services Parsons Inc., *Science Applications International Corporation, fuel cell, hand book,* 5th edn. US Department of Energy, **2000.**

[23] J. O'M. Bockris and S. Srinivasan, *The Electrochemistry of Fuel Cells*, McGraw-Hill, New York, **1969**.

[24] F. W. Ostwald, *Presidential address to Bunsen Gesellschaft; predicted pollution if heat engines are used for energy production. Recommended electrochemical pathway*. J. Electrochem., **1894**, 1, 122.

[25] W. Jacques *Worked out in detail the reduction of fuel costs for a boat to cross the Atlantic using electrochemical or chemical engines*. Harper Mag. 94, 199 (Dec. **1896, 1897**).

[26] E. Justi, J. Winsel, *Cold Combustion*, Verlag, Chemie, Wiesbaden, Germany, **1962.**

[27] E. C. Potter on F. T. Bacon, in *Trends in Electrochemistry*. J. O'M. Bockris, D. A. J.

Rand, and B. J. Welch, eds., 7.1, Plenum, New York, **1977**.

[28] A. Damjanovic and M. A. Genshaw, *Experimental proof of Temkin behavior. O adsorption linear with potential*, Electrochimica Acta, **1970**, 15**,** 1281.

[29] H. Wroblowa, M. L. B. Rao, A. Damjanovic, and J. O'M. Bockris, *The stationary potential of Pt contact with in solution*, J. Electroanal. Chem., **1967**, 15**,** 139.

[30] Simons SN, King RB, Prokopius PR, *In: Camara EH Symposium Proceedings Fuel Cells*, **1982**.

[31] Andre J. deBethune, *Fuel Cell Thermodynamics*, J. Electrochem. Soc., **1960**, 107, 937-939.

[32] D. Dunwoody, J. Leddy, *Proton Exchange Membrane Fuel Cells for Transportation Applications,* Electrochem. Soc. Interf., **2005**, 14, 37–39.

[33] Ravi Kumar, Chenxi Xu, Keith Scott, *Graphite oxide/Nafion composite membranes for polymer electrolyte fuel cells*, RSC Advances**, 2012**, 2, 8777–8782.

[34] S.D. Knights, K.M. Colbow, J. St-Pierre, D.P. Wilkinson, *Aging mechanisms and lifetime of PEFC and DMFC,* J. Power Sources, **2004**, 127, 127–134.

[35] Church, Steven, *Del. firm installs fuel cell*, The News Journal, (January 6, **2006**). p. B7.

[36] Carla Heitner, Wirguin, *Recent advances in perfluorinated ionomer membranes: structure, properties and applications,* Journal of membrane science, **1996**, 20, 1-33.

[37] Kenneth A. Mauritz and Robert B. Moore, *State of Understanding of Nafion*, Chem. Rev. **2004**, 104, 4535-4585.

[38] K. D. Kreuer, T. Dippel, and J. Maier, S. Gottesfeld, G. Halpert, and A. Landgrebe, Editors, PV 95-23, p. 241, *The Electrochemical Society Proceedings Series*, Pennington, NJ **1995**.

[39] A. Eisenberg, *Clustering of Ions in Organic Polymers. A Theoretical Approach*, Macromolecules, **1970**, 3, 147.

[40] K. A. Mauritz, C. J. Hora, and A. J. Hopfinger, *Advances in Chemistry Series,* A. Eisenberg, Editor, Chap. 8, American Chemical Society, Washington, DC, **1980**.

[41] S. Gottesfeld and T. A. Zawodzinski, *Advances in Electrochemical Science and Engineering*, Vol. 5, p. 245, Wiley, New York, **1997**.

[42] M. Wakizoe, O. A. Velev, and S. Srinivasan, *Analysis of proton exchange membrane fuel cell performance with alternate membranes*, Electrochim. Acta, **1995**, 40, 335-344.

[43] J. A. Kolde, B. Bahar, M. S. Wilson, T. A. Zawodzinski, and S. Gottesfeld, S. Gottesfeld, G. Halpert, and A. Landgrebe, Editors, PV 95-23, p. 193, *The Electrochemical Society Proceedings Series*, Pennington, NJ (**1995**).

[44] T. A. Davies, J. D. Genders, and D. Pletcher, *The Electrochemical Consultancy*, Romsey, U.K. **1997**.

[45] Gupta, B., Scherer, G. G. J., *Modified polypropylene fibers with enhanced moisture absorption and disperse dyeability,* Appl. Polym. Sci., **1993**, 50, 2129.

[46] Wiley, R. H., Venkatachalam, T. K, *Sulfonation of polystyrene crosslinked with pure* m-*divinylbenzene,* J. Polym. Sci. Part A, **1966**, 4, 1892-1894.

[47] Wiley, R. H.; Venkatachalam, T. K, J. *Rates of sulfonation of polystyrenes crosslinked with pure* p-*, 2:1/*m*:* p-*, and commercial divinylbenzenes,* Polym. Sci. Part A, **1965**, 3, 1063-1067.

[48] Gupta, B., Scherer, G. G, J., *Development of radiation-grafted FEP-g-polystyrene membranes: Some property–structure correlations*, Appl. Polym. Sci., **1993**, 50, 2129.

[49] Kuhn, H. Gubler, L. Schmidt, T. J. Scherer, G. G. Brack, H.P. Simbek, K. Rager, T. Geiger, F. *Proceedings of the 2nd European PEFC Forum*, June 30-July 4, **2003**, Lucerne, Switzerland, p 69.

[50] Kerres, D.; Cui, W.; Reichle, S, *New sulfonated engineering polymers via the metalation route.* J. Polym. Sci., Part A, **1996**, 34, 2421.

[51] Rikukawa, M.; Sanui, K, *Proton-conducting polymer electrolyte membranes based on hydrocarbon polymers*, Prog. Polym. Sci., **2000**, 25, 1463.

[52] S. Slade, S. A. Campbell, T. R. Ralph, and F. C. Walsh, *Ionic conductivity of an extruded Nafion 1100 EW series of membranes*, Journal of the Electrochemical Society, **2002**, 149, 12, A1556-A1564.

[53] Aharoni, S.M. and M.H. Litt, *Synthesis and properties of some properties of poly-(2,5-trimethylene benzimidazole) and poly-(2,5-trimethylene) benzimidazole hydrochloride. Journal of polymer science,* Journal of polymer science, Part A, **1973**, 12(3), 639.

[54] K. Scott, S. Pilditch and M. Mamlouk, *Modeling and experimental validation of a high temperature polymer electrolyte fuel cell,* J. Appl. Electrochem., **2007**, 37 (11), 1245–1259.

[55] Q. Li, J. O. Jensen, R. F. Savinell and N. J. Bjerrum, *proton exchange membranes based on polybenzimidazole for fuel cells*, Prog. Polym. Sci., **2009**, 34(5), 449–477.

[56] D. A. Boysen, C. R. I. Uda, T. Chisholm and S. M. Haile, *High-Performance Solid Acid Fuel Cells Through Humidity Stabilization*, Science, **2004**, 303(5654), 68–70.

[57] Mamlouk M, Scott K. *A study of oxygen reduction on carbon-supported platinum fuel cell electrocatalysts in polybenzimidazole/phosphoric acid*. *Proceedings of the Institution of Mechanical Engineers,* Part A: Journal of Power and Energy **2011**, 225(A2), 161-174.

[58] Yu Jun, Hadis Zarrin, Michael Fowler, Zhongwei Chen, *Functionalized titania nanotube composite membranes for high temperature proton exchange membrane fuel cells*, International journal of hydrogen energy, **2011**, 36, 6073-6081.

[59] Peighambardoust S, Rowshanzamir S, Amjadi M. *Review of the proton exchange membranes for fuel cell applications*, International Journal of Hydrogen Energy, **2010**, 35, 9349-9384.

[60] Aksoy E, Akata B, Bac N, Hasirci N, *Preparation and characterization of zeolite beta-polyurethane composite membranes*, J Appl Polym Sci, **2007**, 104, 3378-87.

[61] Li Q, He R, Jensen J, Bjerrum N, *Approaches and recent development of polymer electrolyte membranes for fuel cells operating above 100 ^{o}C,* Chem Mater **2003**, 15, 4896-915.

[62] Licoccia S, Traversa E, *Increasing the operation temperature of polymer electrolyte membranes for fuel cells: from nanocomposites to hybrids,* J Power Sources, **2006**, 159, 12-20.

[63] Nagarale R, Shin W, Singh P, *Progress in ionic organic inorganic composite membranes for fuel cell applications,* Polym Chem, **2009**, 1, 388-408.

[64] Jalani N, Dunn K, Datta R, *Synthesis and characterization of NafioneMO2 (M = Zr, Si, Ti) nanocomposite membranes for higher temperature PEM fuel cells,* Electrochim Acta, **2005**, 51, 553-560.

[65] D'Epifanio A, Navarra M, Weise F, Mecheri B, Farrington J, Licoccia S, et al., *Composite nafion/sulfated zirconia membranes: effect of the filler surface properties on proton transport characteristics*. Chem Mater, **2009**, 22, 813-821.

[66] Shao Z, Xu H, Li M, Hsing I, *Hybrid nafion-inorganic oxides membrane doped with heteropolyacids for high temperature operation of proton exchange membrane fuel cell*, Solid State Ionics, **2006**, 177, 779-785.

[67] Chalkovaa E, Wang C, Komarneni S, Lee J, Fedkin M, Lvov S, *Composite proton conductive membranes for elevated temperature and reduced relative humidity PEMFC,* ECS Trans, **2009**.

[68] Matos B, Arico´ E, Linardi M, Ferlauto A, Santiago E,Fonseca F, *Thermal properties of NafioneTiO2 composite electrolytes for PEM fuel cell*, J Therm Anal Calorim, **2009**, 9, 591-594.

[69] Wang H, Holmberg B, Huang L, Wang Z, Mitra A, Norbeck J, *Nafion-bifunctional silica composite proton conductive membranes,* J Mater Chem, **2002**, 12, 834-837.

[70] H. Xiuchong, T. Haolin, and P. Mu, *Synthesis and performance of water-retention PEMs with nafion/intercalating montmorillonite hybrid,* Journal of Applied Polymer Science, **2008**,108, 529-534.

[71] Watanabe, M. Uchida, H. Seki. Y, Emori, M. Stonehart, *Self-Humidifying Polymer Electrolyte Membranes for Fuel Cells*, J. Electrochem. Soc. **1996**, 143, 3847.

[72] Adjemian, K. Bocarsly, *Function and Characterization of Metal Oxide−Nafion Composite Membranes for Elevated-Temperature H_2/O_2 PEM Fuel Cells*, Chem. Mater. **2006**, 18, 2238.

[73] Alberti, G. Casciola, M. *Solid state protonic conductors, present main applications and future prospects,* Solid State Ionics, **2001**, 145, 3-16.

[74] Przyluski, J. Wieczorek, *Proton polymeric electrolytes a review,* W. Synth. Met. **1991**, 45, 323.

[75] Billy B. Bardin, Robert J. Davis, Effect of water on silica-supported phosphotungstic acid catalysts for 1-butene double bond shift and alkane skeletal isomerisation, Applied Catalysis A: General, **2000**, 200, 219–231.

[76] T. Okuhara, N. Mizuno, M. Misono, *Catalytic Chemistry of Heteropoly Compounds, Adv. Catal.,* **1996**, 41, 113.

[77] R.J.J. Jansen, H.M. van Veldhuizen, M.A. Schwegler, H. van Bekkum, Recl. Trav. Chim., *Recent (1987-1993) developments in heteropolyacid catalysts in acid catalyzed reactions and oxidation catalysis*, Pays-Bas, **1994**, 113 (1994), 115.

[78] C.L. Hill, *Introduction and General Overview of Cyclodextrin Chemistry*, Chem. Rev., **1998**, 98, 1.

[79] M. Misono, Stud. *New Catalytic Aspects of Heteropolyacids and Related Compounds - to the Molecular Design of Practical Catalysts,* Surf. Sci. Catal., **1993**, 75, 69.

[80] M.T. Pope, *Heteropoly and Isopoly Oxometalates*, Springer-Verlag, Berlin, **1983**.

[81] T. Okuhara, T. Hashimoto, T. Hibi, M. Misono, *Catalysis by heteropoly compounds*, J. Catal., **1985**, 93, 224.

[82] N. Essayem, G. Coudurier, J.C. Vedrine, D. Habermacher, J. Sommer, *Metal-Catalysed Reactions* **of** *Hydrocarbons,* J. Catal., **1999**, 183, 292.

[83] S.M. Haile, D.A. Boysen, C.R.I. Chisholm, R.B. Merle, *Solid acids as fuel cell electrolytes*, Nature, **2001**, 410, 910–913.

[84] D.A. Boysen, T. Uda, C.R.I. Chisholm, S.M. Haile, *High-Performance Solid Acid Fuel Cells Through Humidity Stabilization*, Science, **2004**, 303, 68–70.

[85] M. Nagao, T. Kamiya, P. Heo, A. Tomita, T. Hibino, M. Sano, *Proton Conduction in* In^{3+}*-Doped* SnP_2O_7 *at Intermediate Temperatures*, Journal of the Electrochemical Society, **2006**, 153, A1604–A1609.

[86] Y. Li, T. Kunitake, Y. Aoki, E. Muto, Efficient, *Anhydrous Proton-Conducting Nanofilms of Y-Doped Zirconium Pyrophosphate at Intermediate Temperatures, Advanced Materials*, **2008**, 20, 2398–2404.

[87] Y.C. Jin, Y.B. Shen, T. Hibino, *Proton conduction in metal pyrophosphates (MP_2O_7) at intermediate temperatures*, Journal of Materials Chemistry, **2010**, 20, 6214–6217.

[88] P. Heo, K. Ito, A. Tomita, T. Hibino, *A Proton-Conducting Fuel Cell Operating with Hydrocarbon Fuels*, Angewandte Chemie International Edition, **2008**, 47, 7841–7844.

[89] Kreuer, K. D. *On the development of proton conducting materials for technological applications***,** Solid State Ionics, **1997**, 97, 1-15.

[90] Yanbai Shen, Pilwon Heo, Chanho Pak, Hyuk Chang, Takashi Hibino, *Intermediate-temperature, non-humidified proton exchange membrane fuel cell with a highly proton-conducting Fe0.4Ta0.5P2O7 electrolyte*, Electrochemistry Communications, **2012**, 24, 82–84.

[91] David A. Burwell, Kathleen G. Valentine, Jozef H. Timmermans, and Thompson, *Structural Studies of Oriented Zirconium Bis(phosphonoacetic acid) Using Solid-state 31P and 13C NMR,* J. Am. Chem. SOC. **1992**, 114, 4144-4150.

[92] Clearfield, A. Smith, J. *Crystallography and structure of alpha-zirconium bis (monohydrogen orthophosphate) monohydrate,* Inorg. Chem. **1969**, 8, 431-436.

[93] Alberti, G. Casciola, M. Palombari, R. J. *Inorgano-organic proton conducting membranes for fuel cells and sensors at medium temperatures Membr*. Sci. **2000**, 172, 233.

[94] Yamanaka, S. Tanaka, Formation region and structural model of γ-zirconium phosphate, M. J. Inorg. Nucl. Chem., **1979**, 41, 45.

[95] Nakamura, O. Ogino, I. Kodama, T. *Temperature and humidity ranges of some hydrates of high-proton-conductive dodecamolybdophosphoric acid and dodecatungstophosphoric acid crystals under an atmosphere of hydrogen or either oxygen or air*, Solid State Ionics, **1981**, 3-4, 347-351.

[96] Giordano, N. Staiti, P. Hocevar, S. Arico, A. S. *High performance fuel cell based on phosphotungstic acid as proton conducting electrolyte*, Electrochim. Acta, **1996,** 41, 397.

[97] T. Okuhara, *New catalytic functions of heteropoly compounds as solid acids*, Catalysis Today, **2002**, 73, 167–176.

[98] V. Ramani, H.R. Kunz, J.M. Fenton, *Stabilized heteropolyacid/Nafion® composite membranes for elevated temperature/low relative humidity PEFC operation*, Electrochimica Acta, **2005**, 50, 1181–1187.

[99] V. Ramani, H.R. Kunz, J.M. Fenton, *Metal dioxide supported heteropolyacid/Nafion® composite membranes for elevated temperature/low relative humidity PEFC operation*, Journal of Membrane Science, **2006**, 279, 506–512.

[100] Crisholm, C. R. I. Haile, S. M. *Superprotonic behavior of Cs_2 (HSO_4) (H_2PO_4) – a new solid acid in the $CsHSO_4$–CsH_2PO_4 system*, Solid State Ionics, **2000**, 229, 136-137.

[101] Haile, S.M. Lentz, G. Kreuer, K. D. Maier, *Superprotonic conductivity in $Cs_3(HSO_4)_2(H_2PO_4)$*, J. Solid State Ionics, **1995**, 77, 128.

[102] Haile, S. M. Boysen, D. A. Chisholm, C. R. I. Merle, R. B. *Solid acids as fuel cell electrolytes*, Nature, **2001**, 410, 910.

[103] Adjemian, K. T.; Srinivasan, S.; Benziger, J.; Bocarsly, A. B. *Investigation of PEMFC operation above 100 °C employing perfluorosulfonic acid silicon oxide composite membranes,* J of Power Sources, **2002**, 109, 356.

[104] Chalkovaa E, Wang C, Komarneni S, Lee J, Fedkin M, Lvov S. *Composite proton conductive membranes for elevated temperature and reduced relative humidity PEMFC*, ECS Trans**; 2009**.

[105] Kalappa P, Lee J., *Proton conducting membranes based on sulfonated poly (ether ether ketone)/TiO_2 nanocomposites for a direct methanol fuel cell*, Polym Int, **2007**, 56, 371-375.

[106] Dmitriy A. Dikin, S. Stankovich, Eric J. Zimney, Richard D. Piner, Geoffrey H.B. Dommett, Guennadi Evmenenko, SonBinh T. Nguyen, Rodney S. Ruoff, *Preparation and characterization of graphene oxide paper*, Nature, **2007**, 448, 457.

[107] Brian Seger, Prashant V. Kamat, *Electrocatalytically Active Graphene-Platinum Nanocomposites. Role of 2-D Carbon Support in PEM Fuel Cells*, J. Phy. Chem. C, **2009,** 113, 7990–7995.

[108] Stankovich, S. Dikin, D. A. Piner, R. D. Kohlhaas, K. A. Kleinhammes, A. Jia, Y. Wu, Y. Nguyen, S. T. Ruoff, R. S. *Synthesis of graphene-based nanosheets via chemical reduction of exfoliated graphite oxide*, Carbon, **2007**, 45, 1558–1565.

[109] Tapas Kuilla, Sambhu Bhadrab, Dahu Yaoa, Nam Hoon Kimc, Saswata Bosed, Joong Hee Lee, *Recent advances in graphene based polymer composites*, Progress in Polymer Science, **2012**, 35, 1350–1375.

[110] Ravi Kumar, Mohamed Mamlouk, Keith Scott, *A Graphite Oxide Paper Polymer Electrolyte for Direct Methanol Fuel Cells,* International Journal of Electrochemistry Volume **2011**, Article ID 434186, 7.

[111] M. Shi, F.C. Anson, *Dehydration of protonated Nafion coatings induced by cation exchange and monitored by quartz crystal microgravimetry.* Journal of Electroanalytical Chemistry, **1997**, 425, 117-123.

[112] C. Huang, K.S. Tan, J. Lin, K. L. Tan, *XRD and XPS analysis of the degradation of the polymer electrolyte in H2-O2 fuel cell.* Chemical Physics Letters, **2003**, 371, 80 - 85.

[113] S. Kundu, K. Karan, M. Fowler, L.C. Simon, B. Peppley, E. Halliop, *Influence of micro-porous layer and operating conditions on the fluoride release rate and degradation of PEMFC membrane electrode assemblies.* Journal of Power Sources, **2008**, 179, 693-699.

[114] A. Ohma, S. Suga, S. Yamamoto, K. Shinohara, *Membrane Degradation Behavior during Opeon-Circuit Voltage Hold Test.* Journal of The Electrochemical Society, **2007**, 154(8), B757-B760.

[115] S. Kocha, J.D. Yang, J.S. Yi, *Characterization of Gas Crossover and Its Implications in PEM Fuel Cells,* AIChE Journal, **2006**, **52**(5).

[116] M. Inaba, T. Kinumoto, M. Kiriake, R. Umebayashi, A. Tasaka , Z. Ogumi, *Gas crossover and membrane degradation in polymer electrolyte fuel cells.* Electrochimica Acta, **2006**, 51, 5746 – 5753.

[117] M. Crum, W. Liu, *Effective Testing Matrix for Studying Membrane Durability in PEM Fuel Cells: Part 2. Mechanical Durability and Combined Mechanical and Chemical Durability.* ECS Transactions, **2006**, 3(1), 541 - 550.

[118] C. Huang, Z.S. Liu, D.Q. Mu, *The Mechanical Changes in the MEA of PEM Fuel Cells due to Load Cycling.* ECS Transactions, **2008**, 16(2), 1987-1996.

[119] X. Huang, W. Yoon, *Inhomogeneous Degradation of Polymer Electrolyte Membrane in PEM Fuel Cells* in *216th ECS Meeting*. **2008**. Vienna, Austria: The Electrochemical Society.

[120] R. Solasi, Y. Zou, X. Huang, K. Reifsnider, D. Condit, *On mechanical behavior and in-plane modeling of constrained PEM fuel cell membranes subjected to hydration and temperature cycles.* Journal of Power Sources, **2007**, 167, 366-377.

[121] Xi. Huang, R. Solasi, Y. Zou, M. Feshler, K. Reifsnider, D. Condit, S. Burlatsky, T. Madden, *Mechanical Endurance of Polymer Electrolyte Membrane and PEM Fuel Cell Durability.* Journal of Polymer Science: Part B: Polymer Physics, **2006**, 44, 2346-2357.

[122] J. Benziger, E. Chia, J.F. Moxley, I.J. Kevrekidis, *The dynamic response of PEM fuelcells to changes in load.* Chemical Engineering Science, **2005**, 60, 1743-1759.

[123] S. Zhang, X. Yuan, H. Wang, W. Merida, J. Shen, S. Wu, J. Zhang, H. Zhu, *A review of accelerated stress tests of MEA durability in PEM fuel cells.* International Journal of Hydrogen Energy, **2009**, 34, 388–404.

[124] G.H. Guvelioglu, H.G. Stenger, *Flow rate and humidification effects on a PEM fuel cell performance and operation.* Journal of Power Sources, **2007**, 163, 882–891.

[125] E. Endoh, S. Terasono, H. Widjaja, Y.Takimoto, *Degradation Study of MEA for PEMFCs under Low Humidity Conditions.* Electrochemical and Solid-State Letters, **2004**, 7(7), A209-A211.

[126] J.F. Chiou, D.R. Paul, *Gas Permeation in a Dry Nafion Membrane.* Ind. Eng. Chem. Res., **1988**, 27, 216 –2164.

[127] B. Wahdame, D. Candusso, F. Harel, X. Francois, M.C. Pera, D. Hissel, J.-M. Kauffmann, *Analysis of a PEMFC durability test under low humidity conditions and stack behaviour modelling using experimental design techniques.* Journal of Power Sources, **2008**, 182, 429–440.

[128] Zhongqing Jiang, Xinsheng Zhao, Yongzhu Fu, Arumugam Manthiram, *Composite membranes based on sulfonated poly (ether ether ketone) and SDBS-adsorbed graphene oxide for direct methanol fuel cells*, J. Mater. Chem., **2012**, 22, 24852.

[129] Guifen Chena, Shengyong Zhaib, Yanling Zhaia, Ke Zhanga, Qiaoli Yuea, Lei Wanga,

Jinsheng Zhaoa, Huaisheng Wanga, Jifeng Liua, Jianbo Jia, *Preparation of sulfonic functionalized graphene oxide as ion-exchange material and its application into electrochemiluminescence analysis*, Biosensors and Bioelectronics, **2011**, 26, 3136–3141.

[130] Lu Zhang, Zhipeng Wang, Chen Xu, Yi Li, Jianping Gao, Wei Wangc. Yu Liu, *High strength graphene oxide/polyvinyl alcohol composite hydrogels*, J. Mater. Chem., **2011**, 21, 10399-10406.

[131] Qian Liu, Laizhou Song, Zhihui Zhang, Xiaowei Liu, *Preparation and characterization of the PVDF-based composite membrane for direct methanol fuel cells*, International Journal of Energy and Environment, **2010**, 1, 643-656.

[132] Jung-Hwan Jung, Jin-Han Jeon, Vadahanambi Sridhar, Il-Kwon Oh, *Electro-active graphene-Nafion actuators,* Carbon, **2011**, 149, 1279 –1289.

[133] Zhongwei Chen, Drew Higgins, Aiping Yu, Lei Zhang, Jiujun Zhang, *A review on non-precious metal electrocatalysts for PEM fuel cells,* Energy Environ. Sci., **2011**, 4, 3167.

[134] Stamenkovic, V. R. et al. *Trends in electrocatalysis on extended and nanoscale Pt-bimetallic alloy surfaces,* Nature Mater. **2007**, 6, 241-247.

[135] Yano, H., Kataoka, M., Yamashita, H., Uchida, H. & Watanabe, M. *Oxygen reduction activity of carbon-supported Pt_M (MDV, Ni, Cr, Co, and Fe) alloys prepared by nanocapsule method,* Langmuir, **2007**, 23, 6438-6445.

[136] Stamenkovic, V. R., Mun, B. S., Mayrhofer, K. J. J., Ross, P. N. & Markovic, N. M. *Effect of surface composition on electronic structure, stability, and electrocatalytic properties of Pt-transition metal alloys: Pt-skin versus Pt-skeleton surfaces*, J. Am. Chem. Soc. **2006**, 128, 8813-8819.

[137] Ying Liu, William E, Mustain, *High Stability, High Activity Pt/ITO Oxygen Reduction*

Electrocatalysts, J. Am. Chem. Soc. **2013**, 135, 530−533.

[138] Antolini, E., Salgado, J. R. C. & Gonzalez, E. R, *The stability of Pt-M (M=first row transition metal) alloy catalysts and its effect on the activity in low temperature fuel cells-a literature review and tests on a Pt-Co catalyst,* J. Power Sources, **2006**, 160, 957-968.

[139] Min, M. K., Cho, J. H., Cho, K. W. & Kim, H. *Particle size and alloying effects of Pt-based alloy catalysts for fuel cell applications*, Electrochim. Acta, **2000**, 45, 4211-4217.

[140] J. Chen, B. Lim, E. P. Lee, Y. Xia, *Shape-controlled synthesis of platinum nanocrystals for catalytic and electrocatalytic applications,* Nano Today, **2009**, 4, 81–95.

[141] Y. Zheng, Y. Jiao, M. Jaroniec, Y. Jin, S. Z. Qiao, *Nanostructured Metal-Free Electrochemical Catalysts for Highly Efficient Oxygen Reduction*, Small, **2012**, 8, 3550 – 3566.

[142] J. K. Nørskov, J. Rossmeisl, A. Logadottir, L. Lindqvist, J. R. Kitchin, T. Bligaard, H. Jonson, *Origin of the Overpotential for Oxygen Reduction at a Fuel-Cell Cathode*, J. Phys. Chem. B, **2004**, 108, 17886 – 17892.

[143] D. Yu, E. Nagelli, F. Du, L. Dai, *Metal-Free Carbon Nanomaterials Become More Active than Metal Catalysts and Last Longer*, J. Phys. Chem. Lett., **2010**, 1, 2165–2173.

[144] J. Zhang, K. Sasaki, E. Sutter, R. R. Adzic, *Stabilization of Platinum Oxygen-Reduction Electrocatalysts Using Gold Clusters*, Science, **2007**, 315, 220 – 222.

[145] K. J. Kinoshita, *Particle Size Effects for Oxygen Reduction on Highly Dispersed Platinum in Acid Electrolytes*, J. Electrochem. Soc. **1990**, 137, 84 –848.

[146] V. R. Stamenkovic, B. Fowler, B. S. Mun,G. F.Wang, P. N. Ross, C. A. Lucas, N. M. Markovic, *Improved Oxygen Reduction Activity on $Pt_3Ni(111)$ via Increased Surface Site Availability*, Science, **2007**, 315, 493–497.

[147] C. Wang, N. M. Markovic, V. R. Stamenkovic, *Advanced Platinum Alloy Electrocatalysts for the Oxygen Reduction Reaction*, ACS Catal. **2012**, 2, 89 –898.

[148] J. Greeley, I. E. L. Stephens, A. S. Bondarenko, T. P. Johansson, H. A. Hansen, T. F. Jaramillo, J. Rossmeisl, I. Chorkendorff, J. K. Nørskov, *Alloys of platinum and early transition metals as oxygen reduction electrocatalysts*, Nat. Chem. **2009**, 1,552 – 556.

[149] S. H. Sun, C. B. Murray, D. Weller, L. Folks, A. Moser, *Monodisperse FePt Nanoparticles and Ferromagnetic FePt Nanocrystal Superlattices Science*, **2000**, 287, 1989 – 1992.

[150] M. Chen, J. Kim, J. P. Liu, H. Y. Fan, S. H. Sun, *Synthesis of FePt Nanocubes and Their Oriented Self-Assembly*, J. Am. Chem. Soc. **2006**, 128, 7132–7133.

[151] Petrow, H.G. and R.J. Allen, *Finely particulated colloidal platinum compound and sol for producing the same, and method of preparation of fuel cell electrodes and the like employing the same*. **1977**: United States.

[152] Srinivasan, S., et al., *Advances in solid polymer electrolyte fuel cell technology with low platinum loading electrodes.* Journal of Power Sources, **1988**, **22**(3–4), 359-375.

[153] S. Sun, S. Anders, T. Thomson, J. E. E. Baglin, M. F. Toney, H. F. Hamann, C. B. Murray, B. D. Terris, *Controlled Synthesis and Assembly of FePt Nanoparticles*, J. Phys. Chem. B**, 2003**, 107, 5419–5425.

[154] Farhana S. Saleh and E. Bradley Easton, *Diagnosing Degradation within PEM Fuel Cell Catalyst Layers Using Electrochemical Impedance Spectroscopy*, Journal of The Electrochemical Society, **2012**, 159 (5), B546-B553.

[155] Y. Y. Shao, G. P. Yin, Y. Z. Gao, and P. F. Shi, *Durability Study of Pt/C and Pt/CNTs Catalysts under Simulated PEM Fuel Cell Conditions,* J. Electrochem. Soc., **2006**, 153, A1093.

[156] C. A. Reiser, L. Bregoli, T. W. Patterson, J. S. Yi, J. D. L. Yang, M. L. Perry, and T. D. Jarvi, *A Reverse-Current Decay Mechanism for Fuel Cells*, Electrochem. Solid State Lett. **2005**, 8, A273-A276.

[157] D. A. Stevens, M. T. Hicks, G. M. Haugen, and J. R. Dahn, *Effect of Carbon Type and Humidification on Degradation of the Carbon*, J. Electrochem. Soc., **2005**, 152, A2309.

[158] Y. Shao, in *Investigation on the stability of Pt/carbon nanotube catalysts and novel methods for the preparation of the electrodes for PEMFC, Ph.D. Thesis*, Harbin Institute of Technology, Harbin, China (**2006**).

[159] M. Mathias, H. Gasteiger, R. Makharia, S. Kocha, T. Fuller, and J. Pisco, *ACS National Meeting Book of Abstracts*, 228(1), FUEL-2 (**2004**).

[160] M. S. Wilson, F. H. Garzon, K. E. Sickafus, and S. Gottesfeld, *Surface Area Loss of Supported Platinum in Polymer Electrolyte Fuel Cells,* J. Electrochem. Soc., **1993**, 140, 2872.

[161] M. Fowler, J. C. Amphlett, R. F. Mann, B. A. Peppley, and P. R. Roberge, *Issues associated with Voltage Degradation in a PEMFC Michael*, J. New Mater. Electrochem. Syst., **2002**, 5, 255.

[162] N. Sisofo, *4th Annual Inter. Fuel Cell Testing Workshop*, Vancouver, BC, Canada, September **2007**, 12–13.

[163] A. Taniguchi, T. Akita, K. Yasuda, Y. Miyazaki, *Analysis of electrocatalyst degradation in PEMFC caused by cell reversal during fuel starvation*, J. Power Sources, **2004,** 130, 42–49.

[164] L.M. Roen, C.H. Paik, T.D. Jarvi, *Electrocatalytic Corrosion of Carbon Support in PEMFC Cathodes*, Electrochem. Solid-State Lett. **2004**, 7, A19–A22.

[165] B. Du, R. Pollard, J. Elter, *Proceedings of Fuel Cell Seminar 2006*, Honolulu, Hawaii, USA, November, **2006**, 61–64.

[166] Shanna D. Knight, Kevin M. Colbow, Jean St-Pierre, David P. Wilkinson, *Aging mechanisms and lifetime of PEFC and DMFC,* Journal of Power Sources, **2004**, 127, 127–134.

[167] Zempachi Ogumi, Masafumi Nose, Choo Hyun-Suk, Takeshi Abe, *Electrochemical Oxidation Mechanism of Highly Oriented Pyrolytic Graphite in Sulfuric Acid Solution*, ECS Trans. **2008** 13(17), 111-118.

[168] R.C. McDonald, C.K. Mittelsteadt, E.L. Thompson, *Effects of Deep Temperature Cycling on Nafion® 112 Membranes and Membrane Electrode Assemblies*, Fuel Cells**, 2004**, 4, 208–213.

[169] M. Inaba, T. Kinumoto, M. Kiriake, R. Umebayashi, A. Tasaka, Z. Ogumi, *Gas crossover and membrane degradation in polymer electrolyte fuel cells*, Electrochim. Acta, **2006**, 51, 5746–5753.

[170] C. Bock, H. Halvorsen, B. MacDougall, J. Zhang (Ed.), *PEM Fuel Cell Catalysts and Catalyst Layers*, Springer, London (**2008**), 447.

[171] Z. Liu, Z.Q. Tian, S.P. Jiang, *Synthesis and characterization of Nafion-stabilized Pt nanoparticles for polymer electrolyte fuel cells,* Electrochim Acta. **2006,** 52, 1213-1220.

[172] G. Sasikumar, J.W. Ihm, H. Ryu, *Dependence of optimum Nafion content in catalyst layer on platinum loading*, J. Power Sources, **2004**,132, 11-17.

[173] S.T. Oyama, *The Chemistry of Transition Metal Carbides and Nitrides,* first ed., Springer, **1996**.

[174] O.T. Musthafa, S. Sampath, *High Performance Platinised Titanium Nitride Catalyst for Methanol Oxidation,* Chem. Commun., **2008**, 1, 67–69.

[175] W. Schintlmeister, O. Pacher, K. Pfaffinger and T. Raine, *Structure and Strength Effects in CVD Titanium Carbide and Titanium Nitride Coatings*, J. Electrochem. Soc., **1976**, 123, 924.

[176] C. Y. Ting, *TiN as a high temperature diffusion barrier for arsenic and boron,* Thin Solid Films, **1984**, 119, 11.

[177] Toth, L.E. *Transition Metal Carbides and Nitrides*, Academic Press: New York, NY, USA, **1971**.

[178] Oyama, S.T, *The Chemistry of Transition Metal Carbides and Nitrides*, Blackie Academic and Professional: Glasgow, UK, **1996**.

[179] Gogotsi, Y.G. Andrievski, R.A. *Materials Science of Carbides, Nitrides and Borides*, Kluwer Academic publisher: Dordrecht, The Netherlands, **1999**.

[180] Milosev I, Strehblow H, Navinsek B, Metikos-Hukovic M, *Electrochemical and thermal oxidation of TiN coatings studied by XPS,* Surf Interface Anal, **1995**, 23, 529-539.

[181] Bharat Avasarala, Pradeep Haldar, *On the stability of TiN-based electrocatalysts for fuel cell Applications*, International journal of Hydrogen Energy, **2011**, 36, 3965-3974.

[182] Dong Jin Ham and Jae Sung Lee, *Transition Metal Carbides and Nitrides as Electrode Materials for Low Temperature Fuel Cells*, Energies, **2009**, 2, 873-899.

[183] B. Avasarala, T. Murray, W. Li, P. Haldar, *Titanium nitride nanoparticles based electrocatalysts for proton exchange membrane fuel cells,* J. Mater. Chem. **2009**, 19, 1803–1805.

[184] Saha NC, Tompkins HG, *Titanium nitride oxidation chemistry: an x-ray photoelectron spectroscopy study*, J Appl Phys, **1992**, 72, 3072-3079.

Chapter 3. Experimental and Theoretical Methods

This chapter describes the experimental and theoretical methods used in this research

3.1 Experimental section

3.1.1 Chemicals and Reagents

All chemicals and reagents were purchased from commercial chemical suppliers. Sulphuric acid, nitric acid, phosphoric acid and hydrochloric acid were obtained from Alfa aesar and used as received. Methanol, absolute ethanol, 30% w/v hydrogen peroxide, formaldehyde, acetone, acetic acid, were AR grade reagents and used as received. AR grade sulfanilic acid, sodium nitrate, potassium ferrocyanide, potassium ferricyanide, sodium hydroxide, potassium permanganate and sodium borohydride were purchased from fisher scientific and used as received. Titanium nitride powder (3 μm size), Pt black, $PdCl_2$, H_2PtCl_6, were purchased from Sigma Aldrich and used as received. 20 wt% Pt supported on advanced carbon was procured from Alfa aesar. Natural graphite was obtained from Alfa aesar.

All the glassware was rinsed with chromic acid followed by thorough washing with soap water and again with deionised water and dried. Deionised water (Millipore, 18 MΩcm) was used to prepare all solutions.

3.1.2 Preparation of graphite oxide

Graphite oxide was synthesised from natural flake graphite (Graphite flake, natural, 325 meshes (99.8%)) by the modified Hummers method [1]. In this method 200 mg of graphite particles were immersed in concentrated sulfuric acid (46 ml) and $KMnO_4$ (6 g) was added slowly in small quantities in which temperature was maintained between the 0 and 5 ^{o}c using an ice bath, after the complete oxidation of $KMnO_4$, the mixture was heated to 37 ^{o}c and kept at this temperature about 30 min. Then 12 ml of distilled water was added slowly to this mixture and then the temperature of mixture was raised to 95 ^{o}c and it was maintained for about 15 min, this mixture was further diluted with 280 ml of water and later 20 ml of 30% H_2O_2 was added and left for 5 min, then solid was filtered off and washed with 5% HCl until filtrate was free from sulphate ions. Graphite oxide thus obtained was further washed thoroughly with water and dried in air for 24 hours.

3.1.3 Synthesis of sulfonated graphite oxide (SGO) through aryl diazonium reaction of sulfanilic acid

The aryl diazonium salt used for sulfonation was prepared as following [2]: To a 100 mL beaker placed 5 mL NaOH (2%) and 0.05 g sulfanilic acid (SA), and allowed SA to dissolve in warm water bath. To the above solution 0.02 g $NaNO_2$ was added at RT, after $NaNO_2$ dissolved the mixed solution was added into 10 mL ice water and 1 mL of concentrated HCl under stirring, the temperature was kept at 0 ^oC for 15 min and diazonium salt was formed. Then the diazonium salt solution was added drop wise into 50 mL of GO (1 mg/mL) solution and the mixed solution was stirred vigorously for 4 h in an ice water bath. After centrifuging and washing with water for several times, the obtained SGO was dispersed in water and stored at RT for use.

3.1.4 GO and SGO paper polymer electrolyte membrane

3.1.4.1 Fabrication of GO and SGO free standing paper

Colloidal solutions of graphite oxide and sulfonated graphite oxide were prepared in water at a concentration of 2 mg cm^{-3} (mg/ml) using an ultrasonic water bath. Free standing GO and SGO papers (figure 3.1; thickness of ~35 µm) were prepared by filtration of the resulting colloid through a membrane filter (cellulose acetate membrane filter; 47 mm in diameter, 0.2 µm pore size) followed by air drying and peeling from the filter [3].

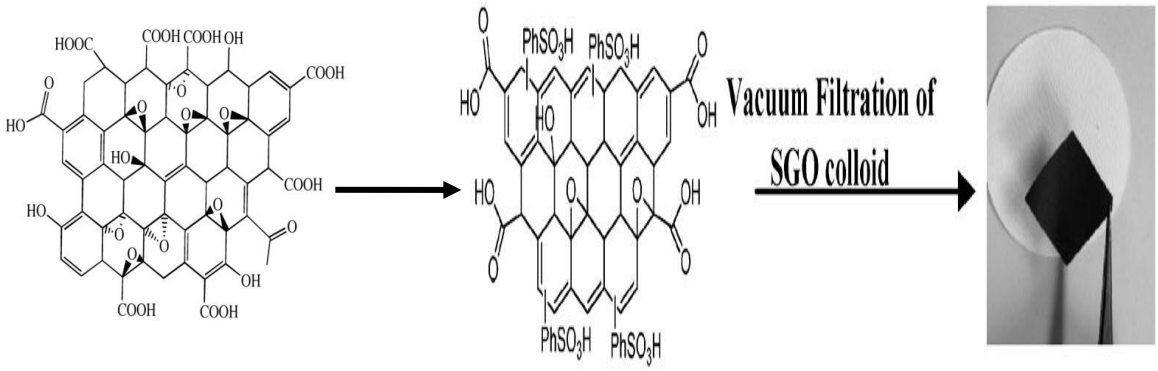

Figure 3.1, Schematics of fabrication of GO and SGO paper by vacuum filtration of colloidal solution GO and SGO

3.1.4.2 Fabrication of Nafion® laminated sulfonated graphite oxide paper

Sulfonated graphite oxide paper prepared from vacuum filtration has been used to laminate the Nafion. Nafion (5% solution) is dissolved in 2-propanol and drop coated on both side of the surface of SGO paper and dried at 60 ^{o}C, the coating is continued until the achievement of few micrometer thickness layer of Nafion on SGO paper.

3.1.5 Preparation of composite membranes for polymer electrolyte fuel cells

3.1.5.1 GO and SGO/Nafion composite membranes

Composite membranes were prepared by dissolving precast Nafion® membrane (5% Nafion® solution in lower aliphatic alcohols, Sigma Aldrich) in dimethylacetamide (DMAc) and mixing with a solution of GO in DMAc solution with a mass ratio of 2%, 4% or 6% and 4% SGO. The mixture was stirred for 1 h and the composite membranes were prepared by casting this solution on a glass plate and dried at 70 ^{o}C. The resulting membranes were peeling off and dried at 120 ^{o}C in an oven for 2 h. Finally, membranes were pre-treated by boiling for 1 h in 5% H_2O_2, water, 0.5 M H_2SO_4 and water in sequence. The dry membrane thickness was measured at 10 random points over their surface using a digital micrometer.

3.1.6 Preparation of SGO/Sulfonated poly ether-ether Ketone composite membranes for polymer electrolyte membrane fuel cells

3.1.6.1 Sulfonation of poly ether-ether ketone

Sulfonated poly ether-ether Ketone **(**SPEEK**)** was prepared by electrophilic substitution of poly ether-ether ketone **(**PEEK) using 98% H_2SO_4 [4]. PEEK was first dried in oven at 80 ^{o}C for 24 h before sulfonation. Then, the dried PEEK (5 g) was gradually dissolved into 100 mL sulphuric acid (H_2SO_4, 98%) in a three-neck flask for about 3 h at room temperature, followed by vigorous stirring at 45 ^{o}C for 8 h. Afterward, the polymer solution was gradually precipitated into ice-cold water under mechanical agitation. Finally, the polymer precipitate was filtered, washed several times with de-ionized water until pH reached neutral and then dried first at room temperature for 24 h and then at 60 ^{o}C for another 24 h. The sulfonation degree (DS) was determined by acid base titration method.

3.1.6.2 Preparation of recast SPEEK, SGO/SPEEK composite membranes

SPEEK (10 wt%) was dissolved in dimethylacetamide (DMAc) and used for preparation of recast and composite membranes. SGO/SPEEK composite membranes were prepared by mixing certain wt% of SGO in SPEEK solution and sonicated for 1 h, then casting this solution on a glass plate and dried at 70 ^{o}C followed by annealing at 80 ^{o}C for 12 h. The membranes were peeled off from the glass plate and soaked in 0.5 M H_2SO_4 for 2 days and washed with deionised water and stored in deionised water for further use.

3.1.7 Water uptake test and Ion Exchange Capacity (IEC) measurements

Membrane samples (Nafion and SPEEK composite membranes) with an area of 5 cm^2 were dried at 70 ^{o}C for 24 h, weigh in a dried state (W_{dry}), and then soaked with deionised water at a room temperature for 24 h. The membranes were carefully blotted of all surface water and weighed again (W_{wet}). The water uptake was calculated from the following equation.

$$\text{Water uptake (\%)} = 100 \times (W_{wet} - W_{dry})/ W_{dry}. \qquad (3.1)$$

The ion exchange capacity (IEC) of the membranes was measured with the classical titration technique. The samples were soaked in a large volume of 0.1 mol L^{-1} HCl solution, washed with distilled water to remove excess HCl, and then immersed in 1 M NaCl aqueous solution to release protons from the membrane. The released H^+ was back titrated with a 0.01 M NaOH aqueous solution using phenolphthalein as an indicator. The IEC value (in meq g^{-1}), which is defined as milli equivalents (meq) of sulfonic groups per gram of dried sample, was obtained from following equation.

$$\text{IEC (meq g}^{-1}) = V_{NaOH} \times C_{NaOH}/ W_{dry} \qquad (3.2)$$

Where V_{NaOH} is the volume of NaOH consumed, C_{NaOH} is the concentration of NaOH and W_{dry} is the weight of the dry membrane (g).

3.1.8 Proton conductivity measurements

Membrane samples with an area of 0.5 x 1.5 cm^2 were cut into pieces and used for measuring in-plane proton conductivity (figure 3.2). AC impedance measurements were carried out between frequencies of 20 kHz and 1 kHz, using a four-point probe method with a Frequency Response Analyzer (Voltech TF2000, UK). The method involves four equally spaced probes in contact with the measured material: two of the probes were used to source current whilst the other two were used to measure the voltage drop. The cell was operated at various relative humidity and temperature.

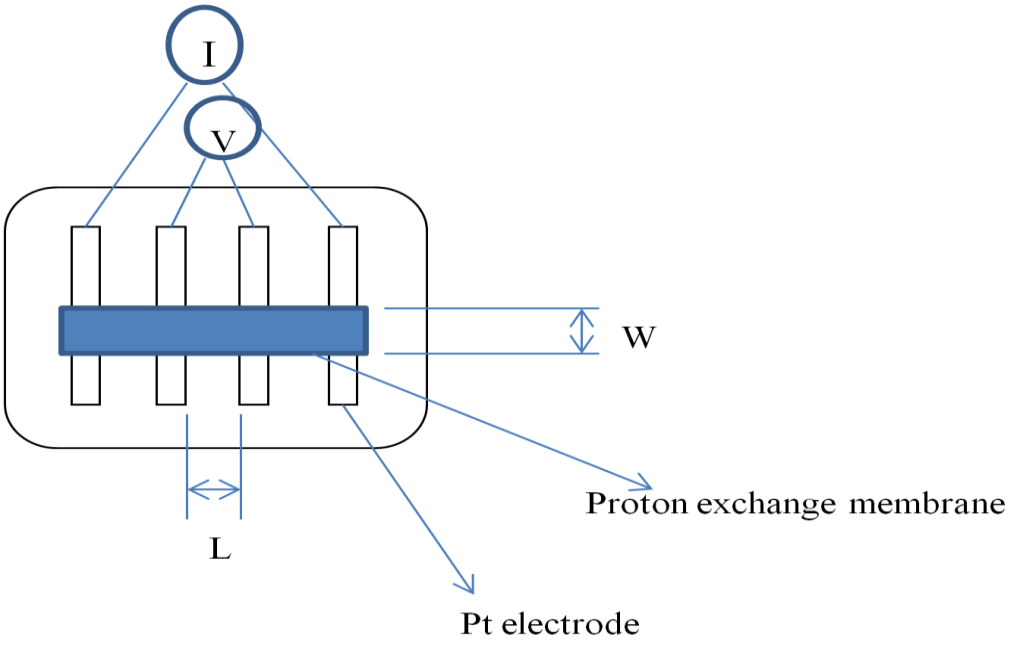

Figure 3.2, Schematic representation of in-plane proton transport measurement cell

Calculation of in-plane proton conductivity using the following equation;

$$\sigma_{ip} = L/R*A \qquad (3.3a)$$

Where σ_{ip} is the in-plane proton conductivity ($S.cm^{-1}$), L is the distance between the Pt electrodes (0.5 cm), R is the resistance (ohms) and A is the area of the membrane (cm^2).

Through plane conductivity of the membrane was measured by AC impedance spectroscopy from membrane electrode assembly. The resistance associated with the membrane at zero phase angles was used to estimate the through-plane proton conductivity of the membrane using the equation, (3.3b);

$$\sigma_{tp} = L/R*A \qquad (3.3b)$$

Where σ_{tp} is the through-plane proton conductivity ($S.cm^{-1}$), L is the membrane thickness, R is the bilk resistance of the membrane and A is the area of the membrane (cm^2).

Activation energy of proton conductivity was calculated using the Arrhenius equation (3.3c)

$$k = A\, e^{-Ea/RT} \qquad (3.3c)$$

3.1.9 Preparation of membrane electrode assembly (MEAs)

To prepare the fuel cell membrane electrode assemblies, the polymer electrolyte membrane was sandwiched between anode catalyst layer and cathode catalyst layer (the catalyst loadings in different MEA are mentioned in the results and discussion part). The catalyst ink was made by ultrasonicating the catalyst with 2-propanol and 20 wt% Nafion® ionomer, and the ink was sprayed onto gas diffusion electrodes (carbon paper) with a wet proofed micro-porous layer (H2315 T10AC1), purchased from Freudenberg (FFCCT, Germany). The MEA was hot pressed at 125 ^{o}C and a pressure of 60 kg cm^{-2} for 3 minutes.

3.1.10 Fuel cell tests

The MEA was set between two titanium blocks and the active electrode area (1 cm^{2}) was formed by the parallel gas flow channels area (figure 3.3). Electric cartridge heaters were inserted to the titanium blocks to maintain the desired temperature, which was monitored by imbedded thermocouples and controlled with a temperature controller. Gold-plated steel bolts were screwed into the blocks to allow electrical contact. The diagrammatic representation of fuel cell system is shown in figure 3.4. H_2 and O_2 (humidified) were fed to each side of the cell at a flow rate of 0.1 and 0.07 dm^{3} min^{-1} respectively. The cell was conditioned at 0.3 V for 1 h before polarisation studies.

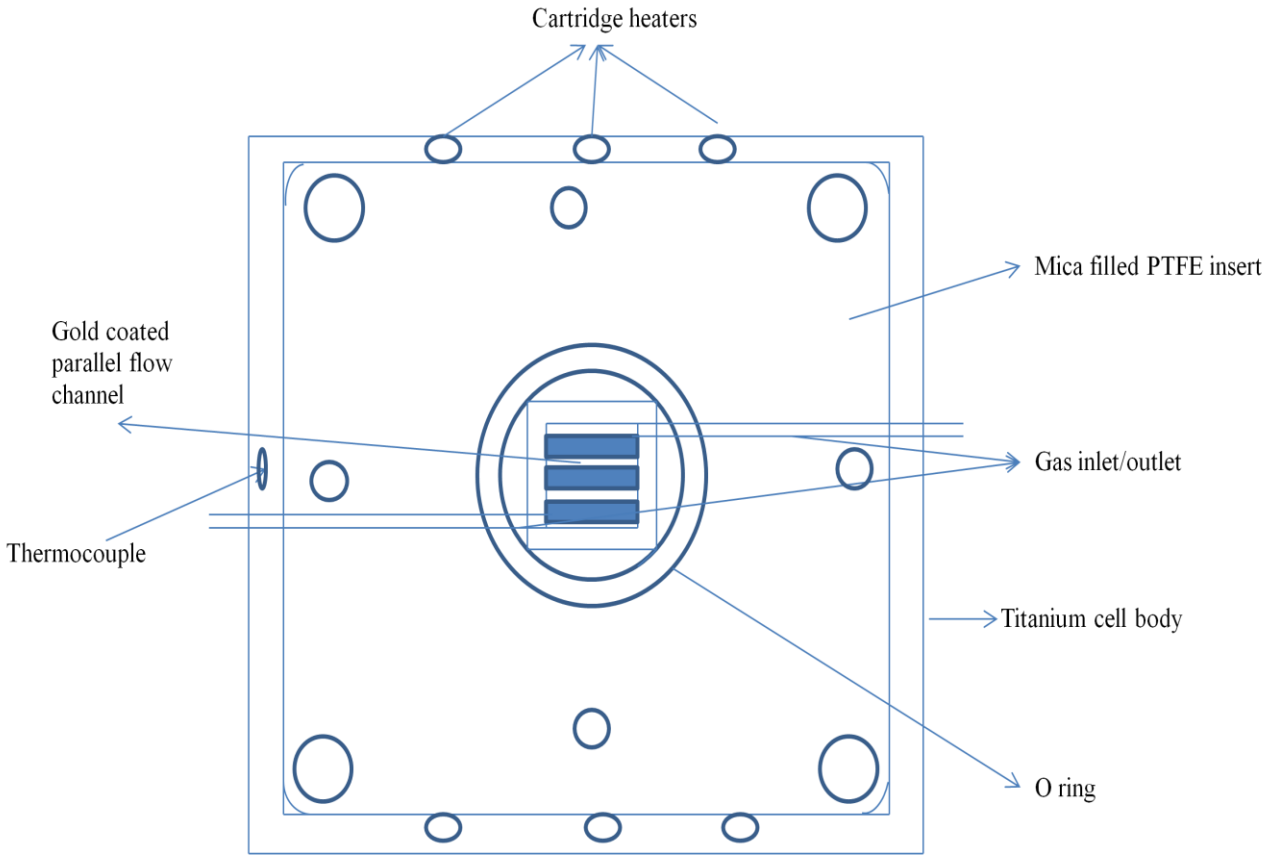

Figure 3.3, Schematics of titanium testing fuel cell with flow channels

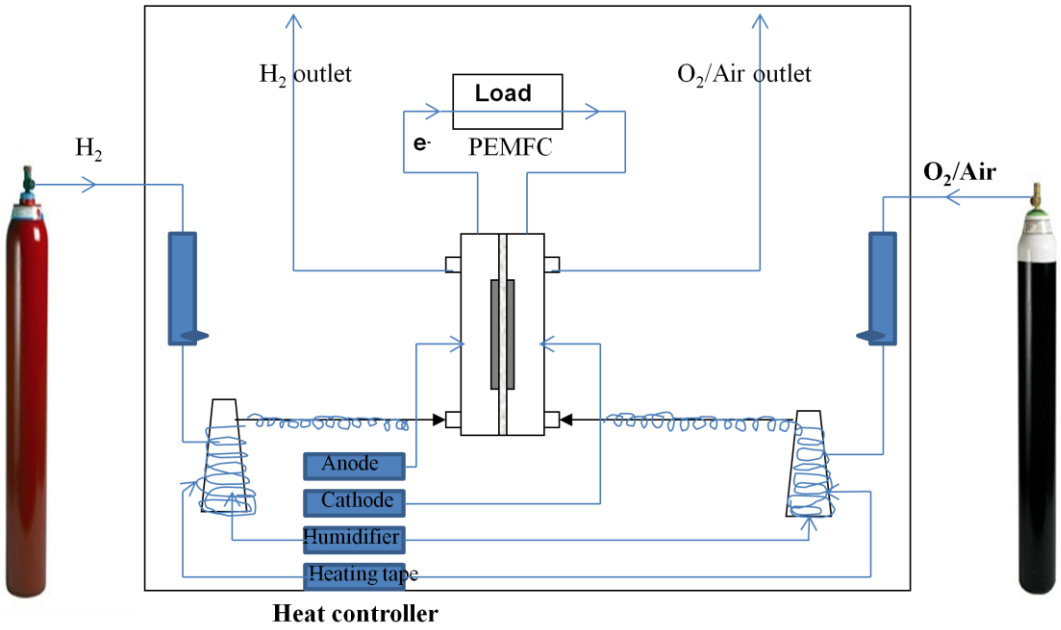

Figure 3.4, Diagrammatic representation of fuel cell system

3.1.11 Preparation of cathode electrocatalyst

3.1.11.1 Preparation of Nafion® stabilised Platinum nanoparticles supported on TiN (Pt/TiN) by chemical reduction

The synthesis of Nafion® stabilised Platinum nanoparticles was carried out by chemical reduction method using TiN, hexachloroplatinic acid hexa hydrate ($H_2PtCl_6.6H_20$), Nafion® (10%) and sodium borohydride ($NaBH_4$) [5]. In brief, hexachloroplatinic acid is stirred with Nafion® (10%; 200 µl) for 1h. 5 ml of 87 mM $NaBH_4$ is added drop by drop to produce Nafion® stabilised Pt colloid. Excess Nafion was removed by washing the colloid with 1:4 v/v water and acetone. A TiN powder is added to the purified Pt colloid and sonicated for 1h. Finally the solvent was evaporated and dried at 60 ^oC.

3.1.11.2 Preparation of Platinum nanoparticles supported on TiN (Pt/TiN) by impregnation

The TiN supported Pt nanoparticles were produced using an impregnation method [6]. In a typical synthesis, hexachloroplatinic acid hexa hydrate ($H_2PtCl_6.6H_20$) was dissolved in deionised water, and certain amount of TiN powder was added and sonicated for 30 minutes. The slurry was heated at 80 ^oC under magnetic stirrer to allow the solvent to evaporate. The resulting powder was heat treated in a tubular furnace at 400 ^oC under hydrogen stream for 3 h.

3.1.11.3 Preparation of Platinum-Cobalt nanoparticles supported on TiN (Pt-Co/TiN)

The TiN supported Pt-Co alloy nanoparticles were produced using an impregnation method [7, 8]. In a typical synthesis, hexachloroplatinic acid hexa hydrate ($H_2PtCl_6.6H_20$) and cobalt chloride hexa hydrate ($CoCl_2.6H_2O$) were dissolved in deionised water, and certain amount of TiN powder was added and sonicated for 30 minutes. The slurry was heated at 80 ^oC under magnetic stirrer to allow the solvent to evaporate. The resulting powder was heat treated in a tubular furnace at 400 ^oC under hydrogen stream for 3 h.

3.1.12 Electrochemical evaluation of cathode electrocatalyst

3.1.12.1 Electrochemical active surface area and durability test by cyclic voltammetry

Electrocatalytic activity and durability of catalysts were performed in a standard three electrode set up (figure 3.5) using rotating disc electrode (RDE) with a potentiostat (Autolab PGSTAT302N, Echochemie) and rotation control. A silver/silver chloride electrode (3 M KCl) is used as a reference electrode and potentials are referred to

reversible hydrogen electrode (RHE) (Appendix B). Glassy carbon electrode disc (5 mm diameter, 0.1962 cm^{-2}) is used as the working electrode substrate. Catalyst ink was prepared by ultrasonically mixing the catalyst in water and ethanol (1:1 v/v) and pipetting 5 µl of suspension onto the glassy carbon disc electrode to achieve a catalyst loading of 20 µg cm^{-2}. After drying, a drop of Nafion® (5%) solution is pipeted onto glassy carbon electrode surface as a binder to attach the catalyst and also acts as a proton carrier.

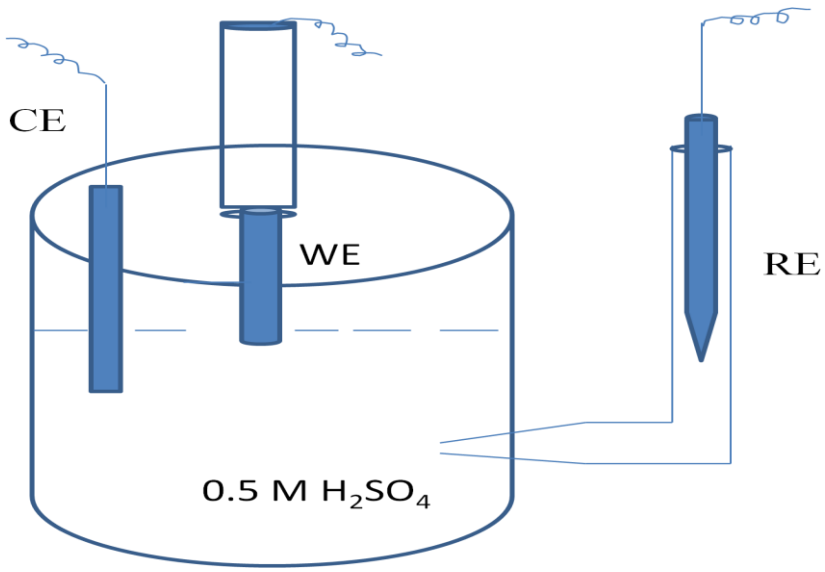

Figure 3.5, Standard three electrode set up of electrochemical system

Cyclic voltammetry was performed at 50 mV s^{-1} between 0 to +1.2 V vs. RHE in an N_2 saturated 0.5 M H_2SO_4 and H_3PO_4 at room temperature. Electrochemical active surface area in m^2 g^{-1}_{Pt} was measured from the area under the hydrogen desorption peaks of CV curves after double-layer corrections. Accelerated catalyst degradation test was performed between 0.6 to 1.2 V at 50 mV s^{-1}.

The CV recorded for Pt/C in an N_2 saturated is 0.5 M H_2SO_4 is shown in figure 3.6 at a scan rate of 50 mV s^{-1}. The working electrode (Pt/C) potential is scanned between 0.0 to 1.2 V vs. RHE. The CV can be divided into three segments: H underpotential deposition region (~0.05 to 0.34 V vs. RHE), double layer region (0.34 to 0.8 V vs. RHE) and Pt oxide formation region (above 0.8 V vs. RHE). As the potential increases (forward scan), pre-adsorbed H atoms on Pt surface are oxidised to H^+ and desorbs from Pt surface and diffuse into electrolyte; as the potential increases further (above 0.7 V vs. RHE) water starts to adsorb and dissociates on Pt surface forming Pt-OH and continue to form Pt oxides as the potential increases. On the reverse scan, as the potential

decreases Pt oxide is being reduced. When the potential is reached to 0.34 V vs. RHE the protons from the electrolyte will adsorb on Pt and be reduced. In the potential region of 0.34 to 0.8 V, the Pt surface is free of H or OH/O, and the current observed is mainly a contribution of double layer capacitance (anion adsorption from the electrolyte such as SO_4^{2-}). The large surface area of carbon is also contributing to the capacitive current. The electrochemical surface area (ECSA) of Pt can be calculated by integrating the hydrogen desorption charge (Q_{Hdes} C cm^{-2}). Assuming the Pt electric charge density of 210 µC $cm^{-2}{}_{Pt}$ and knowing the Pt loading, ECSA can be estimated.

$$ECSA = QHdes*100 /210\ \mu C \times Pt_{loading} \qquad (3.4)$$

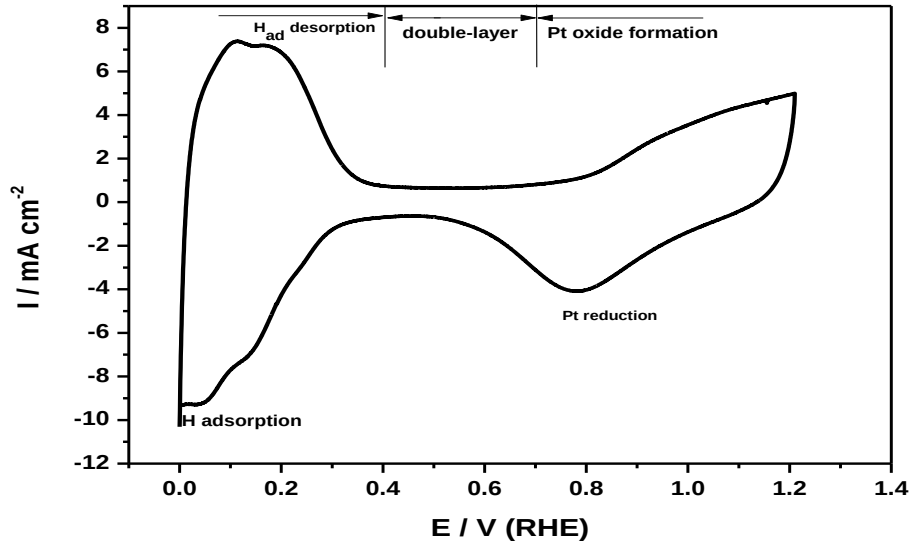

Figure 3.6, Typical cyclic voltammogram of Pt in an N_2 saturated 0.5 M H_2SO_4 at a scan rate of 50 mV s^{-1}

3.1.12.2 Oxygen reduction reaction studies

The oxygen reduction reaction (ORR) on the rotating disc electrode (RDE) was studied for the electrocatalysts using linear sweep voltammetry (LSV) at a scan rate of 5 mV s^{-1} in an oxygen saturated 0.5 M H_2SO_4 and H_3PO_4 solutions. The catalyst ink (prepared as per the procedure in section 3.1.12a) was drop casted onto the glassy carbon disc electrode.

3.1.13 Characterisation techniques

3.1.13.1 FT-IR spectroscopy

Fourier Transform infrared (FT-IR) spectroscopy is an important technique in organic chemistry. FT-IR was used to identify the presence of certain functional groups in a molecule. In this research FT-IR spectroscopy was used to understand the chemical interactions between the functional groups of graphite oxide, Nafion and SPEEK. Fourier transform infrared spectroscopy (FTIR) was measured on Varian 800 FT-IR spectrometer system with wave number between 4000 and 500 cm^{-1}.

The most useful IR region lies between 4000-500 cm^{-1}. IR radiation does not have enough energy to induce electronic transitions as seen with UV. For a molecule to absorb IR, the vibrations or rotations within a molecule must cause a net change in the dipole moment of the molecule. The alternating electrical field of the radiation interacts with fluctuations in the dipole moment of the molecule. If the frequency of the radiation matches the vibrational frequency of the molecule then radiation will be absorbed, causing a change in the amplitude of molecular vibration. Rotational levels are quantised, and absorption of IR by gases yields line spectra. However, in liquids or solids, these lines broaden into a continuum due to molecular collisions and other interaction [9, 10].

The positions of atoms in a molecule are not fixed; they are subject to a number of different vibrations. Vibrations fall into the two main categories of stretching and bending. Stretching causes change in inter-atomic distance along bond axis and bending cause change in angle between two bonds.

Traditional infrared techniques experience difficulties due to the one wave number at a time nature of data acquisition. This leads to either a poor signal to noise ratio in a spectrum or a very long time needed to obtain a high quality spectrum. These problems can be overcome using Fourier transform infrared spectroscopy (FT-IR) which is based on the interferometer originally designed by Michelson and a mathematical procedure developed by Fourier that converts response from the time to the frequency domain [11].

Figure 3.7, shows the schematic of the FT-IR instrument. The IR source passes into the optical system and impinges on a beam splitter that comprises a very thin film of germanium. Approximately 50% of the light passes through the film and is reflected back along its path by a fixed mirror, where half of the light intensity (25% of the original light intensity) is reflected by the same beam splitter, through the sample cell,

to the infrared sensor. The other 50% fraction of the incident light is reflected at right angles to its incident path onto a moving mirror. Light from the moving mirror returns along its original path and half of the light intensity is transmitted through the beam splitter, through the sample cell, to the infrared sensor. As a result, 25% of the incident collimated light from the source reaches the sensor from the fixed mirror and 25% from the movable mirror. Now the path length of the two light beams striking the sensor will be different so there will be destructive and constructive interference. Actually, the system constitutes a form of the Michelson interferometer.

A spectrometer measures the radiation intensity as a function of the wavelength of the light behind a sample. At the vibrational frequencies of the molecules an intensity decrease is obtained and a transmittance or absorbance spectrum is plotted.

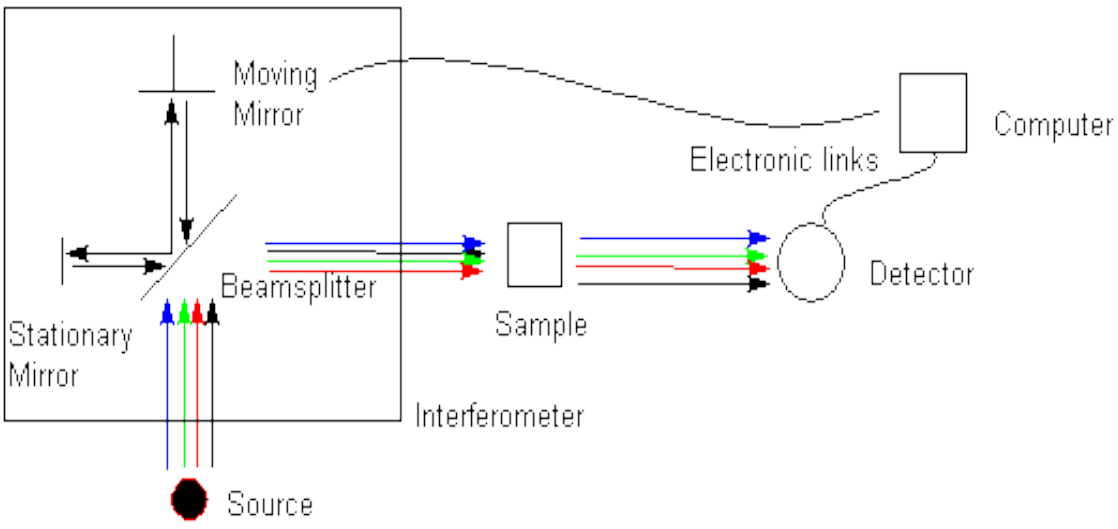

Figure 3.7, Diagrammatic representation of IR spectrometer [12]

The intensity of IR absorption is governed by the Beer-Lambert law:

$$I = I_o e^{-\varepsilon cd} \qquad (3.5)$$

Here, I_o and I denote the intensities of the incident and transmitted beams, respectively, ε (mol cm^{-1}) is the molecular absorption coefficient, and c and d are the concentration of the sample and the cell length, respectively. In IR spectroscopy, it is customary to plot the percentage transmission (T) versus wave number (ν):

$$T\ (\%) = I/I_o * 100 \qquad (3.6)$$

It should be noted that T (%) is not proportional to c. For quantitative analysis, the absorbance (A) defined here should be used: $A = \log I/I_o = \varepsilon cd$ (3.7)

3.1.13.2 Raman Spectroscopy

Raman spectroscopy is commonly used in chemistry to observe vibrational, rotational and low frequency modes in a system. Since the vibrational information is specific to the chemical bonds and symmetry of molecules, therefore it provides a fingerprint by which the molecule can be identified. Raman spectroscopy was carried out using Raman spectrometer (HORIBA JOBIN YVON) with liquid nitrogen cooled Ge detector. A Nd-YAG laser (with a wavelength of 1064 nm) was used as the excitation source and the number scans used was 1024. All the spectra were recorded with a laser power of 300 mW with a radiation spot size of 100 μm.

In theory, vibrational transitions can be observed in either IR or Raman spectra. In the former, we measure the absorption of infrared light by the sample as a function of frequency.

Figure 3.8, shows the energy level diagram of states involved in the Raman signal. In Raman spectroscopy, the sample is irradiated by intense laser beams in the UV-visible region (ν_o), and the scattered light is usually observed in the direction perpendicular to the incident beam, The scattered light consists of two types: one, called Rayleigh scattering, is strong and has the same frequency as the incident beam (ν_o), and the other, called Raman scattering, is very weak (~ 10^{-5} of the incident beam) and has frequencies $\nu_o \pm \nu_m$, where ν_m is a vibrational frequency of a molecule. The $\nu_o - \nu_m$ and $\nu_o + \nu_m$ lines are called the Stokes and anti-Stokes lines, respectively. Thus, in Raman spectroscopy, we measure the vibrational frequency (ν_m) as a shift from the incident beam frequency (ν_o). In contrast to IR spectra, Raman spectra are measured in the UV-visible region where the excitation as well as Raman lines appear [13, 14].

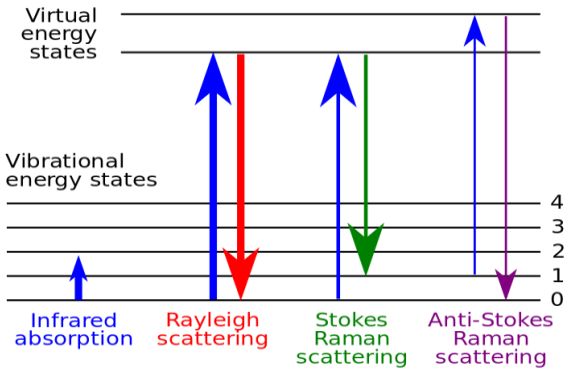

Figure 3.8, Energy level diagram [15]

To determine whether the vibration is active in the IR and Raman spectra, the selection rules must be applied to each normal vibration. Since the origins of IR and Raman spectra are markedly different, their selection rules are also distinctively different. According to quantum mechanics [16, 17] a vibration is IR-active if the dipole moment is changed during the vibration and is Raman-active if the polarisability is changed during the vibration.

3.1.13.3 X-ray diffraction (XRD)

X-ray diffraction (XRD) is widely used for determining the atomic and molecular structure of crystalline material. In this research powder XRD measurements were carried out using (Siemens D 5005 model) a diffractometer with Cu Kα source (λ=1.5418 Å) in the scan range between 10 and 80^o at a rate of 2^o per min.

The X-rays (electromagnetic radiations) are generated in a cathode ray tube by heating a filament to produce electrons, accelerating the electrons toward a target (Cu, Al, Mg and Mo) by applying a voltage, and bombarding the target material with electrons [18]. When electrons have sufficient energy to dislodge inner shell electrons of the target material, characteristic X-ray spectra are produced. These spectra consist of several components, the most common being K_α and K_β. The specific wavelengths are characteristic of the target material (Cu, Fe, Mo, and Cr). Copper is the most common target material for single-crystal diffraction, with CuK_α radiation = 1.5418Å [19]. These X-rays are collimated and directed onto the sample (figure 3.9). As the sample and detector are rotated, the intensity of the reflected X-rays is recorded. When the geometry of the incident X-rays impinging the sample satisfies the Bragg Equation, constructive interference occurs and a peak in intensity occurs [20]. A detector records and processes this X-ray signal and converts the signal to a count rate.

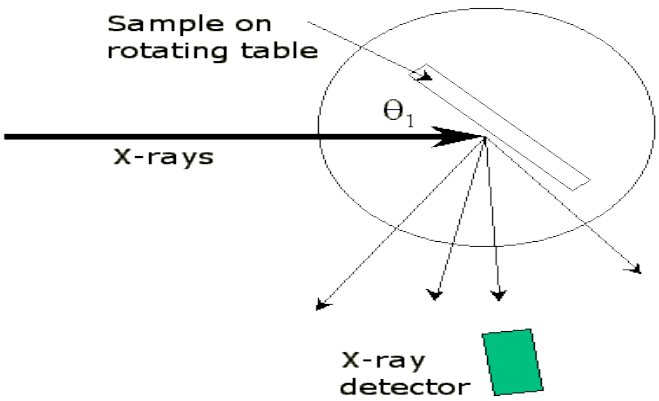

Figure 3.9, Schematic representation of X-ray instrumental set up [21]

In principle, XRD relies in the diffraction of light. The atoms are regularly arranged in a crystalline materials and the interatomic space is in the order of wavelength of X-ray (0.1 – 100 A^o) [22]. Figure 3.10 shows the diffraction of X-rays from crystal planes. When the Bragg's condition is satisfied, scattered X-ray constructively interfere an intense peak is obtained.

$$2d_{hkl} \sin\boldsymbol{\theta} = n\lambda \qquad (3.8)$$

Where d_{hkl} is the spacing between the lattice plane with the Miller indices h, k and l. n is the order of diffraction (n=1, 2, 3 etc.) and λ is the wavelength of X-ray.

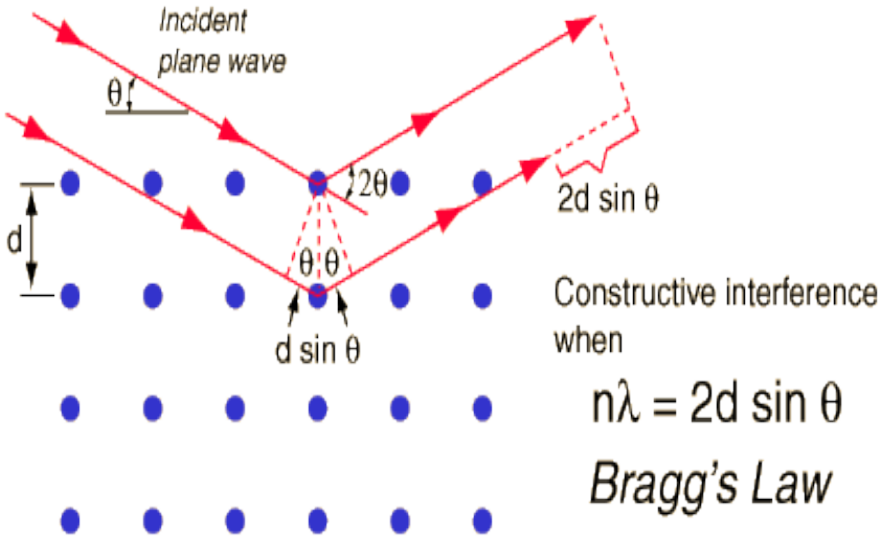

Figure 3.10, Illustration of Bragg's law [23]

The XRD could be used to distinguish between crystalline and amorphous state of compound. A crystalline sample shows a sharp XRD peak whereas amorphous compound exhibits a broad peak. It was found that peaks broaden as the crystallite size decreases and the peak broadness is used to measure the crystallite size using the Debye-Scherrer formula [24].

$$t=k\lambda/\beta\cos\theta \qquad (3.9)$$

Where λ is the wavelength of X-ray, β is the full width at half maximum (2θ), and K is the shape factor usually takes the value of 0.89.

3.1.13.4 X-ray photoelectron spectroscopy (XPS)

X-ray photoelectron spectroscopy (XPS) is a quantitative technique that measures the elemental composition and oxidation states of the element in the material being analysed. XPS is also known as ESCA (Electron Spectroscopy for Chemical Analysis) that provides the quantitative analysis of the surface composition. In this research XPS data was collected using Thermo K-Alpha (Thermo Scientific, East Grinstead, UK) using a monochromatic AlKα source at 100W.

XPS is based upon photo-ionisation and analysis of the kinetic energy distribution of the emitted photoelectrons to study the composition and electronic state of the surface region of a sample. The kinetic energy distribution of the emitted photoelectrons (i.e. the number of emitted photoelectrons as a function of their kinetic energy) can be measured using any appropriate electron energy analyser and an X-ray photoelectron spectrum can be recorded (figure 3.12) [25].

The energy of a photon of all types of electromagnetic radiation is given by the Einstein relation [26]

$$E = h\nu \qquad (3.10)$$

In XPS, the photon is absorbed by an atom in a molecule or solid, leading to ionisation and the emission of a core (inner shell) electron as shown in the figure 3.11 and is given by the equation.

$$A + h\nu \rightarrow A^{+} + e^{-} \qquad (3.11)$$

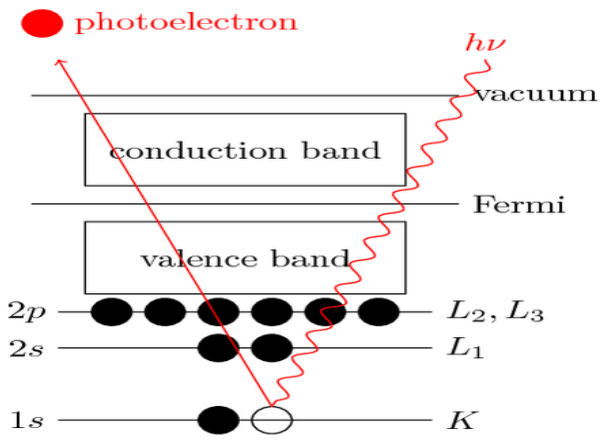

Figure 3.11, Photo-ionisation of an atom [27]

The difference in energy between the ionised and neutral atoms is generally called the binding energy (BE) of the electron [28].

$$KE = h\nu - BE \qquad (3.12)$$

For each and every element, there will be a characteristic binding energy associated with each core atomic orbital therefore each element will give rise to a characteristic set of peaks in the photoelectron spectrum at kinetic energies determined by the photon energy and the respective binding energies [29]. The presence of peaks at particular energies therefore indicates the presence of a specific element in the sample under study furthermore; the intensity of the peaks is related to the concentration of the element within the sampled region.

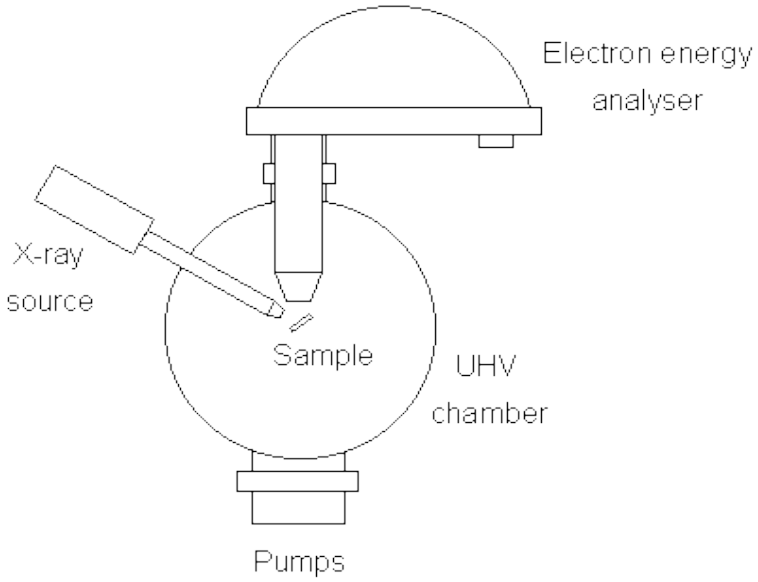

Figure 3.12, Schematic of XPS instrument [30]

3.1.13.5 Scanning electron microscope (SEM) and Energy dispersive X-ray spectroscopy (EDS)

The surface and cross sectional morphology of the material can be obtained using a scanning electron microscope. The SEM is a microscope that uses electrons instead of light to form an image. In this research, JSM-5300LV (Japan) scanning electron microscope (SEM) was used to investigate the morphology of the membranes and electrocatalyst. The membrane samples were cut by nitrogen snapping and mounted on holder facing the membrane opposite towards the light source to see the cross section morphology of the composite membrane.

In theory, electrons are thermionically emitted from a tungsten or lanthanum hexaboride (LaB_6) cathode and are accelerated towards an anode; alternatively, electrons can be emitted via field emission (FE) [31]. The electron beam, which has an energy ranging from a few hundred eV to 100 keV, passes through a pairs of scanning coils in the objective lens. When the primary electron beam interacts with the sample, the electrons lose energy by repeated scattering and absorption within the interaction volume, which depends on the beam accelerating voltage the atomic number of sample and the sample density, extending from 100 nm to around 5 µm into the surface as shown in figure 3.13a. Figure 3.13b shows the schematic representation of interaction of incident beam with the sample. The beam travels through electromagnetic fields and lenses, which focus the beam down toward the sample. Once the beam hits the sample, electrons and X-rays are ejected from the sample. Detectors collect these X-rays, backscattered electrons, and secondary electrons and convert them into a signal that is sent to a screen similar to a television screen and produces the final image.

Energy dispersive X-ray spectroscopy (EDS) technique is used for elemental analysis of samples. This technique relies on interactions between incident charged particles such as electrons and the sample. In principle, a high energy incident beam will knock out an electron in an inner shell of atoms in the sample, creating an electron hole. Then an electron from an outer, high energy shell will fill that hole and release the energy differences between these two shells in the form of an X-ray. Since the energy differences between electron shells are closely related to the atomic structure, the X-ray shall be a characteristic of an atom, which allows the elemental composition of the sample to be measured. The systems provide limited detection of elements below C in the periodic table. The detection limit is around 0.1 % depending on the element [32].

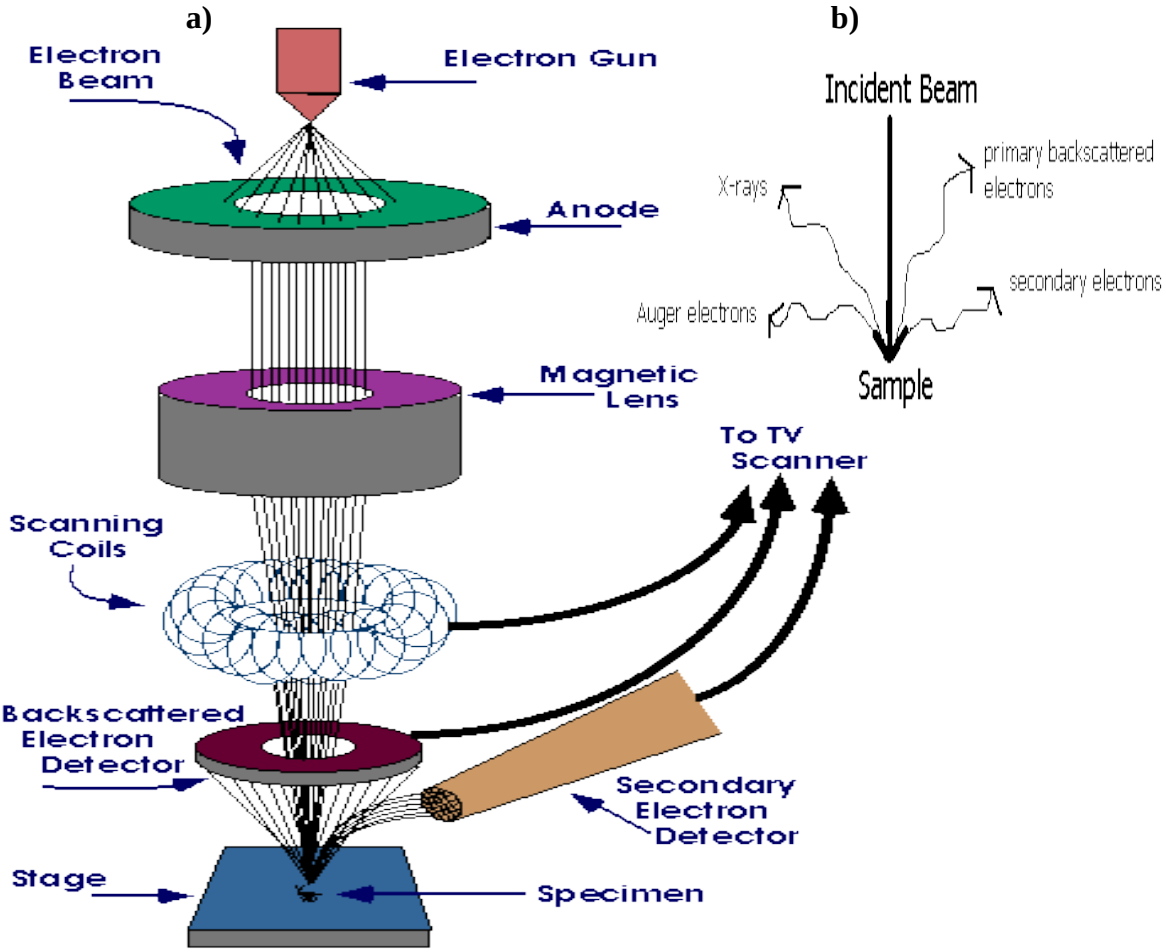

Figure 3.13, a) Schematic representation of SEM and b) interaction of incident beam with the sample [33]

3.1.13.6 Transmission electron microscope (TEM)

The transmission electron microscopy (TEM) is used to analyse the nanosized (up to1 nm) material for their structure, atomic columns, composition and crystallographic information. In this research, TEM was investigated by Philips CM 100 Compustage (FEI), and images are collected using an AMT CCD camera (Deben).

In this technique, an electron beam interacts and passes through a specimen. The electrons are emitted by a source and are focused and magnified by a system of magnetic lenses. The schematic of TEM is shown in figure 3.14a. The electron beam is confined by the two condenser lenses which also control the brightness of the beam, passes the condenser aperture and hit the sample surface. The electrons that are elastically scattered consist the transmitted beams, which pass through the objective lens (figure 3.14b). The objective lens forms the image display and the following apertures, the objective and selected area aperture are used to choose of the elastically

scattered electrons that will form the image of the microscope [34]. Finally, the beam goes to the magnifying system that is consisted of three lenses, the first and second intermediate lenses which control the magnification of the image and the projector lens. The formed image is shown either on a fluorescent screen or in monitor or both and is printed on a photographic film.

Different types of images are obtained in TEM, using the apertures properly and the different types of electrons. As a result, diffraction patterns are shown because of the scattered electrons. If the unscattered beam is selected, we obtain the bright field Image. Dark field images are attained if diffracted beams are selected by the objective aperture. Also TEM can be used to analyse the samples for EDX (Energy Dispersive X-ray), EELS (Electron Energy Loss Spectrum), EFTEM (Energy Filtered Transmission Electron Microscopy) [35].

Samples for TEM analysis were prepared by drop coating the slurry/colloid on carbon coated copper grid and allowing the solvent to evaporate under light.

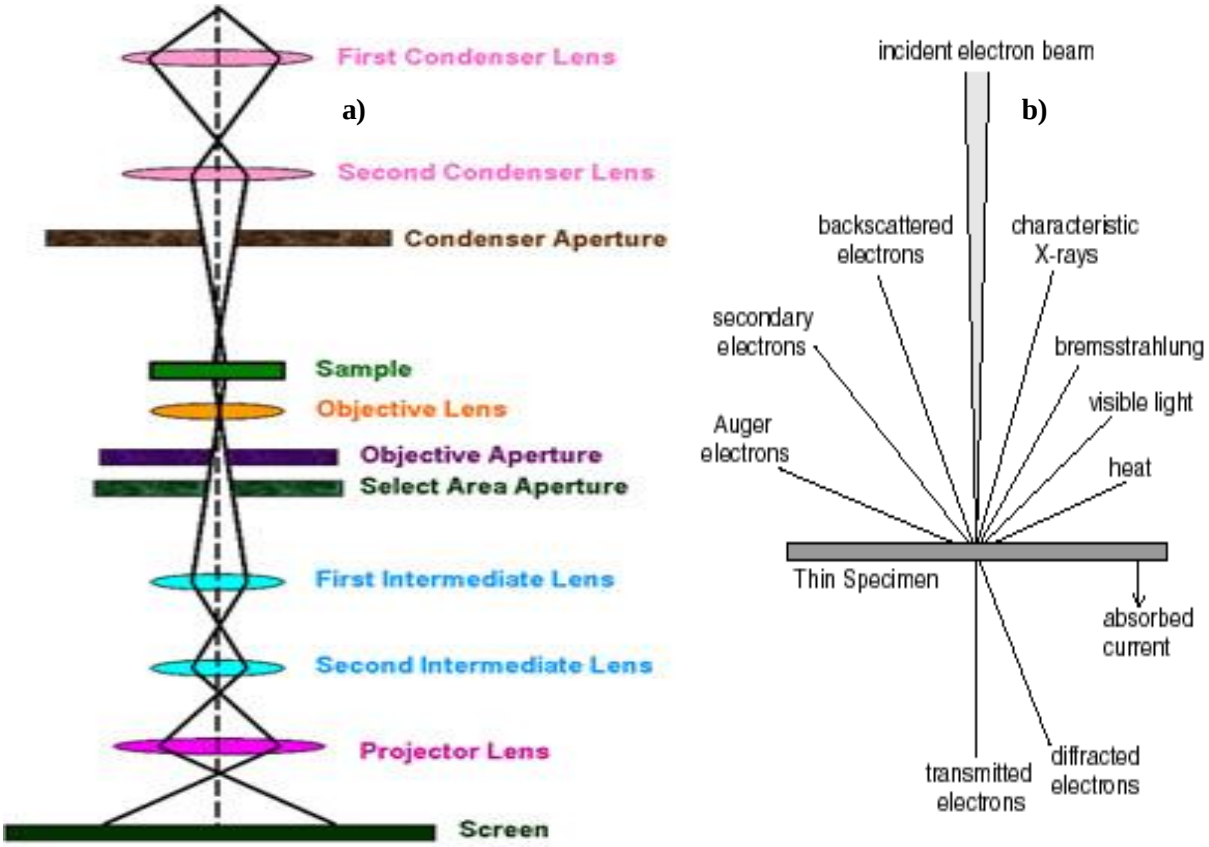

Figure 3.14, a) Schematic representation of TEM and b) interactions between incident beam and sample [36]

3.1.13.7 Thermo-gravimetric analysis (TGA)

Thermogravimetric analysis (TGA) is widely used to study the thermal behaviour of the material. In this research the thermal stability of the polymer electrolyte membranes were measured by thermo-gravimetric analysis using a STA6000 machine over a temperature range of 30-700 ^{o}C with a scan rate of 5 ^{o}C min^{-1} under Helium flow (30 ml min^{-1}).

In this technique, mass change of the sample is monitored while heating the sample in a controlled atmosphere (He, N_2, O_2 and air etc) in a controlled temperature programme. The mass change versus the temperature is plotted for thermal analysis. A decrease in mass indicates a degradation of sample whereas an increase weight in oxidising atmosphere indicates an oxide formation.

3.1.13.8 Mechanical strength measurement

To understand the materials ability to withstand an applied stress mechanical measurements are widely used. In this research, polymer electrolyte membranes tensile strength measurement was carried out with an Instron 4505 machine with a displacement speed of 2 mm per minute. Membrane samples with an area of 5x2 cm^2 were cut and used for mechanical studies.

Tensile strength was calculated by using the equation;

Tensile strength (MPa) = (load at break) / (original width) (original thickness) (3.13)

Percentage elongation was calculated by using the equation;

Percent elongation = (elongation at rupture) x 100 / (Initial gage length) (3.14)

Young's modulus is calculated by drawing a tangent to the initial linear portion of the stress strain curve, selecting any point on this tangent, and dividing the tensile stress by the corresponding strain. The result is expressed in gigapascals (GPa).

Young's modulus = tensile stress / tensile strain (3.15)

3.2 Theoretical background of electrochemical methods

3.2.1 Cyclic Voltammetry and Linear Sweep Voltammetry

Linear sweep voltammetry (LSV) and cyclic voltammetry (CV) are well known potentiodynamic electrochemical techniques, often used to examine the electrochemical properties of electrode. These techniques are based on a linear-potential waveform, wherein the potential is continuously varied as a linear function of time. The rate of change of potential with time is referred to as the scan rate (v). In LSV, the working electrode potential is scanned from a lower limit ($E_{initial}$) to upper limit (E_{final}) linearly with time (figure 3.15) In the case of cyclic voltammetry the potential of the working electrode is swept between two potential ends (figure 3.16) , but on reaching the potential (E_{final}), the sweep is reversed. In both LSV and CV experiments, the cell current is recorded as a function of applied potential. The importance of CV is revealed from its ability to rapidly provide considerable information on the thermodynamics of redox processes, kinetics of heterogeneous electron-transfer reactions, coupled chemical-reactions and adsorption processes [37, 38].

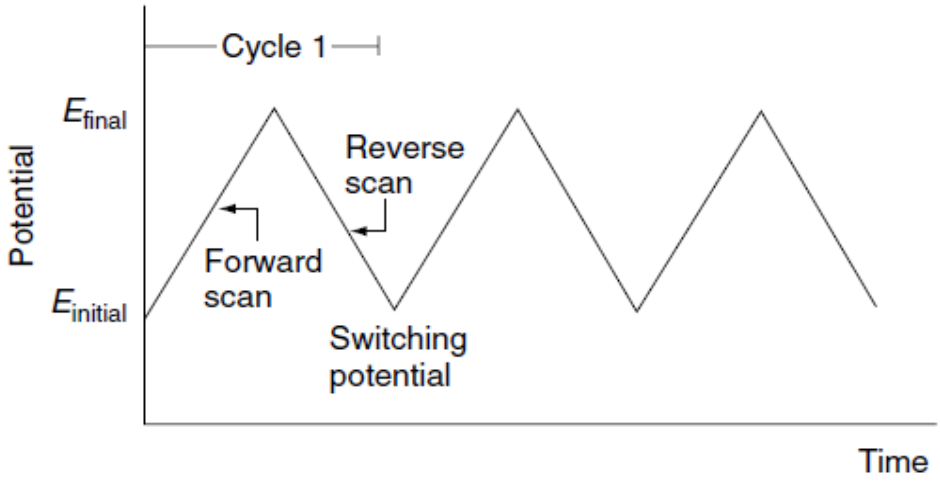

Figure 3.15, Potential-time excitation signal in cyclic voltammetry [39]

Consider the reaction:

$$O + ne^- \Leftrightarrow R \qquad (3.16)$$

When the working electrode is swept between the two set potentials at a fixed scan rate, where the electrolyte containing oxidised and reduced forms of the chemical species.

The Nernst equation for an ideal reversible electrode is given by the equation,

$$E = E^{o} + (RT/nF) \ln C_O / C_R \qquad (3.17)$$

Where E^o is the formal potential, R is the universal gas constant, T is absolute temperature in Kelvin, n is the number of electrons transferred during the electrochemical reaction, F is the Faraday constant, and C_O and C_R represent the surface concentrations of oxidised and reduced forms of the species [40].

At equilibrium, the surface concentrations of O and R are equal. After the cathodic peak potential, the current decays as a result of the depletion of O in the electrode/electrolyte interfacial region and the current is given by,

$$I = D_O \, n \, F \, A \, (dC_O / dx) \qquad (3.18)$$

Where D_O is the diffusion coefficient of O, A is the surface area of the electrode and (dC_O/dx) is the concentration gradient at the electrode surface.

A typical cyclic voltammogram is shown in figure 3.8 and is predicted for an ideal, reversible system. The peak current i_p is given by the equation (3.19) called the Randles-Sevick equation [41],

$$i_p = (2.69 \times 105) \, n^{3/2} A D^{1/2} \nu^{1/2} C \qquad (3.19)$$

Where i_p is the peak current (in amperes), n is the number of electrons involved in the redox reaction, A is the electrode area (in cm^2), D is the diffusion coefficient of analyte (cm^2 sec^{-1}), ν is the potential sweep rate (in volts sec^{-1}), and C is the concentration of analyte in bulk solution (in moles cm^{-3}).

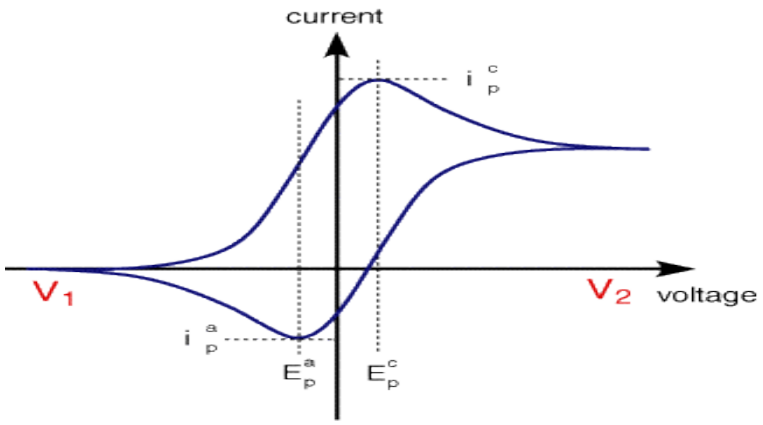

Figure 3.16, Typical cyclic voltammogram recorded for reversible redox reaction [42]

A redox couple in which both species rapidly exchange electrons with the working electrode is termed an electrochemically reversible couple. The formal reduction

potential *(E^o)* for a reversible couple is centred between Epa and Epc. Therefore *$E^o$is* given by the equation (3.20)

$$E^o = Epa + Epc/2 \qquad (3.20)$$

For a reversible electrochemical reaction the potential difference between the two current peaks (ΔE) is given by the equation (3.21).

$$\Delta E = E_{pa} - E_{pc} = 2.303RT/nF = (59/n)\ mV \qquad (3.21)$$

For a reversible reaction the ratio of peak currents is equal to one.

The half- wave potential $E_{1/2}$ ($E_{1/2}$, where the current is half of the peak current) is given by the equation (3.22)

$$Ep/2 = E_{1/2} \pm (28/n)\ mV \qquad (3.22)$$

For a reversible redox system, the electron transfer rates at all potentials are significantly greater than the rate of mass transport and therefore, Nernst equilibrium is always maintained at the electrode surface [43].

Electrochemical irreversibility and quasi-reversibility of the system is caused by slow electron exchange of the redox species with the working electrode**.** In the case of irreversible process, the individual peaks are reduced in size and widely separated as shown in the cyclic voltammogram A (figure 3.17).

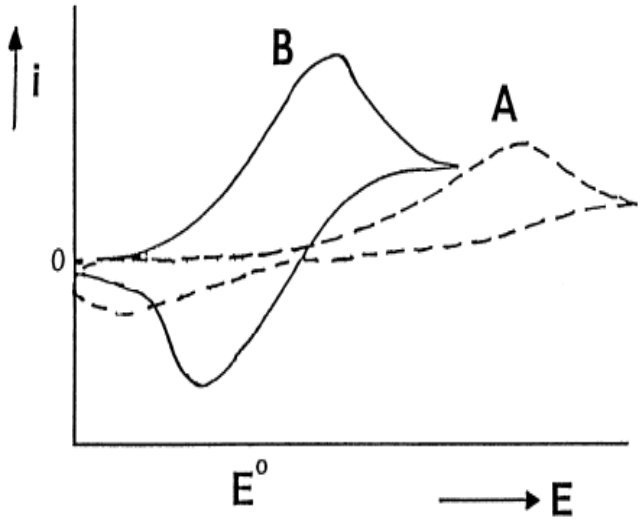

Figure 3.17, Cyclic voltammograms for irreversible (curve A) and quasi-reversible (curve B) redox processes [44]

The irreversible systems are characterised by a shift of peak potential with the scan rate is given by the equation:

$$E_p = E^o - RT/\alpha n_a F\,[0.78 - \ln k^o/D_{1/2} + \ln (\alpha n_a F\nu/RT)^{1/2} \qquad (3.23)$$

Where α is the transfer coefficient and n_a is the number electrons involved in the charge transfer reaction. Thus, *Ep* occurs at potential higher than E^o, with overpotential related to k^o and α. Independent of value of k^o, such peak displacement can be compensated by an appropriate change of scan rate. The peak potential and half-peak potential (25 ^oC) will differ by $48/\alpha n$ mV. Hence, the voltammogram become more dawn out as αn decreases [45]. The peak current is given by the equation (3.24),

$$I_p = -(2.99 \times 10^5)\, A\, n\, (\alpha\, n)^{1/2}\, C_O\, D_O{}^{1/2}\, \nu^{1/2} \qquad (3.24)$$

The ratio of the reversible to irreversible current peak is 1.27.

For quasi-reversible systems the current is controlled by both the charge transfer and mass transport. The shape of the CV is a function of $K^o/\sqrt{\pi aD}$ (where $a = nF\nu/RT$). As $K^o/\sqrt{\pi aD}$ increases, the process approaches the reversible case. For small values of $K^o/\sqrt{\pi aD}$ (at very fast scan rate ν) the system exhibits an irreversible behaviour. Over all the voltammograms of a quasi reversible system are more dawn-out and exhibit a large separation in peak potentials compared to those of a reversible system (curve B, in figure 3.17).

3.2.2 Origin of Tafel equation

The kinetics of the reaction plays a vital role in understand the mechanism of any reaction. In the case of electrochemical reaction, electron transfer being the rate determining step.

Consider the electron transfer reaction:

$$O + ne^- <=> R \qquad (3.25)$$

At equilibrium, the exchange current ($i_{0)}$ is directly proportional to the standard rate constant and is given by the equation (3.26)

$$i_0 = i_c = i_a = nFAk^oC \qquad (3.26)$$

Where i_c and i_a are the cathodic and anodic components, respectively.

The Butler-Volmer reaction represents the current-potential relationship for the reaction 3.25 and is expressed in terms of exchange current density

$$i = i_0 [\exp(-\alpha nF\eta/RT) - \exp((1-\alpha)\, nF\eta/RT)] \qquad (3.27)$$

Where i is the electrode current density (A/m^2; i=I/A), i_o is the exchange current density (A/m^2), η is the overpotential (η=E-Eeq), α is the charge transfer coefficient, F is the Faraday constant (96500 C) and n is the number of electrons involved in the reaction, R is the gas constant (8.314 J K^{-1} mol^{-1}) and T is the absolute temperature.

Where η = E-Eeq is the overpotential (the extra potential beyond the equilibration potential leading to a net current i). The overvoltage is always defined with respect to a specific reaction, for which the equilibrium potential is known [46].

Equation (3.12) can be used for extracting information on i_0 and α, which are important kinetic parameters. For sufficiently large overpotential (η >118 mV/n), one of the exponential terms in Eq. (3.12) will be negligible compared with the other. For example, at large negative overpotentials, $i_c >> i_a$ and Eq. (3.28) becomes

$$i = i_0 [\exp(-\alpha nF\eta/RT) \qquad (3.28)$$

and hence, we get

$$\ln i = \ln i_0 - \alpha nF\eta/RT \qquad (3.29)$$

This logarithmic current-potential dependence was derived by Tafel, and is known as the Tafel equation. By plotting log i against η one obtains the Tafel plots for the cathodic and anodic branches of the current-overpotential curve (Figure 3.18). Such plots are linear only at high overpotential values; deviations from linearity are observed as η approaches zero. Extrapolation of the linear portions of these plots to the zero overpotential gives an intercept, which corresponds to logi_0; the slope can be used to obtain the value of the transfer coefficient α. The value of i_0 determined in this way is at a specific temperature and concentration of reactants. It will also be a function of the specific surface area.

Another form of the Tafel equation is obtained by rearrangement of Eq. (3.29):

$$\eta = a - b\log i \qquad (3.30)$$

with b, the Tafel slope, having the value of $2.303RT/\alpha nF$. For α=0.5 and n=1, this corresponds to 118 mV (at 25 °C). Equation (3.30) indicates that the application of small potentials (beyond the equilibrium potential) can increase the current by many orders of magnitude. In practice, however, the current could not rise to an infinite value because of restrictions imposed by the rate at which the reactant reaches the surface.

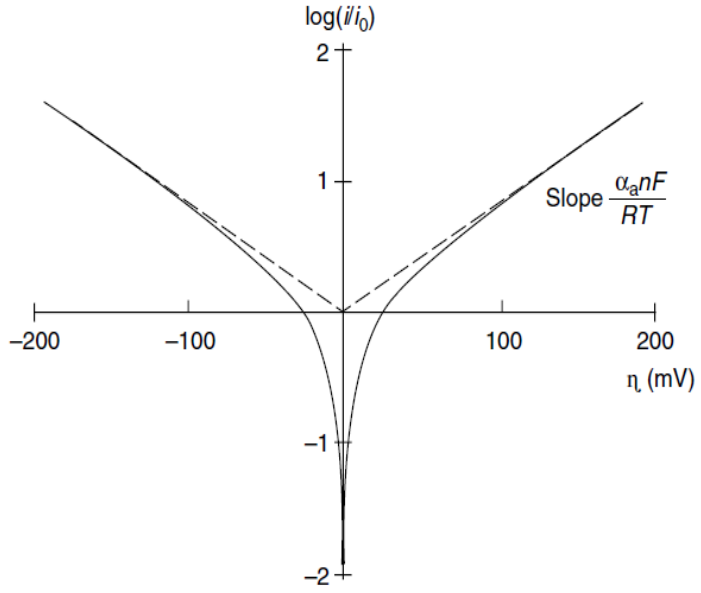

Figure 3.18, Tafel plots for cathodic and anodic branches of the current-potential curve [47]

3.2.3 Electrochemical impedance spectroscopy (EIS)

Electrochemical impedance spectroscopy (EIS) is an electrochemical method, employed to understand the interfacial behaviour of electrochemical systems. The electrode impedance is measured as a function of the frequency of the ac source. The theory of the technique is to explain the equivalent resistance and capacitance values in terms of interfacial phenomena. The measured total impedance of the electrochemical cell could be represented by an equivalent circuit comprising resistors (R) and capacitances (C) in series and/or in parallel.

On applying ac voltage (e) across the cell, the corresponding current (i) passing through it, can be expressed as,

$$i = i_o \, \mathrm{Sin}\, \omega t \qquad (3.31)$$

where ω is the angular frequency ($\omega = 2\pi f$, f being the frequency) and i_o is the value of i at t = 0.

The circuit containing resistance and capacitance in series are shown in figure 3.19. The total voltage drop across the circuit, E, is given by

$$E = E_1 + E_2 \qquad (3.32)$$

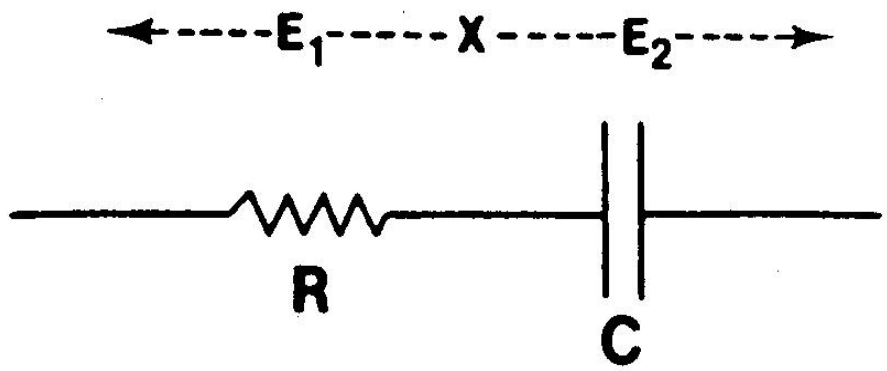

Figure 3.19, Series combination of resistance and capacitance with respective voltage drops E_1 and E_2, across them [48]

The impedance (Z) of the circuit is expressed as,

$$Z = E/I \qquad (3.33)$$

The total impedance of the circuit is given by,

$$Z = R + (1/j\omega C) = R - (j/\omega C) \qquad (3.34)$$

Equation (3.34) contains both real and imaginary terms, namely R and $(-j/\omega C)$, respectively, and is called the complex impedance, Z*, which is expressed as,

$$Z^* = Z' - jZ'' \qquad (3.35)$$

Where $Z' = R$ and $Z'' = 1/\omega C$.

It may be noted that the parameters such as impedance (Z), modulus of impedance |Z|, real part (Z'), imaginary part (Z''), phase angle (ϕ) are interrelated and are functions of frequency (f). Impedance data are represented graphically in Cartesian coordinates or in complex coordinates as shown in figure 3.20a. The plot of log |Z| and ϕ versus log f is called Bode plot. In the Bode log |Z| plot, if the resistor and capacitor are connected in series, the impedance is contributed by both the elements and the magnitude of each contribution varies with the ac frequency as shown in figure 3.20b. If they are in parallel as shown in figure 3.20c, log |Z| decreases linearly with log f with a slope value of -1.

For an electrochemical system, complex impedance spectra in the form Nyquist and Bode plots provide valuable information on various parameters such as bulk resistance of the electrolyte, charge-transfer resistance that is useful in evaluating various characteristics of the electrode reactions such as rate constant etc., Warburg impedance that provides information about the mass transport. From bulk resistance, ionic

conductivity (σ) of the electrolyte can be determined using the equation,

$$\sigma = L / RA \qquad (3.36)$$

Where L is the distance between the two electrodes, A is the area of electrode and R is the bulk resistance of the electrolyte, which is evaluated from the high-frequency intercept on the real impedance axis of the Nyquist plot.

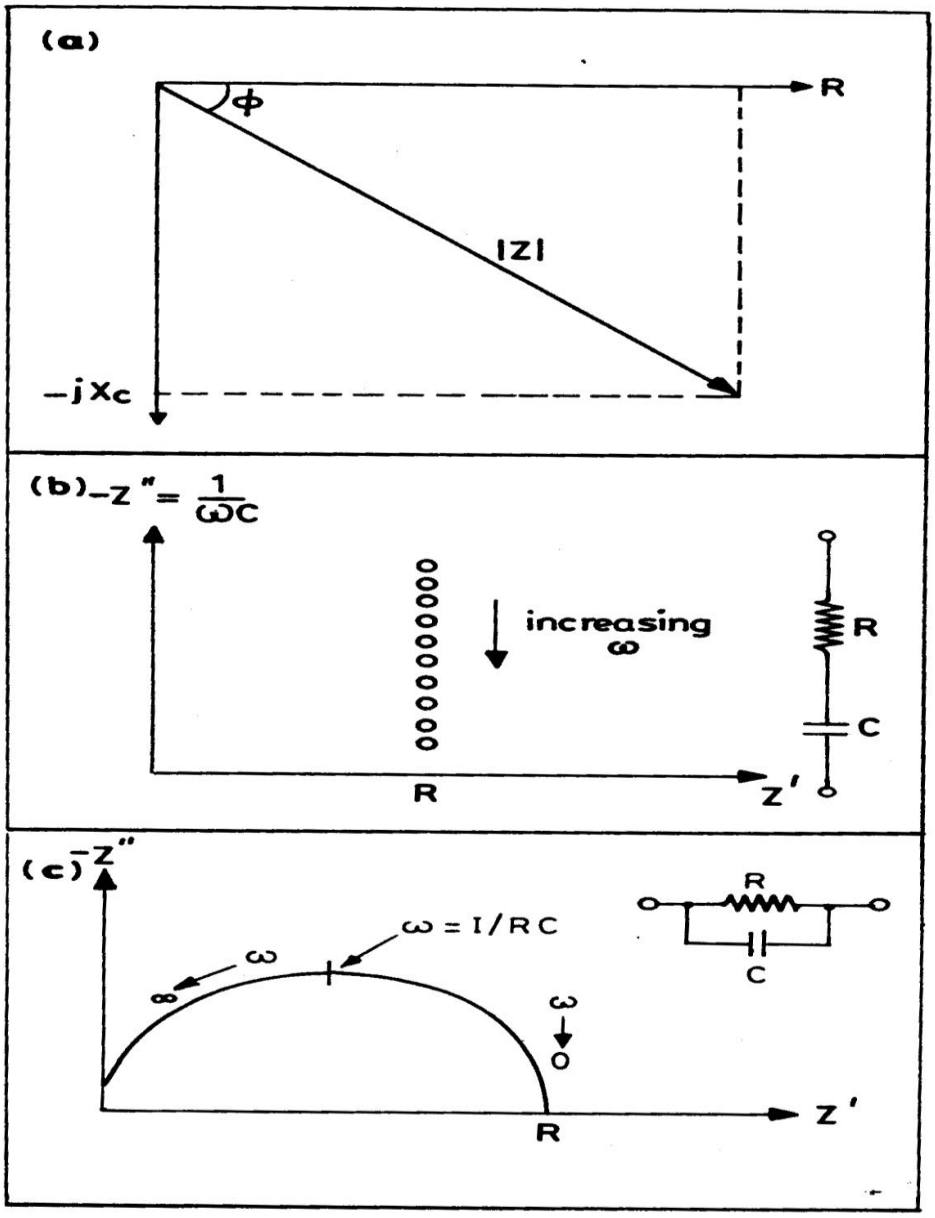

Figure 3.20, (a) Argand diagram showing relationship among resistance (R), capacitive reactance (X_c), modulus of impedance |Z| and phase angle (ϕ), (b) Complex plane (Argand) diagram for a series RC circuit and (c) Complex plane diagram for a parallel RC circuit [49]

3.2.4 Rotating disc electrode (RDE)

The evaluation of electrocatalytic activity (HOR and ORR) of the electrocatalyst directly in the fuel device is somewhat expensive and time-consuming. The rotating disc electrode (RDE), which involves the use of small electrode for screening the electrocatalyst, is often used as an alternative tool. The schematic of three electrode system, including the RDE working electrode is shown in Figure 3.21.

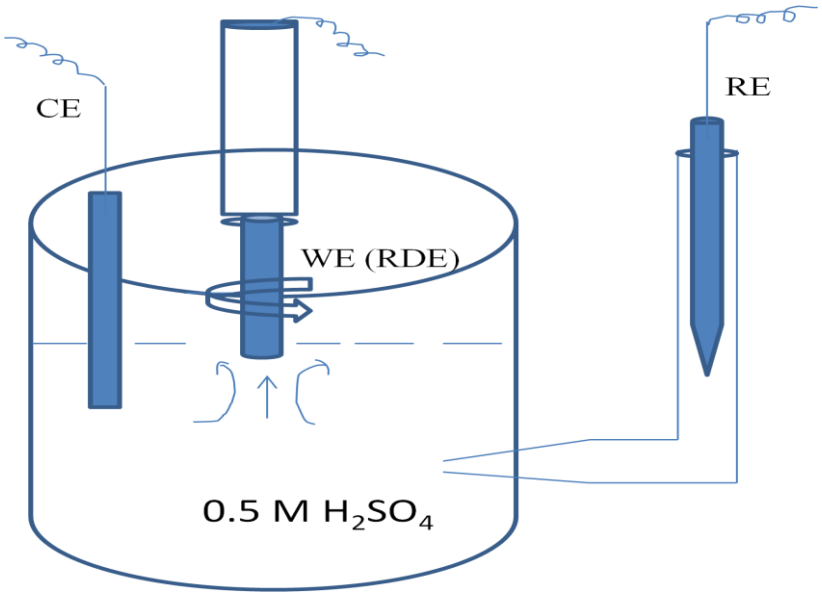

Figure 3.21, Schematic of an electrochemical cell with rotating disc electrode

In this research, the glassy carbon (GC) based RDE electrode was employed to analyse the in house prepared electrocatalyst to evaluate for its stability, durability and oxygen reduction reaction. This allowed us to compare the electrocatalytic property with conventional Pt/C.

The electrochemical reaction involves gas reactants such as hydrogen and oxygen. Because of the slow electrocatalytic activity and poor mass transport of the reactant gas, the RDE technique use convection to enhance the rate of mass transport to the electrode. The convection induced by the rotation of working electrode results in increased current compared to voltammetric measurements performed in the quiescent solution [50].

The fuel cell catalysts are generally evaluated for HOR and ORR activity. Using the RDE technique, the mechanism of the reaction and kinetic parameters can be determined.

The kinetic current (I_k) was calculated from Koutecky-Levich equation which is expressed by

$$1/I = (1/I_k) + (1/I_d) \qquad (3.37)$$

Where I is the measured current, I_k is the kinetic current and I_d the diffusion limited current. The I_d term can be obtained from the Levich equation:

$$I_d = 0.62nFAD^{2/3}\upsilon^{-1/6}\omega^{1/2}C_{O2} \qquad (3.38)$$

Where n is the number of electrons transferred; F is Faraday's constant (96,485 C mol^{-1}); A is the area of the electrode (0:196 cm^2); D is the diffusion coefficient of O_2 in 0.5 M H_2SO_4 solution ($2.1x10^{-5}$ cm^2 s^{-1}); υ is the kinematic viscosity of the electrolyte ($1.01x10^{-2}$ cm^2 s^{-1}); ω is the angular frequency of rotation, $\omega = 2\pi f/60$, f is the rotation rate in r.p.m. and C_{O2} is the concentration of molecular oxygen in 0.5 M H_2SO_4 is $1.03x10^{-3}$ M.

Plotting $1/I$ vs. $1/\omega^{1/2}$ known as the Koutecky-Levich plot (figure 3.21) will generate the straight line with y-axis intercept given by the value $1/I_k$ and the slope being $1/B$. From the y-axis intercept, the kinetic current (I_k) and from the slope $1/B$ (B=$0.62nFCoDo^{2/3}\upsilon^{-1/6}$ is the Levich constant) the number of electron being involved during the reaction can be determined.

$$n = B/0.62nFCoDo^{2/3}\upsilon^{-1/6} \qquad (3.39)$$

The kinetic current (typically at 0.9 V for ORR) can be normalised to electrochemical surface area obtained from cyclic voltammograms to estimate mass activities (mA/mg_{Pt}) and specific activities ($mA\ cm^2{}_{Pt}$) by using the following equations.

$$\text{Mass activity} = I/m \qquad (3.40)$$

Where I is the current at 0.9 V and m is the Pt loading

$$\text{Specific activity} = \text{mass activity/ECSA*100} \qquad (3.41)$$

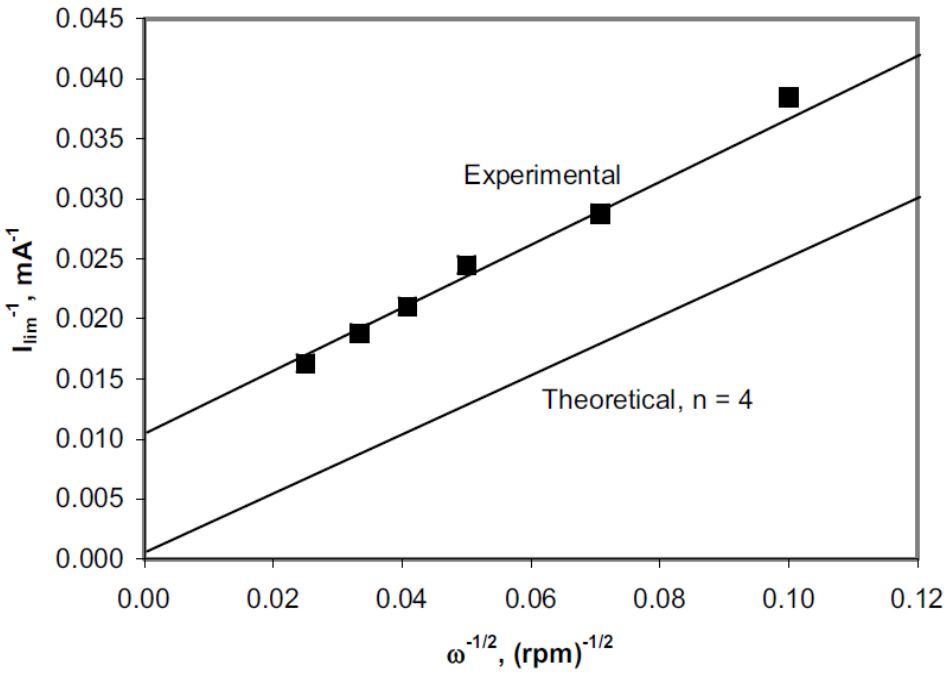

Figure 3.21, Koutecky-Levich plot [51]

References

[1] William S. Hummers Jr., and Richard E. Offeman, *Preparation of graphitic oxide*, J. American Chemical Society, **1958**, 80, 1339.

[2] Tai-Feng Hung, Bei Wangb, Chi-Wen Tsai, Meng-Hsiu Tu, Guo-Xiu Wangb, Ru-Shi Liu Din Ping Tsai, Man-Yin Lo, Der-Shiuh Shy, Xue-Kun Xing, *Sulfonation of graphene nanosheet-supported platinum via a simple thermal-treatment toward its oxygen reduction activity in acid medium*, Int J hydrogen energy, **2012**, 37, 14205-14210.

[3] Ravikumar, Scott K, *Freestanding sulfonated graphene oxide paper: a new polymer electrolyte for polymer electrolyte fuel cells*, Chemical communications, **2012**, 48(45), 5584-5586.

[4] Deeksha Gupta, Veena Choudhary, *Sulfonated poly(ether ether ketone)/ethylene glycol/polyhedral oligosilsesquioxane hybrid membranes for fuel cell applications*, Int J Hydrogen Energy, **2012**, 37, 5979-5991.

[5] Oliver J. Curnick, Paula M. Mendes, Bruno G. Pollet, *Enhanced durability of a Pt/C electrocatalyst derived from Nafion-stabilised colloidal platinum nanoparticles*, Electrochemistry Communications, **2012**, 12, 1017–1020.

[6] M. M. Ottakam Thotiyl, T. Ravikumar and S. Sampath, *Platinum particles supported on titanium nitride: an efficient electrode material for the oxidation of methanol in alkaline media*, J. Mater. Chem., **2010**, 20, 10643–10651.

[7] Deli Wang, Huolin L. Xin, Robert Hovden, Hongsen Wang, Yingchao Yu1, David A. Muller, Francis J. DiSalvo, Héctor D. Abruña, *Structurally ordered intermetallic platinum–cobalt core–shell nanoparticles with enhanced activity and stability as oxygen reduction electrocatalysts*, Nature materials, **2013**, 12, 81-87.

[8] Yano, H., Kataoka, M., Yamashita, H., Uchida, H. & Watanabe, M. *Oxygen reduction activity of carbon-supported Pt-M (MDV, Ni, Cr, Co, and Fe) alloys prepared by nanocapsule method.* Langmuir, **2007**, 23, 6438-6445.

[9] G. M. Barrow, *Molecular Spectroscopy*, New York: McGraw-Hill International Book Company, **1962**.

[10] H. W. Siesler and K. Holland-Moritz, *Infrared and Raman spectroscopy of polymers*, New York: Marcel Dekker, **1980**.

[11] C. N. Banwell and E. M. McCash, *Fundaments of Molecular Spectroscopy*, London: McGraw-Hill International Book Company, **1994**.

[12] H. Yamada, N. Tani, and Y. Yamamoto, Infrared specular reflection and SERS spectra of molecules adsorbed on smooth surfaces, *J. Electron Spectrosc.*, **1983**, 30, 13.

[13] D. A. Long, *Raman Spectrometry*, London: McGraw-Hill International Book Company, **1977**.

[14] H. Bara´nska, A. ÃLabudzi´nska, and J. Terpi´nski, *Laser Raman spectrometer Analytical applications*. Chichester: Wiley, **1987**.

[15] G. Turrel and J. Corset, *Raman microscopy: developments and applications*. London: Academic Press Limited, **1996**.

[16] M. K. Nazeeruddin, M. Gr¨atzel, K. Kalyanasundaram, R. B. Girling, and R. E. Hester, *Raman characterization of charge-transfer transitions in ligand-bridged binuclear polypyridyl complexes of ruthenium (II),* J. Chem. Soc., Dalton Trans., **1993**, 323.

[17] Z.-Q. Tian, B. Ren, and D.-Y. Wu, *Surface-enhanced Raman scattering: from noble to transition metals and from rough surfaces to ordered nanostructured*, J. Phys. Chem. B, **2002**, 106, 9463.

[18] B.E. Warren, *X-ray Diffraction*, New York, **1969**.

[19] Clegg W, *Crystal Structure Determination (Oxford Chemistry Primer)*, Oxford: Oxford University Press, **1998**.

[20] Giacovazzo C, *Fundamentals of Crystallography*, Oxford: Oxford University Press, **1992**.

[21] Zachariasen WH, *Theory of X-ray Diffraction in Crystals*, New York, **1945**.

[22] O'Keeffe M, Hyde B G, *Crystal Structures; I. Patterns and Symmetry*, Washington, DC: Mineralogical Society of America, Monograph Series, **1996**.

[23] McPherson A, Introduction *to Macromolecular Crystallography*, John Wiley & Sons, **2003**.

[24] Massa W, *Crystal Structure Determination*, Berlin: Springer, **2004**.

[25] Hüfner, S, *Photoelectron spectroscopy: principles and applications*, Springer Verlag, **1995**.

[26] Turner, D. W, Jobory, M, *Determination of Ionization Potentials by Photoelectron Energy Measurement*, Journal of Chemical Physics, **1962**, 37(12), 3007.

[27] J.T.Grant and D.Briggs, *Surface Analysis by Auger and X-ray Photoelectron Spectroscopy*, IM Publications, Chichester, UK, **2003**.

[28] M.P.Seah and D.Briggs, *Practical Surface Analysis by Auger and X-ray Photoelectron Spectroscopy*, Wiley & Sons, Chichester, UK, **1992**.

[29] Ghosh, P.K, *Introduction to Photoelectron Spectroscopy*, John Wiley & Sons, **1983**.

[30] B.V.Crist, *Handbooks of Monochromatic XPS Spectra,* XPS International LLC, Mountain View, CA, USA, **2005**.

[31] Zworykin VA, Hillier J, Snyder RL, *A scanning electron microscope*, ASTM Bull, **1942**, 117, 15–23.

[32] McMullan. D, *Scanning electron microscope*, Proc Roy Microsc Soc., **1988**, 23, 283–288.

[33] McMullan. D, *Scanning electron microscopy 1928–1965*, Scanning, **2006**, 17(3), 175.

[34] Williams, D and Carter, C. B, *Transmission Electron Microscopy. 1 – Basics*, Plenum Press, **1996**.

[35] Champness, P. E, *Electron Diffraction in the Transmission Electron Microscope*. Garland Science, **2001**.

[36] Fultz, B and Howe, J, *Transmission Electron Microscopy and Diffractometry of Materials*, Springer, **2007**.

[37] F. Scholz (Ed.), *Electroanalytical Methods*, Springer-Verlag Berlin Heidelberg, New York **2002**.

[38] R. Greef, R. Peat, L. M. Peter, D. Pletcher and J. Robinson, *Instrumental Methods in Electrochemistry*, Ellis Horwood Ltd. **1995**.

[39] A. J. Bard and L. R. Faulkner, *Electrochemical Methods, Fundamentals and Applications*, John Wiley & Sons, Inc. New York **1980**.

[40] J. E. B. Randles, *A cathode ray polarograph*, Trans. Faraday Soc., **1948**, 44, 327.

[41] A. Sevick, Coll. Czech, *The fundamentals of electrochemistry*, Chem. Comm., **1948**, 13 349.

[42] R. S. Nicholson and I. Shain, *Theory of stationary electrode polarography*, Anal. Chem., **1964**, 36, 706.

[43] Koryta. J, Dvorak. J, *Principles of Electrochemistry*, Wiley, Chichester, UK, **1987.**

[44] Gileadi, E., *Electrode Kinetics*, VCH Publishers, New York, **1993**.

[45] Brett, C. Oliveira Brett, A. M., *Electrochemistry: Principles, Methods and Applications*, Oxford Univ. Press, Oxford, UK, **1993**.

[46] Smyth, M.; Vos, J., *Analytical Voltammetry*, Elsevier, Amsterdam, **1992**.

[47] Rieger, P., *Electrochemistry*, Prentice-Hall, Englewood Cliffs, NJ, **1987**.

[48] Joseph wang, Analytical Electrochemistry, 3rd ed, John Wiley & Sons, Inc., Hoboken, New Jersey, **1948**.

[49] Evgenij Barsoukov and J. Ross Macdonald, *Impedance Spectroscopy,* Second Edition, John Wiley & Sons, Inc, **2005**.

[50] Cynthia G. Zoski, *Handbook of Electrochemistry*, Elsevier, **2007.**

[51] Zhang L, Song C, Zhang J, Wang H, Wilkinson DP. *Temperature and pH dependent Oxygen reduction catalysed by iron fluoro-porphyrin adsorbed on a graphite electrode.* J Electrochem Soc, **2005**, 152, A2421-A2426.

Chapter 4. Functionalised Graphite Oxide Paper as Proton Conductor

This chapter discuss the properties of graphite oxide (GO) as a bi-functional additive being both hydrating and proton conducting. The GO and SGO free standing paper has been fabricated and evaluated for its stability and proton transport mechanism.

4.1Introduction

Proton exchange membrane fuel cells have been the focus of interest due to ever increasing energy demands. A variety of polymer electrolyte membranes (PEMs) have been fabricated and studied for polymer electrolyte membrane fuel cells (PEMFCs) [1]. Most of the membranes possess limitations, which hinder the successful commercialisation of PEMFC technology. Perfluorinated sulfonic acid (PFSA) based membranes remain the benchmark due to their excellent proton conductivity under humidified conditions [2]. The high temperature operation (above 80 ^{o}C) of fuel cell would enhance the fuel cell performance by enhancing the electrochemical kinetics, improves the CO tolerance of Pt electrocatalyst and reduces the noble electrocatalyst (Pt) loading [3]. The proton conductivity of PFSA based membrane depends on hydration level and therefore, it is not practical to uses these membranes above 80 ^{o}C. The development high temperature polymer electrolyte membranes have been the most important areas of research in PEMFC [4]. One of the promising routes to make PEM for HTPEMFC is the fabrication of inorganic-organic composite membranes [5, 6]. Considerable amount of research efforts have been made to develop PFSA composite membranes with inorganic hydrophilic oxide materials [7, 8]. The improved water retention and proton conductivity of PFSA composite membranes enable them to operate at high temperature. However, the proton conductivity of these composite membranes is still lower than the pristine PFSA membranes [9, 10]. Functionalised GO (sulfonated graphite oxide) is used as a bi-functional additive being both hydrating and proton conducting to fabricate composite membranes for high temperature PEMFC.

4.2 Results and Discussion

4.2.1 Formation of free standing graphite oxide and sulfonated graphite oxide paper

Preparation and characterisation of graphite oxide (exfoliated graphite oxide in water yielding colloidal suspension of graphene oxide sheets) paper was reported by D.A. Dikin et al. [11] and they proposed a mechanism for the formation of free standing graphite oxide paper by vacuum filtration. The same mechanism applies to the formation of SGO paper. During the filtration, SGO sheets are assembled onto the surface of Anodisc membrane filter (Cellulose acetate ester used as membrane filter). As the deposition of SGO sheets on top of each other and the water flow decreases. The filtration time depends on the concentration of GO and SGO solution used for desired thickness and normally it can take up to 2 days. After drying, the membrane can be peel from the filter and it can be folded like normal paper or membrane. GO and SGO are hydrophilic, but a piece of these papers left in water for several hours does not disintegrate and maintains its shape. If the paper is handled while it is still wet, it will disintegrate but it will regain its mechanical strength when it is dried and it can be handled. This behaviour indicates that no covalent bonding was achieved between the GO or SGO sheets. Stiffness and flexibility is a result of unique interlocking arrangement of nanoscale SGO sheets.

Figure 4.1, Schematic representation of GO and SGO paper fabrication

4.2.2 Physicochemical characterisation of functionalised graphite oxide

FTIR studies confirmed the successful oxidation of graphite to graphite oxide and sulfonated graphite oxide, as shown in the figure 4.2. The presence of different types of oxygen functionalities in GO and SGO shows a characteristic peaks between 1000-3600 cm^{-1} and are assigned as follows; the peak observed at 1717 and 1725 cm^{-1} ($\upsilon_{C=O}$) from carbonyl and carboxylic groups. The peak observed at 1025 and 1049 cm^{-1}(υ_{C-O}) is from carbonyl, carboxylic and epoxy groups. The peak at 1346 cm^{-1} is assigned to SO_3H on SGO. The peak at 1621 cm^{-1} observed in SGO is due to restoration of sp^2 carbon. Hydrogen bonded (Carboxyl OH) O-H stretching vibrations observed at 3160 to 3368 cm^{-1} for GO and SGO.

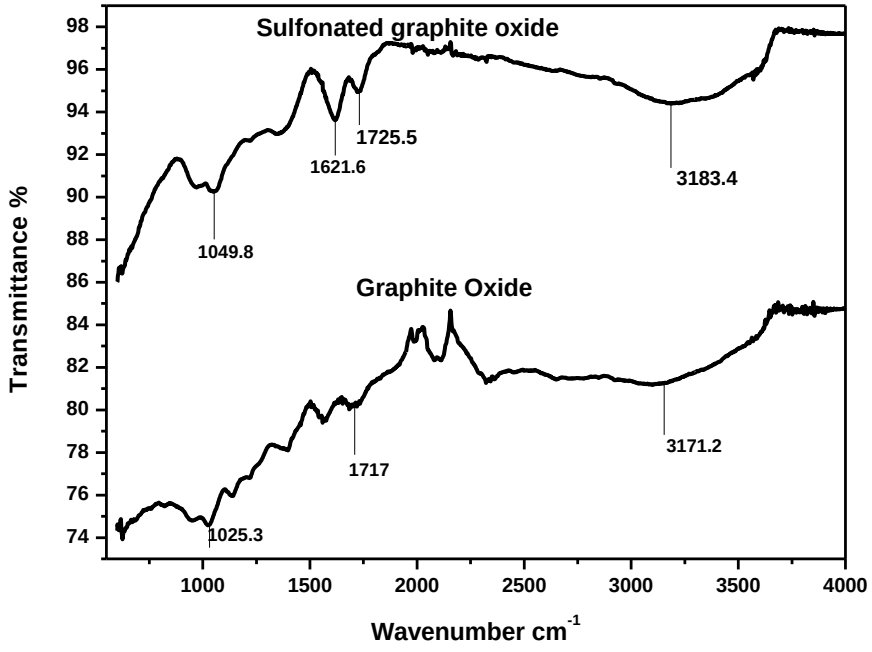

Figure 4.2, FT-IR spectra of GO and SGO

The elemental analysis of GO and SGO was performed by EDS on different areas of paper and an average wt% and at% data is presented in Table 4.1. The SGO had higher concentration of surface oxygen; 43.17 at. %, compared to GO, 36.22 at. %. The sulphur content in SGO is about 10.72 wt%; therefore the degree of sulfonation is ~11%. (The degree of sulfonation is directly proportional to the sulphur content).

Table 4.1, EDX data of graphite oxide and sulfonated graphite oxide obtained from ESEM

Material	Carbon		Oxygen		Sulphur	
	Wt%	At%	Wt%	At%	Wt%	At%
GO	56.93	63.78	43.07	36.22	-	-
SGO	42.35	51.89	46.93	43.17	10.72	4.93

Raman spectroscopy is widely used to characterise the graphene based materials. Raman spectra of GO and SGO are shown in figure 4.3. The D band (the symmetry A_{1g} mode of sp^2 carbon) at 1350 cm^{-1} and a G band (the E_{2g} mode of sp^2 carbon atom) observed at 1590 cm^{-1} is consistent with literature reported values [12]. After sulfonation the intensity ratio of the D to G band slightly increases (SGO I_D/I_G =0.86; GO I_D/I_G =0.84) which is due to sulfonation reducing the basal plane to produce more sp^2 carbon domains.

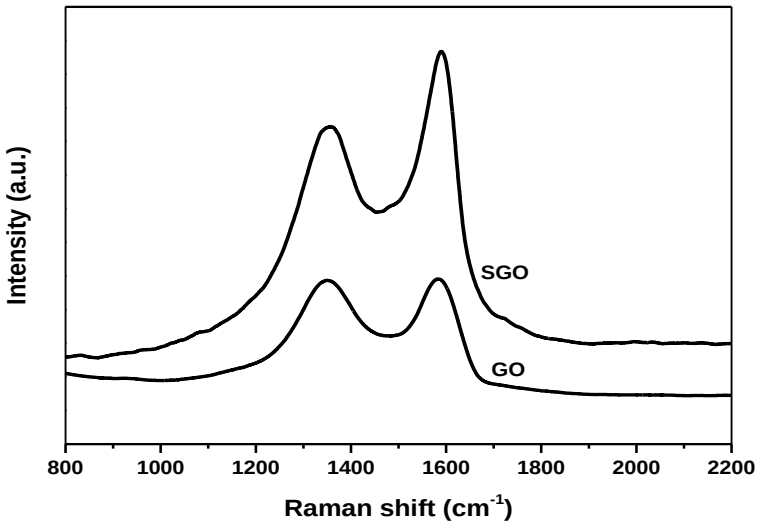

Figure 4.3, Raman spectra of GO and SGO

Figure 4.4 shows the XRD patterns of graphite oxide, sulfonated graphite oxide and graphite powder. The peak observed at 26.45º in the graphite sample corresponds to the interplanar distance between the different graphene layers. Chemical oxidation of graphite disrupts the ordering of layers and introduces a variety of functional groups (hydroxyl, epoxide, carboxyl, etc.) as the C-C bonds are broken during the oxidation process. The functional groups increase the interplanar distance between the sheets which increases the distance between graphene oxide sheets. Therefore the XRD peak

shifts from higher angle to a smaller angles, thus the appearance of broader peak at around 11.26º (001) in GO. The calculated interplanar distance (d-spacing) for GO is about 0.79 nm and SGO is about 0.75 nm (calculations are shown in Appendix A). After sulfonation, the disruption of GO structure and increased the attractive interaction between the GO layers occur [13]. This was confirmed by X-ray diffraction pattern of SGO, the shift of 2θ towards higher angle was observed in SGO.

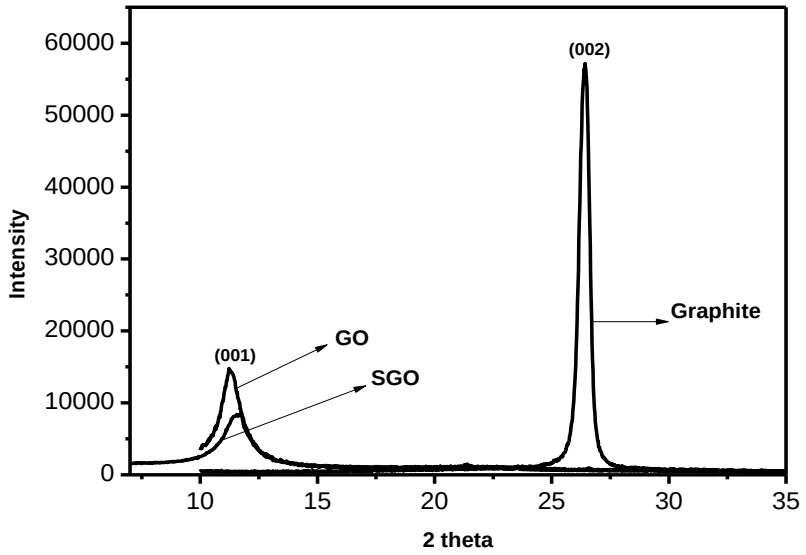

Figure 4.4, X-ray diffraction of graphite oxide, sulfonated graphite oxide and graphite

The bonding nature is analysed using X-ray photoelectron spectroscopy (XPS) and the survey spectrum of GO and SGO is shown in figure 4.5a and 4.5b. A characteristic peak was observed for SGO (Figure 4.5b) at a binding energy of 169.03 eV, and is attributed to sulfur 2p component. This confirms the attachment of sulfonic acid group onto the graphene oxide nanosheets. Furthermore, the spectrum was deconvoluted for C 1s and O 1s to understand the surface functional groups and is shown in figure 4.5c-4.5f. The high intensity peak observed at 285.38 eV (Figure 4.5d) is attributed to the C-S bond in addition to all other functional groups. The deconvoluted O 1s XPS peaks of GO in Figure 4.5e are composed of three components including O-C=O, C=O and C–OH with their binding energy at 531.2, 532.6 and 534.5 eV, respectively. The deconvoluted O 1s XPS spectrum (Figure 4.6f) shows a peak at 532.94 eV, assigned to a combination of C=O and O=S=O bonds, and confirms the presence of SO_3H on graphite oxide.

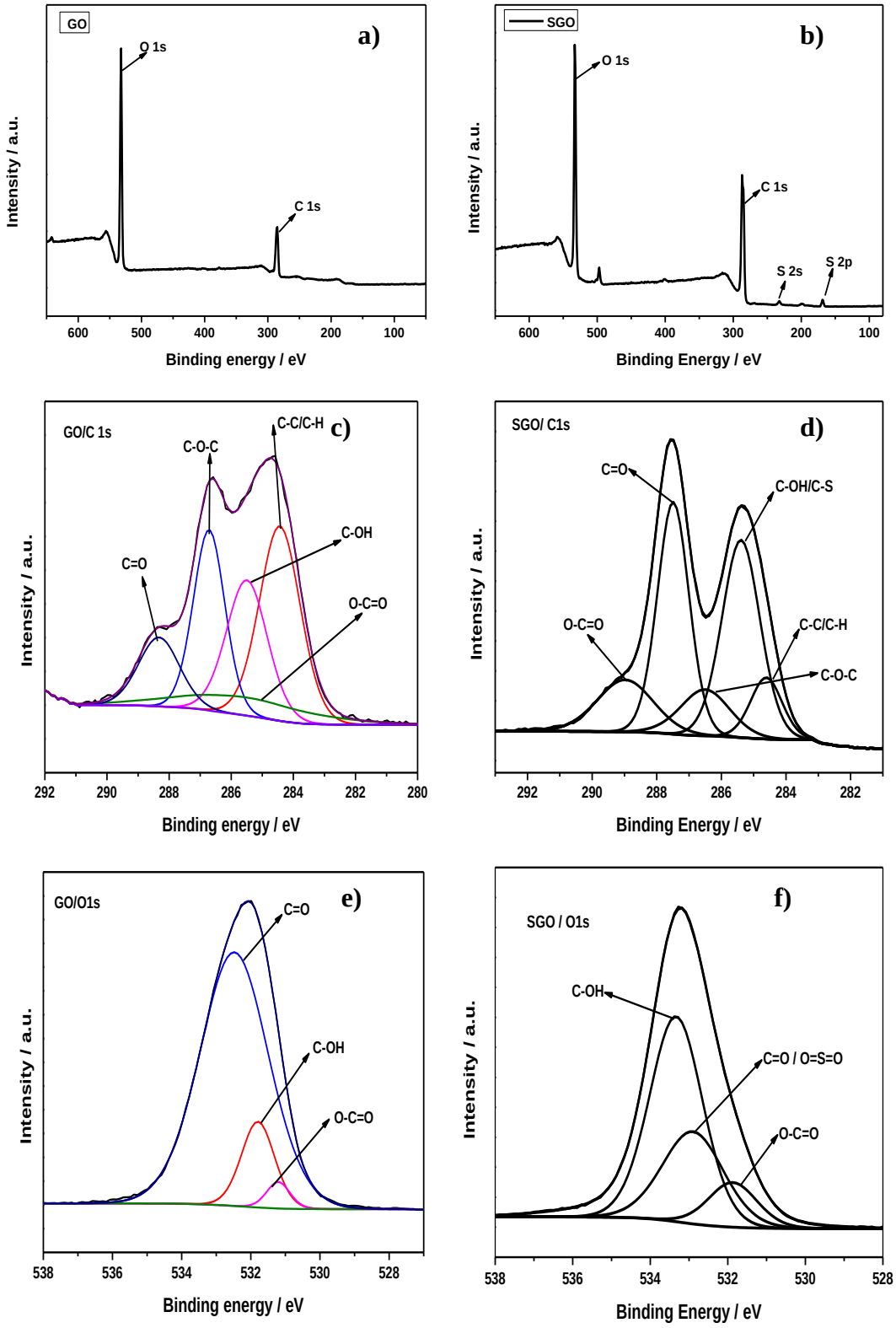

Figure 4.5, XPS survey spectrum of a) GO and b) SGO, c and d are C 1s deconvoluted XPS spectra and e and f are O 1s deconvoluted XPS spectra

A thermogravimetric analysis of graphite oxide and sulfonated graphite oxide is given in figure 4.6. GO showed much lower thermal stability due to the reduced van der Waals interactions, and a mass loss of 15% below 150 ^{o}C was observed in both GO and SGO which could be attributed to the adsorbed water and bounded water. From 150 to 200 ^{o}C mass losses of about 30% takes place by loss of oxygen containing functionalities such as CO, CO_2 etc. The remaining mass losses of 20% up to 400 ^{o}C were due to the weakening of van der Waals forces between the GO layers which disrupts the stacking of graphite oxide sheets thus accelerating the process of weight loss in GO.

After sulfonation, a lower mass loss took place after 220 ^{o}C, which indicates that SGO was more thermo-stable than GO [9]. In the case of SGO, sulfonation decreased the disruption of GO structure and increased the attractive interaction between the GO layers. This was confirmed by the X-ray diffraction pattern (see the figure 4.4) of SGO, the shift of 2θ towards higher angle was observed in SGO.

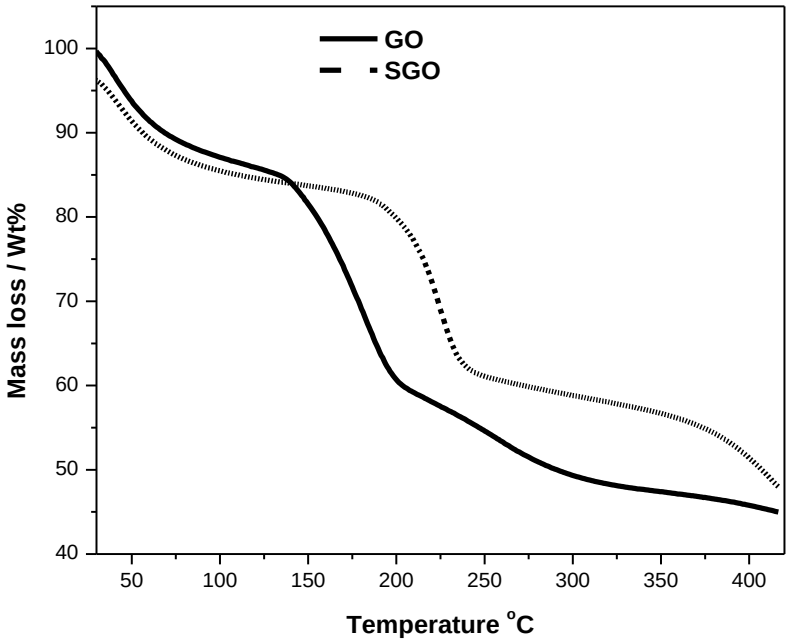

Figure 4.6, Thermogravimetric analysis of GO and SGO

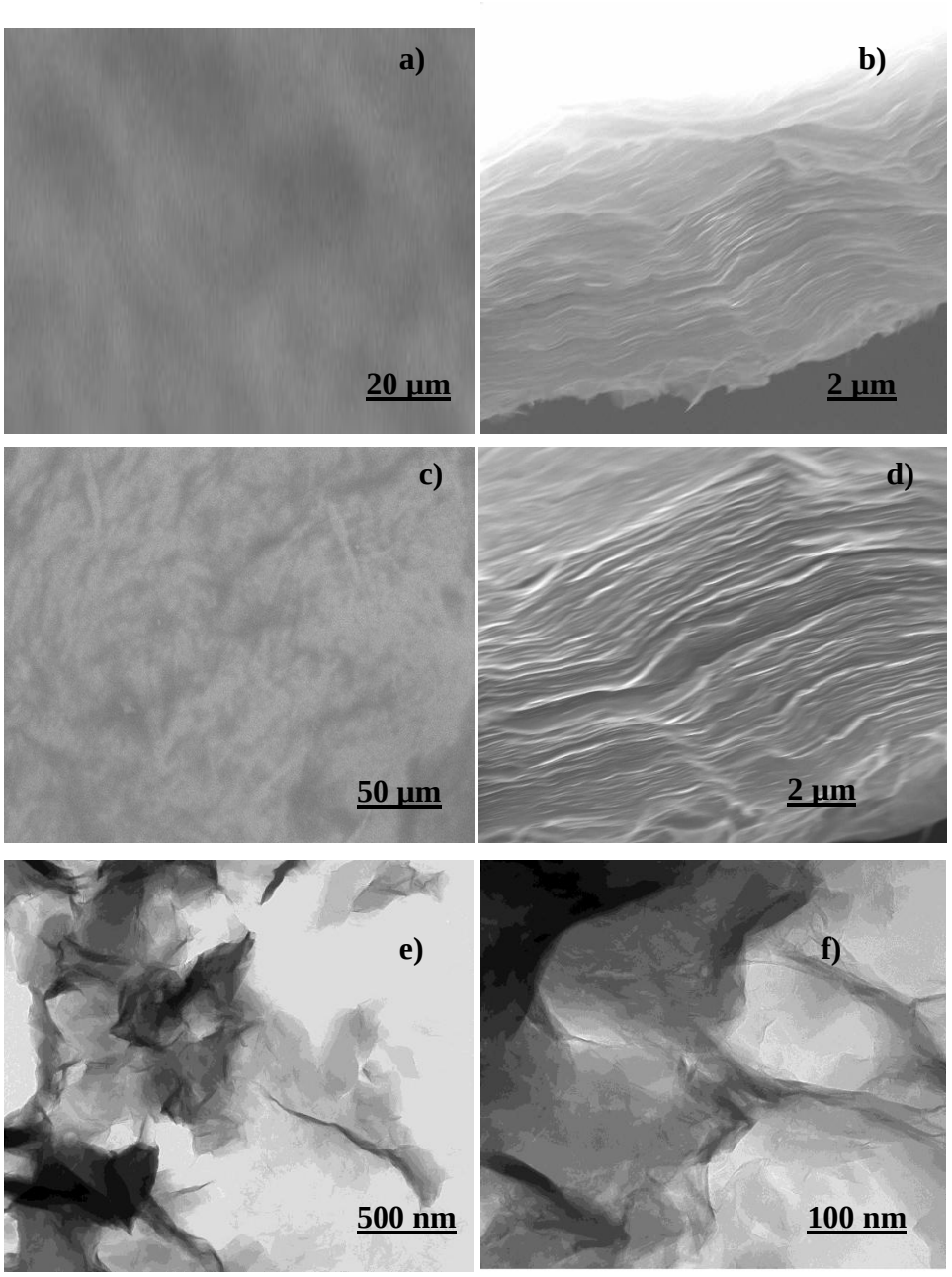

Figure 4.7, SEM images of GO and SGO a and c) Surface morphology, b and d) Cross section SEM images, c and d) TEM images of SGO

Figure 4.7a-4.7d shows scanning electron microscopy (SEM) images of surface and cross section of graphite oxide and sulfonated graphite oxide. It is seen from the images the surface appears to be smooth. Cross section image reveals the stacking of less densely packed thin wavy layers through the entire cross section. A TEM image of sulfonated graphite oxide is shown in figure 4.7e and 4.7f, in which SGO nano sheets appeared relatively flat, exfoliated and wrinkled, which is in good agreement with literature reported morphology [11].

Mechanical measurements of SGO paper samples were performed on Instron 4505 machine and measurements were repeated for three samples (20mm X 11mm; 35µm) for reproducibility. Figure 4.8a shows a typical plot of stress vs. strain for SGO paper. The maximum tensile stress calculated is about19.46 MPa and Young's modulus (figure 4.8b) is 1.59 GPa. These results indicate that SGO paper is stiff and brittle.

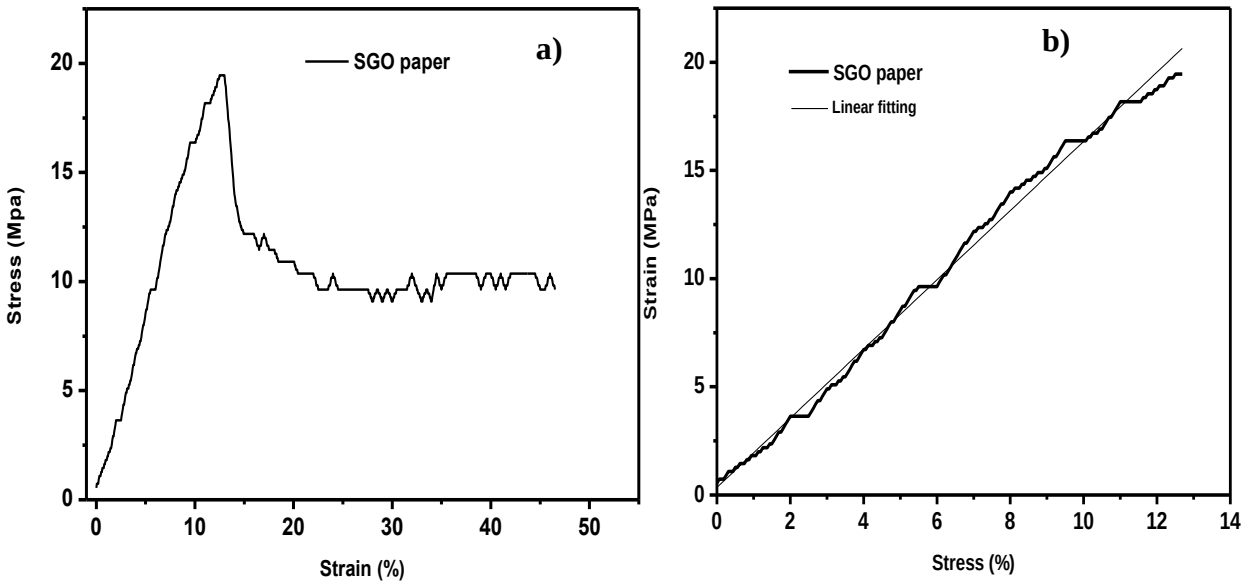

Figure 4.8, a) Stress vs. Strain curve of SGO paper and b) Young's modulus plot

4.2.3 Proton conductivity

The main role of polymer electrolyte is to transport the protons being generated during the anodic oxidation of hydrogen from anode to cathode. GO and SGO is proposed to use as an additives to fabricate Nafion® based composite materials, and therefore, proton conductivity is measured for GO and SGO free standing paper.

The temperature dependant proton conductivity (in-plane (σ_{ip}) and through-plane (σ_{tp})) of the SGO paper is shown in figure 4.9. The σ_{ip} and σ_{tp} conductivity values are 0.04 and 0.012 $S.cm^{-1}$ at 303 K respectively and are the conductivity range of Nafion® between 0.01 to 0.1 $S.cm^{-1}$ in a humid environment. The σ_{ip} and σ_{tp} conductivity values of GO paper are 0.008 and 0.004 $S.cm^{-1}$ at 303 K and these values are lower than SGO paper.

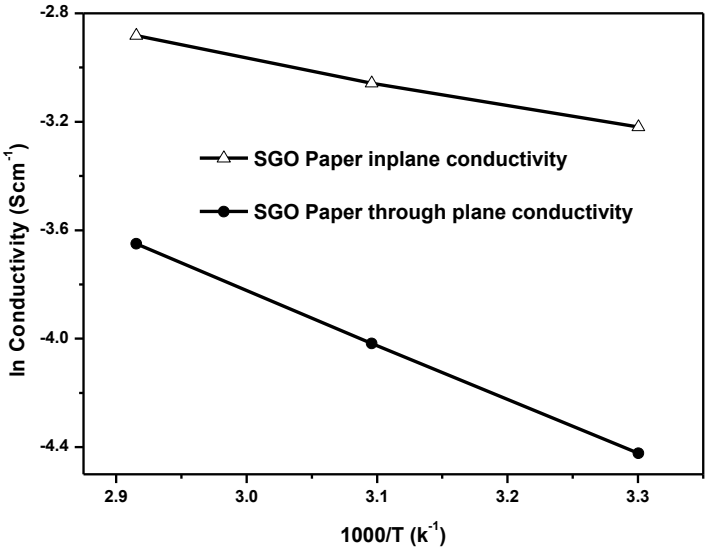

Figure 4.9, Temperature-dependent proton conductivity of SGO paper at 100% relative humidity

The mechanism of proton conductivity in solids, is based on two methods; one is the vehicular model, where formation of an ion adduct with carrier molecule occurs- if it is water then protons form hydronium ions. In a non-vehicular model, hopping of protons occurs from site to site without carrier a molecule which is called a Grothus-type mechanism [14, 15]. Based on these mechanisms, proton transport mechanism of GO and SGO is discussed. The typical representation of in-plane and through-plane proton hopping is shown in scheme 4.1. Through-plane proton conductivity of GO and SGO paper is attributed to Grothus-type mechanism, in which re-organization of hydrogen bonds play a vital role in the presence of water between each GO and SGO layer. The measured layer to layer distance for GO and SGO are about 0.79 nm and 0.75 nm (from XRD) can be attributed to an approximate one-molecule-thick layer of water that is presumably hydrogen-bonded between the GO and SGO sheets [16], which interconnects proton conducting paths between SGO layers. The presence of sulfonic acid and oxygen containing functional groups (COOH, COC) on edges and basal planes contribute to in-plane proton transport. Arrangement of oxygen atoms in rectangular fashion, with a lattice constant of 0.27 nm x 0.41 nm, which in turn leads to a vehicular mode of proton transportation which is also contributed to in-plane proton transport [17, 18]. The IEC value of SGO paper is 1.1 $meqg^{-1}$ (IEC value obtained from the titration) which is more than that of Nafion® 115 which is about 0.93 $meqg^{-1}$ [19]. The

conductivity data reveals that $\sigma_{ip} > \sigma_{tp}$. The presence of water between the layers is mainly contributes to σ_{tp}, whereas all other functional groups support σ_{ip}. Furthermore, the activation energy calculated for the SGO paper is 7.2 kJ mol^{-1} (σ_{ip}) and 16.6 kJ mol^{-1} (σ_{tp}). The lower in activation energy of σ_{ip} is explains the better proton conductivity.

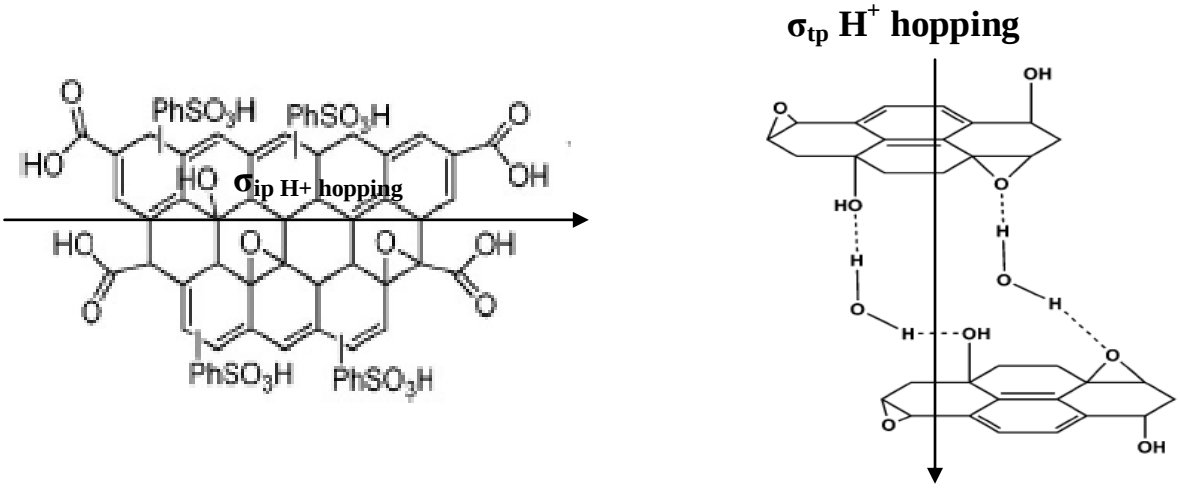

Scheme 4.1, Schematic representation of proton transport

A thin layer of Nafion® (~3 µm) is coated on both the side of SGO paper and is called as Nafion® laminated SGO paper. The presence of Nafion® layer on SGO film reduces gas crossover and improves the mechanical stability under a humid environment. The in-plane proton conductivity of Nafion® laminated SGO paper is shown in figure 4.10. The Nafion® laminated SGO paper exhibited a proton conductivity of 0.12 $S.cm^{-1}$.

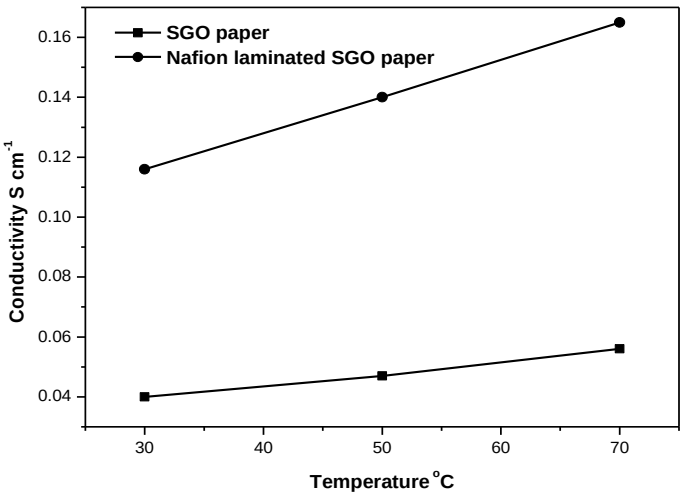

Figure 4.10, In-plane proton conductivity of SGO paper and Nafion® laminated SGO paper at 100% relative humidity

4.2.4 Fuel cell performance of SGO paper MEA

Single cell polarisation plot shown in figure 4.11a was obtained from MEA fabricated with SGO paper. MEA was fabricated using 20% Pt/C (anode; 0.4 mg cm^{-2}) and 50% Pt/C (cathode; 0.4 mg cm^{-2}). The cell was operated at 40 ^{o}C and fed with 25% humidified hydrogen and dry oxygen gases at a flow rate of 0.4 and 0.7 dm^3 min^{-1} respectively (the relative humidity of the cell was kept at 25% to maintain the stability of SGO paper under fuel cell operation) . The open circuit potential (OCP) obtained with SGO paper MEA was 0.72 V, which was significantly lower than achieved with Nafion® based membrane (~1.0 V). Due to its porous nature gas crossover occurs, which affects the cell OCP. The H_2 gas cross over measurement of SGO paper MEA was performed by passing hydrogen on anode and argon gas was fed with cathode. The measured H_2 crossover current (4.3 mA cm^{-2}) which was more than that of Nafion® membrane based MEAs (1 mA cm^{-2}). The SGO paper MEA gave a maximum power density of 113 mW cm^{-2} at 0.39 V. Figure 4.11b shows the SGO paper MEA single cell durability operated at 40 ^{o}C galvanostatically (200 mA cm^{-2}) with 25% RH. The data suggested that the MEA was stable in the above operating condition without failure up to 10 h.

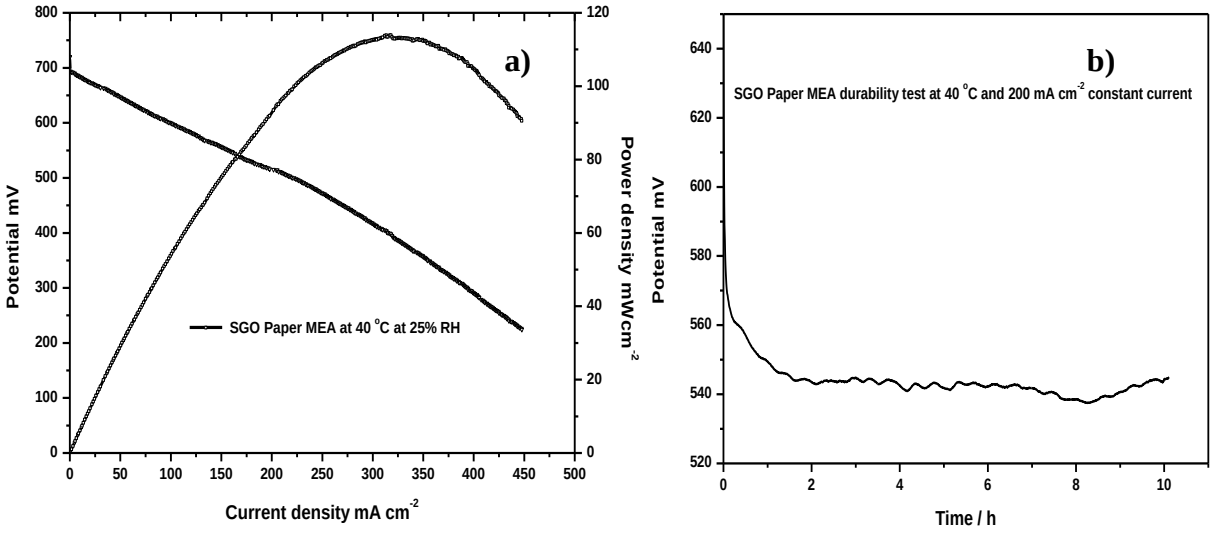

Figure 4.11, a) Polarisation curve obtained for SGO paper MEA at 40 ^{o}C with 25% RH and b) durability of SGO paper MEA at 40 ^{o}C and 200 mA cm^{-2} constant current loading with 25% relative humidity

A layer of Nafion® is laminated on both the sides of SGO paper, to reduce the gas crossover and improves the mechanical stability. The Nafion® lamination of SGO paper assumed to improves the fuel performance. The fuel cell performance of Nafion® laminated SGO paper is shown in figure 4.12. It is seen from the polarisation curve, the OCP of the MEA is about 0.98 V which is higher than that of SGO paper MEA (0.72 V). The layer of Nafion® on both sides of the SGO paper reduces the gas crossover and eventually enhances the OCP. The power density of Nafion® laminated SGO paper MEA is increased by about 50 mW cm^{-2}, however this is not a significant improvement compared to the Nafion® membrane based MEAs. The through-plane conductivity of Nafion® laminated SGO measured from the MEA is about 0.006 $S.cm^{-1}$ which is lower than that of SGO paper MEA, this is due the Nafion® layer which is not in good contact with SGO paper (when the Nafion® laminated SGO paper was soaked in 0.5 M H_2SO_4, the Nafion® layer became slightly separated from SGO paper), which increases the resistance of the MEA. Therefore the fuel cell performance of Nafion® laminated SGO paper is very low compare to Nafion® membrane based MEA. Due to H_2 crossover, SGO paper based MEA was not investigated for high temperature operation.

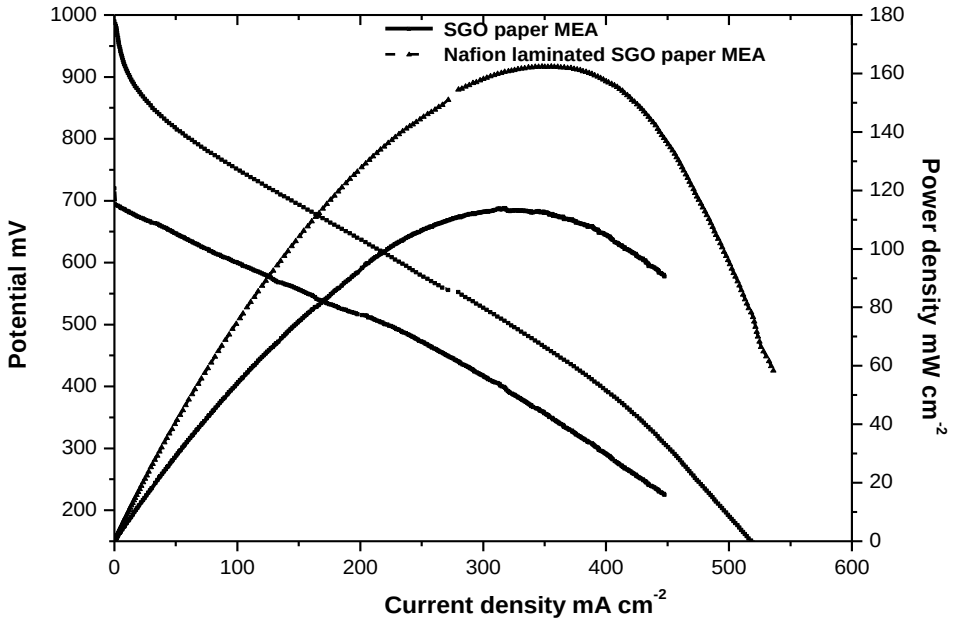

Figure 4.12, Polarisation curve obtained for Nafion® laminated SGO paper MEA at 40 ^oC with 25% relative humidity

4.3 Conclusions

The free standing sulfonated graphite oxide paper was used as a PEM and the proton transport mechanism and its fuel cell performance has been evaluated. The presence of different acidic functional groups (SO_3H, COOH, OH, and COC) on SGO is the reason for the proton conductivity of SGO paper. The MEA made with the SGO paper gave reasonable fuel cell performance. The lower fuel cell performance (113 mW cm^{-2}) of SGO paper MEA was due to fuel crossover. The Nafion® laminated SGO paper showed a higher OCP and fuel cell performance. The direct use of SGO paper as a PEM is considered to be impractical, but it could be used as an additive to make composite membranes because SGO is bifunctional being both hydrating and proton conducting.

References

[1] M. Z. Jacobson, W. G. Colella, D. M. Golden, *Cleaning the Air and Improving Health with Hydrogen Fuel-Cell Vehicles*, Science, **2005**, 308, 1901-1905,

[2] Wu X, Scott K, Mamlouk M. *A PBI-$Sb_{0.2}Sn_{0.8}P_2O_7$-H_3PO_4, Composite Membrane for Intermediate Temperature Fuel Cells*, *Fuel Cells*, **2011**, 11(5), 620-625.

[3] Hongting Pu, Lu Liu, Zhihong Chang, Junjie Yuan, Organic/inorganic composite membranes based on polybenzimidazole and nano-SiO_2, Electrochimica Acta, **2009**, 54, 7536–7541.

[4] A. K. Sahu, G. Selvarani, S. Pitchumani, P. Sridhar, and A. K. Shukla, *A Sol-Gel Modified Alternative Nafion-Silica Composite Membrane for Polymer Electrolyte Fuel Cells*, Journal of The Electrochemical Society, **2007**, 154 (2), B123-B132.

[5] V. DiNoto, R. Gliubizzi, E. Negro, G. Pace, *Effect of SiO_2 on Relaxation Phenomena and Mechanism of Ion Conductivity of [Nafion/$(SiO_2)_x$] Composite Membranes*, J. Phys. Chem. B, **2006**, 110, 24972.

[6] D.A. Boysen, T. Uda, C.R.I. Chisholm, S.M. Haile, *High-Performance Solid Acid Fuel Cells Through Humidity Stabilization*, Science, **2004**, 303, 68–70.

[7] K. T. Adjemian, S. Srinivasan, J. Benziger, and A. B. Bocarsly, *Investigation of PEMFC operation above 100 °C employing perfluorosulfonic acid silicon oxide composite membranes*, J. Power Sources, **2002**, 109, 356-364.

[8] Stankovich, S. et al., *Graphene-based composite materials*, Nature, **2006**, 442, 282–286.

[9] Lerf, A. et al., *Hydration behavior and dynamics of water molecules in graphite oxide*, J. Phys. Chem. Solids, **2006**, 67, 1106–1110.

[10] Stankovich, S. et al., *Stable aqueous dispersions of graphitic nanoplatelets via the reduction of exfoliated graphite oxide in the presence of poly (sodium 4-styrenesulfonate)*, J. Mater. Chem., **2006**, 16, 155–158.

[11] D.A. Dikin et al., *Preparation and characterization of graphene oxide paper*, Nature, **2007**, 448, 457-460.

[12] Voggu, R., Das, B., Routt, C. S. & Rao, C. N., *Effect of charge transfer interaction of graphene with electron donor and acceptor molecules examined using Raman spectroscopy and cognate techniques*. J. Phys.: Condens. Matter, **2008**, 20, 472204–472208.

[13] Gao, W., Alemany, L. B., Ci, L. & Ajayan, P. M., *New insights into the structure and reduction of graphite oxide*, Nat. Chem., **2009**, 1, 403–408.

[14] Noam Agmon, *The Grothus mechanism*, Chemical physics letters, **1995**, 244, 456-462.

[15] J. D. Bernal, R. H. Fowler, J. Chem. Phys., **1933**, 1, 515.

[16] Scholz, W.& Boehm, H. P. Untersuchungen am graphitoxid. VI. Betrachtungen zur struktur des graphitoxids. Z. Anorg. Allg. Chem., **1969**, 369, 327–340.

[17] D. Pandey, R. Reifenberger, and R. Piner, Scanning probe microscopy study of exfoliated oxidized graphene sheets, Surface Science, **2008**, 602 (9), 1607–1613.

[18] 8 R. Kumar, M. Mamlouk, and K. Scott, A Graphite Oxide Paper Polymer Electrolyte for Direct Methanol Fuel Cells, International Journal of Electrochemistry, Volume **2011**, Article ID 434186, 7 pages.

Chapter 5. Graphite oxide and Sulfonated graphite oxide-Nafion composite polymer electrolyte membrane for PEMFCs

This chapter covers the physicochemical characterisation, proton conductivity measurements, fuel cell characterisation, stability and durability test of recast Nafion, graphite oxide (GO) and Sulfonated graphite oxide/Nafion composite membranes.

5.1 Introduction

Polymer electrolyte membrane fuel cells have been proposed as one of the most promising power sources for realising the hydrogen economy and for alleviating issues like environmental pollution. Polymer electrolyte membrane fuel cells are, however, not in widespread commercial use and research attempts to improve the performance and minimise expensive components have been triggered over recent decades [1, 2]. Requirements for an excellent membrane are high proton conductivity, chemical resistivity, thermo-mechanical stability and durability under dynamic operations [3, 4]. The typical membranes currently used for the PEMFCs such as Nafion® or other perflourosulfonic acid polymer (e.g. Aciplex® and Flemion®) show a significant loss in conductivity at elevated temperature due to the dehydration of water from the membrane [5, 6]. The proton exchange membranes used in PEMFCs are thin, to increase the proton conductivity, and which accelerates the membrane dehydration. In order to enhance the operating temperature preventing loss of water is very important, and several approaches have been attempted to prevent loss of water from the membrane [7, 8]. One approach is incorporating oxide materials into the polymer matrix such as ZrO_2, SiO_2 and TiO_2 [9, 10].

Nafion® and similar materials are made up of hydrophobic polytertrafluoroethylene (PTFE) backbone and hydrophilic sulfonic acid ester side chain. Nafion® also has an intermediate region associated with inverted micelles or ionic clusters with water at an approximate ratio of 70:1000 [11]. The proton conductivity generally increases with the water content in Nafion® [12]. Graphite oxide contains different kinds of oxygen functionalities, such as carboxylic, hydroxyl, epoxy and sulfonic acid groups. Due to the presence of oxygen functionalities, GO can be easily hydrated and the acidic functional groups and intermolecular hydrogen bonding can provide abundant proton conducting paths [13].

5.2 Results and Discussion

5.2.1 Physicochemical characterisation of composite membranes

FTIR of recast Nafion, GO/Nafion and SGO/Nafion composite membranes was used to analyse the extent of chemical interaction between GO, SGO and Nafion. FTIR spectra shown in Figure 5.1a, of recast Nafion, GO/Nafion composite membrane and GO shows characteristic of -COC- symmetric stretching bands at 968 and 980 cm^{-1}, whereas considerable broadening occurred in -SO_3- symmetric stretching vibrations bands at 1056 cm^{-1} and asymmetric stretching of -SO_3- groups at 1201 cm^{-1}. The double broadening observed in bending vibrations of O-H deformation peak at 1724 cm^{-1} and peak at 3440 cm^{-1} correspond to intermolecular hydrogen bonding and indicate interactions between the dispersed GO and the hydrate groups of Nafion polymer matrix.

FTIR spectra of recast Nafion, SGO/Nafion and SGO are shown in Figure 5.1b. A peak observed at 1346 cm^{-1} for SO_3H confirms the sulfonation of GO and at 3183 cm^{-1} for O-H stretching vibrations. Intermolecular hydrogen bonding between dispersed SGO nanosheets and the hydrate groups of Nafion are observed at 3440 cm^{-1}.

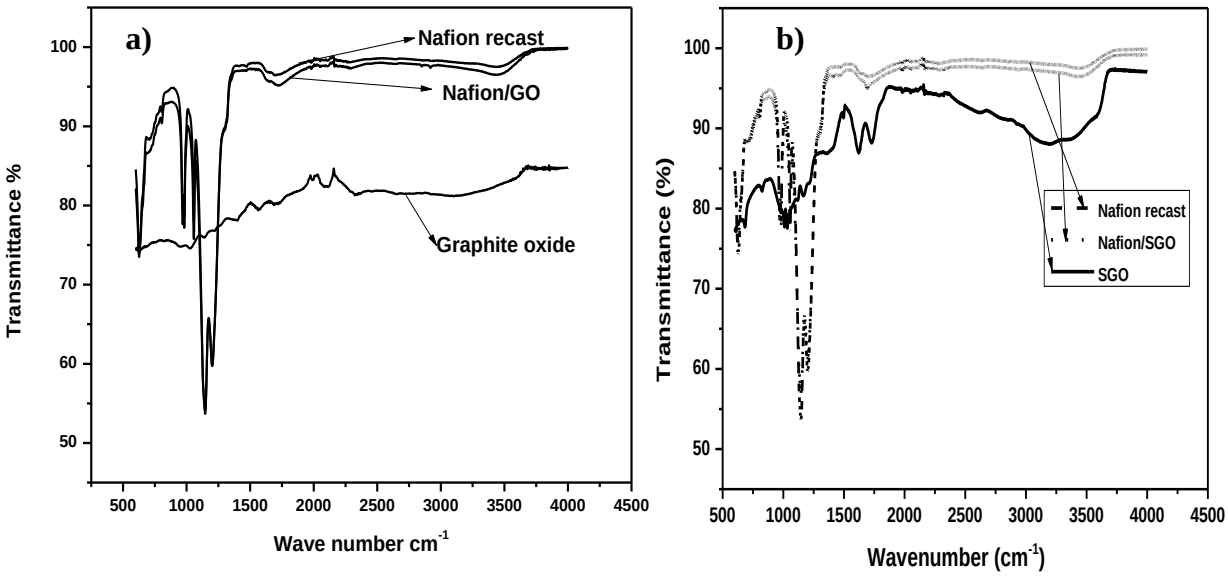

Figure 5.1, FT-IR Spectra of a) recast Nafion, GO/Nafion composite and GO paper and b) recast Nafion, SGO/Nafion composite and SGO paper

The morphologies of recast Nafion, GO/Nafion and SGO/Nafion composite membranes were characterised by SEM and data are shown in Figure 5.2a and 5.2b. The cross section SEM image of the Nafion recast has smooth morphology [15]. In case of the composite membrane, nano-sized graphene oxide sheets are uniformly distributed in the polymer matrix (figure 5.2a). Figure 5.2c and 5.2d shows TEM images of GO and SGO/Nafion composite membrane. The GO and SGO nano sheets remained exfoliated and randomly distributed over the whole membrane and tightly held in the polymer matrix due to strong interfacial interactions [16]. Hence, ion conducting paths are interconnected between GO, SGO and Nafion which potentially enhances the proton conductivity.

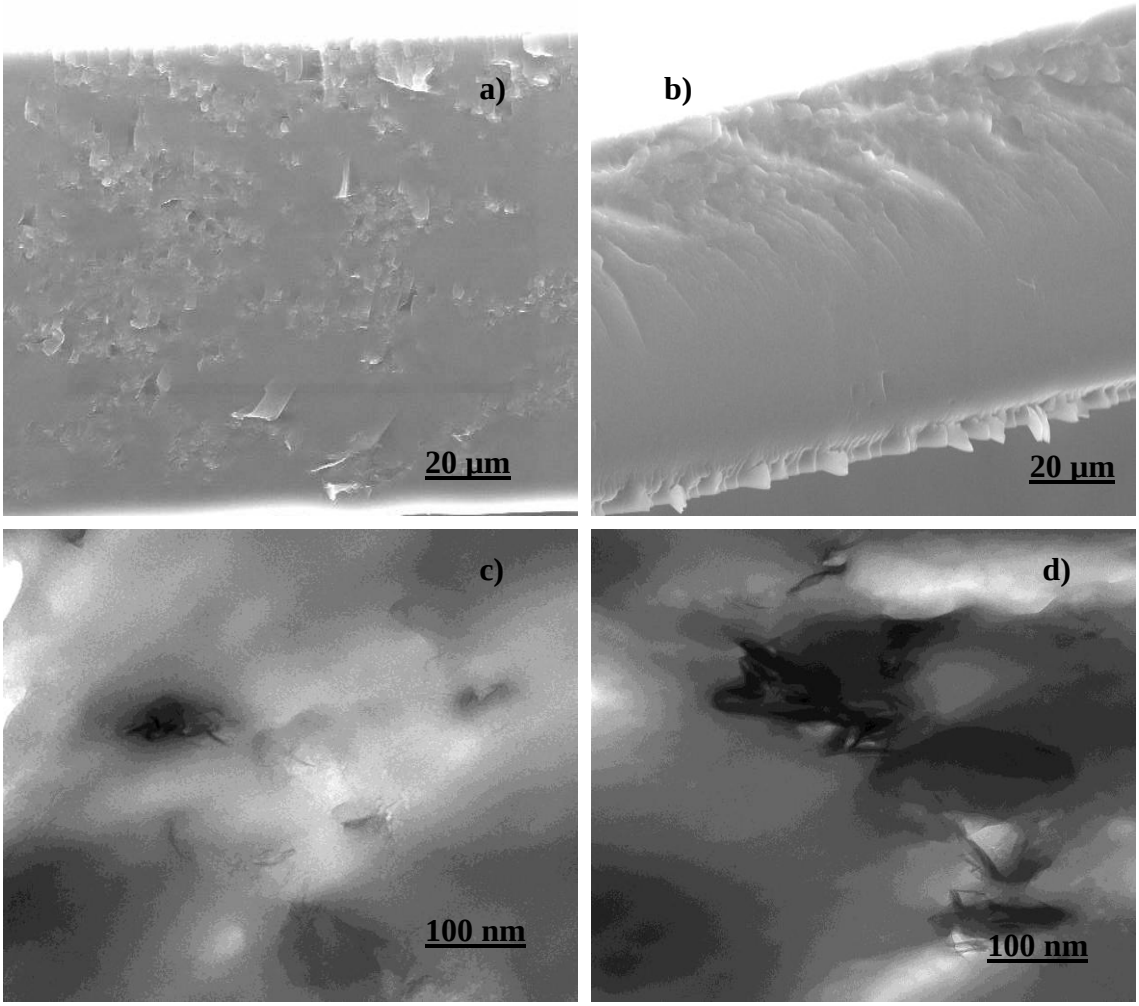

Figure 5.2, SEM cross section images of (a) GO/Nafion composite membrane; (b) recast Nafion, c) TEM image of GO/Nafion and d) TEM image SGO/Nafion composite membranes

Figure 5.3, shows TGA and DTA of recast Nafion, GO/Nafion and SGO/Nafion composite membranes. A small initial weight loss of 5% at 70 ^{o}C and another of 2% at 148 ^{o}C was observed for recast Nafion, GO/Nafion membranes, which could be attributed to the loss of water. The weight loss in GO/Nafion from 149 to 259 ^{o}C was due to the loss of surface functional groups on GO and also loss of bonded water on both membranes. The degradation of sulfonic groups (from Nafion) in the side chains was observed at around 280 ^{o}C for both the membranes. The sharp exothermic DTA peak observed for recast Nafion was due to degradation of PTFE back bone (onset of PTFE backbone degradation at 350 ^{o}C and ends at 550 ^{o}C), whereas GO/Nafion showed a less intense broad peak at around 490 ^{o}C. An initial weight loss of 5.5% at 195 ^{o}C and another of 2% at 308 ^{o}C was observed for SGO/Nafion composite membrane, which could be attributed to the loss of water. However, recast Nafion membrane showed a weight loss of about twice that of the composite membrane. SGO/Nafion composite membrane showed 14% mass loss from 300 to 450 ^{o}C due to the loss of surface functional groups on SGO. The SGO/Nafion showed broad exothermic peak at 560 ^{o}C. The PTFE back bone degradation is increased in the sequence GO/Nafion, recast Nafion and SGO/Nafion.

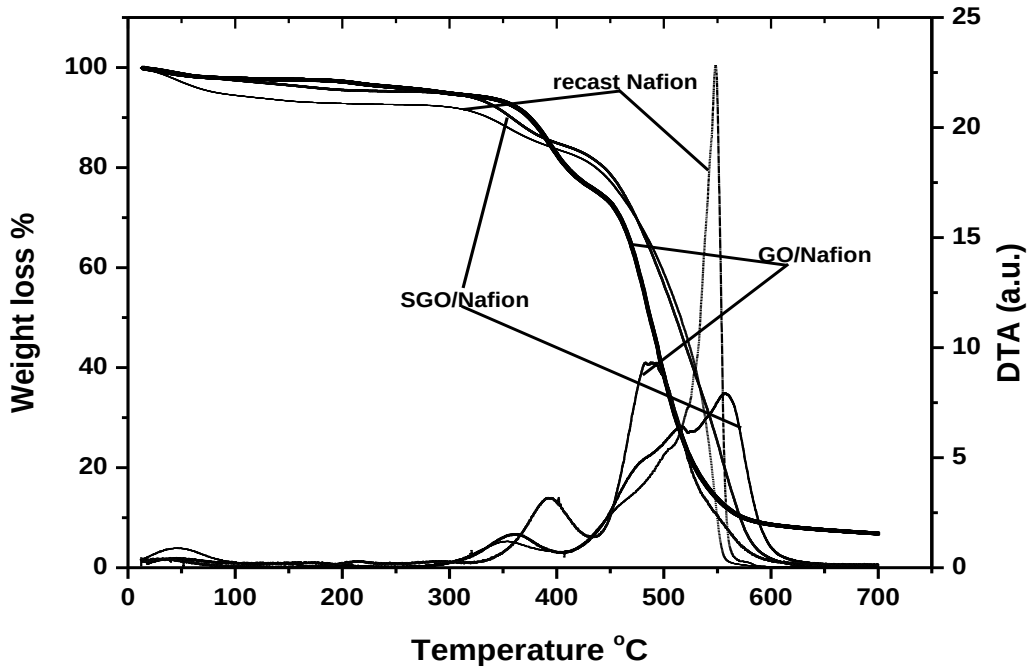

Figure 5.3, TGA and DTA of recast Nafion, GO/Nafion and SGO/Nafion composite membranes over a temperature range of 10 to 700 ^{o}C

The tensile properties of recast Nafion, GO and SGO/Nafion composite membranes are shown in figure 5.4. The membranes had the similar thickness (~50 µm). The data indicate that the incorporation of GO and SGO nano sheets into Nafion polymer matrix can enhance the tensile strength of the composite membranes. The Tensile strength value reached a maximum value of 8.17 MPa for SGO composite membrane (4 wt% of SGO), whereas GO/Nafion showed 6.64 MPa. In contrast the recast Nafion membrane had only a value of 3.36 MPa. The Young's modulus obtained from figure 5.4b is about 0.7, 0.52 and 0.28 GPa for SGO/Nafion, GO/Nafion and recast Nafion respectively. The percentage elongations of composite membranes were 42.3%, 31.3% and 16.9% for SGO/Nafion, GO/Nafion and recast Nafion respectively. The enhanced tensile strength was attributed to the uniform distribution of GO or SGO nano sheets in the Nafion polymer matrix, which helped to distribute the stress over all the area of the membrane.

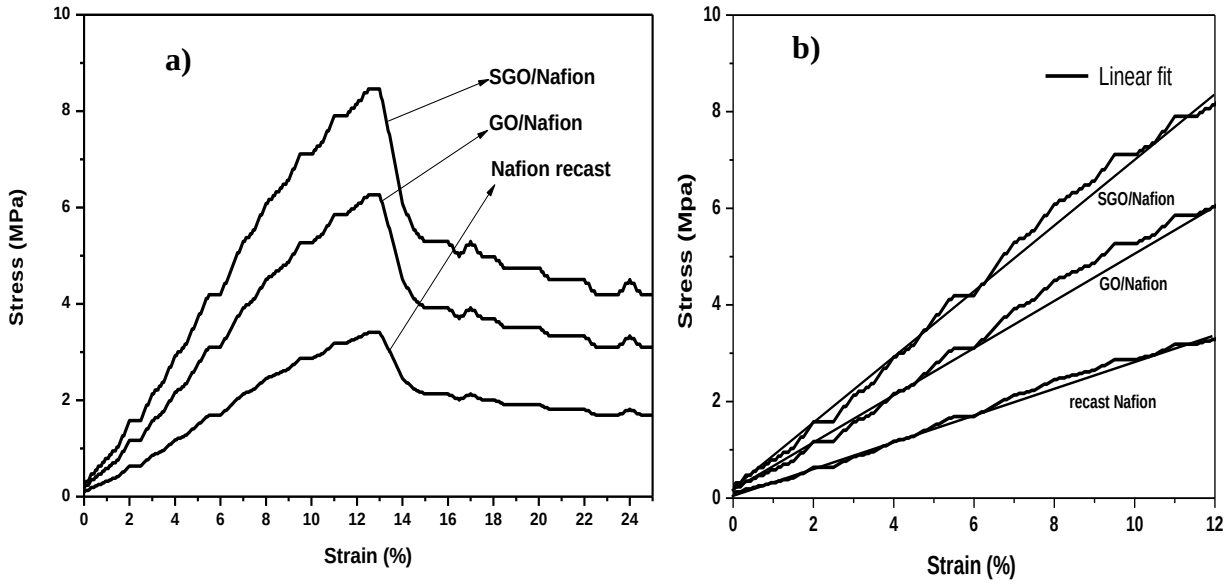

Figure 5.4, a) Stress vs. Strain curves of recast Nafion, GO (4 wt%) and SGO (4 wt%)/Nafion composite membrane and b) Young's modulus plots

The proton conductivity of PFSA based membranes depends on the hydration level and thus it is very important to measure the water uptake. In the case of Nafion® the ionic domains are interconnected by interfacial water, which is loosely bound to the membranes and play a vital role in proton conduction. Water uptake of recast Nafion, Nafion® 212, SGO/Nafion and various GO/Nafion composite membranes are shown in Table 5.1. Water uptake increases with increase in the GO content up to 4 wt%, and with a further increase of GO, no significant increase in water uptake of the membrane

occurred. The water uptake increased with increase GO content due to hydrophilic nature of GO, and after certain amount there was no further increase (and perhaps a slight decrease) in water uptake due to the amphiphilic nature of the Nafion® membrane. This behaviour is often attributed to the micellar nature of hydrophilic pools dispersed in the hydrophobic domain, which is disrupted in non-optimum concentrations of fillers. Similarly, the increased stiffness of the Nafion membrane resulted in reduced water uptake which was observed in 6 wt% of graphite oxide.

The average number of water molecule per sulfonic acid group or the degree of hydration (λ; loosely bound and free water) was measured using water uptake and IEC values.

$$\lambda = \text{Water uptake}/M_{w,\,H2O} \text{x IEC}$$

The GO and SGO/Nafion exhibited a λ value of 14.97 and 14.60, and these values are higher than that of recast Nafion. The composite membrane contains more weakly bound and free water, which could be attributed to higher concentration of sulfonic acid groups. The λ value of GO/Nafion is a little higher than SGO/Nafion, because GO is more hydrophilic than SGO. After sulfonation, some functional groups vanish, which could be attributed to differences in λ between the GO and SGO/Nafion composite membrane.

Table 5.1, Water uptake and IEC values of recast Nafion, Nafion® 112, GO and SGO/Nafion composite membranes

Membranes	Membrane Thickness(μm)	Water uptake	λ (nH_2O/-SO_3H)	IEC Values(meqg^{-1})
Nafion recast	50 ±2	21.2%	13.23	0.89
GO 2%/Nafion	50 ±3	27.9%	-	1.21
GO 4%/Nafion	50 ±3	37.2%	14.97	1.38
GO 6%/Nafion	50 ±3	36.1%	-	1.26
Nafion® 112	54 ±2	22.1%	-	0.86
SGO4%/Nafion	50 ±2	37.8%	14.60	1.43

5.2.2 Proton conductivity

The proton conductivity of GO and SGO paper was discussed in the previous chapter (chapter 4), and the SGO has a higher proton conductivity than GO. The effect of GO and SGO on the proton conductivity of Nafion membrane is evaluated and discussed in this section.

In order to maintain good hydration and corresponding proton conductivity of the composite membrane, the filler material should be optimised without affecting the parent polymer structure [17]. Figure 5.5a, shows temperature dependant ionic conductivity (in-plane) of GO/Nafion composite membrane with different GO content under fully humidified conditions (~100% RH). The GO (4 wt%) /Nafion membrane exhibited proton conductivities higher than that of the composite membranes with GO content of 2 and 6 wt%.

The proton conductivity passes through a maximum value at an optimum concentration of the incorporated species (GO and SGO) in composites of amphiphilic proton-conducting polymers like Nafion® is often attributed to the micellar nature of the hydrophilic pools dispersed in the hydrophobic domains, which is disrupted at non-optimum concentrations of the fillers [18]. By a similar argument, the increased stiffness of Nafion® membranes, which resulted in reduced water uptake, thereby adversely affected the proton conductivity. The SGO/Nafion composite membrane was made with 4 wt% of SGO (according to optimised content of GO). Figure 5.5b shows the proton conductivity of recast Nafion, Nafion® 112, GO (4 wt%) /Nafion and SGO (4 wt%) /Nafion composite membranes measured under fully humidified conditions. The composite membranes were found to exhibit proton conductivities higher than those of recast Nafion and Nafion® 112 membrane at all temperature employed in this study (30-80 ^{o}C). The SGO (4 wt%) /Nafion composite membrane had a conductivity of 0.16 S.cm^{-1} which was higher than that of GO/Nafion, recast Nafion and Nafion® 112 at 80 ^{o}C.

The proton conductivity of these Nafion composite membranes strictly on the hydration level, although operating the fuel cell at high temperature it is difficult to maintain 100% RH. Therefore the composite membranes are designed to operate at high temperature with low relative humidity. The proton conductivity data vs. relative humidity at 80 ^{o}C is shown in figure 5.5c. At 30% RH recast Nafion and Nafion® 112 had proton conductivity of 0.0045 and 0.0091 S.cm^{-1} respectively, whereas GO and SGO

composite membranes had conductivities of 0.032 and 0.036 S.cm^{-1} which are far superior than unmodified Nafion membranes. Figure 5.5d, shows the plots of proton conductivity vs. relative humidity at 120 ^{o}C, the GO and SGO/Nafion composite membranes had a significant proton conductivity of 0.026 and 0.029 S.cm^{-1} at 25% RH which was ~6 times greater than that of commercial Nafion® 112 (0.005 S.cm^{-1}). The improved proton conductivity of composite membranes is attributed to the content of GO and SGO (large amount of sulfonic acid content) nano filler that holds more water and consequently could facilitate proton transport. The proton conduction in solids (Grotthus-type mechanism) in which reorganization of hydrogen bonds plays a vital role in hydrated GO [19]. The presence of different acidic functional groups like carboxylic acid and hydroxyl groups could provide more facile hopping of protons, which in turn help to increase proton transport.

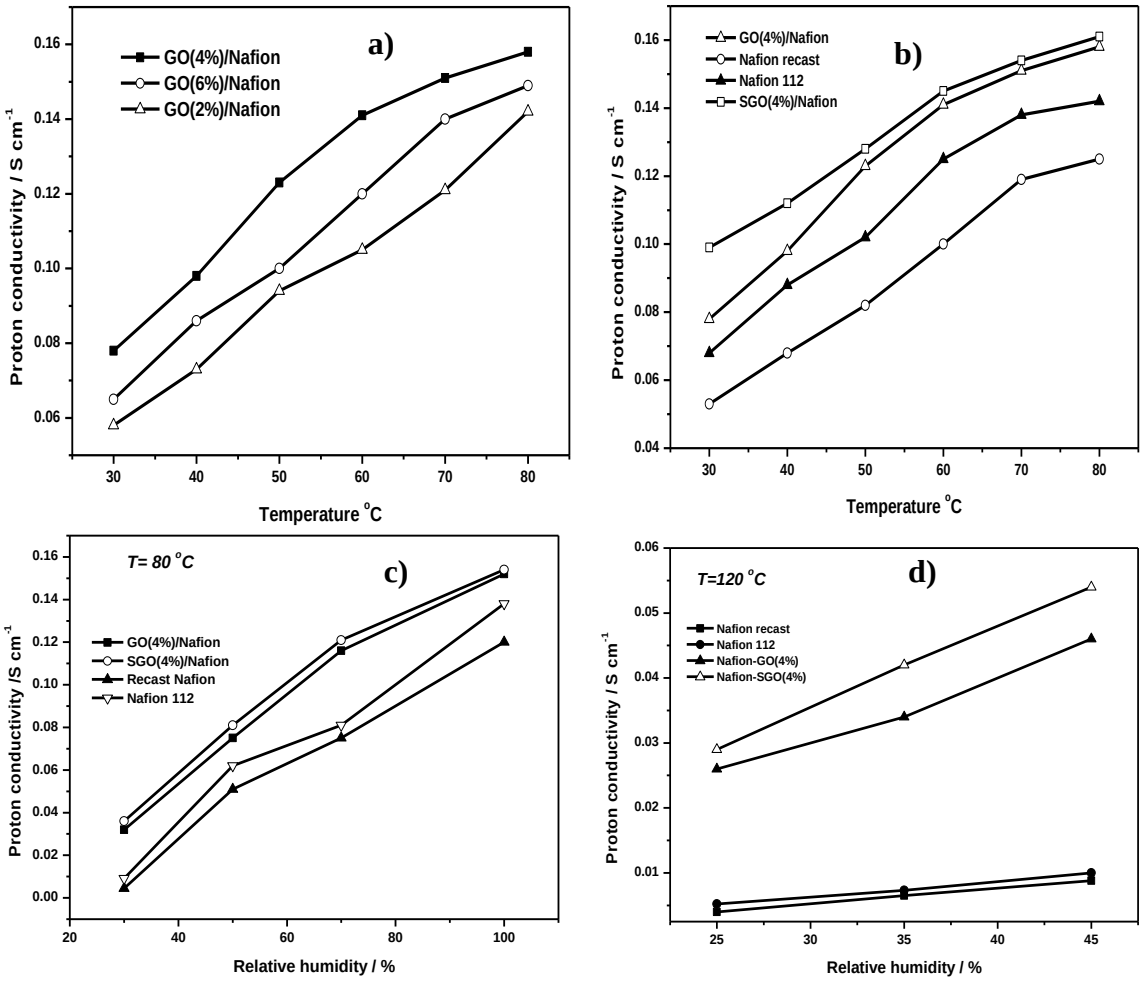

Figure 5.5, Temperature and RH dependent proton conductivity plots of recast Nafion, GO and SGO/Nafion and Nafion® 112 membranes

The IEC values are shown in Table 5.1; SGO and GO/Nafion composite membrane had higher IEC values of 1.43 and 1.38 meq g^{-1} compared to all other membranes. The activation energies (figure 5.6) calculated for the recast Nafion, Nafion® 112 and GO and SGO/Nafion composite membranes, are 14.2, 13.26, 12.98 and 11.2 kJ mol^{-1} respectively, which suggests that proton transport in the case of the composite membranes was more facile than that of recast Nafion and Nafion® 112 membranes.

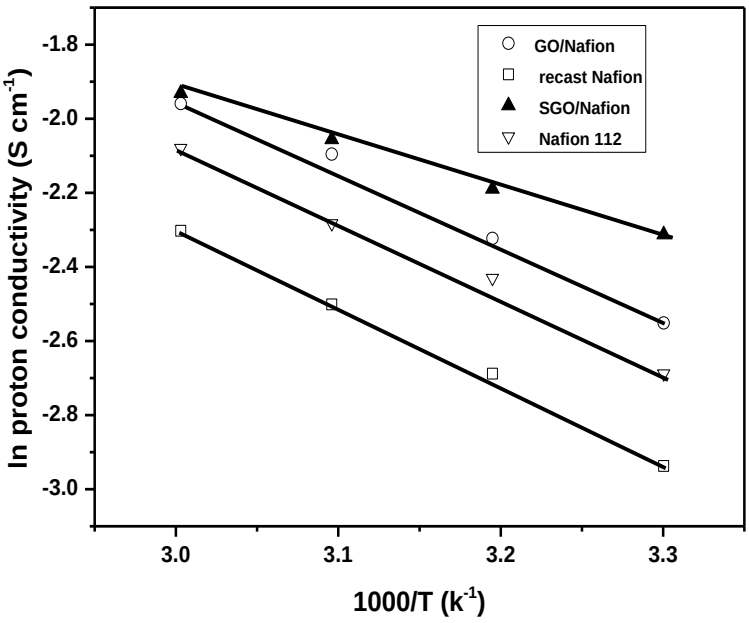

Figure 5.6, Arrhenius plot of recast Nafion, Nafion® 112, GO/Nafion and SGO/Nafion membranes

5.2.3 Fuel cell performance

The composite membranes fuel cell performance was evaluated for low and high temperature (60 and 120 ^{o}C) H_2/O_2 or air fuel cells. The polarisation (i-v curves) and power density curves were used to evaluate the composite membrane fuel cell performance. The LTPEMFCs were operated under fully humidified (100% RH) conditions, whereas HTPEMFCs were operated under low relative humidity (25% RH). The fuel cell performance of composite membranes was compared with recast Nafion membrane of approximately the same thickness.

Figure 5.7a, shows the single cell polarisation plots obtained with MEAs from recast Nafion, GO and SGO/Nafion composite membranes at 60 ^{o}C fed with H_2/O_2 at a flow rate of 0.2 and 0.5 standard litres per minute (slpm). The anode (20% Pt/C; 0.2 mg cm^{-2}) and cathode (20% Pt/C; 0.5 mg cm^{-2}) catalyst loading were constant for all the MEAs. The open circuit voltage (OCV) of the composite membrane was ~1.0 V, which indicates that membrane had reasonably low gas permeability and no significant electronic conductivity of GO or SGO which would otherwise adversely affect the OCV. It is seen from the figure 5.7a; at lower current density region (~0.1 A cm^{-2}) the composite membrane based MEAs showed about 40 mV lower activation polarisation potential compare to recast Nafion. The SGO/Nafion showed better electrode kinetics compared to GO/Nafion and recast Nafion. All the MEAs showed approximately 0.5 A cm^{-2} difference in the limiting current density and are in the order of SGO/Nafion > GO/Nafion > recast Nafion. The SGO/Nafion composite membrane showed enhanced fuel cell performance compared to that of GO/Nafion and recast Nafion membrane. Further, from the conductivity data, the SGO/Nafion composite membrane had a higher proton conductivity compare to GO/Nafion and recast Nafion and it was expected to give the greatest maximum power density, i.e. of 670 mW cm^{-2} cf. a value of 400 mW cm^{-2} for the recast Nafion and 570 mW cm^{-2} for GO/Nafion composite membrane at 60 ^{o}C.

Figure 5.7b displays the polarisation and power density curves derived from H_2/air fuel cell at 60 ^{o}C for the recast Nafion, GO and SGO/Nafion composite membrane based MEAs. The MEAs fed with air (1 slpm; ~21% of O_2) on cathode shows the OCP of ~1.0 V which was the same as that of O_2 fed MEAs. The GO and SGO/Nafion composite membrane based MEAs reached the limiting current density of 1.18 and 1.26 A cm^{-2}, whereas recast Nafion reached only 0.7 A cm^{-2}. The peak power density for

SGO/Nafion was 300 mW cm^2 which is higher than that of GO/Nafion (260 mW cm^{-2}) and recast Nafion (210 mW cm^{-2}). The air fed MEAs fuel cell performance was comparatively lower than that of O_2 fed MEAs due to lower concentration of O_2.

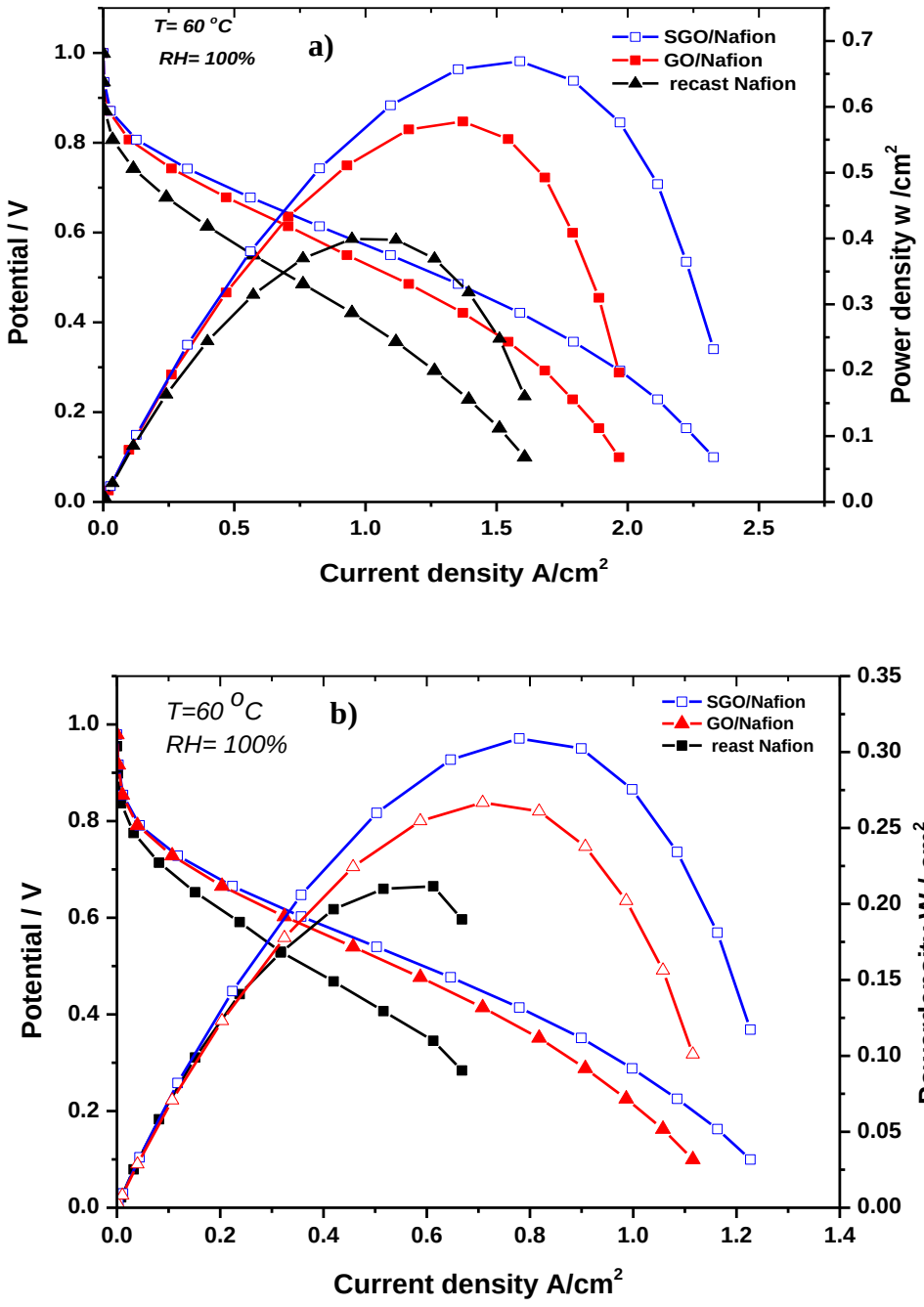

Figure 5.7, (a) Polarisation curves of H_2/O_2 (humidified) fuel cell at 60 ^oC (flow rate of 0.2 and 0.5 slpm) and (b) Polarisation curves of H_2/Air (humidified) fuel cell at 60 ^oC (flow rate of 0.2 and1slpm)

The internal cell conductivities estimated from the linear region of the polarisation curves obtained at 60 ^{o}C were 0.015, 0.018 and 0.035 S.cm^{-1} for the recast Nafion, GO/Nafion and SGO/Nafion composite membrane based MEAs respectively. These values are much lower than the membrane conductivities indicating significant voltage losses due to electrode polarisation and electrode layer resistances.

Figure 5.8, shows the single cell polarisation plots of recast Nafion and GO and SGO/Nafion composite membrane at 120 ^{o}C with 25% RH fed with H_2/O_2. The OCV of all the MEAs was more than 0.9 V. It is seen from the polarisation curves, the composite membrane based MEAs showed better electrode kinetics compared to recast Nafion. The GO and SGO/Nafion based MEAs showed 2 fold increase in the limiting current density compared to recast Nafion. The SGO/Nafion composite membrane showed better fuel cell performance compared to that of GO/Nafion and recast Nafion membrane at 120 ^{o}C with 25% RH. SGO/Nafion gave the maximum peak power density of 240 mW cm^{-2}. The GO/Nafion composite membrane gave a power density of 200 mW cm^{-2}, which was 2 times higher than that of recast Nafion (98 mW cm^{-2}), and little lower than SGO/Nafion composite membrane.

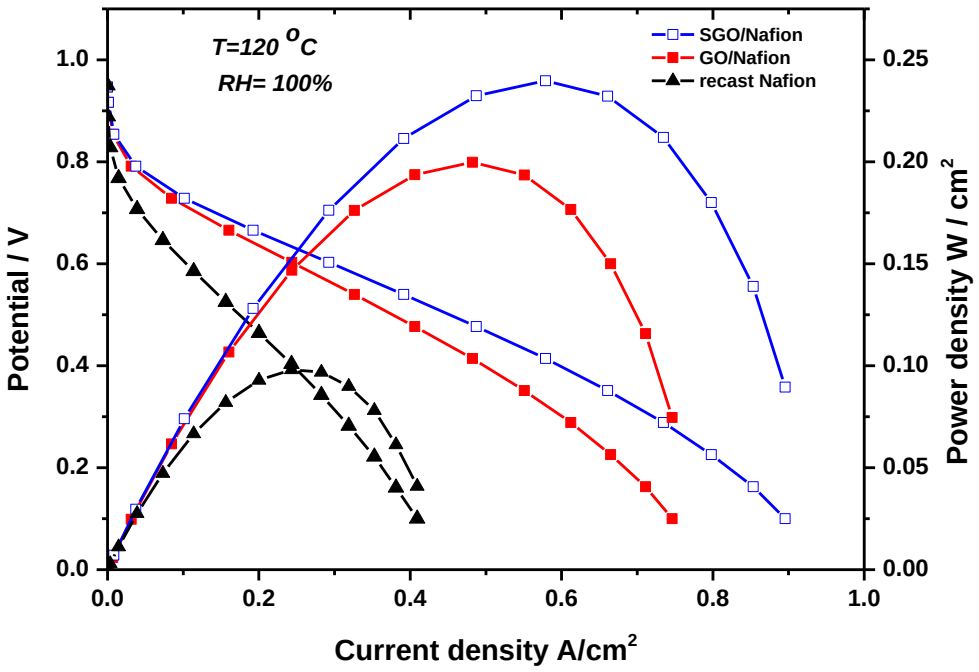

Figure 5.8, Polarisation curves of H_2/O_2 fuel cell at 120 ^{o}C and 25% RH fed with H_2/O_2 (flow rate of 0.2 and 0.5 slpm)

The comparison of fuel cell peak current and power densities obtained from all the MEAs are shown in Table 5.2a and 5.2b provides current and power densities at 0.6 V.

Table 5.2a, Fuel cell peak current and power densities

MEAs	I_{peak} (A cm^{-2})			W_{peak}(W cm^{-2})		
	60 °C H_2/O_2	60 °C H_2/Air	120°C H_2/O_2	60 °C H_2/O_2	60 °C H_2/Air	120°C H_2/O_2
recast Nafion	0.98	0.61	0 .24	0.4	0.21	0.098
GO/Nafion	1.37	0.70	0.48	0.57	0.26	0.2
SGO/Nafion	1.6	0.77	0.57	0.67	0 .30	0.24

Table 5.2b, Fuel cell current and power densities at 0.6 V

MEAs	I (A cm^{-2}) @ 0.6 V			W (W cm^{-2}) @ 0.6 V		
	60 °C H_2/O_2	60 °C H_2/Air	120°C H_2/O_2	60 °C H_2/O_2	60 °C H_2/Air	120°C H_2/O_2
recast Nafion	0.39	0.23	0.11	0.24	0.14	0.066
GO/Nafion	0.7	0.32	0.24	0.43	0.17	0.14
SGO/Nafion	0.82	0.35	0.29	0.5	0.2	0.17

Achieving the operating cell voltage (V) near to the equilibrium cell voltage (Ve) is the key challenge in electrochemical energy conversion systems. However, one cannot change the I_{max} for a given reaction; therefore fuel cell polarisation passes through a maximum current. This is because of resistances associated with in the cell components.

In order to consider the kinetics of fuel cell reactions involved in the composite membrane based MEAs, the iR free polarisation curves were constructed for all the fuel cell polarisation curves (figure 5.7 and 5.8) and analysed. Figure 5.9a, shows the iR free polarisation curves of recast Nafion, GO and SGO/Nafion composite membrane based MEAs at 60 ^{o}C for H_2/O_2 fuel cell. It is seen from the figure 5.9a, the iR free cell voltage is above 0.8 V for GO, SGO/Nafion based MEAs, and for recast Nafion 112 MEA is above 0.75 V, this is due to the difference in the membrane resistance (identical electrode compositions). Figure 5.9b shows the Tafel plots obtained from the iR free polarisation curves. The GO and SGO/Nafion composite membrane based MEA showed a Tafel slope of ~64 mV/dec and recast Nafion showed 62 mV/dec. These values are close to the literarature reported value (70 mV/dec). This indicates that the $2e^-$ transfer reactions occur at above 0.7 V.

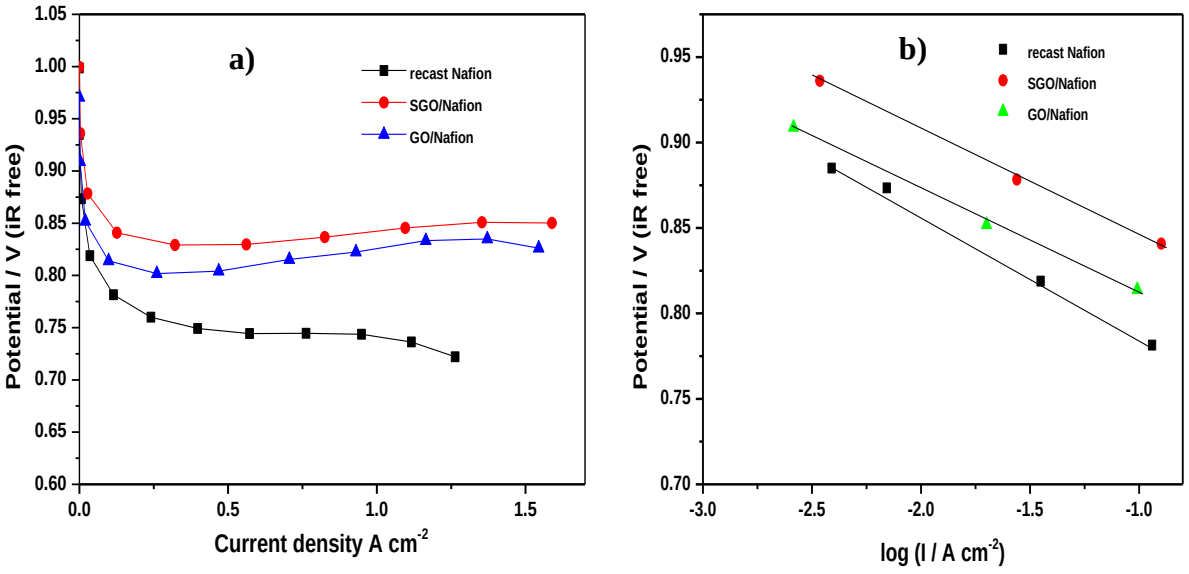

Figure 5.9, a) iR free polarisation curves of recast Nafion, GO and SGO/Nafion MEAs at 60 ^{o}C for H_2/O_2 fuel cell and b) Tafel plots obtained from iR free polarisation curves (figure 5.9a)

Figure 5.10a shows the iR free polarisation curves of recast Nafion, GO and SGO/Nafion composite membrane based MEAs at 60 ^{o}C for H_2/Air fuel cell. All the MEAs showed the iR free cell voltage above 0.7 V. The recast Nafion and GO/Nafion composite membrane showed a Tafel slope (figure 5.10b) of 72 mV/dec, where as SGO/Nafion showed 78 mV/dec. The Tafel slopes are closely related to the literature reported value (70 mV/dec).

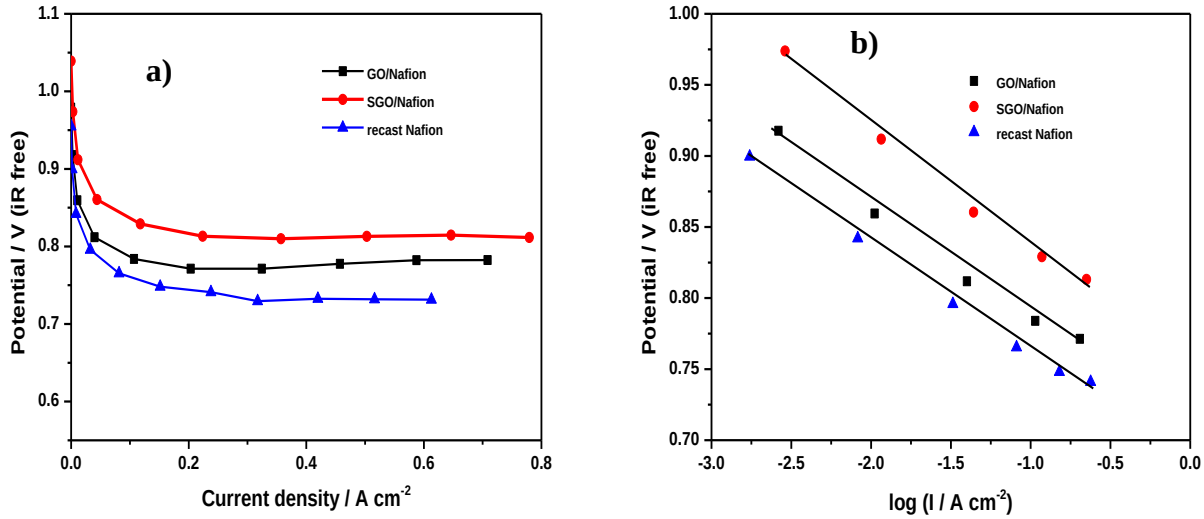

Figure 5.10, a) iR free polarisation curves of recast Nafion, GO and SGO/Nafion MEAs at 60 ^{o}C for H_2/Air fuel cell and b) Tafel plots obtained from iR free polarisation curves

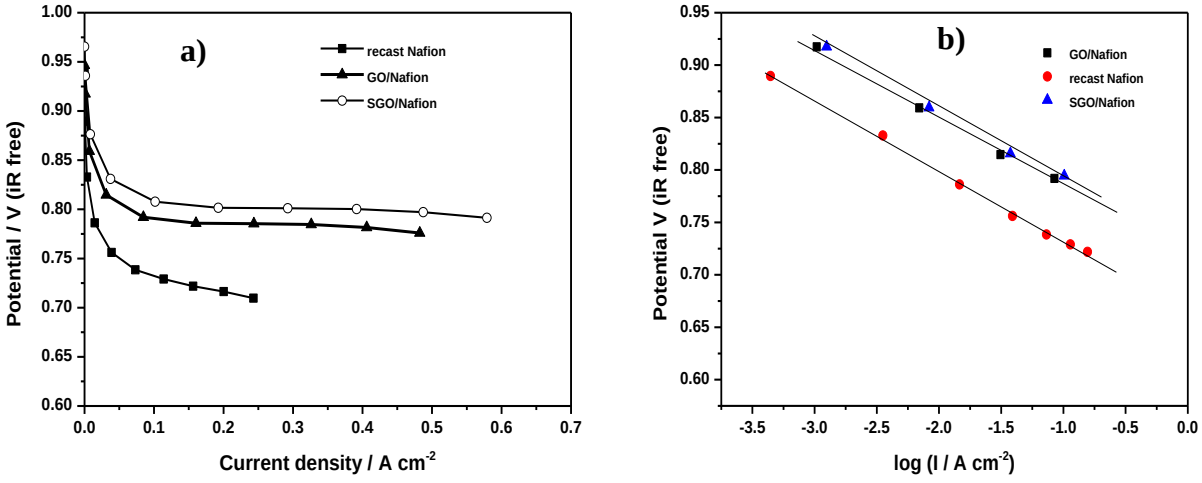

Figure 5.11, a) iR free polarisation curves of recast Nafion, GO and SGO/Nafion MEAs at 120 ^{o}C for H_2/O_2 fuel cell and b) Tafel plots obtained from iR free polarisation curves

Figure 5.11a shows the iR free polarisation curves at 120 ^{o}C for H_2/O_2 fuel cell. All the MEAs showed the iR free cell voltage above 0.7 V. The Tafel slope obtained for the GO and SGO/Nafion composite membranes (figure 5.11b) are 66 mV/dec, where as recast Nafion showed 68 mV/dec. The Tafel slopes are closely consistent with literature reported value.

The AC impedance was measured at 120 ^{o}C for GO and SGO/Nafion MEAs in a frequency range of 100 KHz to 1 KHz, in order to understand the interfacial behaviour and it was shown in figure 5.12. The impedance spectra were recorded at 0.8 V for both MEAs. The cell resistance (at high frequency) values were 1.26 Ω for SGO/Nafion and 1.67 Ω for GO/Nafion. The SGO/Nafion shows lower resistance compare to GO/Nafion this indicates proton transport is more facile in SGO/Nafion composite membrane than GO/Nafion membrane. The through-plane proton conductivity estimated using the resistances from the high frequency region impedance spectra for GO and SGO/Nafion were 0.0043 and 0.0057 S.cm^{-1} respectively. The through-plane conductivity calculated from the polarisation curves of GO and SGO/Nafion composite membranes were 0.0063 and 0.0072 S.cm^{-1} and these values are slightly higher than the conductivity values estimated from impedance spectra.

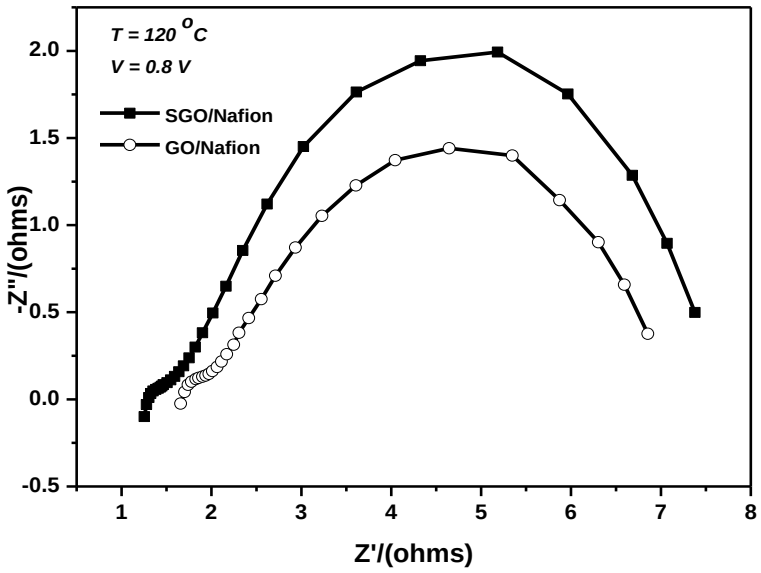

Figure 5.12, Nyquist plots of GO and SGO/Nafion MEAs at 120 ^{o}C and 25% relative humidity

Cyclic voltammetry (CV) were recorded for all the MEAs at 120 ^{o}C and data are shown in figure 5.13. The cathode was fed with N_2 gas (working electrode) and anode fed with H_2 (counter and reference electrode). The protons being generated, on the anode (H_2 oxidation) are transported through PEM to the cathode in order to complete the fuel cell reaction. But in this experiment the cathode is fed with N_2 and thus H_2 is liberated to measure the CV. The CVs of all the MEAs show hydrogen adsorption/desorption region between 0.05 - 0.34 V which is characteristic of Pt in an acidic electrolyte. The GO and SGO/Nafion composite membrane MEAs shows similar current densities (~40 mA cm^{-2}) for the hydrogen desorption region, which is higher than that of recast Nafion (~20 mA cm^{-2}). The hydrogen desorption current density is directly proportional to the concentration of H^+ transported through PEM from anode to the working electrode.

It is seen from the figure hydrogen desorption current density at 60 ^{o}C (figure 5.13a) is approximately twice the current density at 120 ^{o}C (figure 5.13b), this indicate that the rate of proton transfer is more at 60 ^{o}C compare to 120 ^{o}C and this is due to hydration level of membrane that provides the pathways for proton conduction. GO and SGO/Nafion composite membrane based MEAs gave a 2-fold increase in the hydrogen desorption current density at 120 ^{o}C compared with recast Nafion, which confirms the improved proton conductivity at elevated temperature.

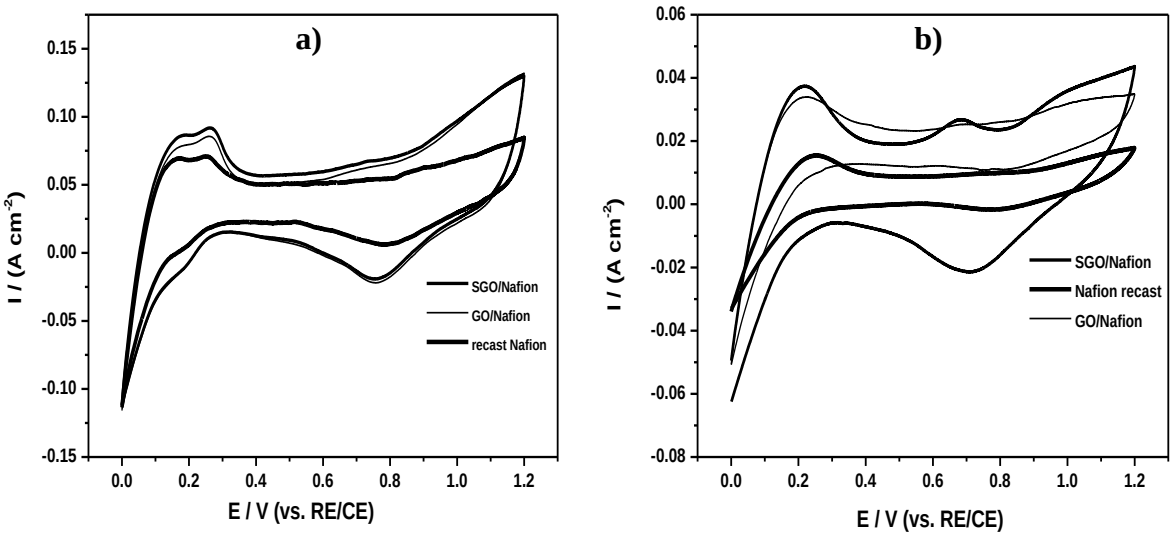

Figure 5.13, CVs of recast Nafion, GO and SGO/Nafion MEAs at 60 ^{o}C and b) 120 ^{o}C and 25% RH at scan rate of 50 mV s^{-1}

A durability test of the composite membrane MEAs were performed at a constant current density of 100 mA cm^{-2} for a period of 10 hours and the data is shown in figure

5.14. GO/Nafion composite membrane based MEA gave a constant potential of around 0.69 V after an hour. SGO/Nafion composite membrane shows about 12 mV increases in the operating potential approximately after 4 hours of operation. The MEAs delivered constant performance during the 10 hours of operation.

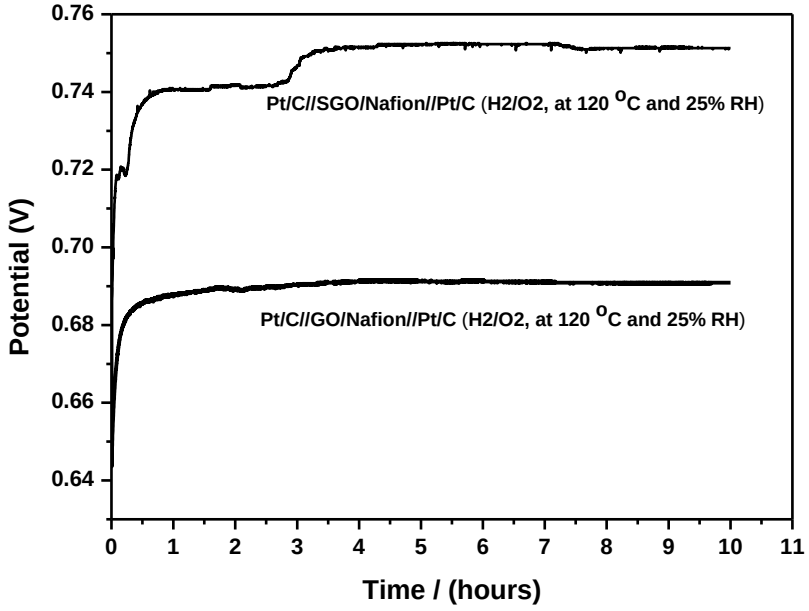

Figure 5.14, Durability of GO and SGO/Nafion MEAs at 120 ^{o}C and at constant current density of 100 mA cm^{-2}

5.2.4 Degradation studies of composite membranes

Durability is the major factor which determines the long term operation of fuel cells [20]. The fuel cell components are prone to undergo, degradation or deterioration under fuel cell operating conditions. Factors such as operating temperature, hydration level, fuel impurities and metal ions from end plates of the fuel cells. The PEM undergoes thermal, mechanical and chemical degradation [21, 22]. The thermo mechanical studies revealed that the composite membranes are more stable than the pristine Nafion membrane.

A Fenton test was employed for testing the PEM degradation by oxidative radicals, a Fenton solution of 3% H_2O_2 containing 4 ppm Fe_2^+ was added as $(NH_4)Fe(SO_4)_2.6H_2O$ for accelerating the effect to produce hydroxide radicals [23]. Membrane samples were immersed in the Fenton solution at 68 ^oC. The morphology of the membranes immersed in the Fenton solution was characterised by SEM. The SEM images of deteriorated recast Nafion membrane is shown in Figure 5.15. It is seen from the surface morphology (figure 5.15a) of recast Nafion; the bubbles were formed on the surface with pinholes and inset shows fresh surface. The cross section SEM image shows very clear pinholes (figure 5.15b).

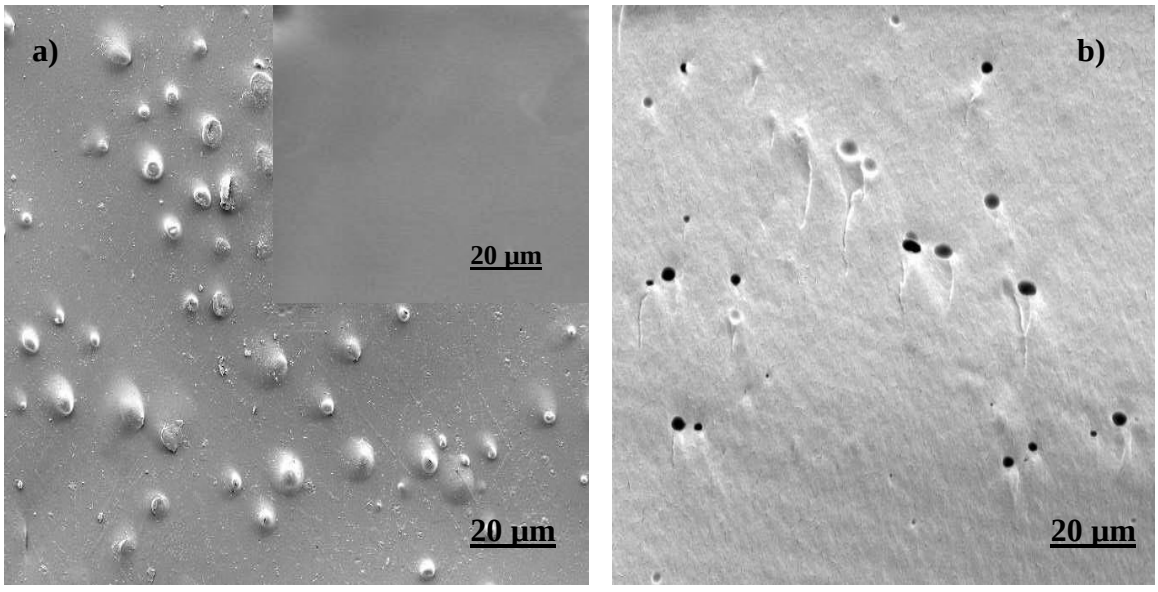

Figure 5.15, SEM images of deteriorated recast Nafion a) Surface image (inset is fresh surface) and b) cross sectional image

The SEM images of GO/Nafion membrane immersed in Fenton solution is shown in figure 5.16. It is seen from the fig 5.16a, that scratches appeared on the surface but not any bubbles or pinholes. A few tiny pinholes can be seen in the cross sectional image (figure 5.16b). This indicates the filler material (GO) in the Nafion polymer matrix inhibits the effect of H_2O_2. The SEM images of SGO/Nafion composite membrane treated with Fenton solution is shown in figure 5.16c and 5.16d. Surface morphology shows scratches on the surface (figure 5.16c) without any significant damage and the cross section shows no pinholes (figure 5.16d).

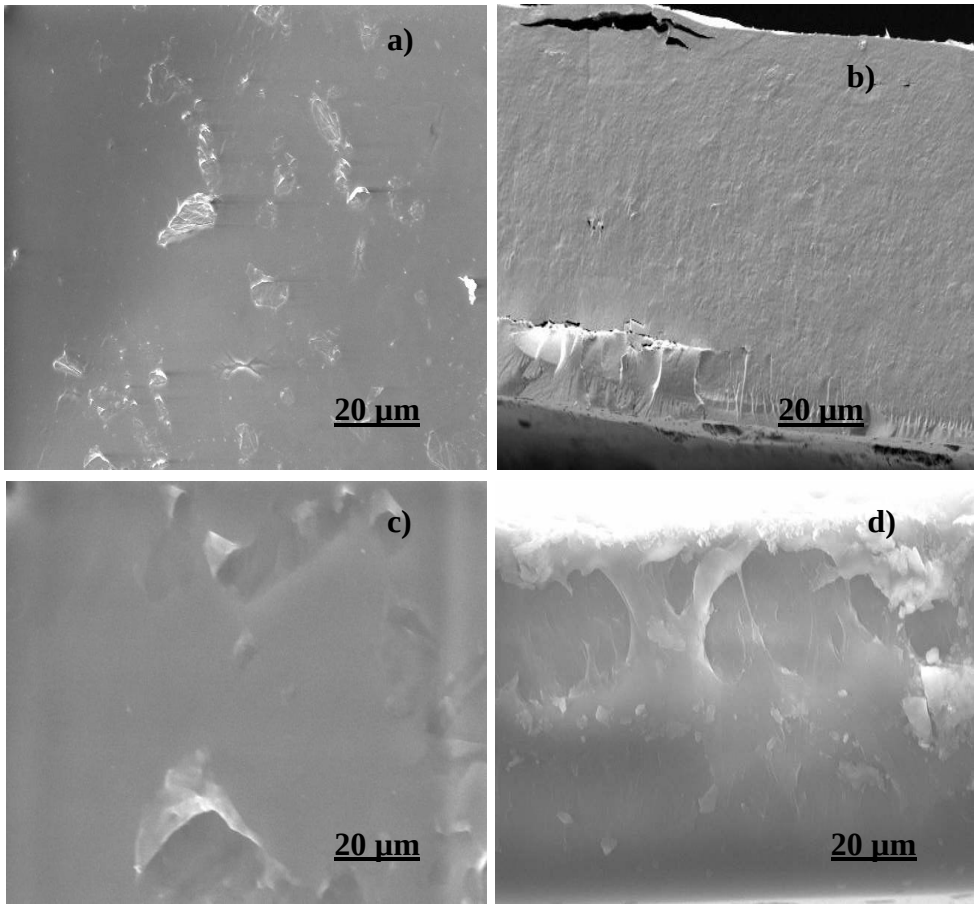

Figure 5.16, SEM images of deteriorated GO/Nafion composite membrane a) Surface image, b) cross sectional image and SEM images of deteriorated SGO/Nafion composite membrane c) surface image and b) cross sectional image

The polymer electrolyte membrane deterioration or degradation by H_2O_2 can be explained based on the radical attack on the functional groups. The chemical degradation of polymer is a consequence of free radicals, being generated on the electrode surface by reactant gas cross over. The free radicals such as peroxy ($^{\cdot}OH$) and hydro peroxy ($^{\cdot}OOH$) are active oxygenated species that attack the polymer and

chemically degrade the membrane [24]. Sulfonic acid and carboxylic end groups in the side chain are key to the mechanism by which radical species can attack the polymer (SO_3H dominate the COOH) [25]. The effect of metal ion impurities (Fe^{2+}, Cu^{2+}) from corrosion of bipolar plates, end plates and also from water generates the free radicals by decomposing H_2O_2 which is formed at fuel cell cathode [26].

One of the important factors which affect the fuel cell performance is crossover i.e. permeation of reactant from one electrode to the other electrode through the PEM [27]. Although crossover of both fuel (hydrogen) and oxidant (oxygen or air) occurs, the oxidant crossover occurs at lower rate and thus most often fuel crossover is the property of interest. This concept provides a simple in situ technique used for diagnosing the PEMFCs.

The cathode was fed with N_2 gas (working electrode) and anode fed with H_2 (counter and reference electrode). The LSV was used to record the hydrogen oxidation current. The working electrode was scanned between 0.05 to 0.5 V vs. CE/RE at a scan rate of 5 mV s^{-1}.

The hydrogen crossover measured for the fresh and degraded membranes are shown in figure 5.17. The MEAs made from the fresh membrane showed lower limiting current densities for hydrogen crossover (figure 5.17a) less than 2 mA cm^{-2}. The degraded recast Nafion membrane (figure 5.17b) showed higher limiting current density of 5 mA cm^{-2}, which is considerably more than that of GO and SGO/Nafion membranes.

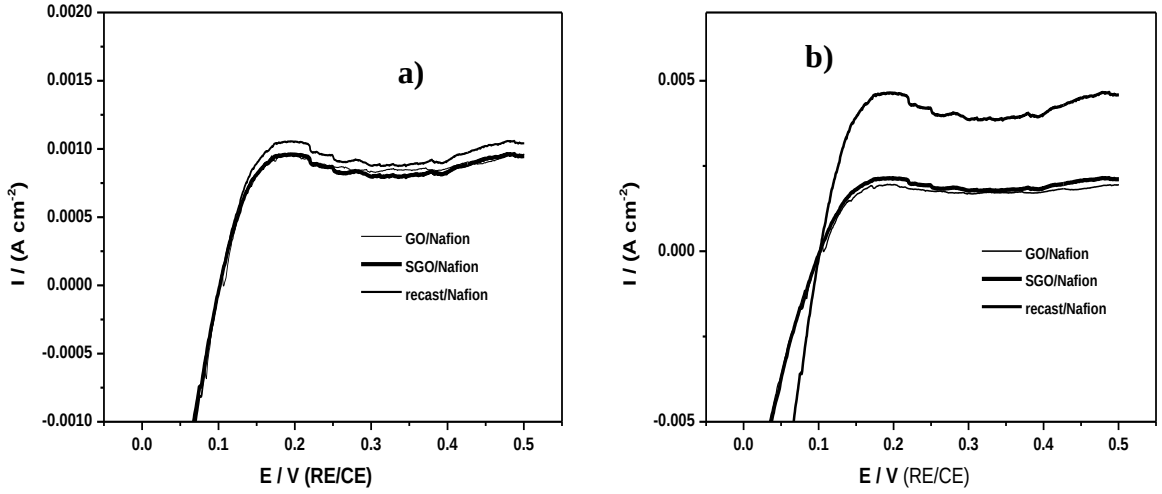

Figure 5.17, Hydrogen crossover measurements a) fresh membranes and b) degraded membranes at 30 ^oC and 100% relative humidity

The concentration of crossover hydrogen can be estimated using Faraday's law

$$J_{\text{crossover, H2}} = i_{\text{lim}}/n.\ F$$

Where i_{lim} is the limiting current density, n is the number of electrons and F is the Faraday constant (96500 C).

The mass transfer limited current density is proportional to the rate of hydrogen crossover from the anode to the cathode via the PEM. The hydrogen crossover flux for fresh membranes at 30 ^{o}C was approximately 6.2×10^{-9} mole cm^2 s for recast Nafion and 5.8×10^{-9} mole cm^2 s for SGO/Nafion. The degraded recast Nafion values were 2.3×10^{-8} mole cm^2 s in contrast, degraded GO and SGO/Nafion composite membrane values were 1.3×10^{-8} mole cm^2 s. These values are closely related to literature reported values, for fresh Nafion based membranes hydrogen crossover flux is around 5.7×10^{-9} and 2.9×10^{-8} mole cm^2 s for degraded membranes [27]. This shows that composite membrane had lower gas crossover compare to recast Nafion.

5.3 Conclusions

The effect of GO and SGO on the fundamental properties of Nafion membrane as well as the overall fuel cell performance has been systematically demonstrated. The increase in proton conductivity with temperature measurements revealed that GO or SGO did not affect the phase separated morphology or the proton conduction mechanism, which is also supported by thermogravimetric analysis. The high proton conductivity of GO and SGO/Nafion composite membranes was due to an increased water intake of GO and SGO/Nafion, and also the presence of different oxygen functionalities on GO, which markedly enhanced proton transport. Studies on mechanical stability revealed that using GO, is a good strategy to increase the mechanical stability without affecting its swelling properties. All the studies on fundamental properties indicated improvement in fuel cell performance, which was seen in a peak power density of 240 mW cm^{-2} for SGO/Nafion compared with that with recast Nafion; 94 mW cm^{-2}. The high temperature fuel cell performance of composite membrane shows better performance than those of recast Nafion. In addition the membrane degradation studies revealed that the GO and SGO/Nafion composite membranes are chemically more stable than recast Nafion. The presence of GO and SGO in the Nafion polymer matrix reduces the fuel crossover. The data indicate that SGO/Nafion composite membranes to be an alternative to current Nafion membranes in the fabrication of PEMFCs with improved efficiency.

References

[1] R. Kannan, M. Parthasarathy, S. U. Maraveedu, S. Kurungot, V. K. Pillai, *Domain Size Manipulation of Perflouorinated Polymer Electrolytes by Sulfonic Acid-Functionalized MWCNTs To Enhance Fuel Cell Performance*, Langmuir, **2009**, 25 (14), 8299–8305.

[2] J. Wu, X. Z. Yuan, J. J. Martin, H. Wang, J. Zhang, J. Shen, S. Wu, W. Merida, *A review of PEM fuel cell durability: Degradation mechanisms and mitigation strategies*, Journal of Power Sources, **2008**, 184, 104-119.

[3] C. Yang, S. Srinivasan, A.B. Bocarsly, S. Tulyani, J.B. Benziger, *A comparison of physical properties and fuel cell performance of Nafion and zirconium phosphate/Nafion composite membranes,* J. Membr. Sci. **2004**, 237, 145–161.

[4] C. Ma, L. Zhang, S. Mukerjee, D. Ofer, B.Nair, *An investigation of proton conduction in select PEM's and reaction layer interfaces-designed for elevated temperature operation,* J. Membr. Sci. **2003**, 219, 123–136.

[5] J. Yu, T.Matsuura, Y. Yoshikawa,M.N. Islam,M. Hori, *In Situ Analysis of Performance Degradation of a PEMFC under Nonsaturated Humidification,* Electrochem Solid-State Lett., **2005**, 8, A156–A158.

[6] Eiji Endoh, Shinji Terazono, Hardiyanto Widjaja , Yasuyuki Takimoto, *Degradation Study of MEA for PEMFCs under Low Humidity Conditions*, Electrochem Solid-State Lett., **2004**, 7, A209-A211.

[7] L. Gubler, S.A. Gürsel, G.G. Scherer, *Radiation Grafted Membranes for Polymer Electrolyte Fuel Cells,* Fuel Cells, **2005**, 5, 317–335.

[8] R.Kannan, Bhalchandr A. Kakade, V. K. Pillai, *Polymer Electrolyte Fuel Cells Using Nafion-Based Composite Membranes with Functionalized Carbon Nanotubes*, Angew.Chem. Int. Ed, **2008**, 47, 2653.

[9] V. Ramani, H.R. Kunz, J.M. Fenton, *Stabilized composite membranes and membrane electrode assemblies for elevated temperature/low relative humidity PEFC operation*, J. Power Sources, **2005**, 152, 182–188.

[10] Ronald K.A.M. Mallant, *PEMFC systems: the need for high temperature polymers as a consequence of PEMFC water and heat management,* Journal of Power Sources, **2003**, 118 424–429.

[11] Olivier Diat, Gerard Gebel, *Fuel cells: Proton channels*, Nature Materials, **2008**, **7**, 13 – 14.

[12] Haubold, H. G. Vad, T. Jungbluth, H. Hiller, *Nano structure of NAFION: a SAXS study*, Electrochimica Acta, **2001**, 46, 1559.

[13]Hadis Zarrin, Drew Higgins, Yu Jun, Zhongwei Chen, and Michael Fowler, *Functionalized Graphene Oxide Nanocomposite Membrane for Low Humidity and High Temperature Proton Exchange Membrane Fuel Cells*, J. Phys. Chem. C. **2011**, 115, 20774–20781.

[14] Mermoux, M. Chabre, Y. Rousseau, A. *FTIR and ^{13}C NMR study of graphite oxide*, Carbon, **1991**, 29, 469.

[15] Jung-Hwan Jung, Jin-Han Jeon, Vadahanambi Sridhar, Il-Kwon Oh, *Electro-active graphene–Nafion actuators*, Carbon, **2011**, 49, 1279 –1289.

[16] S. Ansari, A. Kelarkis, L. Estevez, E.P. Giannelis, *Oriented arrays of graphene in a polymer matrix by in situ reduction of graphite oxide nanosheets*, Small, **2010**, 6 (2), 205–209.

[17] Vito Di Noto, Rocco Gliubizzi, Enrico Negro, Giuseppe Pace, *Effect of SiO2 on Relaxation Phenomena and Mechanism of Ion Conductivity of [Nafion/(SiO2)x] Composite Membranes*, J. Phys. Chem. B, **2006**, 110, 24972-24986.

[18] K. T. Adjemian, R. Dominey, L. Krishnan, H. Ota, P. Majszrik, T. Zhang, J. Mann, B. Kirby, L. Gatto, M. Velo-Simpson, K. Leahy, S. Srinivassan, J. B. Benziger, A. B. Bocarsly, *Function and Characterization of Metal Oxide−Nafion Composite Membranes for Elevated-Temperature H_2/O_2 PEM Fuel Cells*, Chem. Mater., **2006**, **18**, 2238.

[19] K.D. Kreur, *Proton Conductivity: Materials and Applications*, Chem. Mater., **1996**, 8 610.

[20] D.P. Wilkinson, J. St-Pierre, in: W. Vielstich, H.A. Gasteiger, A. Lamm (Eds.), *Handbook of Fuel Cells: Fundamentals, Technology and Applications*, vol. 3, John Wiley & Sons Ltd., **2003**, pp. 611–626.

[21] C.A. Wilkie, J.R. Thomsen, M.L. Mittleman, *Interaction of poly(methyl methacrylate) and nafions*, J. Appl. Polym. Sci. **1991**, 42, 901–909.

[22] J. Surowiec, R. Bogoczek, Studies on the thermal stability of the perfluorinated cation-exchange membrane Nafion-117, J. Therm. Anal., **1998**, 33, 1097–1102.

[23] H. J. H. Fenton, *Oxidation of tartaric acid in presence of iron* , J. Chem. Soc., Trans., **1894**, 65, 899-910.

[24] H.Wang, G.A. Capuano, *Behavior of Radiation-Grafted Polymer Membranes in H_2/O_2 Fuel Cells*, J. Electrochem. Soc., **1998**, 145, 780–784.

[25] D.E. Curtin, R.D. Lousenberg, T.J. Henry, P.C. Tangeman, M.E. Tisack, *Advanced materials for improved PEMFC performance and life*, J. Power Sources, **2004**, 131, 41–48.

[26] M. Inaba, T. Kinumoto, M. Kiriake, R. Umebayashi, A. Tasaka, Z. Ogumi, *Gas crossover and membrane degradation in polymer electrolyte fuel cells,* Electrochimica Acta, **2006**, 51, 5746–5753.

[27] X. Cheng, J. Zhang, Y. Tang, C. Song, J. Shen, D. Song, J. Zhang, *Hydrogen crossover in high-temperature PEM fuel cells*, J. Power Sources, **2007**, 167, 25–31.

Chapter 6. Sulfonated graphite oxide-Sulfonated Poly ether-ether Ketone composite membranes for Polymer electrolyte fuel cell

This chapter described the physicochemical characterisation, proton conductivity studies and fuel cell characterisation of sulfonated poly ether-ether ketone (SPEEK) and SGO/SPEEK composite membrane.

6.1 Introduction

Polymer electrolyte membrane fuel cells (PEMFCs) are attractive as environmental friendly and high energy efficiency alternative energy sources for various applications [1, 2]. Proton exchange membrane (PEM) is a key component of membrane electrode assembly, which supports the catalyst layer and act as a barrier between anode and cathode. Perfluorosulfonic acid (PFSA) based membrane; particularly Nafion® has been a material of choice due to its excellent proton conductivity under fully humidified environment [3]. The non-fluorinated polymer can replace the high cost Nafion® membrane and these polymers include poly ether-ether ketone (PEEK), polybenzimidazole (PBI), and polysulfone (PSF) which have received significant attention to meet the operating requirement for the fuel cell application [4, 5]. The phosphoric acid doped PBI is widely investigated for HTPEMFCs, however the acid leaching at higher temperature (>150 ^{o}C) can significantly affect the fuel cell performance [6]. The proton conductivities of PEEK and PSF polymers are lower than 0.001 S.cm^{-1} and are not suitable for the fuel cell operation and thus sulfonation of these polymers is used to enhance the proton conductivity [7].

Sulfonated poly ether-ether ketone (SPEEK) is an inexpensive polymer electrolyte and it possesses satisfactory mechanical properties, thermal properties and good chemical stability [8]. However, the proton conductivity of SPEEK membrane mainly depends on water content and limits the high temperature fuel cell operation. Incorporation of nanosized inorganic filler materials into polymer matrix can influence properties of the parent polymer, such as proton conductivity, mechanical and thermal stability [9]. The influence of sulfonated graphite oxide (SGO) on SPEEK polymer composite has been investigated and compared with a SPEEK membrane.

6.2 Results and discussion

6.2.1 Physicochemical characterisation

The chemical interactions between the functional groups of SGO and SPEEK were examined by FT-IR spectroscopy and the data is shown in figure 6.1. SPEEK membrane showed a peak at 3399 cm^{-1} arising from the presence of –OH group (from $–SO_3H$). SGO/SPEEK showed a characteristic broad peak at 3391 cm^{-1} for intermolecular hydrogen bond. The intermolecular hydrogen bonding could be formed between –OH groups of SGO and SPEEK $–SO_3H$ groups as well as the $-SO_3H$ groups of SGO and carbonyl group of SPEEK. The peaks at 1020, 1080 and 1253 cm^{-1} were assigned to asymmetric and symmetric stretching vibrations of O=S=O group [10].

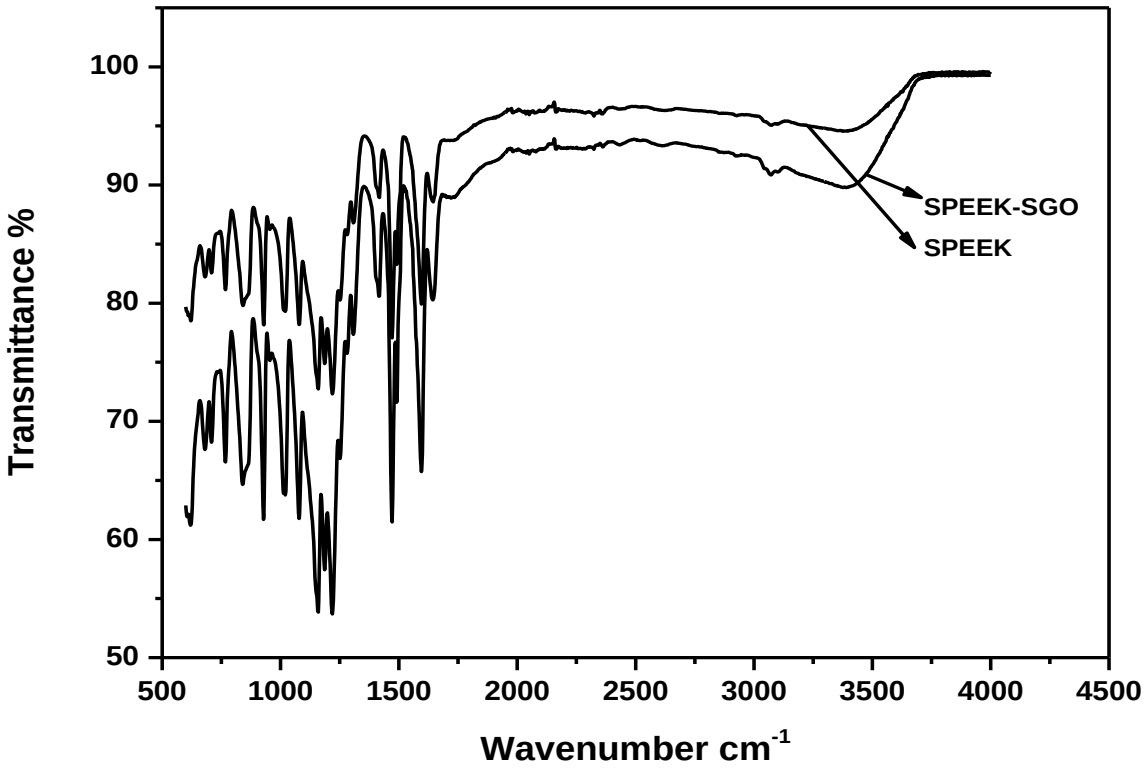

Figure 6.1, FTIR spectra of SPEEK and SGO/SPEEK composite membrane

The morphology of SPEEK and SGO/SPEEK composite membrane is shown in figure 6.2. The cross section SEM image of SPEEK (figure 6.2b) showed a smooth surface, whereas SGO/SPEEK (figure 6.2a) composite membrane showed a distribution of SGO in the SPEEK polymer matrix. The SGO nanosheets remained exfoliated and uniformly distributed over the polymer matrix.

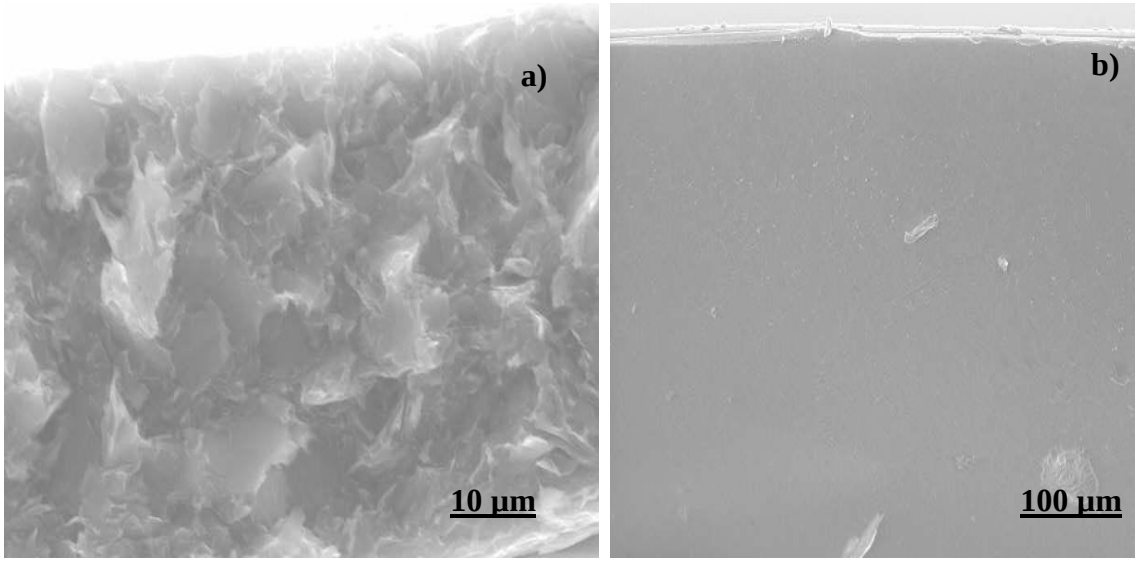

Figure 6.2, Cross section SEM images of a) SGO/SPEEK and b) SPEEK

Water uptake is one of the most important properties of sulfonic acid based polymer electrolyte to be considered for fuel cell application. The water content has a direct influence on the mechanism of proton conductivity and also on the mechanical stability of the polymer; therefore it is essential to have optimal water content in order to balance other properties. The composite membrane showed higher water content of 60% which is about ~2% more than that of neat SPEEK membrane (57.58%). The state of water (free and loosely bound water) can be estimated by λ (degree of hydration). The SGO/SPEEK composite membrane exhibited λ value of 14.49 (which is higher than Nafion based membranes) which is lower than that of SPEEK membrane (16.57). The lower λ value of SGO/SPEEK composite membrane could be attributed to the difference in ion exchange capacity. The ion exchange capacity estimated from classical titration is shown in figure 6.3, the SPEEK exhibits an IEC value of 1.93 meq g^{-1} whereas SGO/SPEEK composite showed 2.3 meq g^{-1}. Sulfonic acid groups and other oxygenated groups on GO markedly improves the water content and IEC of composite membranes. However, SGO/SPEEK composite membrane exhibited lower value of λ compare to SPEEK, due to its high IEC value which indirectly proportional to λ [11].

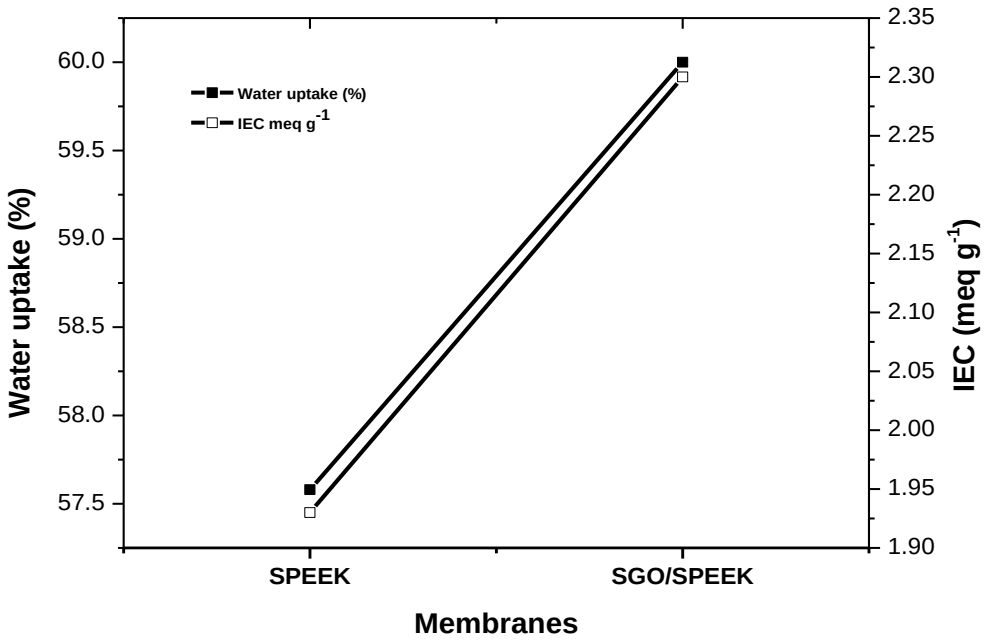

Figure 6.3, Water uptake and ion exchange capacity of SGO/SPEEK and SPEEK membrane

6.2.2 Proton conductivity

The fundamental property of polymer electrolyte membrane is the conduction of protons, and it is an important factor for operating fuel cells. The role of filler material in the polymer matrix is to maintain the desirable hydration level to operate at high temperature as these composite materials can hold more water tightly [12]. Figure 6.4a shows the temperature dependent proton conductivity of SPEEK and SGO/SPEEK composite membrane at 100% relative humidity. It is seen from the figure, as the temperature increases the proton conductivity of both membranes increases. The proton conductivity of SGO/SPEEK at 80 ^{o}C is about 0.23 S.cm^{-1}, greater than that of SPEEK (0.13 S.cm^{-1}). The proton conductivity values of these membranes are far superior than Nafion based membranes; this could be attributed to higher sulfonic acid concentration. It is evident from high water uptake and IEC values. Figure 6.4b, shows the proton conductivity measured at 80 ^{o}C with different relative humidity, the composite membrane showed significant improvement in conductivity compared to SPEEK. SGO/SPEEK had a conductivity of about 0.055 S.cm^{-1} at 30% RH which is higher than that of SPEEK membrane which is about 0.015 S.cm^{-1}. Furthermore the activation energies calculated for SGO/SPEEK and SPEEK from figure 6.4c are 22.21 and 25.02 kJ mol^{-1}. The lower activation energy of SGO/SPEEK supports the improved proton conductivity of SGO/SPEEK. The high surface area SGO interconnects the proton

conducting network between SGO and SPEEK. Introduction of functional groups to the graphene layer increases the inter planar distance and the presence of water in between graphene oxide layers, presumably forms hydrogen bonding (as shown in schematic; figure 6.4d) which creates the path for proton transport [13].

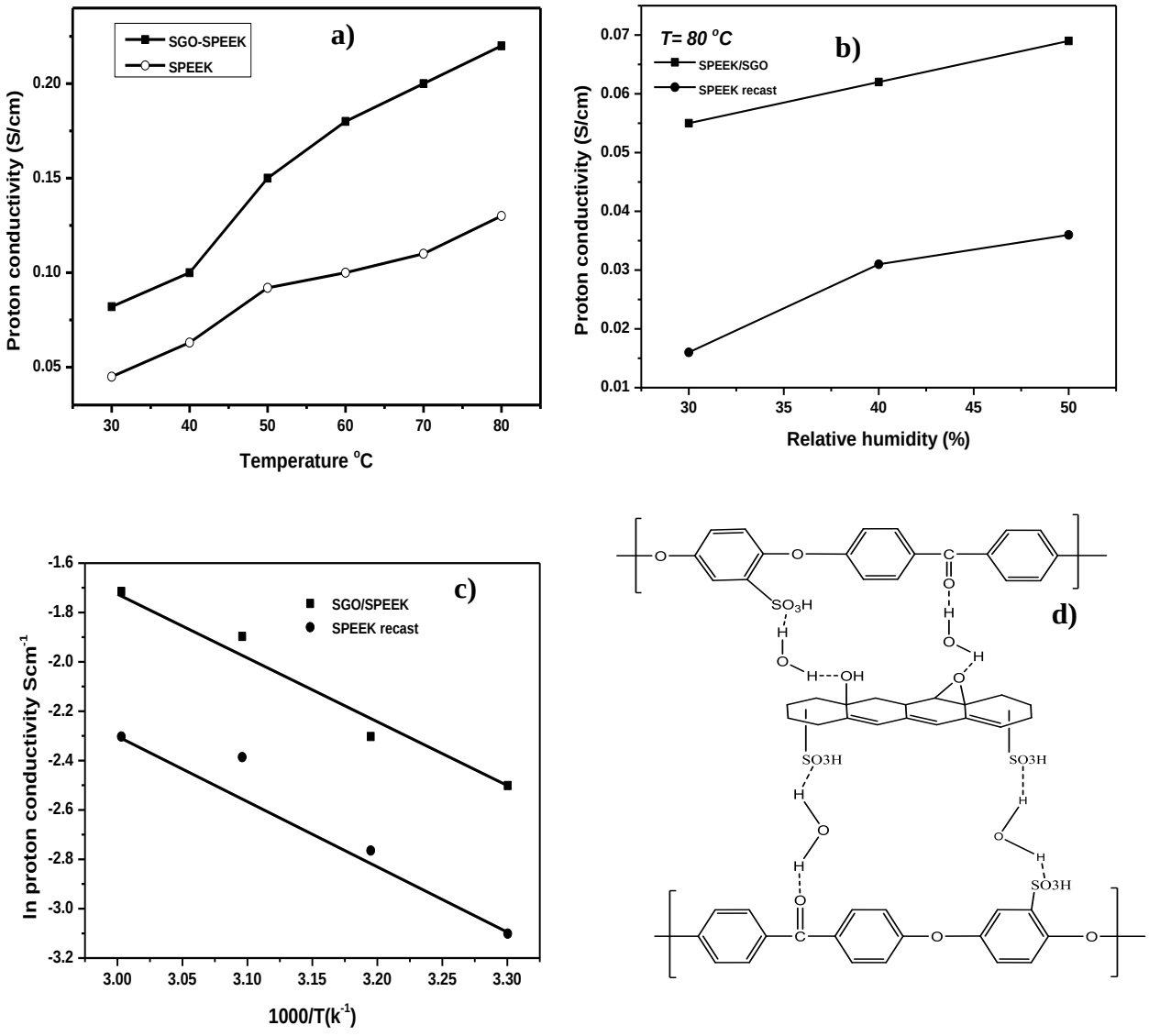

Figure 6.4, a) Proton conductivity at 100% RH, b) proton conductivity at 80 °C with different relative humidity and c) Arrhenius plots and d) typical representation of hydrogen bonding between SGO and SPEEK

6.2.3 Fuel cell performance

The composite membrane and SPEEK membrane were evaluated for low and high temperature fuel cells. The single cell polarisation data obtained with MEAs fabricated from SGO/SPEEK and SPEEK at 40 ^{o}C with 100% RH fed with humidified hydrogen and oxygen at a flow rate of 0.1 and 0.09 dm^3 min^{-1} is shown in figure 6.5. The open circuit voltage (OCV) of both MEAs is more than 0.95 V, indicates negligible gas crossover. The composite membrane showed improved fuel cell performance compare to SPEEK membrane based MEA. The SGO/SPEEK gave the maximum power density of 480 mW cm^{-2} at a current density of 1.28 A cm^{-2}, whereas SPEEK gave 350 mW cm^{-2} at 0.98 A cm^{-2}. It is seen from the figure that both the MEAs delivered approximately same current density, up to a 200 mA cm^{-2}. The SGO/SPEEK MEA showed improved performance as the current increases compared to SPEEK membrane based MEA. The performance improvement is attributed to the enhanced proton conductivity of composite membrane, as the electrode compositions of both the MEAs are identical. The internal cell conductivity estimated from the linear region of fuel cell polarisation curves of SPEEK and SGO/SPEEK MEAs were 0.011 and 0.0186 $S.cm^{-1}$. These conductivities are lower than the membrane conductivity alone and thus indicate that additional "Ohmic" voltage losses occur in the electrode layers.

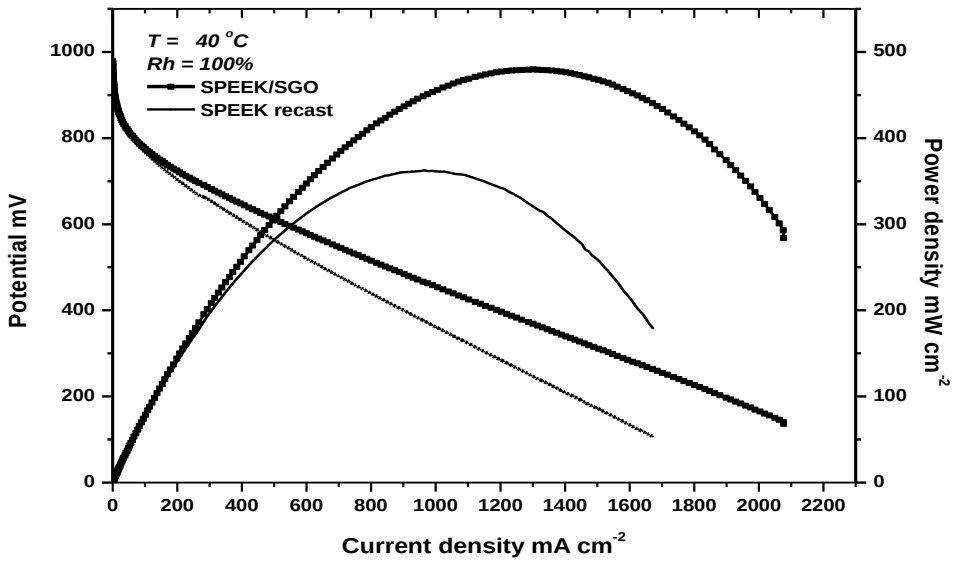

Figure 6.5, Single cell polarisation curves of SPEEK and SGO/SPEEK composite membrane at 40 ^{o}C with 100% relative humidity

Figure 6.6 shows the single cell polarisation curves of SGO/SPEEK and SPEEK MEAs at 80 ^{o}C with 30% RH. The OCP of both the MEAs are higher than 0.95 V. It is seen from the figure in the lower current density region (~300 mA cm^{-2}), the performance of both the MEA were similar. The SPEEK MEA shows significant performance loss at around 500 mA cm^{-2} and gave a maximum power density of 254 mW cm^{-2}. The SGO/SPEEK composite membrane gave the maximum power density of 375 mW cm^{-2} at 1.1 A cm^{-2}. The proton conductivity of the SPEEK membrane depends on hydration level and evaporation of water at above 80 ^{o}C, and significantly affects fuel cell performance. The SGO present in the composite membrane enhances the water retention which improves the proton conductivity and thus enhances the fuel cell performances at high temperature with low relative humidity.

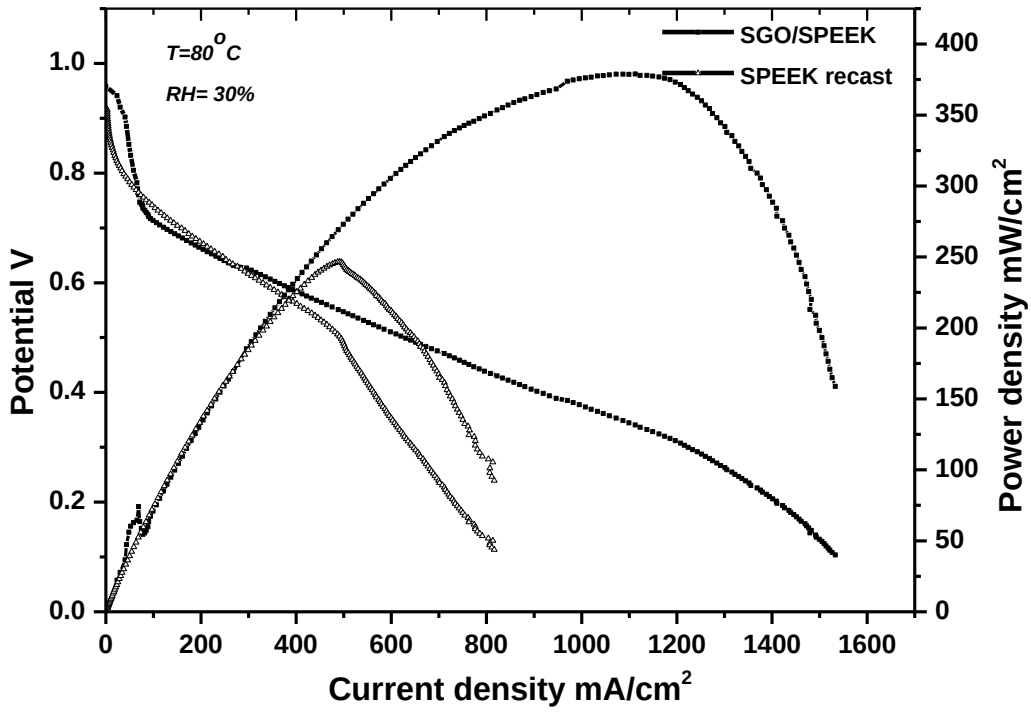

Figure 6.6, Single cell polarisation curves of SPEEK and SGO/SPEEK composite membrane at 80 ^{o}C with 30% relative humidity

The durability data of the SGO/SPEEK based MEA obtained at constant current of 100 mA cm^{-2} with 30% RH at 80 ^{o}C for 30 h is shown in figure 6.7. The data suggested that the MEA was stable in the above operating conditions and delivered constant performance. The cell potential at 100 mA cm^{-2} is approximately 0.69 V and which is comparable to the operating cell potential as shown in the polarisation curve (figure 6.6) at 100 mA cm^{-2}.

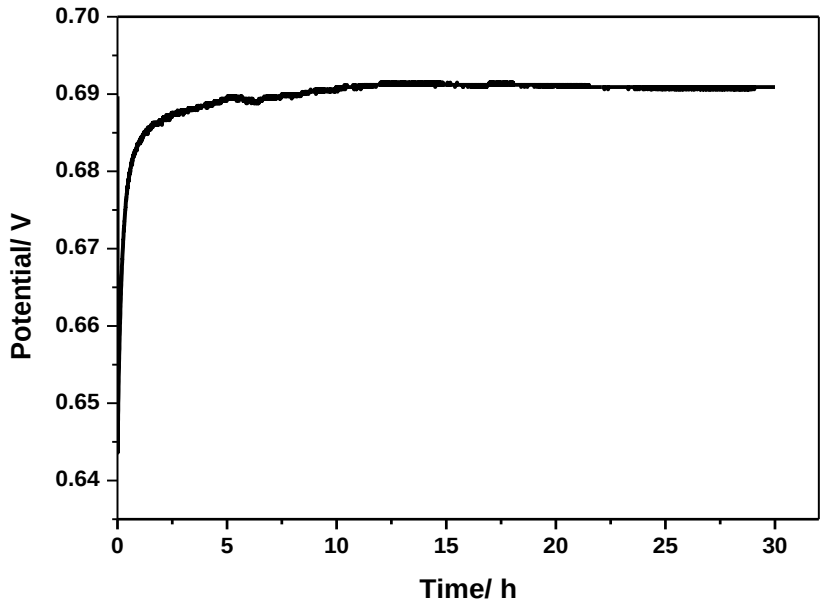

Figure 6.7, Durability test for SGO/SPEEK MEA.

The AC impedance measurements were performed for both the MEAs at 80 ^{o}C with 30% RH to understand the interfacial behaviour. The Nyquist plots of SGO/SPEEK and SPEEK based MEAs are shown in figure 6.8. The SGO/SPEEK composite membrane shows a lower resistance of 0.226 Ω at high frequency region compare to SPEEK based MEA which is about 0.285 Ω. The through-plane proton conductivity estimated using the resistances from the high frequency region impedance spectra for SPEEK and SGO/SPEEK were 0.023 and 0.032 $S.cm^{-1}$ respectively. The through-plane conductivity calculated from the polarisation curves (at 80 ^{o}C and 30% RH) of SPEEK and SGO/SPEEK composite membranes were 0.010 and 0.016 $S.cm^{-1}$ and these values are slightly lower than the conductivity values estimated from impedance spectra, this could be due to voltage losses occur in the electrode layers.

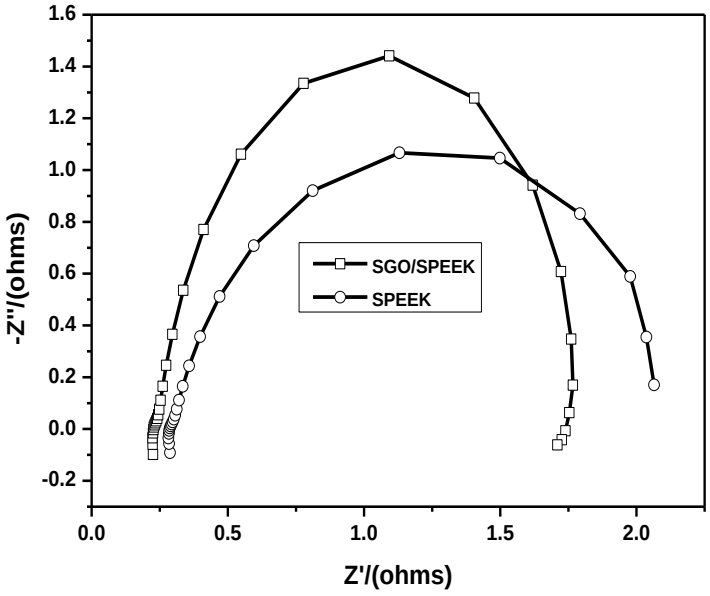

Figure 6.8, Nyquist plots of SPEEK and SPEEK/SGO MEA

6.3 Conclusions

SGO/SPEEK composite membrane was prepared and the effect of SGO on the properties of SPEEK such as proton conductivity and fuel cell performance has been studied. The composite membrane showed high proton conductivity at 100% RH and also at lower relative humidity (30%) which is evident from the IEC value. Sulfonic acid functionalized graphite oxide enhances the proton conductivity by bridging the proton transport channels between sulfonic acid groups on SPEEK.

References

[1] H. Zarrin, D. Higgins, Y. Jun, Z. W. Chen, M. Fowler. *Functionalized Graphene Oxide Nanocomposite Membrane for Low Humidity and High Temperature Proton Exchange Membrane Fuel Cells, J. Phys.Chem.* C, **2011**, 115, 20774–20781.

[2] A. Sacc`a, I. Gatto, A. Carbone, R. Pedicini, E. Passalacqua, *ZrO_2–Nafion composite membranes for polymer electrolyte fuel cells (PEFCs) at intermediate temperature,* J of Power Sources, **2006**, 163, 47-51.

[3] Ravi Kumar, Chenxi Xu, Keith Scott, *Graphite oxide/Nafion composite membranes for polymer electrolyte fuel cells,* RSC Advances, **2012**, 2, 8777–8782.

[4] Hong Wu, Xiaohui Shen, Tao Xu, Weiqiang Hou, Zhongyi Jiang, *Sulfonated poly (ether ether ketone)/amino-acid functionalized titania hybrid proton conductive membranes,* J of power sources, **2012**, 213, 83-92.

[5] Hai-Son Dang, Dukjoon Kim, *Cross-linked poly (arylene ether ketone) electrolyte membranes with enhanced proton conduction for fuel cells*, Int J Hydrogen Energy, **2012**, 37, 19007-19016.

[6] Mamlouk M, Scott K, Phosphoric acid-doped electrodes for a PBI polymer membrane fuel cell *International Journal of Energy Research,* **2011**, 35(6), 507-519.

[7] Lin Du, Xiaoming Yan, Gaohong He, Xuemei Wu, Zhengwen Hu, Yongdong Wang, *SPEEK proton exchange membranes modified with silica sulfuric acid nanoparticles,* Int J Hydrogen Energy, **2012,** 37, 11853-11861.

[8] Ravikumar, Scott K, *Free Standing Sulfonated Graphene Oxide Paper: New Polymer Electrolyte for Polymer Electrolyte Fuel Cells, Chemical Communications,* **2012**, **48**(45), 5584-5586.

[9] Xu CX, Cao YC, Kumar R, Wu X, Wang X, Scott K, *A polybenzimidazole/sulfonated graphite oxide composite membrane for high temperature polymer electrolyte membrane fuel cells, Journal of Materials Chemistry*, **2011**, **21**(30), 11359-11364.

[10] Deeksha Gupta, Veena Choudhary, *Sulfonated poly(ether ether ketone)/ethylene glycol/polyhedral oligosilsesquioxane hybrid membranes for fuel cell applications*, Int J Hydrogen Energy, **2012**, 37, 5979-5991.

[11] D. B. Spry, A. Goun, K. Glusac, David E. Moilanen, and M. D. Fayer, Proton Transport and the Water Environment in Nafion Fuel Cell Membranes and AOT Reverse Micelles, J. AM. CHEM. SOC. **2007**, 129, 8122-8130.

[12] Dmitriy A. Dikin, Sasha Stankovich, Eric J. Zimney, Richard D. Piner, Geoffrey H. B. Dommett, Guennadi Evmenenko, SonBinh T. Nguyen, Rodney S. Ruoff, *Preparation and characterisation of graphene oxide paper,* Nature, **2007**, 448, 457-460.

[13] Jun Liu, Yuhua Xue, and Liming Dai, *Sulfated Graphene Oxide as a Hole-Extraction Layer in High-Performance Polymer Solar Cell, J. Phys.Chem. Lett.* **2012**, 3, 1928-1933.

Chapter 7. Pt (Nafion® stabilised) and Pt-Co alloy nanoparticles supported on titanium nitride: an efficient and durable electrocatalysts for oxygen reduction reaction

This chapter described the detailed study on physicochemical characterisation of Nafion® stabilised Pt nanoparticles and Pt-Co alloy nanoparticles anchored on titanium nitride (TiN). The stability and durability of these electrocatalysts were evaluated using cyclic voltammetry in an N_2 saturated acidic electrolytes such as sulfuric acid and phosphoric acid. The accelerated degradation test (ADT) was performed to assess the durability of the electrocatalysts between the potential ranges of 0.6 to 1.2 V vs. RHE. The electrocatalysts were also tested for oxygen reduction reaction using rotating disc electrode by linear sweep voltammetry (LSV) in an O_2 saturated sulfuric and phosphoric acid. The mass and specific activities were calculated from ORR polarization curves at 0.9 V.

7.1 Introduction

The successful development of polymer electrolyte membrane fuel cell (PEMFC) technology is hindered by significant performance losses under extended operating conditions [1, 2]. Platinum (Pt) nanoparticles supported on carbon (Pt/C) remains the state-of-the-art cathode electrocatalyst in PEMFCs, despite its significant loss of electrocatalytic activity under long term operation, affecting the fuel cell performance [3]. Corrosion of carbon support results in the detachment of Pt particles leading to particle size growth by agglomeration, resulting in loss of active electrochemical surface area [4]. Carbon black (Vulcan XC-72) is the widely used support for anchoring active metal nanoparticles but carbon undergoes corrosion due to harsh operating conditions of fuel cells. Furthermore, Pt enhances carbon corrosion by reducing the oxidation potential, resulting in Pt sintering [5, 6]. A suitable support material should possess corrosion resistance properties to operate under fuel cell operating conditions [7]. In order to alleviate carbon support corrosion and to minimise Pt sintering and dissolution, an alternative support could be used to replace the carbon [8, 9]. In this regard, it is important to explore non carbon based materials, with corrosion resistance and good durability.

Considerable research efforts have been devoted to design corrosion resistant electrocatalyst support based on transition metal nitrides (TMNs) and carbides. In

general, transition metal nitrides exhibit more activity than transition metal carbides for oxygen reduction reaction (ORR) [10]. The physicochemical properties of TMNs are similar to those of TMCs. However, the difference in the number of valence electron between nitrogen and carbon, resulting in the change of geometric and electronic structure and is closely related with catalysis [11]. Of special interest, titanium nitride (TiN) shows more activity for ORR and stability than titanium carbide [12]. TiN shows the high corrosion resistance in electrochemical system. TiN on glass substrate had the corrosion onset potential of +0.6 V (vs. SSE) in 0.5 M H_2SO_4 electrolyte. This result indicates that TiN is stable up to +0.6 V (vs. SSE) without electrochemical redox reaction. And, TiN showed enhanced onset potential (~ +3 V vs. RHE) for corrosion than that of TiC (~+2 V vs. SHE) in 3 M $NaNO_3$ electrolyte carried out with a scan rate of 0.5 V s^{-1}. TiN is considered as a promising catalyst support for noble metal catalyst like platinum [13]. Owing to its unique properties like good electrical conductivity, outstanding corrosion resistance TiN can outperform the carbon support in stability and activity under fuel cell operating conditions. Pt supported on TiN nanoparticles catalytic activity has been evaluated and showed that Pt/TiN exhibits outstanding performance compared to conventional Pt/C by B. Avasarala et al [14].

In addition to the carbon support corrosion, electrochemical corrosion of platinum reduces the electrochemical active surface area, which affects the performance of PEMFC. Stabilising the platinum nanoparticles by employing the stabilising or capping agent hinders the sintering and dissolution of platinum nanoparticles. Nafion® could be used as a stabilising agent, as an active component (Nafion® as ionomer) in the catalysts layer and Nafion® can increase ionomer distribution in the catalyst layer which eventually improves the PEMFC performance by increasing catalyst utilisation [15].

In the case of phosphoric acid based fuel cells, strong adsorption of phosphate anion poisoning the Pt particles is detrimental to catalytic activity. Nafion® layer surrounding the Pt nanoparticles could prevent the poisoning of Pt from adsorption of phosphate anion [16]. Pt undergoes corrosion in phosphoric acid resulting in reduced activity; however the presence of Nafion® layer could protect the Pt from corrosion.

Alloying of Pt with 3d-transition metals (Fe, Co, Cr and Ni) enhance the electrocatalytic activity of PtM alloy due to the electronic coupling between Pt and M [17, 18]. Among these electrocatalyst, Pt-Co alloy systems have attracted attention because of their better ORR activity and stability in acidic environments [19]. The carbon support corrosion is

still the key challenge, in order to alleviate carbon corrosion, carbon is replaced with TiN.

7.2 Results and Discussion

7.2.1 Morphology and structural characterisation

The SEM image of TiN powder and the EDS pattern is shown in figure 7.1. Spherical particles of TiN with an average size of 3 µm are observed in figure 7.1a. The presence of Ti and N is further confirmed from the EDS pattern (figure 7.1b).

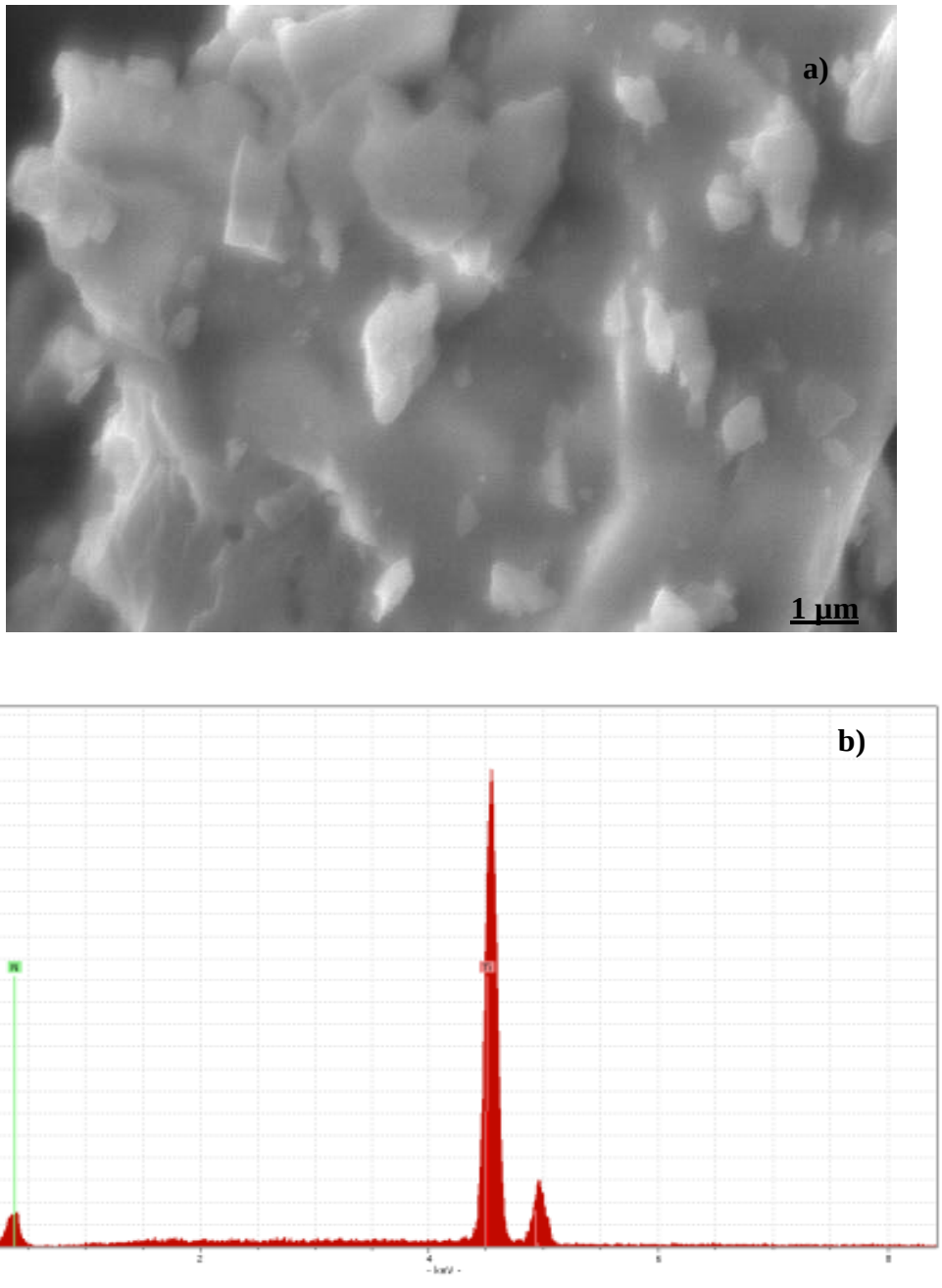

Figure 7.1, a) SEM image of TiN powder and b) EDS patter of TiN powder

The elemental analysis of TiN obtained from the EDS is shown in Table 7.1. The TiN contains 56.74 at. % of Ti and 43.26 at. % of N.

Table 7.1, Elemental analysis of TiN

Element	Wt%	At%
Titanium	81.76	56.74
Nitrogen	18.24	43.26

Figure 7.2a and 7.2b shows TEM images of Nafion® stabilised Pt nanoparticles. Nafion® stabilised Pt nanoparticles forms loosely agglomerated structures with Pt nanoparticles covered by the Nafion® layer, it is necessary to remove the excess Nafion® in order to have sufficient electronic conductivity of Pt particles. The Pt nanoparticles were washed with mixture of water and acetone (1:4 v/v) to remove the excess Nafion®. After removing the excess Nafion® (figure 7.2b), platinum nanoparticles forms loosely agglomerated chain like-structure. The particle size, calculated from more than 100 nanoparticles had a mean size of 4.5 nm.

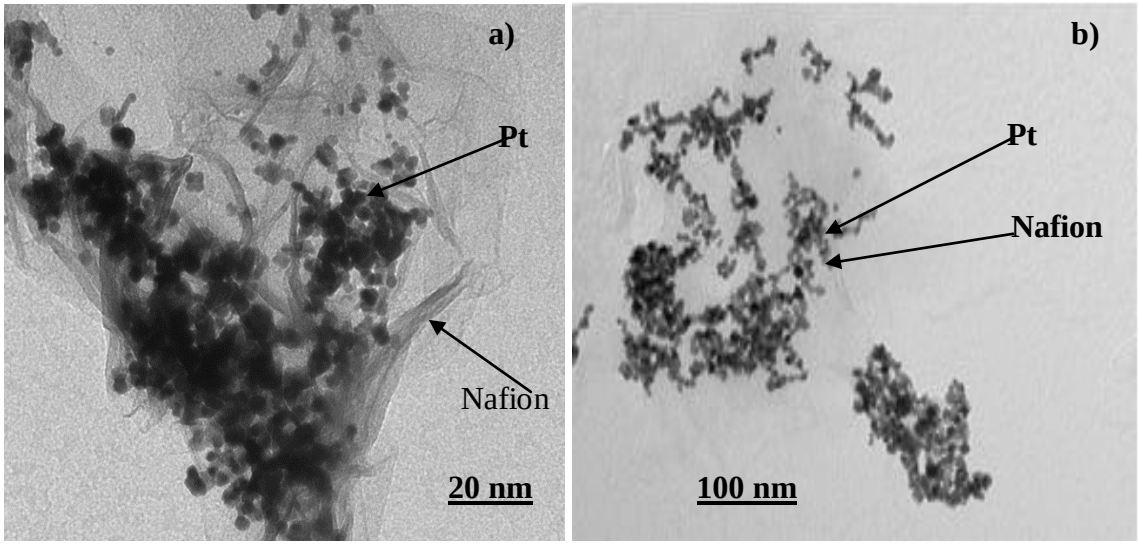

Figure 7.2, TEM images a) Nafion® stab Pt, b) Nafion® stab Pt (washed with acetone)

After removing the excess Nafion®, Pt nanoparticles were supported on TiN support by ultrasonicating the mixture of Nafion® stabilised Pt colloid and TiN powder for 1 hr. The SEM image of Nafion® stabilised Pt/TiN along with EDS pattern is shown in figure 7.3. Pt nanoparticles are agglomerated in the Nafion® polymer matrix and are distributed over the TiN surface (figure 7.3a). The elemental analysis of Pt/TiN obtained from the EDS is shown in Table 7.2. A Nafion® stabilised Pt/TiN contains ~23% of Pt (from EDS data).

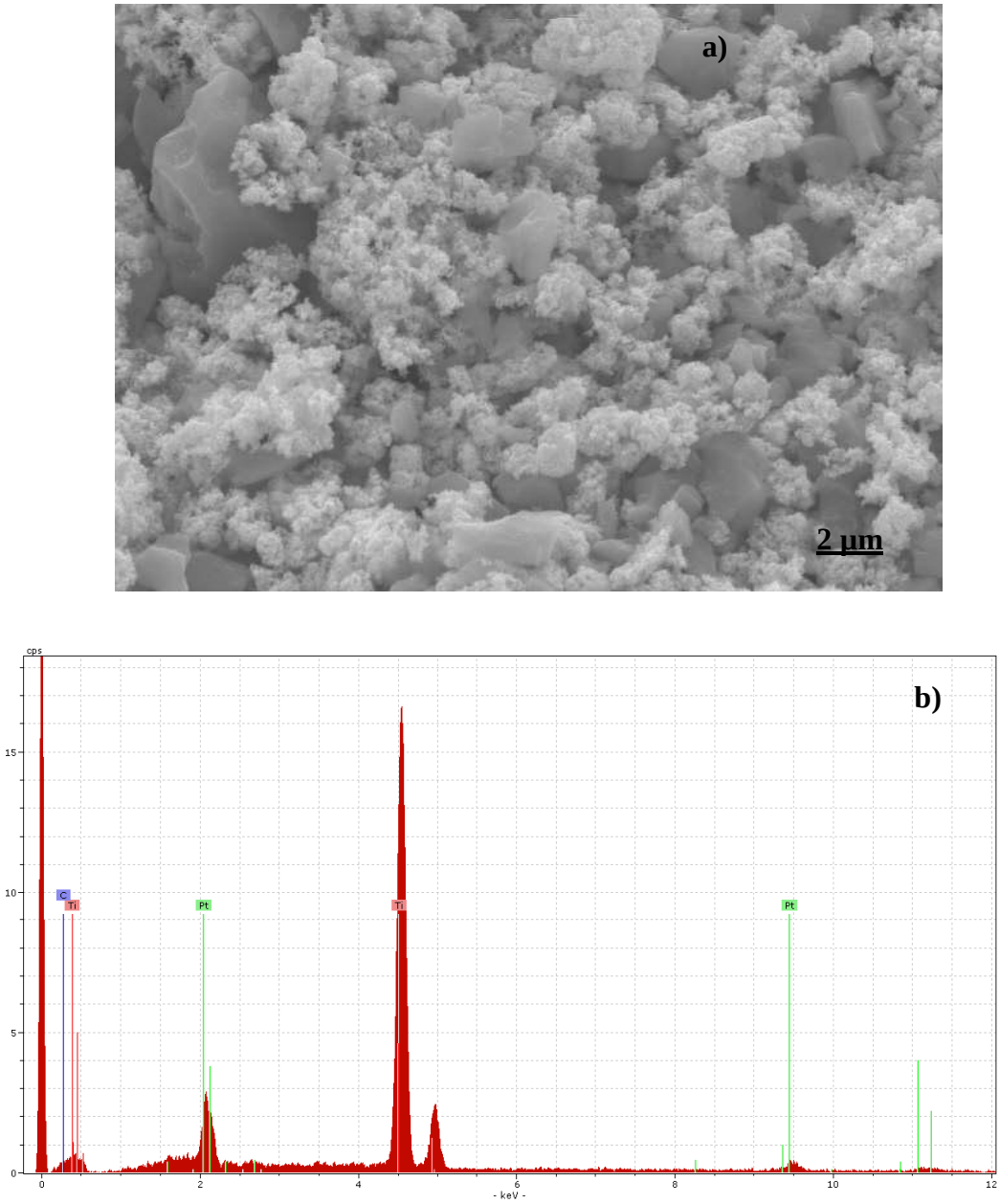

Figure 7.3, a) SEM image of Nafion® stabilised Pt/TiN, b) EDS pattern of Nafion® stabilised Pt/TiN

Table 7.2, Elemental analysis of Nafion® stabilised Pt/TiN

Element	Wt%	At%
Titanium	67.71	64.15
Nitrogen	9.43	30.53
Platinum	22.87	5.32

The TEM images of Nafion® stabilised Pt (Pt/TiN) and commercial Pt/C are shown in figure 7.4. Platinum nanoparticles are well dispersed on carbon support (figure 7.4a). In comparison Nafion® stabilised Pt particles forms loosely agglomerated structures over TiN surface (figure 7.4b). The particle size distribution, calculated from more than 100 nanoparticles, shows that the mean particle size is about 4.5 nm in diameter for Nafion® stabilised Pt/TiN as compared to Pt/C (2 to 3 nm), which is slightly smaller than the value calculated from XRD.

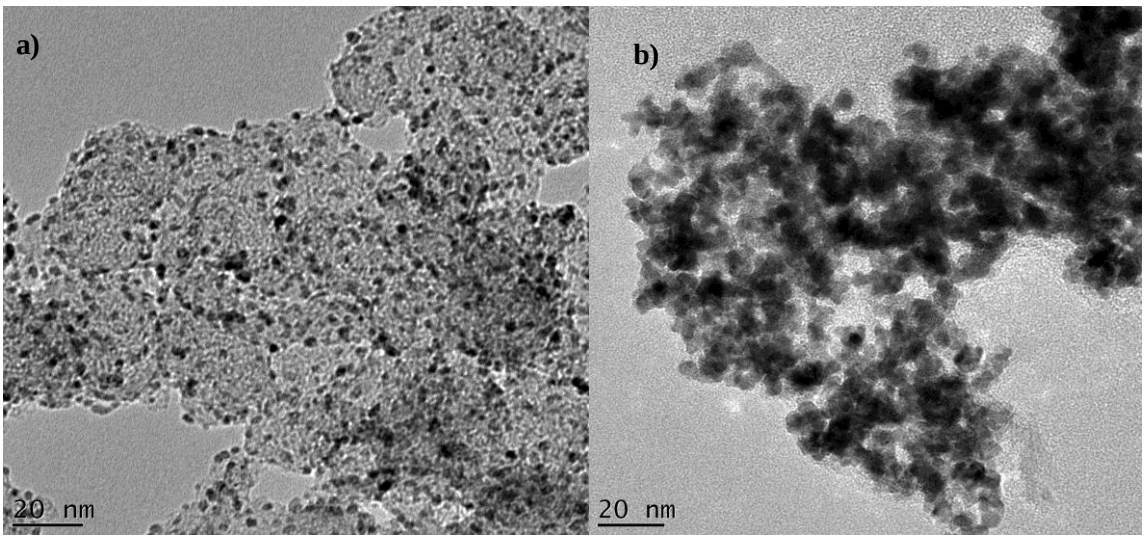

Figure 7.4, HRTEM images a) Pt/C and b) Nafion® stabilised Pt/TiN

Figure 7.5 shows XRD patterns of Nafion® stabilised Pt/TiN, which exhibits the sharp peaks for TiN. The lattice parameter of TiN 'a' is found to be 0.422 nm calculated from (111) diffraction plane of TiN (calculations are shown in Appendix A). Pt shows four diffraction peaks corresponding to the (111), (200), (220) and (311) planes which are consistent with a face centred cubic (FCC) structure. Diffraction peaks of platinum were relatively broader due to smaller particle size. The crystallite size calculated for Pt (111) from the Scherrer formula (calculation is shown in Appendix A) is about 6.5 nm which is slightly more than the particle size measured form TEM images because XRD gives volume-weighted measurements that tend to overestimate the geometric particle size.

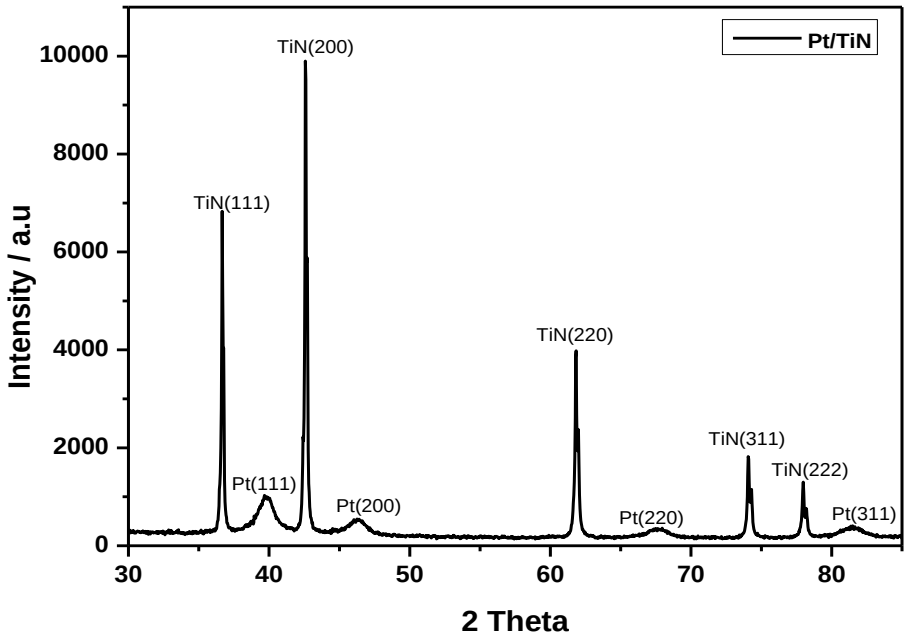

Figure 7.5, X-ray spectrum of Nafion® stabilised Pt/TiN

XPS analysis was performed to analyse the TiN powder, in order to understand the changes in surface and atomic concentration of element on the TiN support, before and after electrochemical oxidation. For XPS characterisation, samples of fresh TiN and TiN cycled (1000 cycles) between 0 and 1.2 V vs. RHE in an N_2 saturated 0.5 M H_2SO_4 at 100 mV s^{-1} were used. XPS survey spectra of untreated and treated TiN powder electrodes exhibited the characteristic Ti 2p, O 1s and N 1s peaks at 528.4, 456.4 and 396.2 eV, and these values are consistent with literature reported values [20, 21].

The presence of oxygen composition on the fresh TiN electrode is attributed to the native oxide/oxynitride layer on its surface [22]. The atomic concentration of elements on the TiN obtained from the survey spectra before and after electrochemical oxidation and is presented in Table 7.3. The atomic concentration of Ti is slightly increased from its initial values, and the atomic concentration of oxygen is decreased from 39.7% to 36.3%, the decrease in the atomic concentration of N can be attributed to the decrease in nitride composition due to its oxidation. The increase of Ti, with a decrease of O and N, suggests that the surface is not predominated by oxide layer after the electrochemical oxidation.

Table 7.3, Atomic concentration of elements on the TiN before and after electrochemical oxidation

Elements	Untreated (at. %)	Treated (at. %)
Ti	40.2	48.2
N	20.1	15.5
O	39.7	36.3

In order to understand the nature of surface groups formed on the TiN surface during the oxidation, the elemental peaks were further analysed. The deconvoluted Ti 2p peaks of untreated and treated TiN electrodes are shown in figure 7.6a and 7.6b. The Ti 2p spectra showed the spin orbit doublet Ti $2p_{3/2}$ and Ti $2p_{1/2}$ peaks. It is seen from the figure 7.6a, the presence of TiN, TiON and TiO_2 components of Ti $2p_{3/2}$ formed due to oxidation and their binding energies are shown in Table 7.4. In the case of treated TiN electrode, the binding energies of Ti $2p_{3/2}$ and $2p_{1/2}$ are shifted to a higher values (Table 7.4). The peaks observed at 459.9 and 464 eV (figure 7.6b) are assigned to tetravalent titanium ion, $Ti(OH)_2^{2+}$, where the Ti ion possibly oxidised to the states of higher valence during electrochemical oxidation.

Figure 7.6c and 7.6d shows the deconvoluted O 1s spectra for the untreated and treated TiN electrode. The peak at 530.2 eV, is assigned to TiO_2, but for the treated electrode (figure 7.6d) this value is shifted to 531.5 eV, which is due to the presence of O-H group. The remaining components on O 1s peaks are labelled in Table 7.4.

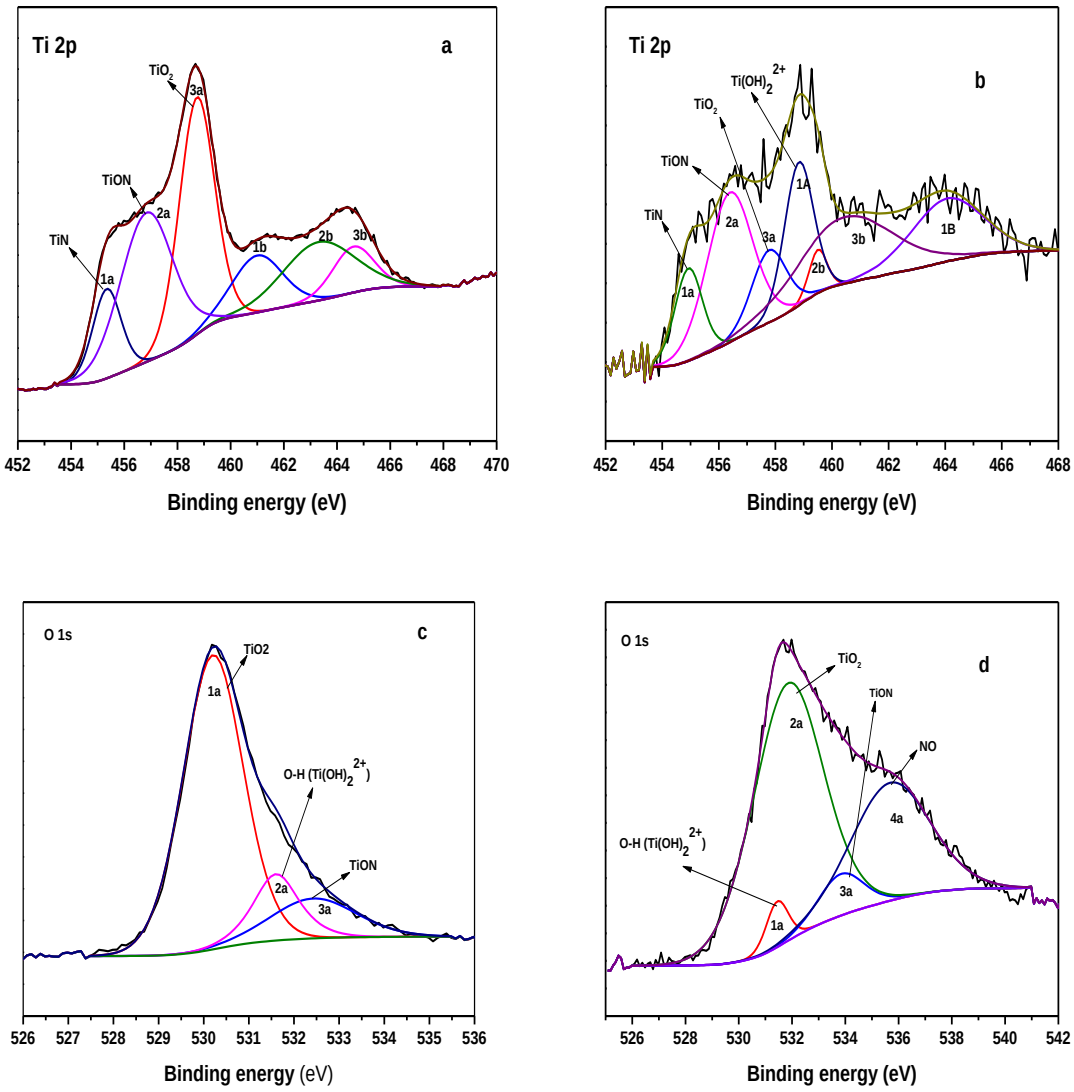

Figure 7.6, Deconvoluted spectra of Ti 2p a) untreated, b) treated TiN electrode and deconvoluted spectra of O 1s c) untreated and d) treated TiN electrode

Table 7.4, Assignments of the component peaks of high resolution XPS of untreated and treated TiN electrode

Peak	Component	Untreated Binding energy (eV)	Treated Binding energy (eV)	Assignment
Ti	1a	455.4	455.3	TiN
$2p_{3/2}$	2a	456.2	456.5	TiON
	3a	458.8	458.9	TiO_2
	1A	-	459.9	$Ti(OH)_2^{2+}$
Ti	1a	461.1	-	TiN
$2p_{1/2}$	2a	463.4	460.0	TiON
	3a	464.7	461.0	TiO_2
	1B	-	464.1	$OH(Ti(OH)_2^{2+})$
O 1s	1a	530.2	531.5	TiO_2
	2a	531.6	531.9	$OH(Ti(OH)_2^{2+})$
	3a	532.5	533.4	TiON
	4b	-	535.7	NO

7.2.2 Electrochemical oxidation behaviour of TiN and Carbon Black

The catalyst support plays a crucial role in the electrocatalytic activity and durability of fuel cell catalyst. A catalyst support should possess high surface area, good electronic conductivity and corrosion resistance. Carbon plays a significant role in the development of an efficient fuel cell catalyst (Pt/C); however it undergoes corrosion under fuel cell operating conditions and affects the electrocatalytic activity.

TiN is an alternative to carbon support, and its stability in acidic electrolytes was evaluated. Figure 7.7a and 7.7c shows the CV curves of TiN and figure 7.7b and 7.7d shows the CV curves of carbon black (CB) electrodes recorded before and after 1000 cycles in an N_2 saturated 0.5 M H_3PO_4 and H_2SO_4 at a scan rate of 100 mV s^{-1}. TiN shows significantly lower current densities than CB under same experimental conditions. TiN exhibits oxide or oxynitride layer on its surface, the presence of oxide or oxynitride creates a passivating surface on TiN resulting in lower oxidation current densities, whereas carbon shows higher oxidation current densities with increasing corrosion rate (as the cycle increases). Also the inert nature of TiN attribute to lower current densities.

The electrochemical oxidation of TiN results in the formation and growth of oxide/oxynitride films on the surface of TiN (in the potential region of 0.5 V to 0.8–0.9 V) by reaction (7.1) predominantly leads to the retardation (or passivation) of the oxidation processes.

$$TiN + 2H_2O \rightarrow TiO_2 + 1/2N_2 + 4H^+ + 4e^- \qquad (7.1)$$

It is seen from the figure 7.7a (0.5 M H_3PO_4) and 7.7c (0.5 M H_2SO_4), the oxidation of TiN in the potential region of 0.5 V to 0.9 V vs. RHE. Carbon exhibited oxidation peak at around 0.6 V vs. RHE which is due to the corrosion of carbon to carbon dioxide (figure 7.7b) (0.5 M H_3PO_4) and 7.7d (0.5 M H_2SO_4)). A drop in oxidation current density was observed in TiN (figure 7.7a and 7.7c) after 1000 cycles; this shows that TiN electrode attains a passivating surface unlike carbon (figure 7.7b and 7.7d), which continues to corrode.

The XRD results confirmed the presence of native oxynitride layer, this is attributed to the lattice parameter ‘a’, the value of ‘a’ for TiN is 0.424 nm; whereas for TiO is 0.418 nm. The value of ‘a’ calculated from XRD is 0.422 nm (calculations are shown in Appendix A); which lies in between the lattice parameter ‘a’ of TiO and TiN.

According to Vegard's Law (According to the law, unit cell parameters should vary linearly with composition for a continuous substitution solid solution in which atoms or ions that substitute for each other are randomly distributed) the lattice parameter 'a' of titanium oxynitride lies between lattice parameter 'a' of TiO and TiN [12].

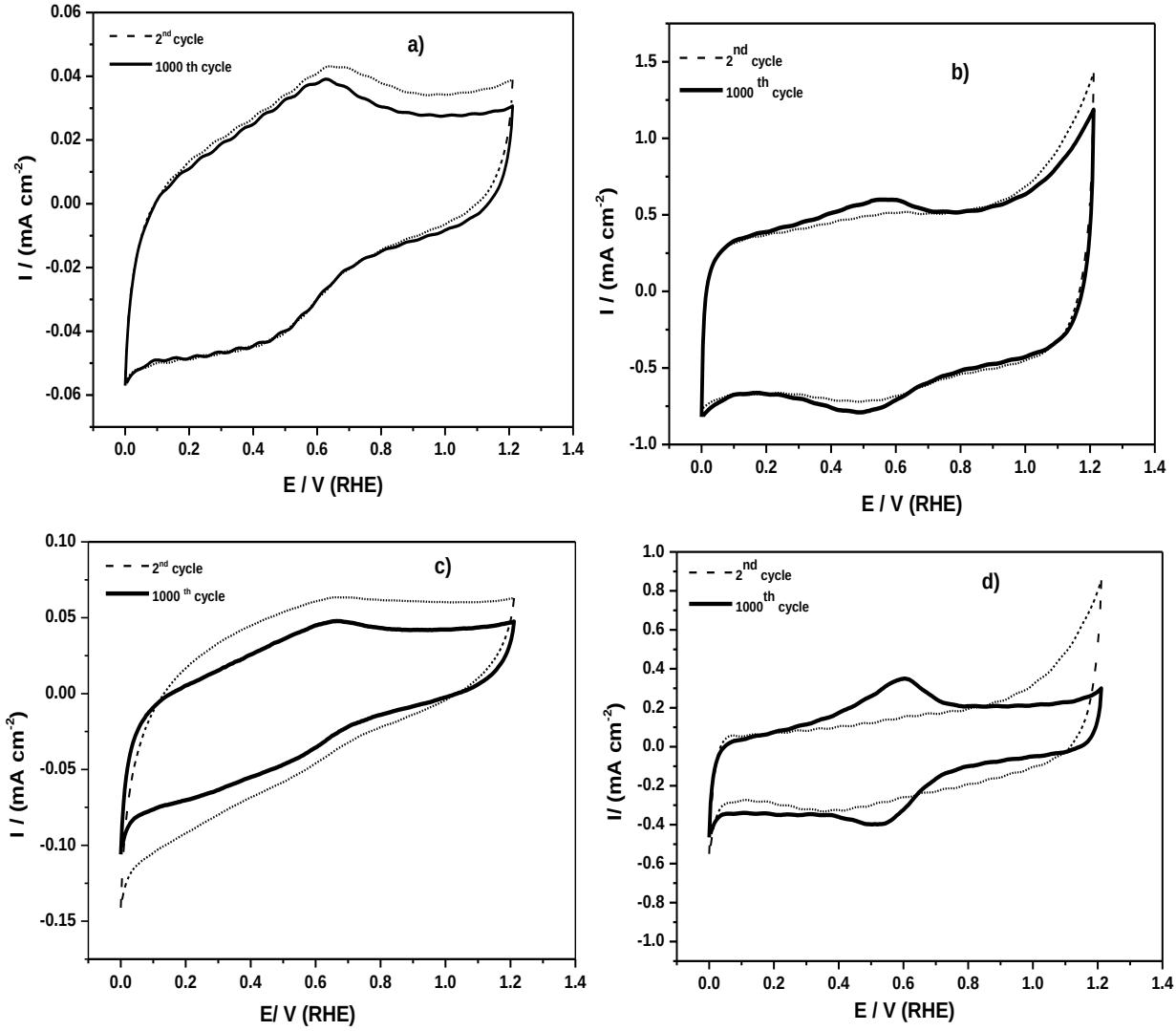

Figure 7.7, CVs recorded in an N_2 saturated 0.5 M H_3PO_4 at 100 mV s^{-1} a) TiN, b) carbon black. CVs recorded in an N_2 saturated 0.5 M H_2SO_4 at 100 mV s^{-1}, c) TiN and d) carbon black

7.2.3 Electrochemical characterisation

7.2.3.1 Electrochemical characterisation of Nafion® stabilised Pt/TiN in H_3PO_4

The Nafion® stabilised Pt/TiN was evaluated for its stability and durability in phosphoric acid and sulfuric acid medium. Figure 7.8a and 7.8b shows CV curves of Pt/C and Nafion® stabilised Pt/TiN before and after accelerated degradation test (ADT) in an N_2 saturated 0.5 M phosphoric acid medium. A Nafion® stabilised Pt/TiN shows similar peak intensity ($H_{ads/des}$) compared to Pt/C, in the hydrogen adsorption/desorption region (0.05 to 0.4 V). The electrochemical active surface area (ECSA) was estimated by using the equation (7.2) from the charge calculated under Hdes (μC cm^{-2}) region (0.05 to 0.4 V) and is shown in Table 7.5.

$$ECSA\ (m^2\ g^{-1}_{pt}) = Q_{Hdes*}100/210\ *L_{Pt} \qquad (7.2)$$

The ECSA estimated for Nafion® stabilised Pt/TiN is found to be 54.90 $m^2\ g^{-1}_{pt}$ and for Pt/C is 53.33 $m^2\ g^{-1}_{pt}$ (close to the literature reported value of 51.2 $m^2\ g^{-1}_{pt}$) with an equal amount of Pt loading (40 μg cm^{-2}) in the electrodes.

Table 7.5, ECSA obtained from CVs of Pt/C and Nafion® stabilised Pt/TiN (0.5 M H_3PO_4)

Catalyst	Pt loading (L_{Pt}) μg cm^{-2}	Q_{Hdes} (mC cm^{-2})		ECSA ($m^2\ g^{-1}_{Pt}$)	
		Before	**After**	**Before**	**After**
Pt/C	40	4.47	0.4	53.33	4.76
Nafion-stab Pt/TiN	40	4.61	1.27	54.90	15.23

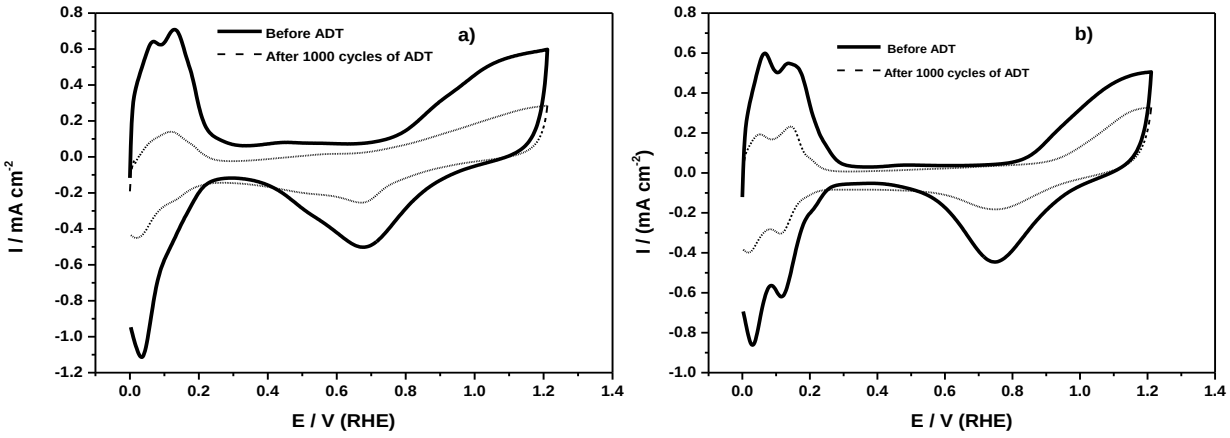

Figure 7.8, a) CVs of Pt/C and 4b) Nafion® stabilised Pt/TiN in N_2 saturated 0.5 M H_3PO_4 at 50 mV s^{-1}

After 1000 cycles of ADT in the potential region between 0.6 to 1.2 V, Pt/C exhibit significant loss of ECSA (4.76 $m^2\ g^{-1}_{pt}$) compared to that of Nafion® stabilised Pt/TiN (15.23 $m^2\ g^{-1}_{pt}$). The better stability and durability of Nafion® stabilised Pt/TiN is attributed to corrosion resistant behaviour of TiN and also the coordination between Nafion and Pt nanoparticles. Good interfacial contact is established between Nafion and Pt, resulting in effective ionomer distribution in the catalyst layer. The enhanced electrochemical stability is due to the Nafion® layer covering the Pt surface inhibiting the aggregation of Pt, owing to the strong steric hindrance effect of sulfonic acid groups on Nafion®. Presence of Nafion® layer surrounding the Pt particles could prevent diffusion of soluble Pt particles by redepositing at the original site.

7.2.3.2 Electrochemical characterisation of Nafion® stabilised Pt/TiN in H_2SO_4

Figure 7.9a and 7.9b shows CV curves of Pt/C and Nafion® stabilised Pt/TiN recorded before and after ADT in an N_2 saturated 0.5 M H_2SO_4. A Nafion® stabilised Pt/TiN shows similar peak intensity to Pt/C, in the potential region 0.05 to 0.4 V for Hads/des. The ECSA (calculated using equation 7.2 and is shown in Table 7.6) of Nafion® stabilised Pt/TiN (74.04 $m^2\ g^{-1}_{pt}$) estimated from the CV curves which is higher than that of Pt/C (52.14 $m^2\ g^{-1}_{pt}$) with a pt loading of 40 µg cm^{-2} in the electrodes.

Table 7.6, ECSA obtained from CVs of Pt/C and Nafion® stabilised Pt/TiN (0.5 M H_2SO_4)

Catalyst	Pt loading (L_{Pt}) µg cm^{-2}	Q_{Hdes} (mC cm^{-2})		ECSA ($m^2\ g^{-1}_{Pt}$)	
		Before	**After**	**Before**	**After**
Pt/C	40	4.37	2.03	52.14	24.28
Nafion-stab Pt/TiN	40	6.21	4.11	74.04	48.98

Considering the higher density of TiN (5.4 g cm^{-3}) as compared to C (1.9 g cm^{-3}), the C to Pt particles ratio per unit mass of electrocatalyst is 1:21 for 20 wt% Pt/C where as the ratio is 1:61 for 20 wt% Pt/TiN. Considering that there are more Pt nanoparticles supported on a single TiN particle than on a C particle. The TEM analysis indicated a minimal amount of unsupported Pt particles suggesting that most of the Pt particles are bound to the substrate. From the above points, it can be reasoned that more catalytically active platinum sites are present in Nafion® stabilised Pt/TiN resulting in higher ECSA.

Accelerated durability test performed in the potential region 0.6 to 1.2 V showed that Nafion® stabilised Pt/TiN is more stable than Pt/C even after 1000 potential cycles. The comparison of ECSA before and after cycling is shown in figure 7.9c. The ECSA of Nafion® stabilised Pt/TiN estimated after 1000 potential cycles is about 48.98 m^2 g^{-1}_{pt} (34% loss), whereas, Pt/C showed 54% loss in ECSA (24.28 m^2 g^{-1}_{pt}). The improved stability and durability of Nafion® stabilised Pt/TiN compared to Pt/C is attributed to corrosion resistance TiN support as well as Nafion surrounding the Pt.

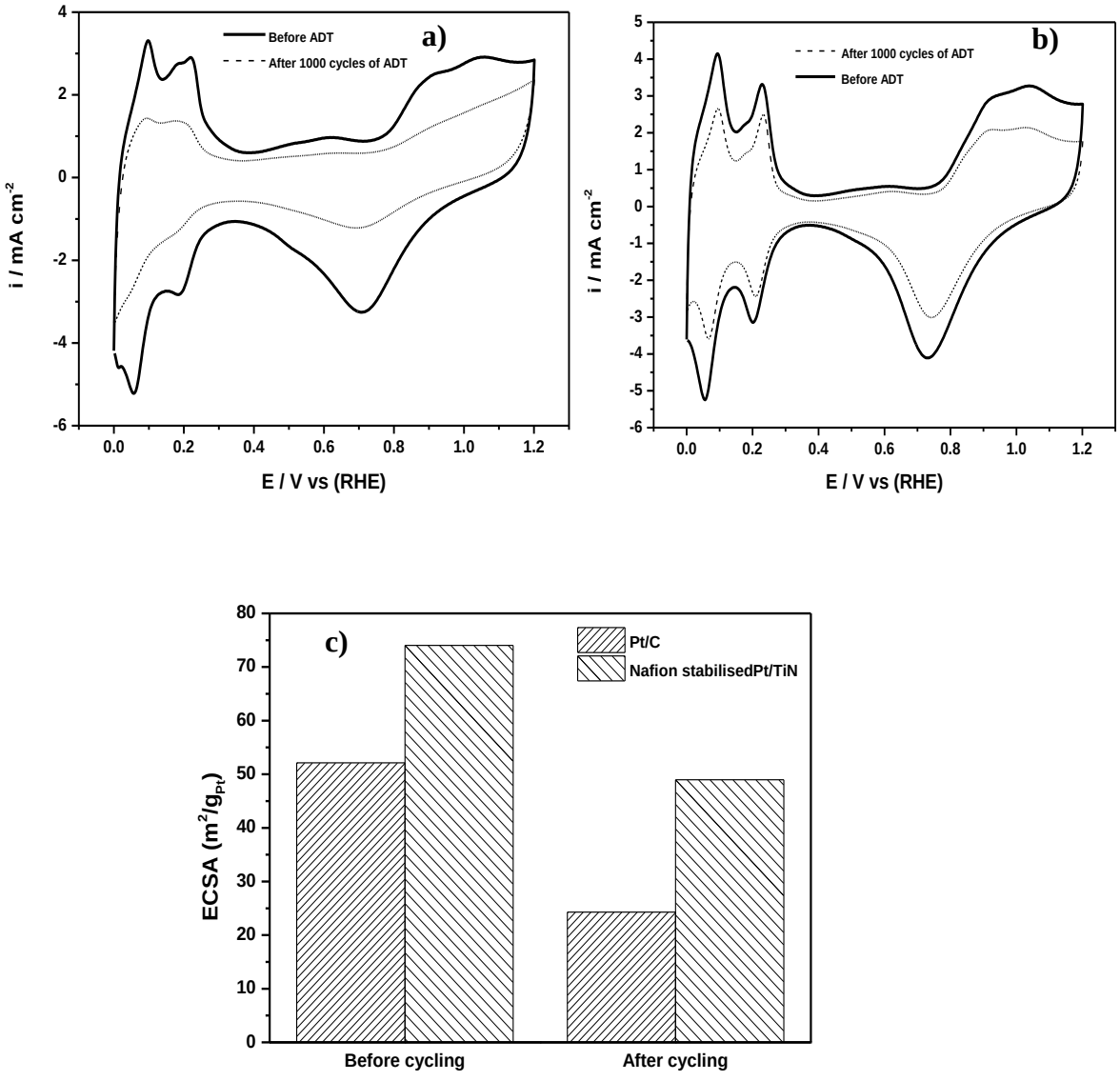

Figure 7.9, a) CVs of Pt/C, b) Nafion® stabilised Pt/TiN in an N_2 saturated 0.5 M H_2SO_4 at 50 mV s^{-1} and c) comparison of ECSA before and after cycling

7.2.4 Oxygen reduction reaction (ORR)

7.2.4.1 ORR of Nafion® stabilised Pt/TiN in H_3PO_4

The ORR polarisation curves measured for Pt/C and Nafion® stabilised Pt/TiN on a rotating disc electrode (RDE) in an O_2 saturated 0.5 M H_3PO_4 at 1600 rpm are shown in figure 7.10a. A Nafion® stabilised Pt/TiN shows a 50 mV higher ORR onset potential than Pt/C. Current approaches the mixed kinetic-diffusion regime at lower overpotentials (+0.75 to +0.85 V) and at higher overpotentials current reaches its diffusion-limited value of ~5.37 mA cm^{-2}. The half-wave potential of an ORR curve is often used to evaluate the activity of catalyst. Nafion® stabilised Pt/TiN showed a positive shift in $E_{1/2}$ of 20 mV compare to Pt/C. The difference in $E_{1/2}$ showed a marked improvement in ORR activity of Nafion® stabilised Pt/TiN. The mass activity and specific activity was calculated from the ORR polarisation curves (figure 7.10a) using the equations 7.3a and 7.3b respectively.

Mass activity (mA $mg^{-1}{}_{Pt}$) (i_m) = i/mass of Pt (7.3a)

Specific activity (µA $cm^{-2}{}_{Pt}$) (i_s) = i_m/ECSA (7.3b)

Figure 7.10b shows the comparison of mass activities at 0.8 and 0.9 V. Nafion® stabilised Pt/TiN (0.9 V; 9.95 mA mg^{-1}) exhibited ~2 times higher value of i_m than that of Pt/C (0.9 V; 4.95 mA mg^{-1}), indicating that Nafion® stabilised Pt/TiN has better catalytic activity. The specific activity calculated for Nafion® stabilised Pt/TiN and Pt/C are 18.12 and 9.28 µA $cm^{-2}{}_{Pt}$ respectively.

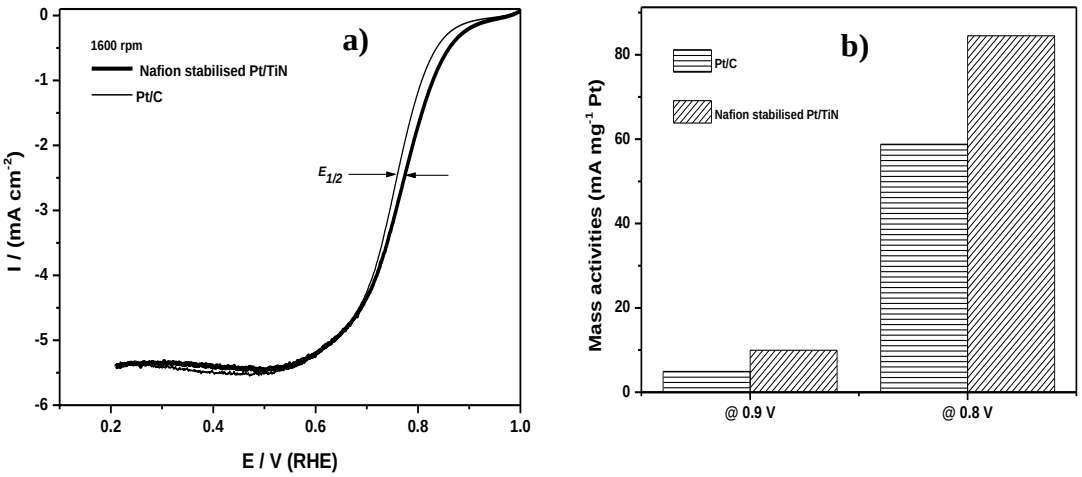

Figure 7.10, a) ORR curves of Pt/C and Nafion® stabilised Pt/TiN in an O_2 saturated 0.5 M H_3PO_4 at 1600 rpm and 5 mV s^{-1} scan rates, b) comparison of mass activities calculated from ORR curves (obtained from figure 7.10a) at 0.9 and 0.8 V

Figure 7.11 shows the ORR polarisation curves recorded before and after 1000 cycles of ADT, Pt/C shows a 70 mV negative shift in half-wave potential whereas Nafion® stabilised Pt/TiN shows about 50 mV negative shift.

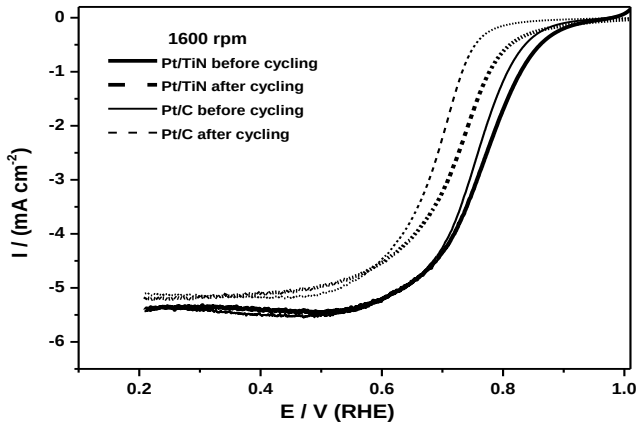

Figure 7.11, ORR curves of Pt/C and Nafion® stabilised Pt/TiN in an O_2 saturated 0.5 M H_3PO_4 at 1600 rpm and 5 mV s^{-1} scan rates, before and after ADT cycling

The rotation rate dependant (400-1600 rpm) polarisation curves for ORR of Nafion® stabilised Pt/TiN is shown in figure 7.12a and they are parallel to each other. Figure 7.12b and 7.12c shows Koutecky-Levich plots of Nafion® stabilised Pt/TiN and Pt/C obtained at 0.8-0.9 V. K-L plots are linear and parallel to each other; this indicates first-order kinetics with respect to molecular oxygen reduction. The number of electrons transferred (*n*), as calculated from (using equation 3.39) the slopes of Koutecky-Levich plots at 0.8 V, is 3.8 for Nafion® stabilised Pt/TiN and 3.7 for Pt/C and these values are close to theoretical value (n = 4), which indicates nearly complete reduction of O_2 to H_2O.

The Tafel plots of Pt/C and Nafion® stabilised Pt/TiN are shown in figure 7.12d. It is seen from the Tafel plots, there are two regions, 60 mV/dec, at lower current densities indicating one-electron transfer reaction being the rate-determining step and another region approximately, at 120 mV/dec at higher current densities indicating that two-electron transfer reaction as the rate-determining step. The ORR exchange current density (i_0) was calculated from the Tafel plots (figure 7.12d). In the Tafel region of 120 mV/dec, the exchange current density for a Pt/C catalayst is 1.42×10^{-8} A cm^{-2} at 20 ^oC and this value is close to the literature reported value of 1.63×10^{-8} A cm^{-2}. A Nafion® stabilised Pt/TiN showed an exchange current density of 8.32×10^{-7} A cm^{-2} at 20 ^oC which is higher than that of Pt/C.

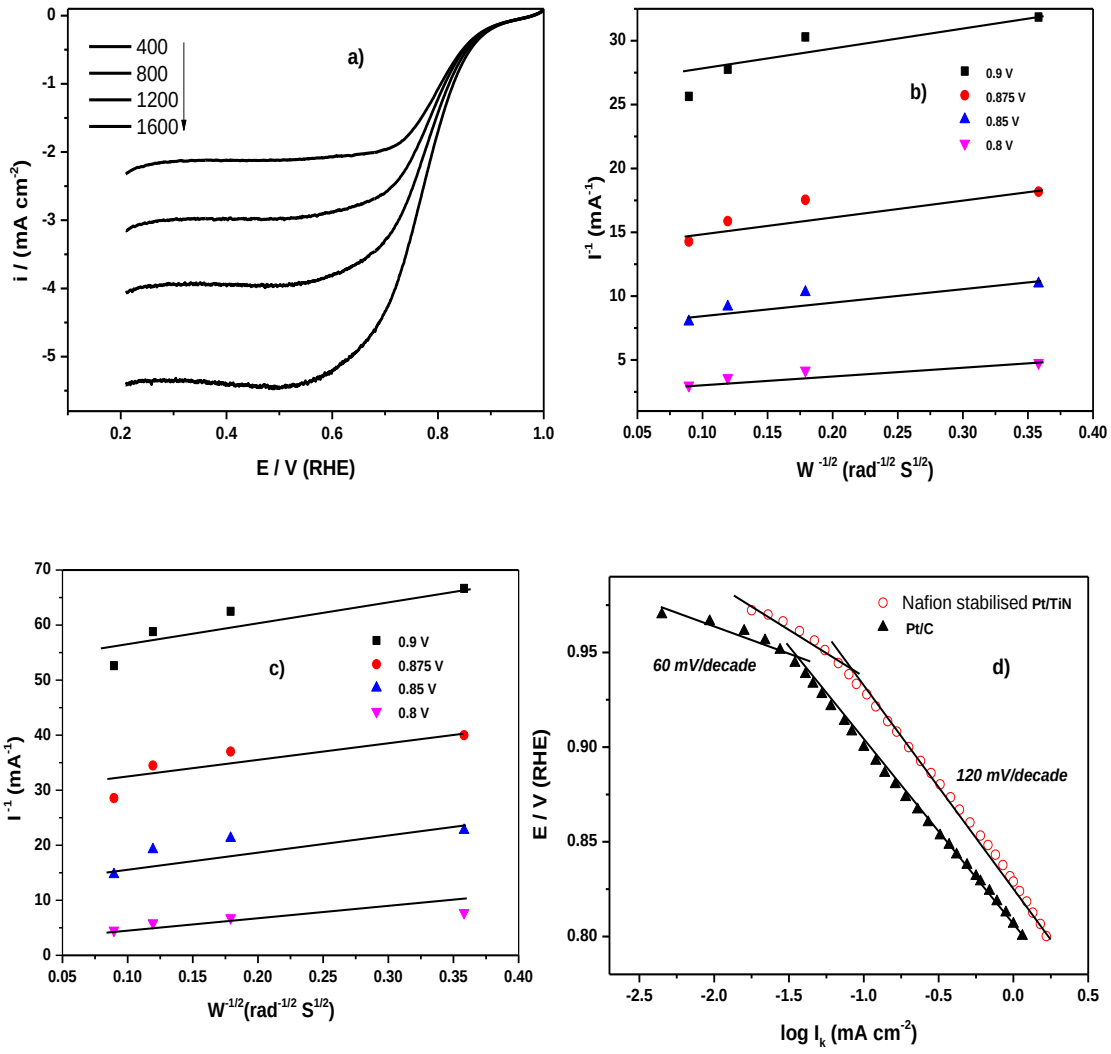

Figure 7.12, a) Rotation rate dependant ORR curves of Nafion® stabilised Pt/TiN in O_2 saturated 0.5 M H_3PO_4, b and c) K-L plots of Nafion® stabilised Pt/TiN (from figure 7.12a) and Pt/C at different potentials and d) Tafel plots of Pt/C and Nafion® stabilised Pt/TiN in O_2 saturated 0.5 M H_3PO_4 obtained from ORR polarisation curves at 1600 rpm at 20 ^oC (figure 7.10a)

7.2.4.2 ORR of Nafion® stabilised Pt/TiN in H_2SO_4

The ORR polarisation curves measured for Pt/C and Nafion® stabilised Pt/TiN on a rotating disc electrode (RDE) in an O_2 saturated 0.5 M H_2SO_4 at 1600 rpm is shown in figure 7.13a. A Nafion® stabilised Pt/TiN showed a 20 mV positive shift in ORR onset potential compared to Pt/C. Current approaches the mixed kinetic-diffusion regime at lower overpotentials (+0.78 to +0.85 V) and at higher overpotentials current reaches its diffusion-limited value of ~5.39 mA cm^{-2} for Pt/C and 5.11 mA cm^{-2} for Nafion® stabilised Pt/TiN. A Nafion® stabilised Pt/TiN showed a 30 mV positive shift in $E_{1/2}$ compared to Pt/C. The mass activity (from ORR curves at 1600 rpm using equation 7.3a) of Nafion® stabilised Pt/TiN (0.9 V; 9.17 mA mg^{-1}_{Pt}) which is higher than that of Pt/C (0.9 V; 5.75 mA mg^{-1}_{Pt}), indicating that Nafion® stabilised Pt/TiN has better ORR activity. The specific activity calculated (using equation 7.3b) from ORR curves (1600 rpm) at 0.9 V for Nafion® stabilised Pt/TiN and Pt/C are 12.32 and 11.02 µA cm^{-2}_{Pt} respectively. The comparison of mass activities of Nafion® stabilised Pt/TiN and Pt/C are shown in figure 7.13b.

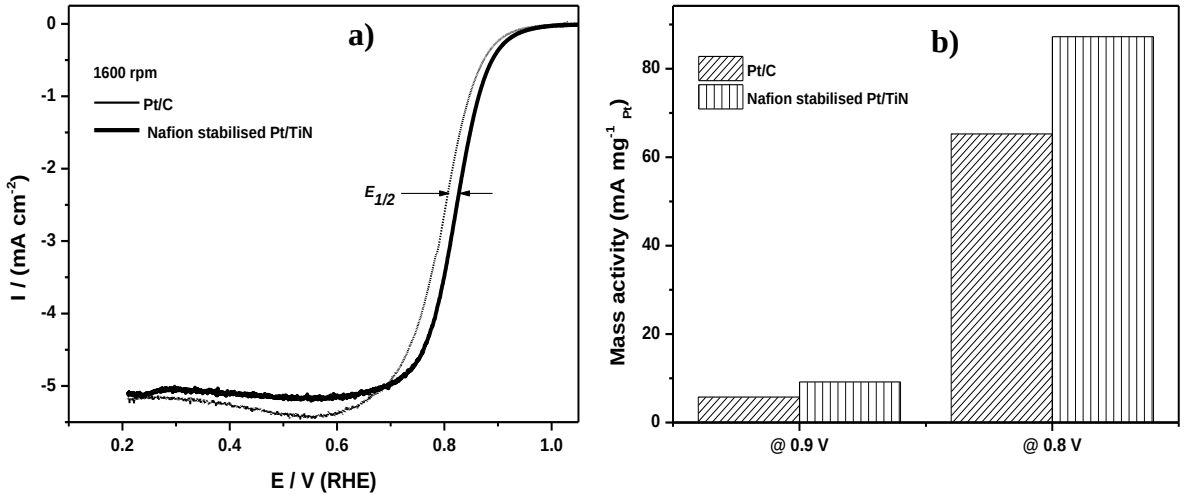

Figure 7.13, a) ORR polarisation curves of Pt/C and Nafion® stabilised Pt/TiN in O_2 saturated 0.5 M H_2SO_4 at 1600 rpm and 5 mV s^{-1} scan rates and b) comparison of mass activities at 0.9 and 0.8 V (obtained from figure 7.13a)

Figure 7.14 shows the ORR polarisation curves recorded before and after 1000 cycles of ADT, Pt/C showed a 60 mV negative shift in half-wave potential whereas Nafion® stabilised Pt/TiN shows about 30 mV shifts.

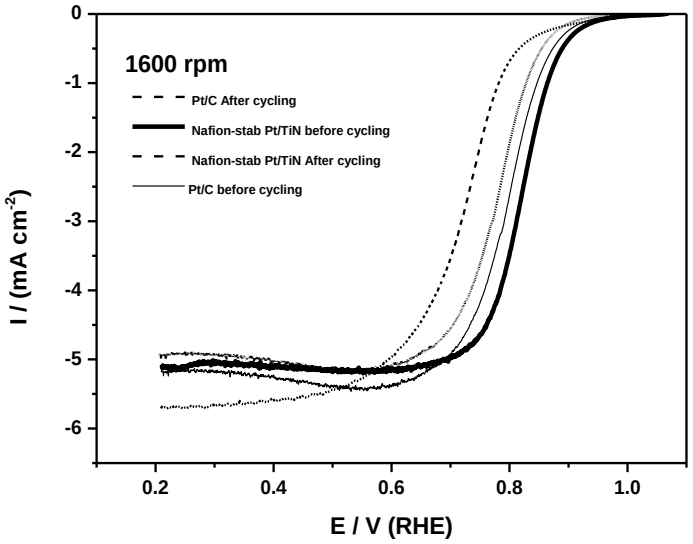

Figure 7.14, ORR polarisation curves of Pt/C and Nafion® stabilised Pt/TiN in an O_2 saturated 0.5 M H_2SO_4 at 1600 rpm and 5 mV s^{-1} scan rates, before and after ADT cycling

The rotation rate dependant (400-1600 rpm) ORR polarisation curves of Nafion® stabilised Pt/TiN is shown in figure 7.15a and they are parallel to each other. Figure 7.15b shows Koutecky-Levich plots of Nafion® stabilised Pt/TiN obtained at 0.8-0.9 V. K-L plots are linear and parallel to each other; this indicates first-order kinetics with respect to molecular oxygen reduction. The number of electrons transferred (*n*), as calculated (using equation 3.39) from the slopes of Koutecky-Levich plots at 0.8 V, is 3.7 for Nafion® stabilised Pt/TiN and 3.6 for Pt/C and these values are close to the theoretical value ($n = 4$), which indicates nearly complete reduction of O_2 to H_2O.

The Tafel plots of Pt/C and Nafion® stabilised Pt/TiN are shown in figure 7.15c. It is seen from the Tafel plots, there are two regions, 60 mV/dec, at lower current densities indicating one-electron transfer reaction being the rate-determining step and another region approximately at 120 mV/dec at higher current densities indicating that two-electron transfer reaction as the rate determining step.

The ORR exchange current density (i_0) was calculated from the Tafel plots (figure 7.15c). In the Tafel region of 120 mV/dec, the exchange current density for a Pt/C catalyst is 5.04×10^{-8} A, while that for Nafion® stabilised Pt/TiN catalyst is 1.03×10^{-7} A cm^{-2} at 20 ^{o}C which is higher than that of Pt/C. The comparison of electrochemical parameters of Pt/C and Nafion® stabilised Pt/TiN is shown in Table 7.7.

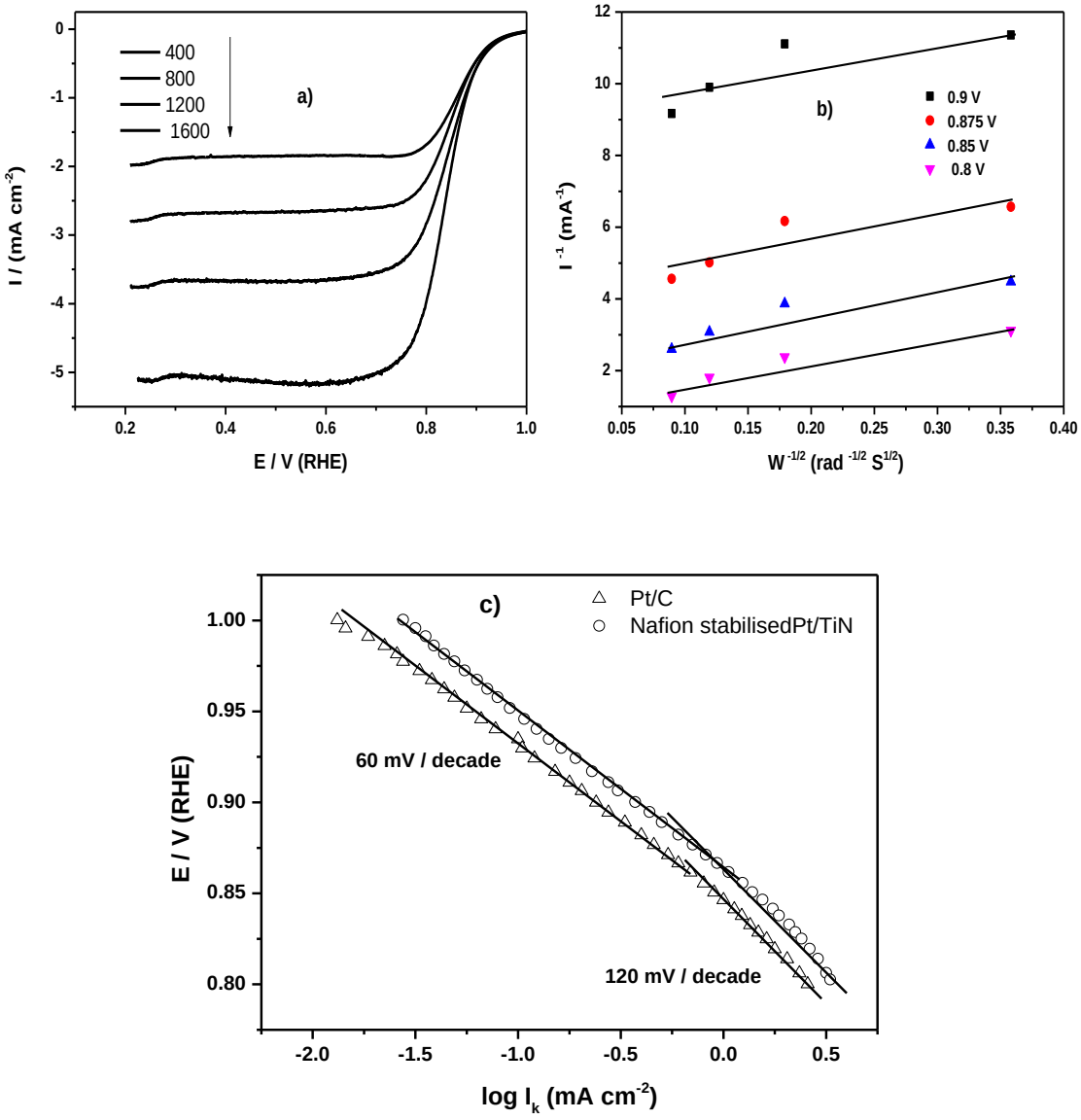

Figure 7.15, a) Rotation rate dependant ORR curves of Nafion® stabilised Pt/TiN, b) K-L plots of Nafion® stabilised Pt/TiN and Pt/C at different potentials and c) Tafel plots of Pt/C and Nafion® stabilised Pt/TiN in an O_2 saturated 0.5 M H_2SO_4

Table 7.7, Comparison of electrochemical parameters of Pt/C and Nafion® stabilised Pt/TiN

Catalyst	0.5 M H_2SO_4					0.5 M H_3PO_4				
	ECSA ($m^2\ g^{-1}_{Pt}$)	i_m	i_s	i_o	n	ECSA ($m^2\ g^{-1}_{Pt}$)	i_m	i_s	i_o	n
Pt/C	52.14	5.75	11.02	$5.04x10^{-8}$	3.6	53.33	4.95	9.28	$1.42x10^{-8}$	3.7
Nafion®-stab Pt/TiN	74.04	9.17	12.32	$1.03x10^{-7}$	3.7	54.90	9.95	18.12	$8.32x10^{-7}$	3.8

(Mass activity @ 0.9V (i_m; mA mg^{-1}_{Pt}), Specific activity @ 0.9V (i_s; µA cm^{-2}_{Pt}) obtained from ORR polarisation curves at 1600 rpm, exchange current density (i_o; A cm^{-2}) and n is the number of electrons)

The improved catalytic activities of Nafion® stabilised Pt nanoparticles supported on TiN are influenced by metal support interactions as it is reported in the literature for TiN supported electocatalysts [12].

The degradation mechanism of Pt/C could be explained as shown in the figure 7.16. Three mechanisms are generally accepted to contribute toward the loss of ECSA for carbon supported Pt nanoparticles. First, electrochemical corrosion occurs on Pt metal particles (Position a; figure 7.16a). The Pt corrosion at the anode is

$$Pt \longrightarrow Pt^{4+}\ 4e^- \qquad (7.4a)$$

Whereas at cathode is

$$PtO_2 + 4H^+ + 2e^- \longrightarrow Pt^{2+} + 2H_2O \qquad (7.4b)$$

Second, unsupported Pt metal particles are formed due to the corrosion of the carbon support (Position b; figure 7.16a). The corrosion reaction is given in equation (7.5)

$$C + 2H_2O \longrightarrow CO_2 + 4H^+ + 4e^- \qquad (7.5)$$

The presence of Pt promotes this corrosion reaction (Position c; figure 16a). The detached Pt particles are readily agglomerated on the surface of supports or ionomer. Third, Pt metal particles or their aggregates grow through Ostwald ripening, that is, Pt

atoms with Pt particles are transported onto other particles to form larger particles (Position d; figure 16a) [13]. Correspondingly, the degradation mechanism of Nafion® stabilised Pt/TiN could be well explained by figure 7.16b, where the Pt nano-particles are stabilized with Nafion, the electrochemical corrosion of Pt could be suppressed with the protection of Nafion layer (Position a_1; figure 7.16b) compared to that of without Nafion layer (Position a; figure 7.16a). Although the carbon support can be degraded, the triple phase boundary always exits on the Pt particle surfaces, and this slows down the loss of ECSA (Position b_1; figure 7.16b). In addition, the ability of Nafion molecules to adhere to the Pt surfaces like tentacles could anchor Pt particles on the support surfaces although some detachment of Pt particles does take place (Position c_1; figure 7.16b). Furthermore, the Nafion could effectively prevent Pt nanoparticles from aggregation on support surfaces because of a strong steric hindrance effect of PFSA with SO_3^- groups (position d1; figure 7.16b). During electrochemical potential cycling, these factors (especially for b_1, c_1 and d_1 positions) may play a positive role and sharply reduce the ECSA loss, which lead to a Pt stabilization.

Also, it is important to consider support factors. Compared to carbon black, the TiN has high chemical stability and unique mechanical property, which could effectively decrease the support degradation.

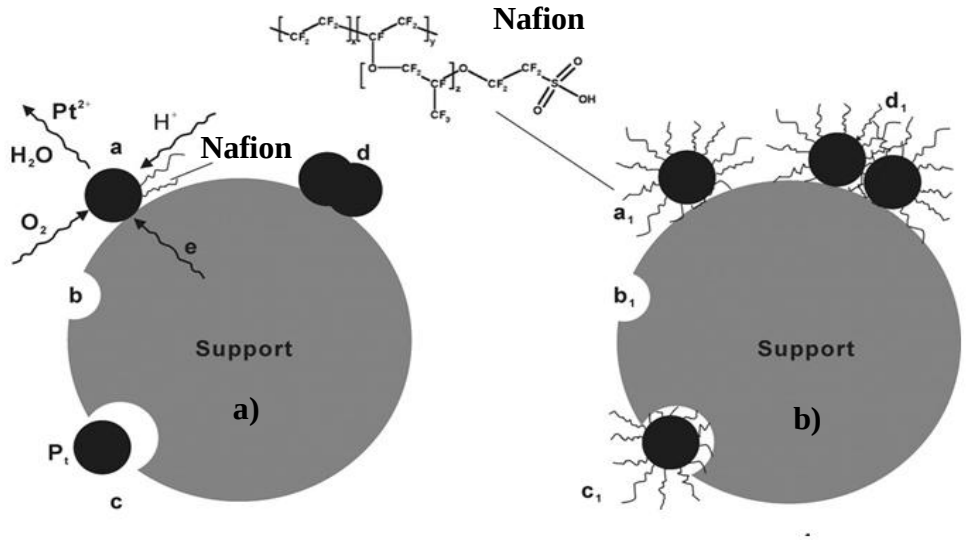

Figure 7.16, Schematic of ECSA loss a) Pt nanoparticles on carbon support and b) Nafion® stabilised Pt/TiN

7.3 Pt-Co nanoparticles supported on titanium nitride: an efficient and durable electrocatalysts for oxygen reduction reaction

7.3.1 Morphology and structural characterisation

Figure 7.17a and 7.17b shows HRTEM images of Pt-Co/TiN. Pt-Co nanoparticles are uniformly distributed over the TiN surface. The particle size distribution, calculated from more than 100 nanoparticles shows that the mean particle size is about 6.5 nm. A selected area electron diffraction (SAED) pattern of Pt-Co/TiN is shown in figure 7.17c. The ring pattern is consistent with an FCC crystal structure in which major diffraction peaks can be indexed to (111), (200), (220) and (311) reflections. Figure 7.17d shows EDS spectrum of Pt-Co/TiN and the elemental analysis revealed that an average Pt-Co ratio of 9.2:3.4 and these values are closely related to value obtained from XPS (9.22: 3.21) and hence the composition is Pt_3Co.

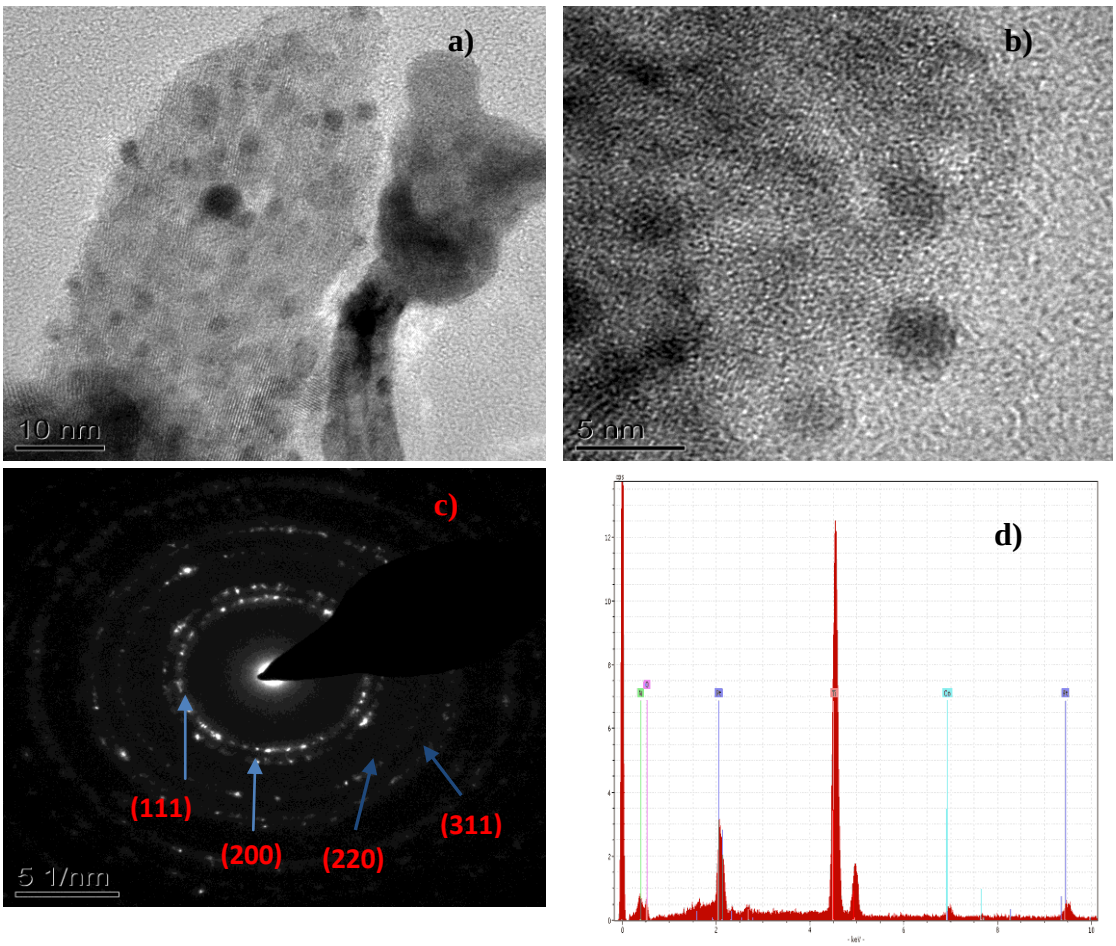

Figure 7.17, a and b) HRTEM images of Pt-Co/TiN, c) SAED pattern of Pt-Co/TiN and d) EDS patter of Pt-Co/TiN

X-ray diffraction pattern of Pt and Pt-Co nanoparticles supported on TiN are shown in figure 7.18. After pre-treatment at 400 ^{o}C, Pt-Co/TiN shows typical face-cantered cubic (FCC) structure for Pt. The planes (111), (200), (220) and (311) corresponding to pure Pt metal consistent with FCC structure. In the case of Pt-Co/TiN the peak positions are shifted to higher angles (inset figure), compare to Pt/TiN, this indicates the Co is incorporated into Pt structure to form an alloy phase. The lattice parameter 'a' calculated (calculation are shown in appendix A) from (220) diffraction plane for Pt (Pt/TiN) is 0.394 nm and 0.387 (Pt-Co/TiN). The particle size calculated (calculations are shown in appendix A for Pt-Co from the Debye-Scherrer equation using full- width at half- maximum of (220) plane is about 8.5 nm. This is slightly more than the particle size measured form TEM images because XRD gives volume-weighted measurements that tend to overestimate the geometric particle size. No characteristic peaks of metallic Co or oxides were observed, and also no distinctive superlattice diffraction peaks were detected around 2θ of 23.1^{o}, 32.8^{o}, 53.2^{o} and 58.6^{o}, confirming the formation of disordered Pt-Co alloys.

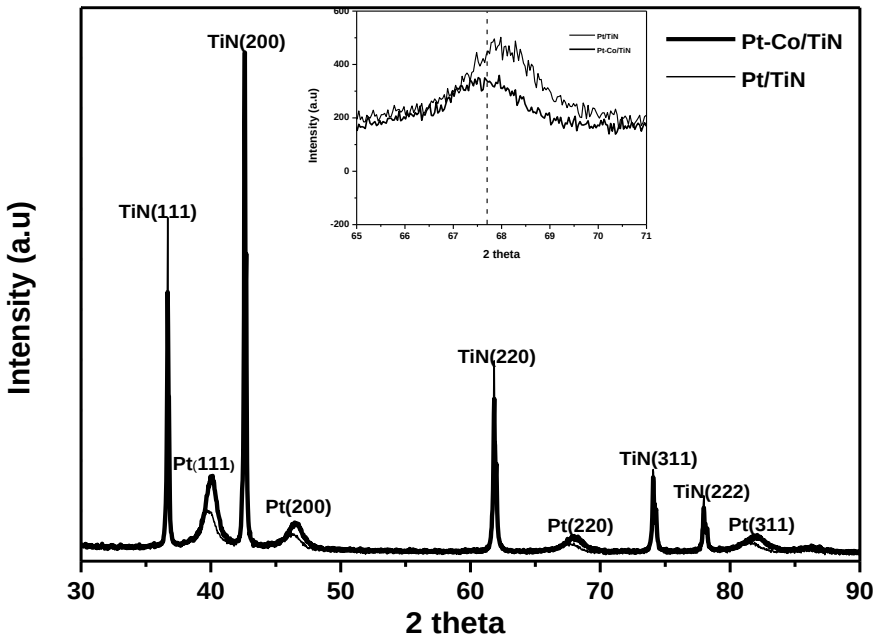

Figure 7.18, X-ray diffraction patterns of Pt and Pt-Co nanoparticles supported on TiN. The inset shows the enlarged region of Pt (220) diffraction peak

XPS analysis was performed to understand the bonding nature and oxidation states of Pt and Co in Pt-Co/TiN. The survey spectrum is shown in the figure 7.19a, and it is seen from the figure the main peaks observed are due to Pt 4f, Pt 4d, Ti 2p and O 1s. The deconvoluted high resolution XPS spectra of Pt 4f from Pt-Co/TiN and Pt/TiN are shown in figure 7.19b and 7.19c. Each spectrum exhibits a broad band that can be curve-fitted into three pairs of peaks, all of which have spin orbital splitting of $4f_{7/2}$ and $4f_{5/2}$ states. In the case of Pt-Co/TiN, the binding energy (BE) of 72.11 eV is corresponding to pt in the zero-valent state. Pt is predominantly metallic in Pt-Co/TiN, but the appearance of two minor peaks with $4f_{7/2}$ at 72.18 eV and 73.28 eV, attributed to Pt-O and PtO_2, respectively, indicates some surface oxidation [23]. The BEs of Pt-Co/TiN shifts to lower value compared to Pt/TiN, this can be elucidated in terms of electronic effect of Co on Pt. The Co, being more electropositive than Pt would donate electrons to Pt, causing negative shift in BE of $4f_{7/2}$ signal of Pt^0 species. The electron withdrawing effect of Pt on Co increases the amount of Pt^0 in Pt-Co/TiN compared with that in the Pt/TiN, indicating the oxide cleansing action of Co on Pt [24]. These effects are expected to enhance the electrocatalytic activity of Pt in Pt-Co alloy [25]. Figure 7.19d shows the high resolution XPS spectrum of Co. The BE of 781.2 eV is corresponding to Co $2p_{3/2}$ in metallic state, which seems to have a positive shift to higher BE compared to bulk 782.6 eV.

The deconvoluted XPS spectra of O 1s for the Pt-Co/TiN and Pt/TiN are shown in figure 7.19e and 7.19f. The deconvoluted components can be identified as Pt-O or physically adsorbed oxygen near 530 eV, together with titanium-oxygen species at BEs close to 532 and 534 eV.

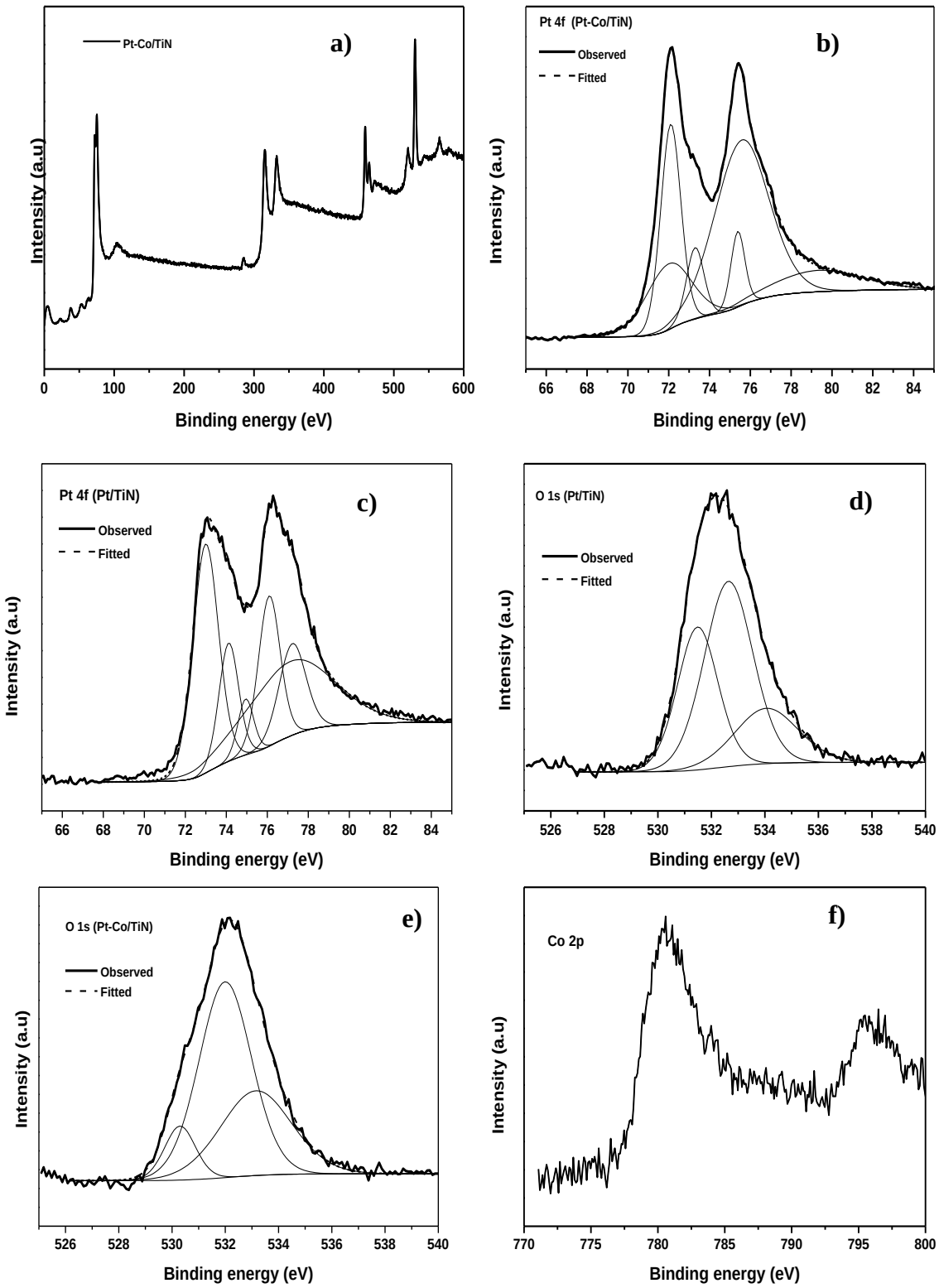

Figure 7.19, a) XPS survey spectrum of Pt-Co/TiN, b and c) deconvoluted spectra of Pt 4f of Pt-Co/TiN and Pt/TiN, d) high resolution XPS spectra of Co, e and f) deconvoluted XPS spectra of O 1s of Pt-Co/TiN and Pt/TiN

7.3.2 Electrochemical characterisation

The durability of Pt/C (E-tek), Pt/TiN and Pt-Co/TiN electrocatalysts was evaluated by accelerated degradation test (ADT) between +0.6 and +1.2 V (Vs. RHE) for 5000 cyclic voltammetry potential cycles in an N_2 saturated 0.5 M sulphuric acid medium at a scan rate of 50 mV s^{-1}. Figure 7.20a, 7.20b and 7.20c shows cyclic voltammograms of Pt-Co/TiN, Pt/TiN and Pt/C measured before and after 1000, and 5000 cycles of ADT. Pt-Co/TiN shows well defined peaks for hydrogen adsorption/desorption (0.05 to 0.4 V) along with Pt oxides (>0.8V) formation and reduction peaks (~0.8 V), and indicates that Pt-Co has Pt rich surface. Pt-Co/TiN exhibits increased peak current densities for hydrogen adsorption/desorption after 1000 cycles, which is due to dissolution of Co on the surface, although peak current densities (Hads/des) for Pt/TiN remains unchanged. But after 5000 potential cycles Pt-Co/TiN shows a minimal loss in ECSA, whereas, Pt/TiN and Pt/C shows significant loss in ECSA (figure 7.20d).

Table 7.8 shows the Q_{Hdes} estimated from CV curves before and after ADT cycles. Pt/C shows increased loss of ECSA as the number of cycles increases, after 5000 potential cycles ECSA had decayed by about 85.33%. After 1000 cycles, ECSA of Pt/TiN remains unchanged but after 5000 cycles it shows about 67% loss. However, the Pt-Co/TiN catalyst showed an increased in ECSA about 5% after 1000 cycles and then after 5000 potential cycles ECSA had decayed about 55%. The comparison of percentage loss in ECSA after 5000 potential cycles of ADT is shown in figure 7.20d.

Table 7.8 Electrochemical parameters obtained from CV curves of Pt/C, Pt/TiN and Pt-Co/TiN electrocatalyst.

Catalyst	Pt loading (L_{Pt}) µg cm^{-2}	Q_{Hdes} (mC cm^{-2})	
		Before	**After**
Pt/C	85	7.78	2.6
Pt/TiN	85	6.14	2.1
Pt-Co/TiN	40	0.62	0.34

Pt-Co/TiN exhibits better stability and durability compared to Pt/TiN and Pt/C. This indicates that apart from alloying the Pt with Co, the TiN support markedly improves the activity, stability and durability of Pt-Co/TiN. TiN has significantly lower rate of electrochemical corrosion over carbon and TiN itself is an active catalyst for ORR, all these properties of TiN improves the overall catalytic activity of Pt-Co/TiN.

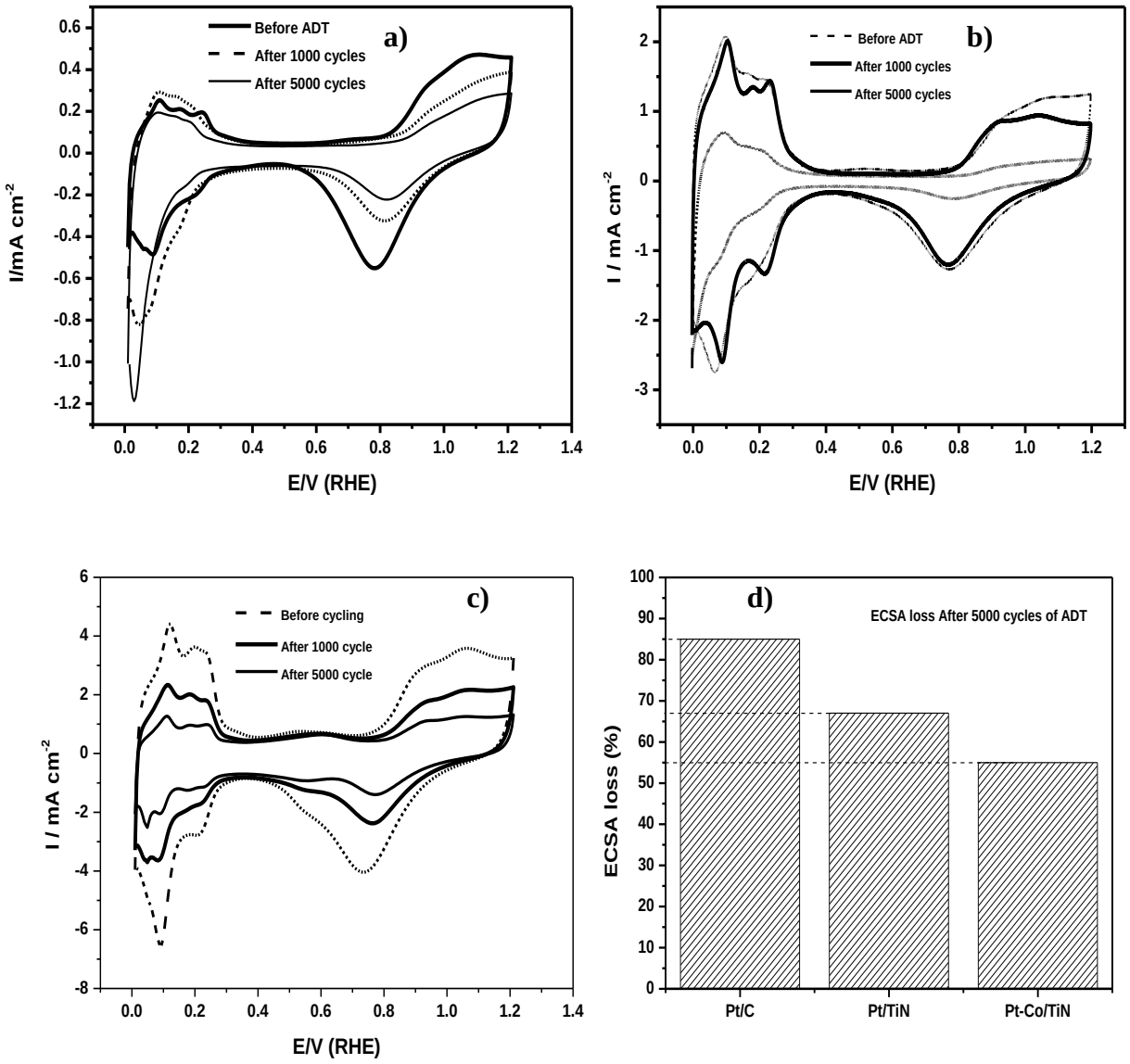

Figure 7.20, a) CVs of Pt-Co/TiN, b) Pt/TiN, c) Pt/C in an N_2 saturated 0.5 M H_2SO_4 before and after ADT cycles and d) percentage loss in ECSA after 5000 potential cycles of ADT

7.3.3 Oxygen reduction reaction (ORR)

The ORR polarisation curves of Pt-Co/TiN, Pt/TiN and Pt/C on a rotating disc electrode (RDE) in an N_2 saturated 0.5 M H_2SO_4 at 1600 rpm is displayed in figure 7.21a. Pt-Co/TiN shows a ~50 mV higher ORR onset potential compare to Pt/C. Pt-Co/TiN had reached a diffusion limited current of -5.68 mA cm^{-2} at higher overpotential region. The current approaches mixed kinetic and diffusion current region between +0.8 to +1.0 V. The half-wave potential ($E_{1/2}$) between the mixed kinetic/diffusion regime is often used to measure the catalytic activity of an electrocatalyst. The half-wave potential, $E_{1/2}$ is arranged in the sequence of increasing order Pt/C < Pt/TiN < Pt-Co/TiN. The difference in $E_{1/2}$ between Pt-Co/TiN and Pt/C is about +32 mV; the positive shift in $E_{1/2}$ indicates marked improvement in catalytic activity. The mass activities calculated from the ORR curves are shown in figure 7.21b. The comparison mass and specific activities calculated from ORR curves (1600 rpm) at 0.9 V are shown in Table 7.9. Pt-Co/TiN exhibits higher mass activity over Pt/TiN and Pt/C. The measured currents were corrected for mass transport to obtain the kinetic current. The specific activities (I_k) at 0.9 V calculated from figure 7.22b, of Pt-Co/TiN are 0.39 mA cm^{-2}_{Pt} and higher than Pt/TiN (0.29 mA cm^{-2}_{Pt}) and Pt/C (0.15 mA cm^{-2}_{Pt}) and these values are in good agreement with the literature reported values.

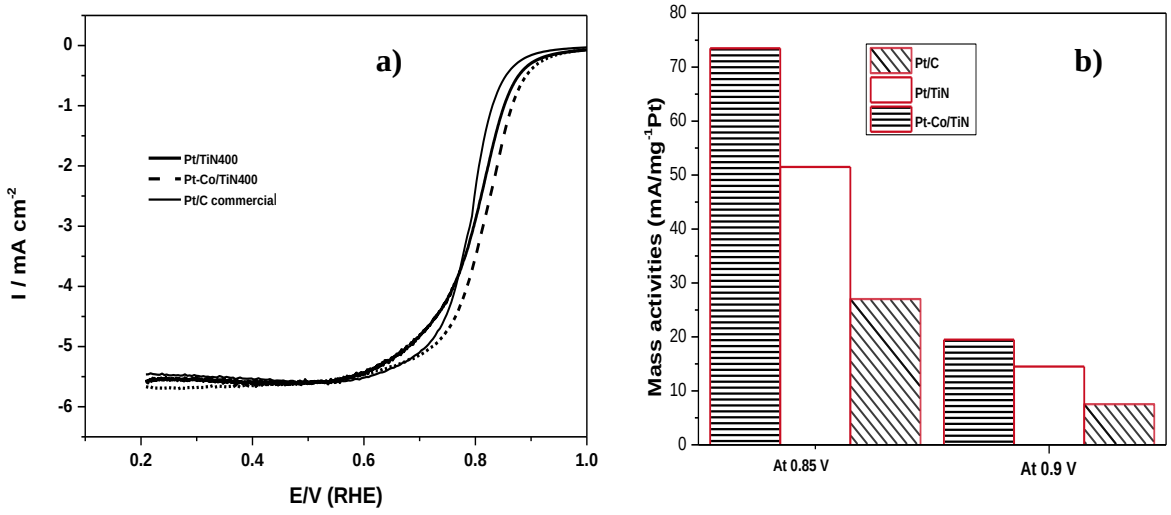

Figure 7.21, a) ORR curves of Pt-Co/TiN, Pt/TiN and Pt/C in an O_2 saturated 0.5 M H_2SO_4 at 1600 rpm and b) Comparison of mass activities at 0.85 and 0.9 V

Table 7.9, Comparison of mass and specific activities

Sample	Mass activities @ 0.9 V (mA/mg $_{Pt}$)	Specific activities @0.9 V $mA^{-1}/cm^2{}_{Pt}$
Pt/C	7.5	0.15
Pt/TiN	14.4	0.29
Pt-Co/TiN	19.6	0.39

The ORR polarisation curves measured before and after 5000 potential cycles are shown in figure 7.22. Pt-Co/TiN catalyst showed a degradation of 100 mV in its half-wave potential, whereas Pt/TiN shows 120 mV degradation in its half-wave potential.

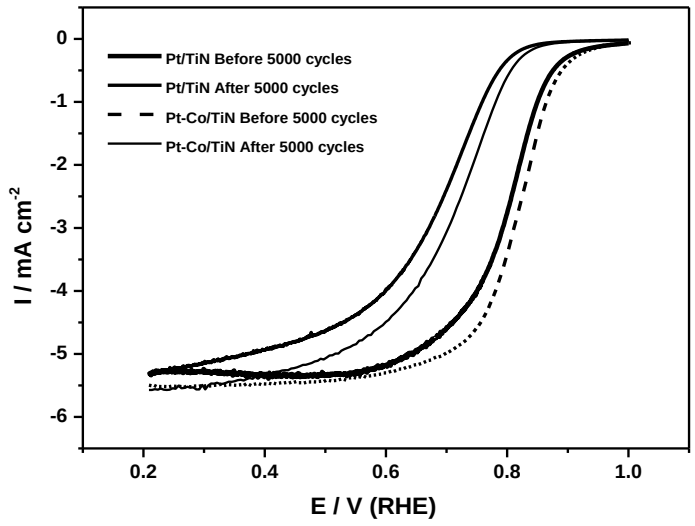

Figure 7.22, ORR curves of Pt-Co/TiN and Pt/TiN before and after 5000 cycles

Figure 7.23a shows Koutecky-Levich plots obtained at 0.8-0.9 V. the K-L plots are linear and parallel to each other; indicating first-order kinetics with respect to molecular oxygen reduction. The number of electrons transferred (*n*), as calculated from the slopes of Koutecky-Levich plot (figure 7.23a) using equation 3.39 at 0.8 V, is 3.92 (~4), which indicates nearly complete reduction of O_2 to H_2O. The Tafel plots of Pt/C, Pt/TiN and Pt-Co/TiN are shown in figure 7.23b. It is seen from the Tafel plots there are two regions, 60 mV/decade at lower current densities indicating one-electron transfer reaction being the rate-determining step and another region of approximately 120 mV/decade at higher current densities, indicating that two-electron transfer reaction as the rate determining step.

The ORR exchange current density (i_0) was calculated from the Tafel plots (figure

7.23b). In the Tafel region of 120 mV/dec, the exchange current density for a Pt/C catalyst is $1.42x10^{-8}$ A cm^{-2} at 20 ^{o}C and this value is close to the literature reported value of $1.63x10^{-8}$ A cm^{-2}. Pt-Co/TiN showed an exchange current density of $1.69x10^{-7}$ A cm^{-2} at 20 ^{o}C which is higher than that of Pt/C and Pt/TiN ($2.23x10^{-7}$ A/cm^{-2}). The comparison of electrochemical parameters of Pt/C, Pt/TiN and Pt-Co/TiN is shown in Table 7.10.

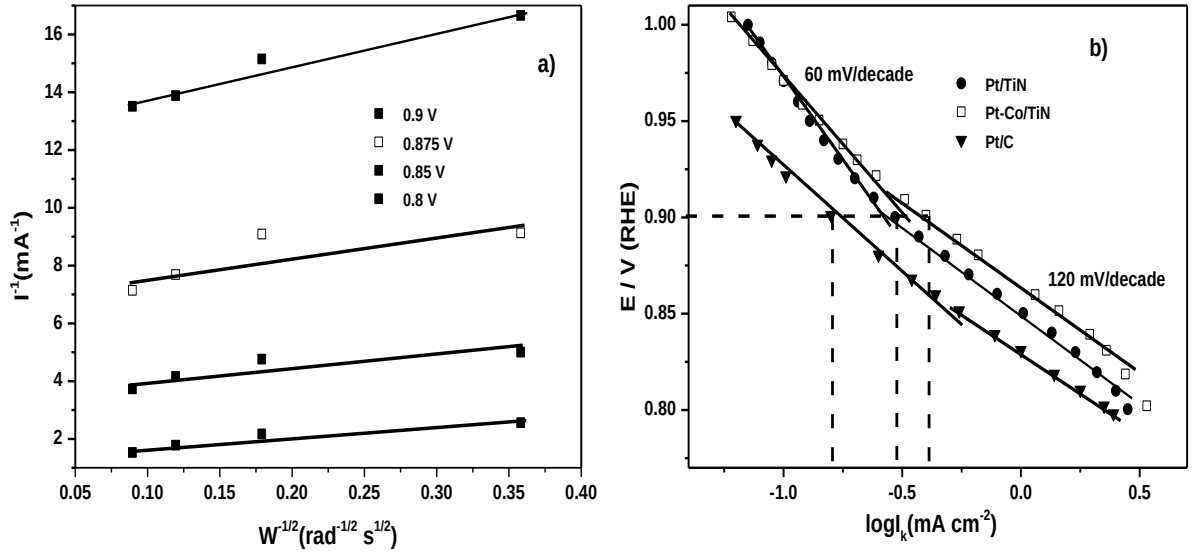

Figure 7.23, a) K-L plots of Pt-Co/TiN and b) Tafel plots of Pt-Co/TiN, Pt/TiN and Pt/C

Table 7.10, Comparison of electrochemical parameters of Pt/C, Pt/TiN and Pt-Co/TiN

Catalyst	0.5 M H_2SO_4			
	i_m (mA $mg^{-1}_{Pt)}$	i_s (mA^{-1} cm^{-2}_{Pt})	i_o (A cm^{-2})	n
Pt/C	7.5	0.15	$1.42x10^{-8}$	3.6
Pt/TiN	14.4	0.29	$1.69x10^{-7}$	3.7
Pt-Co/TiN	19.6	0.39	$2.23x10^{-7}$	3.9

(i_m and i_s @0.9V obtained from ORR polarisation curves at 1600 rpm)

7.4 Conclusions

A Nafion® stabilised Pt/TiN has been prepared and evaluated for its stability, durability and electrocatalytic activity both in sulfuric acid and phosphoric acid medium. The electrochemical analysis showed that Nafion® stabilised Pt/TiN has better electrocatalytic catalytic activity, stability and durability compared to commercial Pt/C under PEMFC operating conditions. The improved durability of Nafion® stabilised Pt/TiN is attributed to both the corrosion resistant TiN support and to the stabilising effect of Nafion®. The results suggest that Nafion® stabilised Pt/TiN can be a suitable cathode electrocatalyst for phosphoric acid based polymer electrolyte membrane fuel cells as well other PEM based fuel cells.

The electrocatalytic activity and stability of Pt-Co/TiN has been evaluated for ORR and compared over Pt/TiN and commercial Pt/C. The improved activity and stability of Pt-Co alloy nanoparticles are attributed to electronic coupling between Pt and Co. Electrochemical corrosion of Pt and also carbon corrosion significantly affects catalytic activity of Pt/C. In this study we replaced carbon with corrosion resistant TiN to support Pt and Pt-Co nanoparticles. Pt-Co/TiN and Pt/TiN showed better stability and electrocatalytic activity over Pt/C; this is attributed to alloying of Pt with Co and corrosion resistant behaviour of TiN and synergistic effect due to metal support interaction.

References

[1] Kumar SMS, Hidyatai N, Herrero J S, Irusta S, Scott K, *Efficient tuning of the Pt nano-particle mono-dispersion on Vulcan XC-72R by selective pre-treatment and electrochemical evaluation of hydrogen oxidation and oxygen reduction reactions,* International Journal of Hydrogen Energy, **2011**, 36(9), 5453.

[2] Mamlouk M, Jang JH, Scott K, *Intermediate Temperature Fuel Cell and Oxygen Reduction Studies with Carbon-Supported Platinum Alloy Catalysts in Phosphoric Acid Based Systems,* Journal of Fuel Cell Science and Technology, **2012**, 9 (1), 11002.

[3] Ruben Ornelas, Alessandro Stassi, Ester Modica, Antonino S. Arico and Vincenzo Antonucci, *Accelerated degradation tests for Pt/C catalysts in sulfuric acid,* ECS Transactions, **2006**, 3(1), 633.

[4] O.J. Curnick, Paula M. Mendes, Bruno G. Pollet, *Enhanced durability of a Pt/C electrocatalyst derived from Nafion-stabilised colloidal platinum nanoparticles,* Electrochemistry Communications, **2010**, 12, 1017.

[5] Daping He, Shichun Mu, Mu Pan, *Perfluorosulfonic acid-functionalized Pt/carbon nanotube catalysts with enhanced stability and performance for use in proton exchange membrane fuel cells,* Carbon, **2010**, 49, 82.

[6] Siguo Chen, Zidong Wei, Xue Qiang Qi, Lichun Dong, Yu-Guo Guo, Lijun Wan, Zhigang Shao, and Li, *Nanostructured Polyaniline-Decorated Pt/C@PANI Core−Shell Catalyst with Enhanced Durability and Activity, J. Am. Chem. Soc., **2012**,* 134(32), 13252.

[7] Dong Jin Ham, Jae Sung Lee, *Transition Metal Carbides and Nitrides as Electrode Materials for Low Temperature Fuel Cells,* Energies, **2009**, 2, 873.

[8] M. M. Ottakam Thotiyl and S. Sampath, *Electrochemical Oxidation of Ethanol in Acid Media on Titanium Nitride Supported Fuel Cell Catalysts,* Electrochemica Acta, **2011**, 56, 3549.

[9] Thotiyl, Ottakam M. M, Ravi Kumar, S.Sampath, *Pd Supported on Titanium Nitride for Efficient Ethanol Oxidation,* J.Phys.Chem, C., **2010**, 114(41), 17934.

[10] Dong Jin Ham and Jae Sung Lee, *Transition Metal Carbides and Nitrides as Electrode Materials for Low Temperature Fuel Cells,* Energies, **2009**, 2, 873-899.

[11] Francois, J.C., Massiani, Y., Gravier, P., Grimblot, J., Gengembre, L., *Characterization and optical properties of thin films formed on TiN coatings during electrochemical treatments*. Thin Solid Films**, 1993**, 223, 223-229.

[12] J. Giner, L. Swette, *Oxygen Reduction on Titanium Nitride in Alkaline Electrolyte*, Nature, **1966**, 211, 1291.

[13] Bharat Avasarala, Thomas Murray, Wenzhen Li, Pradeep Haldar, *Titanium nitride nanoparticles based electrocatalysts for proton exchange membrane fuel cells*, J. Mater. Chem., **2009**, 19, 1803.

[14] Bharat Avasarala, Pradeep Haldar, *Electrochemical oxidation behavior of titanium nitride based electrocatalysts under PEM fuel cell conditions*, Electrochemica acta, **2010**, 55, 9024.

[15] D. L. Wood, J. Chlistunoff, J. Majewski and R. L. Borup, *Nafion Structural Phenomena at Platinum and Carbon Interfaces*, J. Am. Chem. Soc., **2009**, 131 (50), 18096–18104

[16] A. Ignaszak, S. Ye and E. Gyenge, *A Study of the Catalytic Interface for O_2 Electroreduction on Pt: The Interaction between Carbon Support Meso/Microstructure and Ionomer (Nafion) Distribution*, J. Phys. Chem. C, **2009**, 113, 298.

[17] N.C. Saha, H.G. Tompkins, *Titanium nitride oxidation chemistry: An x-ray photoelectron spectroscopy study*, J. Appl. Phys., **1992**, 72, 3072–3079.

[18] Y. Massiani, A. Medjahed, P. Gravier, L. Argeme, L. Fedrizzi, *Electrochemical study of titanium nitride films obtained by reactive sputtering*, Thin Solid Films, **1990**, 191, 305–316.

[19] A. Vesel, M. Mozetic, J. Kovac, A. Zalar, *XPS study of the deposited Ti layer in a magnetron-type sputter ion pump*, Appl. Surf. Sci., **2006**, 253, 2941–2946.

[20] Malheiro, A. R., Perez, J. & Villullas, H. M. *Well-alloyed PtFe/C nanocatalysts of controlled composition and same particle size: Oxygen reduction and methanol tolerance*. J. Electrochem. Soc., **2009**, 156, B51-B58.

[21] Min, M. K., Cho, J. H., Cho, K. W. & Kim, H. *Particle size and alloying effects of Pt-based alloy catalysts for fuel cell applications*, Electrochemica Acta, **2000**, 45, 4211-4217.

[22] Wu, J. B. et al. *Truncated octahedral Pt_3Ni oxygen reduction reaction electrocatalysts*, J. Am. Chem. Soc., **2010**, 132, 4984-4985.

[23] D.Q. Yang, B. Hennequin, E. Sacher, Chem. Mater. XPS *Demonstration of $\pi-\pi$ Interaction between Benzyl Mercaptan and Multiwalled Carbon Nanotubes and Their Use in the Adhesion of Pt Nanoparticles*, Chemistry of Materials, **2006**, 18, 5033–5038.

[24] J.R. Croy, S. Mostafa, L. Hickman, H. Heinrich, B.R. Cuenya, *Bimetallic Pt-Metal catalysts for the decomposition of methanol: Effect of secondary metal on the oxidation state, activity, and selectivity of Pt,* Appl. Catal. A 350, **2008**, 207–216.

[25] R. Ahmadi, M.K. Amini, J.C. Bennett, *Pt–Co alloy nanoparticles synthesized on sulfur-modified carbon nanotubes as electrocatalysts for methanol electrooxidation reaction,* Journal of Catalysis, **2012**, 292, 81–89.

Chapter 8. Conclusions and Future Work

8.1 Conclusions

The Nafion® or similar membrane based polymer electrolyte membrane fuel cells (PEMFC) are limited to low temperature operation of less than 80 ^{o}C. A higher temperature (80-120 ^{o}C) operation of PEMFC would enhance the electrode kinetics, improves the CO tolerance of Pt, reduces the noble metal catalyst loading and simplifies the thermal and water management. The proton conductivity of Nafion® membrane depends on hydration level and the operation of fuel cell above 80 ^{o}C results in dehydration of the membrane which in turn affect the fuel cell performance. The incorporation of inorganic hydrophilic oxide materials into the Nafion® polymer matrix enhances the water retention and corresponding proton conductivity to operate at high temperature.

Functionalised graphite oxide is an insulator and hydrophilic in nature and exhibits the proton conductivity. The presence of acidic functional groups such as carboxylic acid, hydroxyl group, epoxy and sulfonic acid groups on edges and basal plane of the graphene oxide are means to achieve proton transport. The measured in-plane and through-plane proton conductivity values of functionalised graphene oxide paper are 0.04 and 0.012 S.cm^{-1} at 303 K, respectively, and lie in the conductivity range of Nafion between 0.01 to 0.1 S.cm^{-1} in a humid environment. The in-plane proton conductivity is attributed to the presence of functional groups on edges and basal plane. The through-plane proton conductivity is attributed to a Grothus-type mechanism in which reorganisation of hydrogen bonds play a vital role in the presence of water between each graphene layer. These characteristics make functionalised graphite oxide suitable for Nafion® composite membrane for high temperature operation.

Graphite oxide (GO) and sulfonated graphite oxide (SGO) based Nafion® composite membranes offer the good proton conductivity, extending operating temperature up to 120 ^{o}C. The proton conductivity of the composite membranes depends on relative humidity. The content of GO and SGO of 4 wt% in the Nafion® polymer matrix showed higher proton conductivity of 0.026 and 0.029 S.cm^{-1} at 120 ^{o}C and 25% RH, whereas the recast Nafion had a conductivity of 0.012 S.cm^{-1}. The SGO/Nafion composite membrane gave peak power density of 240 mW cm^{-2}, whereas recast Nafion gave a power density of 94 mW cm^{-2} at 120 ^{o}C and 25% RH.

A non-fluorinated polymer such as sulfonated poly ether-ether ketone (SPEEK) is an inexpensive polymer and possesses good thermo mechanical stability. The proton conductivity of SPEEK depends on the degree of sulfonation as well as hydration. At a sulfonation of 60% the proton conductivity was less than Nafion® membrane and above 70 % it becomes partially soluble in water. A SPEEK membrane with a sulfonation of 60% was used to make composite membranes with SGO. A SGO/SPEEK composite membrane had a proton conductivity of 0.055 $S.cm^{-1}$ at 80 ^{o}C and 30% RH, which was higher than that of SPEEK membrane (0.015 $S.cm^{-1}$). The SGO/SPEEK composite membrane gave peak power density of 375 mW cm^{-2}, whereas SPEEK gave a power density of 254 mW cm^{-2} at 80 ^{o}C and 30% RH.

Nafion® stabilised Pt supported on TiN exhibited better ORR activity, stability and durability both in sulfuric acid and phosphoric acid medium than conventional Pt/C. The improved durability of Nafion® stabilised Pt/TiN is attributed to the corrosion resistant TiN support. Nafion® stabilisation of Pt protects the Pt from phosphate ion adsorption, in phosphoric acid medium and showed improved durability than conventional Pt/C. The Nafion® layer surrounding the Pt thought to provide enhanced electrochemically stability by inhibiting sintering and dissolution. Pt-Co alloy nanoparticles supported on TiN (Pt-Co/TiN) showed marked improvement in ORR activity and durability. Pt-Co/TiN electrocatalyst showed about 5% enhancement in ECSA after 1000 potential cycles of ADT, whereas Pt/C showed significant loss in ECSA. After 5000 potential cycles, the ECSA of Pt-Co/TiN decayed about 55%, whereas the ECSA of Pt/C had decayed about 85%. XPS analysis revealed electronic coupling between Pt and Co that enhanced the electrocatalytic activity of Pt-Co alloy catalyst.

8.2 Future work

The proton conductivity of the GO and SGO composite membranes are better than that of Nafion® based membranes, but the fuel cell performance is still lower, in order to achieve the maximum performance, it is required to optimise the membrane electrode assemblies based on the composite membranes. Future work should consider the following

- The optimisation of electrocatalyst loading in the electrocatalyst layer.
- The use of SGO as an ionomer (instead of Nafion® ionomer) in the electrocatalyst layer and optimisation of its content.

- The use of SGO/SPEEK as an ionomer instead of Nafion® ionomer in the electrocatalyst layer of SGO/SPEEK based MEAs.
- The longer term stability tests of GO and SGO composite membrane based MEAs.
- An alternative to Nafion® membrane, other polymers such as poly vinyl alcohol (PVA), functionalised Polyvinylidene difluoride (PVDF) composite membranes with SGO could be prepared.

The electrochemical evaluation of the cathode electrocatalyst based on Nafion® stabilised Pt and Pt-Co alloy nanoparticles supported on TiN support showed enhanced stability, durability and electrocatalytic activity compared to commercial Pt/C. In order to assess these electrocatalyst in fuel cell future work should consider the following aspects

- The fuel cell evaluation of Nafion® stabilised Pt/TiN as cathode electrocatalyst for phosphoric acid based and other PEM (Nafion and SGO/Nafion) based fuel cells and durability test under fuel cell operation.
- The fuel cell characterisation of Pt-Co/TiN as cathode electrocatalyst and durability test under fuel cell operation.

Appendix A

XRD calculations for GO and SGO

The interplanar distances (d) for graphite oxide and sulfonated graphite oxide (001) diffraction plane were calculated using Bragg equation;

According to Bragg equation

$$d = n\lambda / 2\sin\theta$$

Where d is the interplanar distance, n is the order of diffraction and λ is the x-ray wavelength (1.54 A^o).

d (graphite oxide) = 1.54/2sin(11.26) = 7.85 A^o = 0.785 nm

d (sulfonated graphite oxide) = 1.54/2sin(11.36) = 7.51 A^o = 0.751 nm

XRD calculations for TiN, Pt and Pt-Co

Calculation of interplanar distance'd' and lattice parameter 'a' for TiN (111) peak

d (TiN (111)) = 1.54/2sin(37.2) = 2.44 A^o = 0.244 nm

Lattice parameter '*a*' can be calculated using the following equation;

$$a = d\sqrt{h^2+k^2+l^2}$$

a (TiN) = 2.44x1.73 = 4.22 A^0 = 0.422 nm

Calculation of interplanar distance'd' and lattice parameter 'a' for Pt (220) peak

d (Pt/TiN (220)) = 1.54A^o/2sin (67.67) = 1.38 A^o = 0.138 nm

a (Pt/TiN) = 1.54A^ox√2/sin (67.67/2) = 3.94 A^0 = 0.394 nm

Calculation of interplanar distance'd' and lattice parameter 'a' for Pt-Co (220) peak

d (Pt-Co/TiN (220)) = 1.54A^o/2sin (68.04) = 2.75 A^o = 0.275 nm

a (Pt/TiN) = 1.54A^ox√2/sin (68.04/2) = 3.87 A^0 = 0.387 nm

The mean particle sizes for Pt and Pt-Co nanoparticles were evaluated by Scherrer formula; using the full width at half maximum (FWHM) and the peak position of the Gaussian fitted Pt (220) peak.

According to Scherrer Formula:

$$t = K*\lambda/\beta\cos\theta$$

K is the shape factor with a typical value of about 0.9, λ is the X-ray wavelength, i.e., 1.54 A^o here, β is the full width at half maximum (FWHM) in radians, and θ is the Bragg angle. *t is* the mean size of the ordered (crystalline) domains, which may be smaller or equal to the grain size.

t (Pt/TiN) = 0.9 x 1.54 A0 /(0.025 x cos(67.67/2)) = 66.02 A^o = 6.602 nm

t (Pt-Co/TiN) = 0.9 x 1.54 A0 /(0.02 x cos(68.04/2)) = 83.03 A^o = 8.303 nm

Appendix B

RHE conversion

A saturated silver chloride electrode was used as the reference electrode in all electrochemical measurements. The measured potentials versus the Ag/AgCl reference electrode were converted to the reversible hydrogen electrode (RHE) scale via the Nernst equation:

$$E_{RHE} = E_{Ag/AgCl} + 0.059\ pH + E^{o}_{Ag/AgCl}$$

Where E_{RHE} is the converted potential versus RHE, $E_{\mathrm{Ag/AgCl}}$ is the experimental potential measured against the Ag/AgCl reference electrode, and $E^{o}_{\mathrm{Ag/AgCl}}$ is the standard potential of Ag/AgCl at 25 °C (0.1976 V). The electrochemical measurements were carried out in 0.5 M H_2SO_4 and H_3PO_4 (pH = 0.3) at room temperature; therefore,

$$E_{\mathrm{RHE}} = E_{\mathrm{Ag/AgCl}} + 0.059*0.3 + 0.1976\ \mathrm{V}$$

$$E_{\mathrm{RHE}} = E_{\mathrm{Ag/AgCl}} + 0.0177 + 0.1976\ \mathrm{V}$$

$$E_{\mathrm{RHE}} = E_{\mathrm{Ag/AgCl}} + 0.215\ \mathrm{V}$$

Appendix C

List of publications

Book chapter

1) Keith Scott, Chenxi Xu, Wu Xu, Yuancheng Cao and **Ravi Kumar**: *"Innovative Graphene Technologies: Developments, Characterization and Evaluation".* Volume 2 Edited by Atul Tiwari (Smithers Rapra 2013, ISBN 9781909030213).

Journal articles

1) **Ravikumar**, Scott K. Freestanding sulfonated graphene oxide paper: a new polymer electrolyte for polymer electrolyte fuel cells. ***Chemical Communications,*** 2012, 48(45), 5584-5586.

2) **Ravikumar,** Xu CX, Scott K. Graphite oxide/Nafion composite membranes for polymer electrolyte fuel cells. ***RSC Advances,*** 2012, **2**(23), 8777-8782.

3) **Ravikumar,** Mamlouk M, Scott K. A Graphite Oxide Paper Polymer Electrolyte for Direct Methanol Fuel Cells. ***International Journal of Electrochemistry,*** 2011, 434186.

4) **Ravi Kumar**, Sivakumar Pasupathi, Bruno G. Pollet, Keith Scott. Nafion-stabilised platinum nanoparticles supported on titanium nitride: an efficient and durable electrocatalyst for phosphoric acid based polymer electrolyte fuel cells. ***Electrochemica acta,*** 2013, 109, 365-369.

5) **Ravikumar,** Mamlouk M, Scott K. Sulfonated Poly ether-ether Ketone – Sulfonated graphene oxide composite membranes for Polymer electrolyte fuel cell. ***RSC advances,*** 2013(article in press)

6**) Ravikumar,** Keith Scott, Pt-Co nanoparticles supported on titanium nitride as an efficient electrocatalyst for oxygen reduction (To be submitted)

7) Xu CX, Cao YC, **Ravikumar,** Wu X, Wang X, Scott K. A polybenzimidazole/sulfonated graphite oxide composite membrane for high temperature polymer electrolyte membrane fuel cells. ***Journal of Materials Chemistry,*** 2011, 21(30), 11359-11364.

8) Thotiyl, Ottakam, **Ravi Kumar** and S.Sampath. Pd Supported on Titanium Nitride for Efficient Ethanol Oxidation. ***J.Phys.Chem. C.,*** 114(41), 17934, 2010.

9) Thotiyl, Ottakam, **Ravi Kumar** and S.Sampath. Platinum Particles Supported On Titanium Nitride: An Efficient Electrode Material for the Oxidation of Methanol in Alkaline Media. ***Journal of Material Chemistry*** 20(47), 10643, 2010.

10) V. Kiran, **Ravikumar**, N. T. Kalyanasundaram, S. Krishnamurty, A. K. Shukla S.Sampath. Electro-oxidation of Borohydride on Rhodium, Iridium and Rhodium-Iridium Bimetallic Nanoparticles with Implications to Direct Borohydride Fuel Cells. ***J.Electrochem. Soc.***, 157(8), B1201, 2010.